DOCTOR OF PHILOSOPHY

A Universal Magnetic Carrier for use in Cancer Prodrug Therapy

Hobbs, Robert

Award date:
2015

Awarding institution:
Bangor University

A Universal Magnetic Carrier for use in Cancer Prodrug Therapy

A thesis submitted for the degree of

Doctor of Philosophy

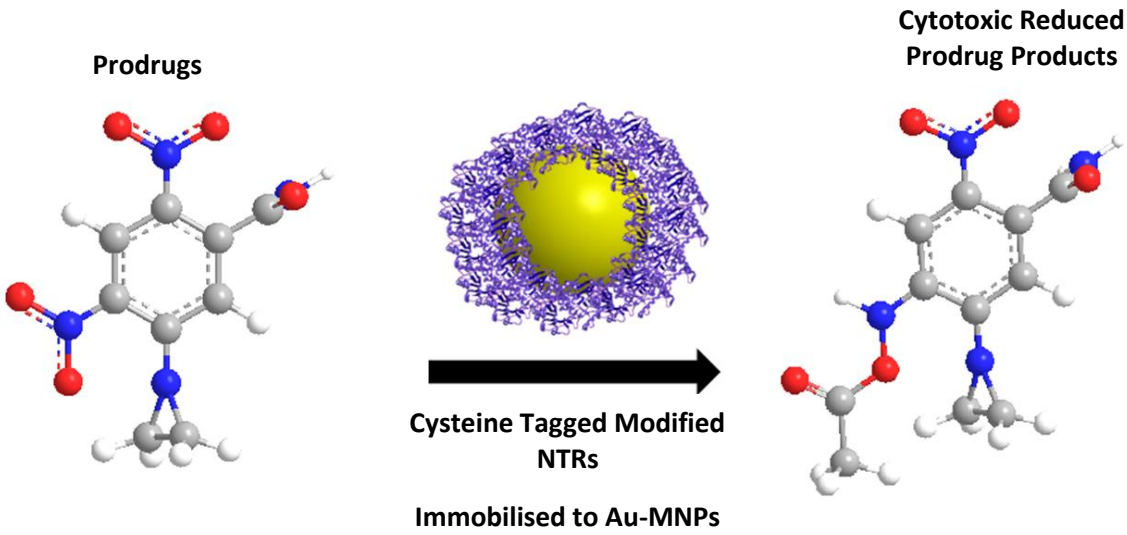

PRIFYSGOL BANGOR UNIVERSITY

Prifysgol Bangor • Bangor University

by
Robert John Hobbs

'The science of today is the technology of tomorrow'

Edward Teller

Declaration and Consent

Details of the Work

I hereby agree to deposit the following item in the digital repository maintained by Bangor University and/or in any other repository authorized for use by Bangor University.

Author Name: Mr Robert Hobbs

Title: A Universal Magnetic Carrier For Use In Cancer Prodrug Therapy

Supervisor/Department: Dr Christopher Gwenin/School of Chemistry

Funding body (if any): KESS/ESF

Qualification/Degree obtained: Doctor of Philosophy in Chemistry

This item is a product of my own research endeavours and is covered by the agreement below in which the item is referred to as "the Work". It is identical in content to that deposited in the Library, subject to point 4 below.

Non-exclusive Rights

Rights granted to the digital repository through this agreement are entirely non-exclusive. I am free to publish the Work in its present version or future versions elsewhere.

I agree that Bangor University may electronically store, copy or translate the Work to any approved medium or format for the purpose of future preservation and accessibility. Bangor University is not under any obligation to reproduce or display the Work in the same formats or resolutions in which it was originally deposited.

Bangor University Digital Repository

I understand that work deposited in the digital repository will be accessible to a wide variety of people and institutions, including automated agents and search engines via the World Wide Web.

I understand that once the Work is deposited, the item and its metadata may be incorporated into public access catalogues or services, national databases of electronic theses and dissertations such as the British Library's EThOS or any service provided by the National Library of Wales.

I understand that the Work may be made available via the National Library of Wales Online Electronic Theses Service under the declared terms and conditions of use (http://www.llgc.org.uk/index.php?id=4676). I agree that as part of this service the National Library of Wales may electronically store, copy or convert the Work to any approved medium or format for the purpose of future preservation and accessibility. The National Library of Wales is not under any obligation to reproduce or display the Work in the same formats or resolutions in which it was originally deposited.

Statement 1:

This work has not previously been accepted in substance for any degree and is not being concurrently submitted in candidature for any degree unless as agreed by the University for approved dual awards.

Signed …….. (candidate)

Date ……..

Statement 2:

This thesis is the result of my own investigations, except where otherwise stated. Where correction services have been used, the extent and nature of the correction is clearly marked in a footnote(s).

All other sources are acknowledged by footnotes and/or a bibliography.

Signed ……. (candidate)

Date …….

Statement 3:

I hereby give consent for my thesis, if accepted, to be available for photocopying, for inter-library loan and for electronic storage (subject to any constraints as defined in statement 4), and for the title and summary to be made available to outside organisations.

Signed ……. (candidate)

Date …….

NB: Candidates on whose behalf a bar on access has been approved by the Academic Registry should use the following version of **Statement 3:**

Statement 3 (bar):

I hereby give consent for my thesis, if accepted, to be available for photocopying, for inter-library loans and for electronic storage (subject to any constraints as defined in statement 4), after expiry of a bar on access.

Signed …… (candidate)

Date ……

Statement 4:

Choose **<u>one</u>** of the following options

a) I agree to deposit an electronic copy of my thesis (the Work) in the Bangor University (BU) Institutional Digital Repository, the British Library ETHOS system, and/or in any other repository authorized for use by Bangor University and where necessary have gained the required permissions for the use of third party material.	
b) I agree to deposit an electronic copy of my thesis (the Work) in the Bangor University (BU) Institutional Digital Repository, the British Library ETHOS system, and/or in any other repository authorized for use by Bangor University when the approved **bar on access** has been lifted.	**YES**
c) I agree to submit my thesis (the Work) electronically via Bangor University's e-submission system, however I **opt-out** of the electronic deposit to the Bangor University (BU) Institutional Digital Repository, the British Library ETHOS system, and/or in any other repository authorized for use by Bangor University, due to lack of permissions for use of third party material.	

Options B should only be used if a bar on access has been approved by the University.

In addition to the above I also agree to the following:

1. That I am the author or have the authority of the author(s) to make this agreement and do hereby give Bangor University the right to make available the Work in the way described above.
2. That the electronic copy of the Work deposited in the digital repository and covered by this agreement, is identical in content to the paper copy of the Work deposited in the Bangor University Library, subject to point 4 below.
3. That I have exercised reasonable care to ensure that the Work is original and, to the best of my knowledge, does not breach any laws – including those relating to defamation, libel and copyright.
4. That I have, in instances where the intellectual property of other authors or copyright holders is included in the Work, and where appropriate, gained explicit permission for the inclusion of that material in the Work, and in the electronic form of the Work as accessed through the open access digital repository, *or* that I have identified and removed that material for which adequate and appropriate permission has not been obtained and which will be inaccessible via the digital repository.
5. That Bangor University does not hold any obligation to take legal action on behalf of the Depositor, or other rights holders, in the event of a breach of intellectual property rights, or any other right, in the material deposited.
6. That I will indemnify and keep indemnified Bangor University and the National Library of Wales from and against any loss, liability, claim or damage, including without limitation any related legal fees and court costs (on a full indemnity bases), related to any breach by myself of any term of this agreement.

Signature: ……

Date …….

Contents

Covering picture is an illustration of the prodrug CB1954 being activated to a cytotoxic hydroxylamine derivative following reduction by a nitroreductase.

Abstract

A Universal Magnetic Carrier for use in Cancer Prodrug Therapy

Magnetic nanoparticles have attracted huge amounts of interest in the scientific and healthcare communities. Fe_3O_4 and γ-Fe_2O_3 are magnetic nanoparticles of particular interest in nanotherapeutics and have already been approved for use by the Medicines and Healthcare Products Regulatory Agency along with the United States Food and Drug Administration.

Magnetic nanoparticle directed enzyme prodrug therapy is a novel drug delivery system being developed in this project to allow targeted cancer treatment. Magnetic nanoparticle directed enzyme prodrug therapy hopes to utilise gold coated magnetic nanoparticles to deliver nitroreductases; immobilised to the particle surface, to the tumour site under a magnetic field. At the tumour site the nitroreductases will convert prodrugs into their active cytotoxic forms destroying the tumour cells.

Gold coated magnetic nanoparticles have been successfully synthesized and the previously modified nitroreductases; NfsB and YfkO in both a –His and –Cys tagged form were expressed and purified. The nitroreductase YfkO-cys was then immobilised onto the synthesised gold coated magnetic nanoparticles *via* gold-thiol bonds. The YfkO-cys retained its enzymatic activity towards the prodrug CB1954 whilst conjugated to the particles and this is believed to be the first successful attempt and report of this system. Furthermore the genetically modified nitroreductase NfsB-cys has been tested on a cell line *in vitro.* Using a combination treatment of nitroreductase (200 nM), cofactor NADH and the prodrug CB1954 (10 µM) the system exhibited an average cell survival rate of ~ 20%.

Acknowledgments

Firstly, and most importantly, I would like to thank my supervisor Dr. C. Gwenin for his support and guidance during this project. Your interest and passion for this work kept me focussed and invested in the project and helped guide me to become a better researcher and scientist. I would also like to thank all the members of the Electrochemistry and Biosensors research group, particularly those working on the cancer project for their camaraderie and keeping me going even through the tough times. I would also like to extend my thanks to the members of my research committee Dr. A. Davies and Dr. L. Jones for their guidance and imparted knowledge on the work. I would also like to thank Dr. P. Holliman who was formerly part of my research committee and never failed to help me strive to improve. I would also like to thank the School of Chemistry technical staff for allowing me to use the equipment in the department and for their advice and training.

I would like to acknowledge KESS and ESF along with Morvus Technologies LTD for funding this PhD.

I would also like to thank Dr. C.J. von Ruhland (School of Medicine, Cardiff University, Cardiff, UK) for his contributions to characterise some of the particles that were produced during this research.

There must also be probably the biggest thanks of all to my wife Eleanore Hobbs for her love, support and patience. Mostly thanks must be given to her for looking after and nurturing our beautiful daughters Isobelle and Arianwen. Thanks must also be bestowed upon my parents Alan and Caroline and my parent in laws Paul and Innys for their love and support.

Finally thanks to my friends Dan Williams, Jennifer Halliwell, Dan Ellis, Leo Furnell, Arthur Connell and Eurig Jones for lending me their ears and keeping me sane and allowing me to moan and talk about things other than my work.

Abbreviations

1T	1 Tesla
Ab	Antibody
ADEPT	Antibody directed enzyme prodrug therapy
AM	Acetomethoxy
APS	Ammonium persulfate
Au-MNP(s)	Gold coated magnetic nanoparticle(s)
bp	Base pair
BSA	Bovine serum albumin
CB1954	5-(1-aziridinyl)-2,4-dinitrobenzamide
CTAB	Cetyltrimethylammonium bromide
cts	Counts
CV	Cyclic voltammetry
ddH_2O	Double distilled water
DDI	Double deionised
DEPT	Directed enzyme prodrug therapy
DLT	Dose limiting toxicity
DMEM	Dulbecco's modified eagle medium
DMSO	Dimethyl sulfoxide
DNA	Deoxyribonucleic acid
DPBS	Dulbecco's phosphate buffered saline
DTD	DT diaphorase
D_{XRD}	X-ray diffraction determined diameter
E. coli	*Escherichia coli*
EBV	Epstein-Barr virus
EDAX	Energy-dispersive X-ray analysis
EDTA	Ethylenediaminetetraacetic acid
EMA	European medicines agency
FBS	Fetal bovine serum
FDA	Food and drug administration
FMN	Flavin mononucleotide
FWHM	Full width half maximum
GDEPT	Gene directed enzyme prodrug therapy
GNP(s)	Gold nanoparticle(s)
HPLC	High-performance liquid chromatography
IB	Imidazole buffer
IMS	Industrial methylated spirit
IPTG	Isopropyl β-D-1-thiogalactopyranoside
kb	Kilobase
k_{cat}	Turnover number
k_{cat}/K_m	Catalytic efficiency
kDa	Kilo dalton
K_m	Michaelis constant
LB	Lysogeny broth
MHRA	Medicines and healthcare products regulatory agency
MNDEPT	Magnetic nanoparticle directed enzyme prodrug therapy
MNP(s)	Magnetic nanoparticle(s)
MRI	Magnetic resonance imaging

MTT	(3-(4,5-Dimethylthiazol-2-yl)-2,5-diphenyltetrazolium bromide)
NAD^+	Nicotinamide adenine dinucleotide (oxidised form)
NADH	Nicotinamide adenine dinucleotide (reduced form)
$NADP^+$	Nicotinamide adenine dinucleotide phosphate (oxidised form)
NADPH	Nicotinamide adenine dinucleotide phosphate (reduced form)
NEAA	Non-essential amino acids
NTR(s)	Nitroreductase(s)
OD	Optical density
PB	Phosphate buffer
PBS	Phosphate buffed saline
PEG	Polyethylene glycol
RES	Reticuloendothelial system
rpm	Revolutions per minute
SCE	Saturated calomel electrode
SD	Standard deviation
SDS	Sodium dodecyl sulfate
SDS-PAGE	Sodium dodecyl sulfate-polyacrylamide gel electrophoresis
SEM	Standard error of mean
SIPP(s)	Superparamagnetic iron platinum particle(s)
SPION(s)	Superparamagnetic iron oxide nanoparticle(s)
SPR	Surface plasmon resonance
SQUID	Superconducting quantum interference device
TBE	Tris-borate Ethylenediaminetetraacetic acid
TEM	Transmission electron microscopy
TEMED	*N*,*N*,*N*′,*N*′-Tetramethylethane-1,2-diamine
TMAOH	Tetramethylammonium hydroxide
TNM	Tumour, node, metastasis
tRNAs	Transfer ribonucleic acid
UV	Ultraviolet
VDEPT	Virus directed enzyme prodrug therapy
V_{max}	Maximum reaction rate
w/v	Weight by volume
xg	Centrifugal force in gravities
XRD	X-ray diffraction

CHAPTER 1

INTRODUCTION

Chapter 1 - Introduction

1.1 Introduction

Cancer is an aggressive and complex disease and is a leading cause of death worldwide, accounting for ~ 8 million deaths annually (2012).[1,2] It is a massive strain on health services across the globe and although mortality rates have been slowly but steadily falling for around the last 30 years, predominately in western countries, this decline is expected to eventually plateau to a fixed share of the population.[3–5] The main reason for this decrease in mortality is attributed to both the scientific and medical professions gathering more information about the disease and therefore reaching a better understanding of its biology and progression.[6] Through substantial funding and investment in cancer treatment research, treatments available to patients are now far more advanced. This is helping to decrease mortality rates further, with approx. £12 billion spent per annum.[7] Whilst there is a current trend of decline in the mortality rates associated with cancer; the global death rate for the disease is set to peak at ~17 million by the year 2030.[8] It is predicted that cancer will still present a considerable problem for many years to come unless even further advances in diagnostics, treatment and patient care come to fruition.[9,10] One of the main and most widely available treatment options accessible to cancer patients is chemotherapy but this has a major disadvantage in that it has prevalent toxic side effects and an inability to be used at an effective/efficient dosage due to its dose limiting toxicity (DLT).[11,12] Thus recent research is swaying heavily to the development of tumour targeting or tumour specific drugs.[13]

The area of research that this project focuses on is facilitating the targeted delivery of the toxic compounds utilising enzymes; it is suggested that this is a promising system for controlling cancerous tumours.[14] It is promising because by directing and only activating the compound to be cytotoxic at the site of a tumour, the treatment would be localised. This would not only limit the damage to non-cancerous cells but by being controlled and localised would allow an increase in dosage of the active compounds; making the treatment more effective due to not being constrained by the DLT of the compounds. This study will look at using a magnetic nanoparticle system as the delivery mechanism to control and localise the targeting of the treatment.

1.1.1 Cancer background

Cancer is currently responsible for approximately 30% of all deaths in the world each year.[15] In the UK more than 1 in 3 people will develop cancer in their lifetime with greater than 300,000 new cases diagnosed each year.[16] Breast, lung, bowel and prostate cancer account for over 50% of all the new cases of cancer.[16] Cancer initiates from alterations to deoxyribonucleic acid (DNA) sequences, this causes a cells biological processes to alter. The conversion of a normal functioning cell into a malignant tumour cell is a complex multi-stage process.[17]

The alteration in DNA sequences leads to the formation of a neoplasm, a new growth of tissue which is not coordinated with the tissue around it and does not behave or function as the neighbouring cells do.[18] Neoplasms occur in three forms; benign, premalignant and malignant. A benign tumour does not aggressively invade neighbouring tissue or grow to an unlimited size or metastasise. A premalignant neoplasm shows uncontrolled growth but as a group of proliferating cells does not invade or spread. Finally, a cancerous/malignant tumour will grow to an unlimited size, invade neighbouring tissue and spread. Ultimately a malignant tumour can be fatal;[18] around 90% of human cancer deaths are attributed to metastasis.[19]

Metastasis is the process whereby cells from a localised tumour spawn and colonise new sites where nutrients and space are not prohibiting; metastasis can be preceded by invasion where the local tumour itself invades the neighbouring tissue.[20] Mutations can occur in DNA sequences by many different methodologies. They can be caused *via* a chemical reaction which occurs when there is direct contact with mutagens or carcinogens;[21] exposure to radiation,[22] infection by viruses,[23] and harmful bacteria.[24] Mutations can also be caused by infection from fungi.[25] The inheritance of certain genetic markers is also linked to the development of cancer with these inherited genes potentially encouraging malignant traits to develop within the individual.[26–28]

Cancer research has, over the years been studied in great detail and as such a complex body of knowledge has been formed on the disease.[29] This research has led to the conclusion that cancer is a disease which involves dynamic changes in the genome.[29] Oncogenes and tumour suppressor genes have been identified as the two classes of cancers genes produced from mutations.[29,30] Oncogenes have a dominant gain of function whereas tumour suppressor genes are the opposite with a loss of function. These have been identified through alteration of both human and animal cancer cells along with experimental models.[30]

Hanahan and Weinberg proposed that there are rules that direct the transformation of normal human cells into malignant cancers.[29] They suggest that there are a small number of traits and acquired capabilities that are shared by most if not all human cancer types. These are proposed as the hallmarks of cancer in their study in 2000,[29] and were subsequently revised in 2011.[31] They proposed that the large catalogue of cancer cell genotypes is an appearance of six essential changes in cell physiology that, together, dictate malignant growth. These six hallmarks were updated to include a further two emerging hallmarks and two enabling characteristics, seen below in Figure 1.1.

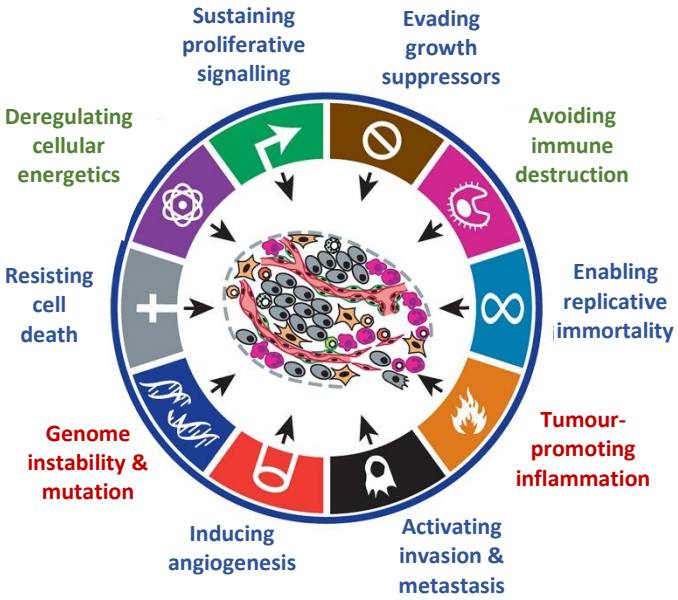

Figure 1.1. An illustration depicting the six hallmarks of cancer (blue text) as proposed by Hanahan and Weinberg in 2000[29] along with the two proposed emerging hallmarks (green text)[31] and the two proposed enabling characteristics (red text).[31]

Sustaining proliferative signalling is one of the six original hallmarks. The ability to sustain continuing proliferation is possibly the most fundamental trait of cancer cells.[31] Normal cells require mitogenic growth signals before they can move from an inactive state to a proliferative state. These signals are transmitted into the cell by transmembrane receptors that bind distinctive classes of signalling molecules. Hanahan and Weinberg surmise that no normal cell can proliferate without such signals and that many of the oncogenes in the cancer catalogue act by mimicking normal growth signalling in one way or another.[29] The deregulation of these signals allow the cancer cells to seize control. Intracellular tyrosine kinase domains, found in cell-surface receptors emit signals *via* branched intracellular signalling pathways that control the cell cycle progression and increases in cell size. There is still a gap in the understanding of the mechanisms that control the release of the mitogenic signals, however the mitogenic signalling in cancer cells is better understood and well reviewed by both Hynes and MacDonald in 2009[32] as well as Lemmon and Schlessinger in 2010.[33] Cancer cells can develop the ability

to maintain proliferative signalling in a variety of altering ways; they can produce growth factor ligands themselves,[34] simulate normal cells in supporting tumour-associated cells that then proceed to supply cancer cells with growth factors.[35]

Cancer cells must also overcome the action of tumour suppressor genes with control programs that can reversely regulate cell proliferation. There are numerous tumour suppressors that can limit cell proliferation and growth, *via* various mechanisms. Most of the discoveries of these have occurred due to emergence of the inactivation of animal and human cancers. The majority of the genes have been characterised as tumour suppressors based on loss or gain of function experiments in the mouse model.[31] Two model suppressors encode the retinoblastoma gene (RB) and TP53 gene; they work as central control nodes within two important cellular regulatory circuits that control a cells ability to proliferate and activate apoptosis. Sherr and McCormick studied the RB and p53 pathways in cancer.[36] The RB protein determines whether or not a cell will proceed through its growth and division cycle; it does this by integrating signals from primarily extracellular sources. Cancer cells that have a defect in the RB function are subsequently missing the control of cell-cycle progression which in turn leads to persistent proliferation.[36] TP53 predominately receives inputs from stress and abnormality sensors that operate within a cell's intracellular system. TP53 can stop cell-cycle progression whereby it detects that genome damage is excessive or if certain parameters are non-optimal such as growth promoting signals and oxygenation; it will stop the cycle progression until optimal conditions are returned.[36] TP53 can also in certain circumstances initiate apoptosis; this can occur if TP53 is presented with alarms such as overwhelming or irreparable damage to cellular subsystems.[36]

Studies conducted by Adams and Cory, 2007[37] alongside Lowe *et al*, 2004[38] have established that apoptosis serves as a natural barrier to cancer development., this alongside many other studies have shed light on the signalling circuits that control apoptotic programming and this discovery has led to the conclusion that apoptosis is initiated in response to a number of physiological stresses that can be experienced by cancer cells during tumorigenesis or as a result of therapy *via* anticancer treatment. Damage to DNA associated with hyperproliferation and raised levels of oncogene signalling, which results in signalling imbalances are significant stresses that can induced apoptosis.[39] The research by Lowe *et al.* alongside Adams and Corey's studies have shed light on the possible that apoptosis is weakened in tumours that successfully progresses to high levels of malignancy and resistance to treatments and therapies.[37,38] Adams and Corey also went on the conclude and define that the apoptotic mechanism consists of both

downstream effector components and upstream regulators and that these regulators can be further subdivided into two main circuits. Briefly, the two circuits are responsible for obtaining and handling extracellular signals that induce cell death and the second for detecting and collating signals that originate intracellularly.[37] Both of these circuits results in the activation of caspases which lead to the disassembly of the cell and leads to it being consumed by both neighbouring cells and phagocytic cells, more detail can be found by referring to the study by Adams and Corey.[37]

By the time Hanahan and Weinberg published their first study into the hallmarks of cancer in 2000[29] it had been widely concluded and accepted that cancer cells require an unlimited ability to replicate to produce tumours; unlike normal cell lines in the body that can only undergo a limited passage of growth and division cycles.[31] This limit can be attributed with two main barriers to proliferation. The two barriers to proliferation are senescence; being defined as an irreversible step into a non-proliferative but still viable state and the second is entry into a crisis phase if this barrier is circumnavigated leading to apoptosis. On very few occasions the cells can emerge from the crisis phase avoided cell death and can then produce and unlimited replicative potential.[31] This transition has been termed immortalization and both Blasco, 2005[40] alongside Shay and Wright, 2000[41] have indicated that telomeres protecting the ends of chromosomes to prevent them from being detected as damaged DNA is a core reason for the cells ability to produce unlimited proliferation. Interestingly telomerase isn't present at any significant level in non-immortalized cell, yet it is seen to be expressed at functionally significant levels in ~ 90% of cells that become immortalized spontaneously.[31]

The importance of angiogenesis has historically only been deemed significant when rapidly growing large tumours had formed. However more recent research leads to the notion that angiogenesis also factors in the microscopic premalignant stage of tumour formation, leading to its confirmation as one of the six integral hallmarks of cancer.[31] Tumours require sustenance from the body such as oxygen and other various nutrients; as well as the facilities to dispose of wastes and carbon dioxide, this is a need is in common with normal tissues.

Tumour associated neovasculature addresses these needs, the development of vasculature involves both vasculogenesis; the initiation of new endothelial cells and their subsequent assembly into tubes and angiogenesis; the sprouting of new vessels from pre-existing vessels. After this change normal vasculature becomes predominately inactive. During tumour progression an 'angiogenic switch' is nearly always in use and remains active which results in normally dormant vasculature to constantly sprout new vessels which aid in the support and

sustenance of enlarging cancerous growths.[42] This proposal is backed up by various further studies which designate that the angiogenic switch is influenced and controlled by countervailing factors that can lead to an induction of angiogenesis to oppose it.[43,44] Angiogenesis can be triggered at a very early step in the multistage development of cancers. A study by Raica *et al* has revealed that the angiogenic switch can be 'tripped' early following histological analyses of various lesions.[42,45]

Talmadge and Fidler, 2010 illustrated that the multistep process of invasion and metastasis is a sequence of discrete steps and is often referred to as the invasion-metastasis cascade, see Figure 1.2.[46] This was building on Fidler's earlier research from 2003.[47]

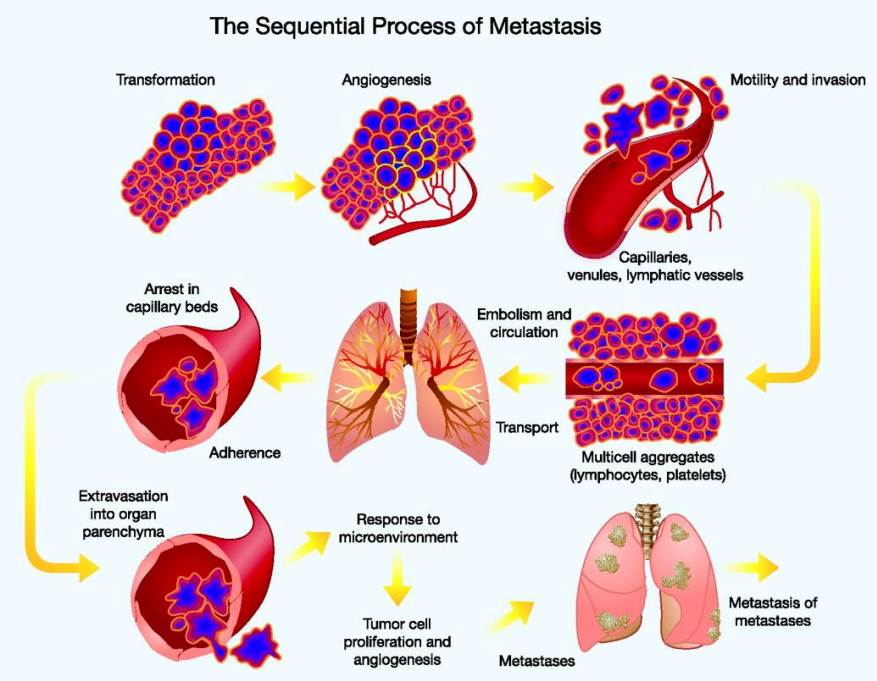

Figure 1.2 A schematic representation of the multistep process of invasion and metastasis.[46]

This illustration indicates a succession of biologic cellular changes, beginning with local invasion and subsequent intravasation of the cancer cells into neighbouring lymphatic and blood vessels, followed by the transport of cancer cells through the haematogenous and lymphatic systems. After this transportation the cancer cells discharge from the lumina of blood and lymphatic vessels into distant tissues; known as extravasation. This leads to the formation micro metastases and the final step is the growth of these micro lesions into a larger tumour, this is defined as colonization.[46] Berx and van Roy, 2009[48] building on Cavallaro and Christofori research in 2004[49] studied a key suppressor of this hallmark; whereby, they determined that the often observed downregulation and occasional mutant inactivation of E-cadherin in human carcinomas lead to the suppression of invasion and metastasis.[48,49]

The developed functional capabilities that allow cancers cells to survive, proliferate and disseminate have been identified and characterised as the six hallmarks mentioned. There are other avenues of ongoing research that suggest there may be other functionally important characteristics to enable development of cancer.[50] Two of the characteristics are of particular importance and have been included in Hanahan and Weinberg's updated review on the hallmarks of cancer.[31] Negrini *et al.* proposed in 2010 that genomic instability in cancer cell is an important attribute.[51] This can lead to random mutations; in genes such as TP53, it is believed that genomic instability results from mutations on DNA repair genes and oncogene-induced DNA damage.[51] The second characteristic revolves around the inflammatory state of premalignant and malignant growths that is driven by cells present in the immune system; leading to the promotion of tumour progression through varying means, see Colotta 2009 for a more in-depth discussion.[52] Further defined attributes have been studied and discussed for their importance to the development of cancer and their inclusion into the list of core hallmarks of cancer. Deregulation of cellular energetics is the first attribute proposed for inclusion into the hallmarks of cancer and is included in the updated review by Hanahan and Weinberg.[31] It involves reprogramming cellular energy metabolism to enable the support of continuous proliferation and growth; it replaces the program present in normal tissues to feed the physical work of associated cells and has been recently well defined in 2014 by Stine *et al.*[53] The second, proposed by Teng *et al.* involves cancer cells avoiding attack and elimination by immune cells.[54]

With all of the above mentioned factors and causes it is clear to see that a whole host of routes are available for a cell to acquire malignant traits and as such there is a vast array of mechanisms and biological pathways in which a cell can acquire the functionality to become malignant. It is therefore imperative that a variety of treatments are needed to combat the various forms this disease can take.[29]

1.1.2 Cancer treatment

Current conventional cancer therapies include a wide range of treatments ranging from surgery, chemotherapy and radiotherapy to hormonal therapy including; antibody therapy, immunotherapy and angiogenesis inhibitor therapy.[55] These wide range of treatments that patients can undergo are administered based on a number of deciding factors. The factors that affect which type or combination of treatments the patient receives are typically the type of cancer affecting the patient; the grade of the cancer, and the stage of cancer.[56] The grade of cancer is determined by how abnormal the tumour cells and tumour tissue look under a microscope and also how quickly a tumour is likely to grow.[57] The stage of cancer is used to describe the size of a cancer and its growth progression.[58] Using a universal staging system called tumour, node, metastasis (TNM) it allows doctors to have a common system to describe cancers. It allows for treatments to be standardised between different hospitals and treatment centres. It also allows for the results of the treatment to be accurately compared on a like for like basis between research studies.[59] To further complicate matters treatment can also be based around a patient's individual needs and circumstances.[59]

Cancer is a complex disease and with it affecting normal functioning parts of the body the need to destroy the affected cells brings a dilemma that needs to be balanced. Cancer treatment needs to be tailored to reach a compromise between the harm caused by many forms of the current treatments and the harm being caused by the cancer.[60] Surgery was once a very invasive and potentially risky treatment with often more harm than good caused.[61] However, with advances in surgical techniques; such as the use of cameras and more advanced surgical tools alongside tighter and more stringent hygiene practises and regulations the invasiveness of surgical procedures can be significantly reduced. Therefore, what was once a very risky treatment option has now become a far more successful and viable option.[62]

The other main form of treatment available is the administration of drugs. This has many disadvantages including their inability to discriminate between the different bioavailable cell types.[63] This means that for them to prove effective; they may need significant chemical design and a detailed understanding of their biological interactions in a physiological environment, in order to avoid the well-known and documented side-effects associated with cancer treatment. The need to eliminate or at the very least minimise these side-effects has led to the development of specific tumour-targeting drugs.[64] The research area behind the production of these drugs, well defined by R. Langer in 1998,[65] has increased at a rapid rate in recent years.[66,67]

One of the main disadvantages surrounding chemotherapies is that at high concentrations severe side-effects can begin to occur; chemotherapy has a DLT and it is when the concentrations breach the DLT there is often damage to healthy cells alongside the target cells preventing higher more effective dosages from being administered.[11] The DLT is a real disadvantage and as a consequence the treatment cannot potentially be administered at an effective concentration with a sufficient frequency of recurring treatment to effectively combat the disease and the treatment may cause considerable harm to the patient.[11,12] The development of tumour-targeting therapies where functionalised biologically active groups can be delivered only to cancer cell sites, is paramount to the reduction of harmful side-effects.[68]

Chemotherapy drugs are cytotoxic to the cancerous cells and broadly speaking they work by impairing the mitosis (cell division) of the cancerous cells.[69,70] Some chemotherapy drugs cause the cells to undergo apoptosis, which is so-called self-programmed cell death.[71] The process of reducing low toxicity compounds to highly cytotoxic drugs by enzymes has shown to be a promising system for controlling cancerous tumours.[14]

Chemotherapy drugs can be further spilt into subdivided mechanistic categories based on how they work. These categories include; alkylating agents, antimetabolites, microtubule inhibitors, intercalating agents and a newly defined category of targeted drugs that inhibit specific proteins in the cells.

Many different cancer therapies have been used through the ages with modern day chemotherapy beginning development in 1942 using mustine, see Figure 1.3.[72]

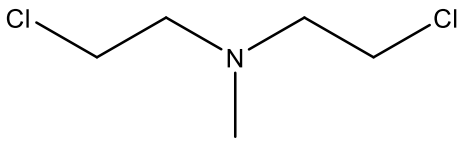

Figure 1.3 Structure of mustine.

1.1.2.1 Alkylating agents

Alkylating agents are the oldest group of chemotherapeutics in use today. Originally derived from mustard gas used in World War I, there are now many types of alkylating agents in use.[73] Alkylating a variety of molecules such as; DNA, RNA and proteins is how the name for this groups of compounds was derived and it is their ability to covalently bind to DNA *via* the alkyl functional group that is the main reason for their derived anti-cancer properties.[74] The compounds can either undergo intrastrand crosslinking; whereby they bind twice to one of the DNA's two strands, or, they can undergo interstrand crosslinking where they bind once to both

strands of the DNA. During cell division a cell trying to replicate or repair cross-linked DNA can cause the DNA strands to break which leads to apoptosis.[75,76] The alkylating agent group of compounds are cell cycle independent drugs due to their ability to work at any given point in the cell cycle process; this leads to the effect they have on cells being dose dependant with a linear correlation between the dosage of drug and the percentage of cell death.[77]

Due to the vast number of compounds defined as alkylating agents they have been further split into six subtypes which are; nitrogen mustards, nitrosoureas, tetrazines, aziridines, cisplatins and their derivatives and finally non-classical alkylating agents. Figure 1.4 defines a name and a structure of an example compound from each subtype.[75,78]

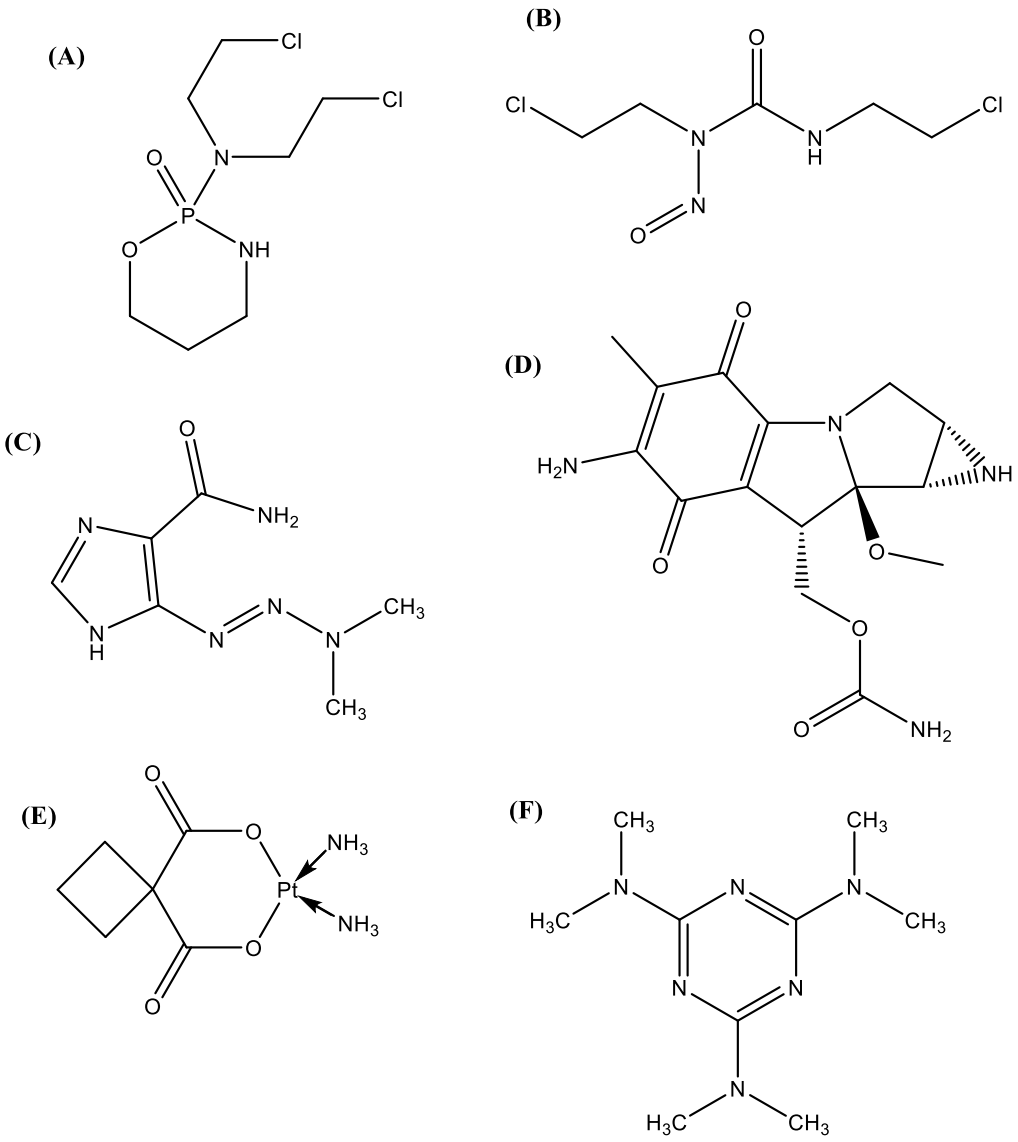

Figure 1.4 Structures of various alkylating agents; (A) Cyclophosphamide, from the nitrogen mustard subtype (B) Carmustine, from the nitrosoureas subtype(C) Dacarbazine, from the tetrazine subtype (D) Mitomycin, from the aziridine subtype (E) Carboplatin, from the cisplatin and derivative subtype and (F) Hexamethylmelamine, from the non-classical alkylating agent subtype.

1.1.2.2 Antimetabolites

The group of molecules classified as antimetabolites work by impeding DNA and RNA synthesis. The antimetabolites share similar structures to the nucleotides of DNA and RNA, they mimic either the nucleobases or nucleosides with alteration to some of the chemical groups.[79] The antimetabolites work by either blocking the enzymes required to synthesis DNA; preventing mitosis, or by being incorporated into DNA/RNA causing damage and inducing apoptosis.[79] In contrast to alkylating agents mentioned previously, antimetabolites are cell cycle dependant, meaning that the percentage of cell death plateaus above a certain dosage and also that they only have an effect during a specific part of the cell cycle, the DNA synthesis step known as the S-phase.[79] Antimetabolites are also divided into further subtypes, these being; anti-folate, thiopurines, fluoropyrimidines and deoxynucleoside analogues.[74,79] see Figure 1.5 for names and structures of examples from each subgroup.

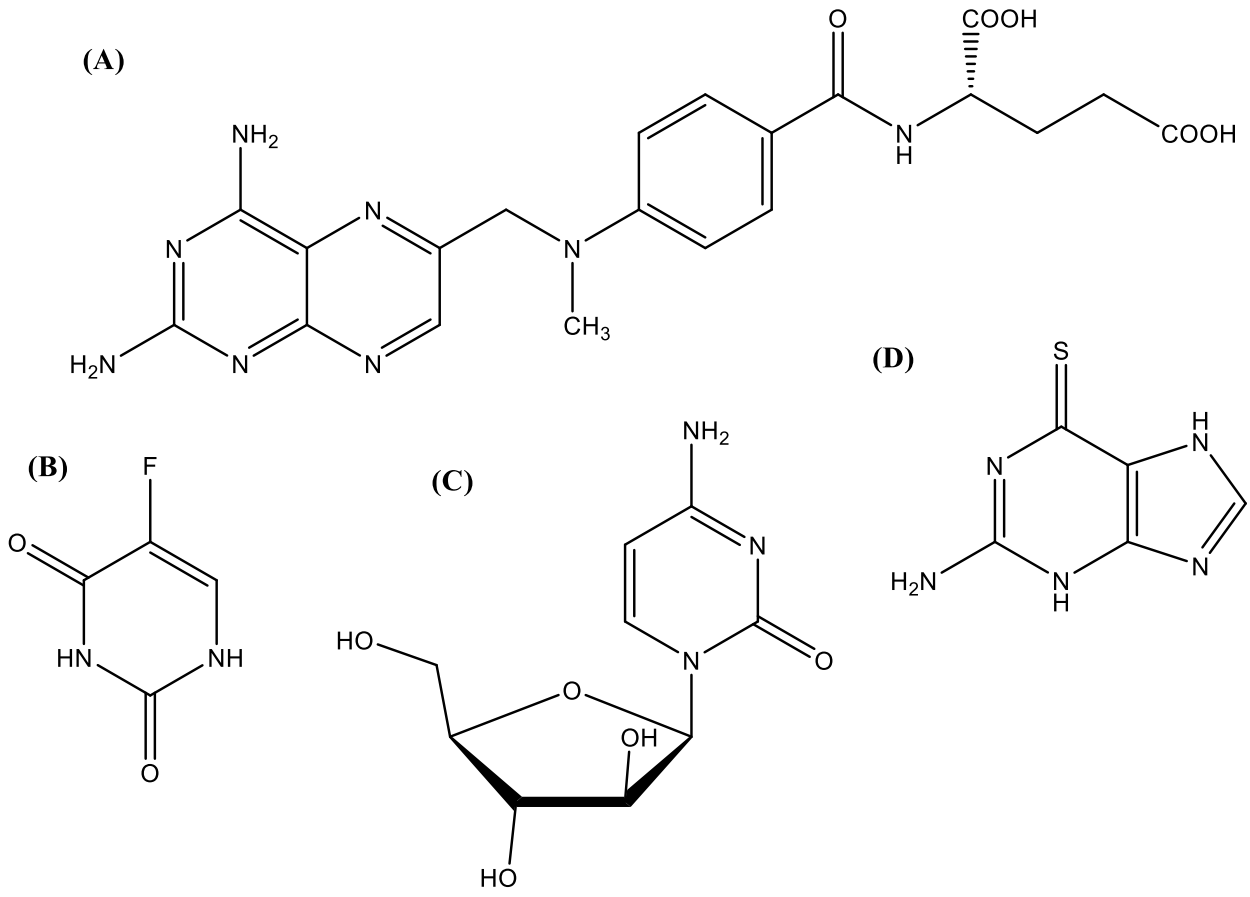

Figure 1.5 Structures of various antimetabolites; (A) Methotrexate from the anti-folate subtype, (B) Fluorouracil from the fluropyrimidine subtype, (C) Cytarabine from the deoxynucleoside analogue subtype and finally Thioguanine from the thiopurine subtype.

1.1.2.3 Microtubule inhibitors

The microtubule inhibitor class of chemotherapy agents work by directly interfering with the tubulin system instead of the DNA.[74] Tubulin binding molecules work by binding to the tubulin protein within the mitotic spindle and prevent polymerisation or depolymerisation into the microtubules which inhibits cell mitosis.[80,81] Paclitaxel, also known as Taxol (Figure 1.6) is one of the most utilised molecules. It was originally isolated from the pacific yew tree in 1962.[82] It is the first line of treatment for ovarian, breast, lung and colon cancer and it is incredibly effective, it is included on the World Health Organisation's list of essential medicines.[83]

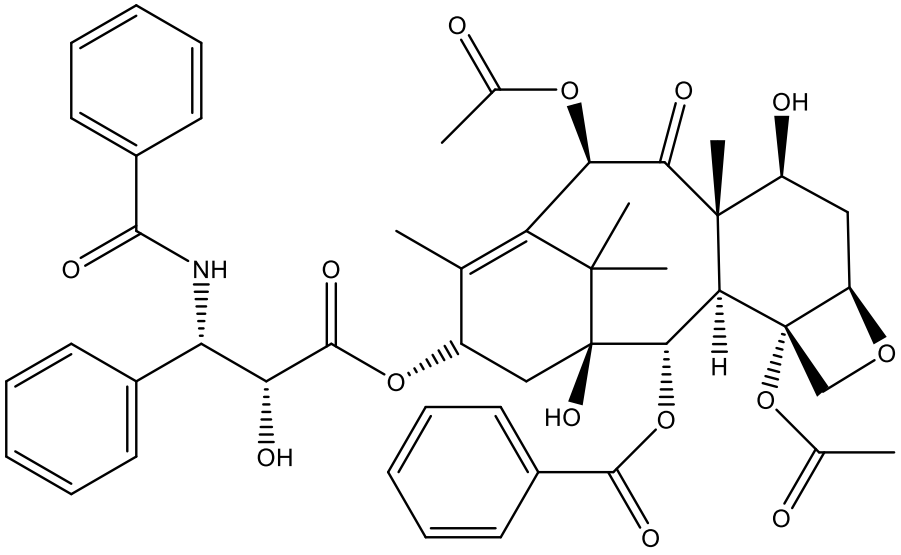

Figure 1.6 Structure of paclitaxel; also known as Taxol, a microtubule inhibitor.

1.1.2.4 Intercalating agents

An intercalating agent is so named because it wedges itself between the bases along DNA, this affects the structure of the DNA subsequently preventing DNA binding proteins such as polymerase, from functioning properly. This in turn stops DNA synthesis, inhibits transcription and prompts mutations. Doxorubicin, Figure 1.7, is an example of an intercalating agent and it works by intercalating with DNA and inhibiting macromolecular biosynthesis.[84–86] What this leads to is the inhibition of topoisomerase II; which relaxes supercoils in DNA for transcription, the doxorubicin stabilizes the enzyme complex after the breaking of the DNA chain for replication the DNA double helix is unable to reseal and therefore replication is stopped.[84]

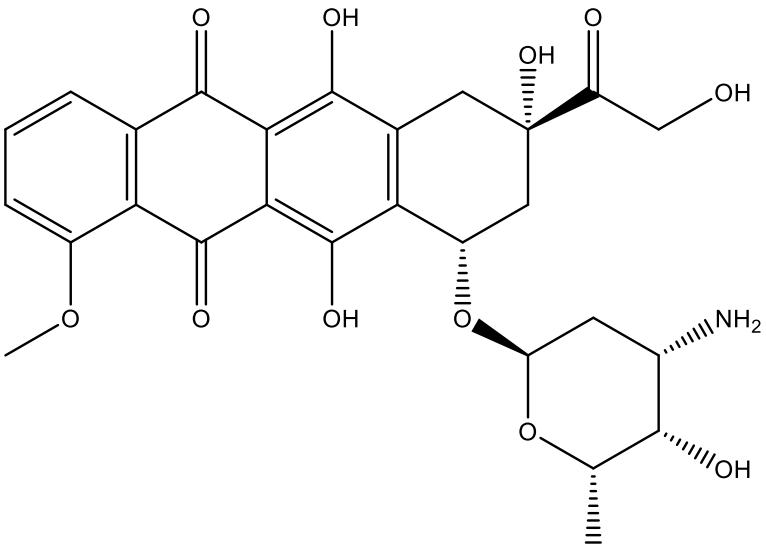

Figure 1.7 The structure of doxorubicin, an intercalating agent used in cancer therapy.

1.1.2.5 Recently targeted drugs that inhibit specific proteins in the cells

Signalling through proteins; known as signal cascade is a necessity in keeping cells alive. Certain proteins in this process utilise a phosphate group to act as an 'on' switch. In healthy cells this is controlled by a tyrosine kinase enzyme; which adds phosphate groups, and is cycled between on and off as required by the cell. In certain cells such as Philadelphia-positive chronic myelogenous leukaemia cells this process is disrupted by the BCR-Abl tyrosine kinase being stuck on and therefore continually adding the phosphate group.[87] The BCR-Abl is retained within the cytoplasm, this retention leads to uncontrolled proliferation. The BCR-Abl tyrosine kinase enzyme isn't present in normal healthy cells and as such only exists in cancer cells. A targeted form of therapy; whereby, only cancer cells are killed through a drug or therapies action is the use of imatinib, see Figure 1.8.[88] The ability to inhibit the BCR-Abl. One form of targeted therapy born out of a desire to inhibit this process is imatinib, and is often classed as a model for research into cancer therapeutics.[89]

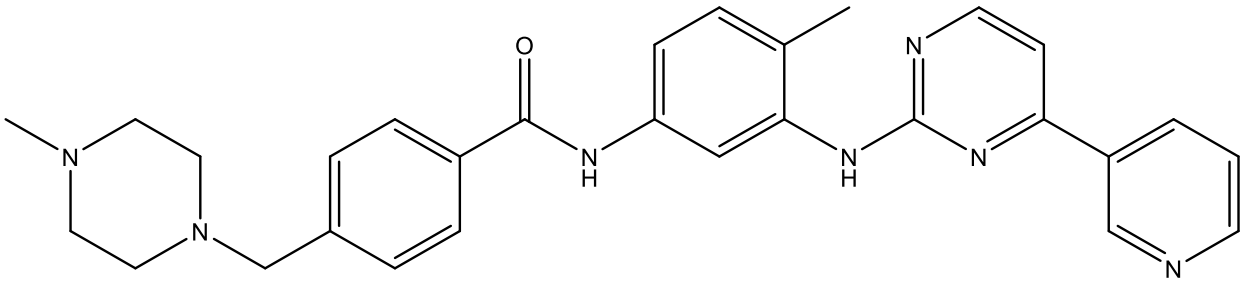

Figure 1.8 Structure of imatinib, a targeted drug that inhibits the BCR-Abl tyrosine kinase enzyme.

Another targeted drug that has been developed is vemurafenib; which has been shown to cause apoptosis in certain melanoma cell lines, see Figure 1.9.[90] It works by disturbing the B-Raf/MEK step on the B-Raf/MEK/ERK pathway, as long as the B-Raf exhibits a common mutation (V600E). This mutation is means that at the 600 amino acid position the normally present valine is replaced by a glutamic acid.[91] This leads to vermurafenib only being a viable treatment for melanoma patients who exhibit this V600E mutation on the B-Raf protein.[91]

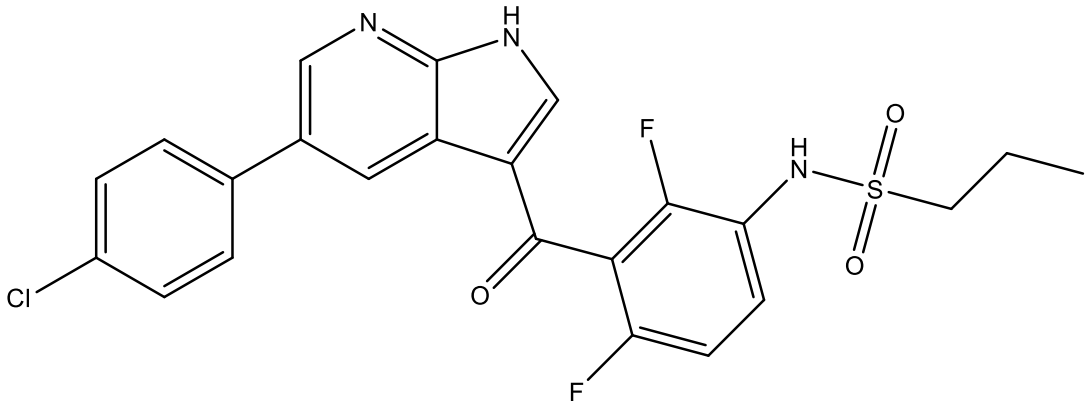

Figure 1.9 Structure of vermurafenib, an inhibitor of the B-Raf/MEK step.

Alongside working on the melanoma patients which have the V600E mutation, ~ 60% of all melanoma patients have the mutation. Vermurafenib has also shown to be have some effectiveness towards the rarer V600K B-Raf mutation. Any melanoma cells without these mutations are not inhibited by the drug. The main disadvantage of Vermurafenib is that is can lead to stimulation of non-mutated B-Raf, which can in turn potentially lead to promotion of tumour growth.[92,93]

Herceptin; the common trade name of trastuzumab is a monoclonal antibody that works by interfering with the HER2/neureceptor.[94] Herceptin is needed to inhibit the HER receptors as these are proteins which are imbedded into cell membrane. They communicate epidermal growth factor signals from outside the cell to intracellular positions, allowing genes to be turned on and off.[95] The HER proteins stimulate proliferation and in certain types of breast cancer the HER2 protein is overexpressed, causing cancer cells to uncontrollably reproduce.[94,95] Therefore, by inhibiting this process and preventing the over expression of HER2 proteins Herceptin is an effective treatment for breast cancer cases where HER2 is overexpressed.

1.2 Directed enzyme prodrug therapy

Directed enzyme prodrug therapies (DEPT) utilise low toxicity prodrugs which are activated to cytotoxic compounds by specific enzymes.[96–98] In order for targeted tumour therapies to work they require the enzyme or cofactor in the treatment to be exclusively present in cancer cells and to be lacking in normal functioning cells. Targeted therapies can also work if the enzymes that originate within the cell or tissue can only be expressed in specific target organs where a tumour is localised.[99] Achieving a therapy by which enzymes or cofactors are exclusively present in cancer cells has led to the development of a range of strategies to deliver enzymes not native to the host exclusively to tumour cells.

1.2.1 Commonly used enzyme-prodrug combinations

There are many different enzyme-prodrug combinations that have been developed and researched.[100] Research by Denny lead to a review of 12 enzymes and 42 prodrugs used in various combinations towards an effective gene directed enzyme prodrug therapy.[100] Table 1.1 lists the 12 enzymes and 42 prodrugs studied, with the most common combinations highlighted red.

Table 1.1 A table showing the combinations of 12 enzymes alongside 42 prodrugs studied by Denny, with the most common combination highlighted in red.[97,100]

Enzyme	Prodrugs			
Thymidine Kinase	**Ganciclovir**	Ganciclovir elaidic acid ester	Penciclovir	Acyclovir
	Valacyclovir	(E)-5-(2-bromovinyl)-2′-deoxyuridine	Zidovudine	2′-Exo-methanocarbathymidine
Carboxypeptidase	**4-[(2-chloroethyl)(2-mesyloxyethyl)amino]benzoyl-L-glutamic acid**	Hydroxy- and amino-aniline mustards	Anthracycline glutamates	Methotrexate α-peptides
CYP Enzymes	**Cyclophosphamide**	Ifosfamide	Acetaminophen	4-Ipomeanol
Nitroreductase	**CB1954**	SN23862	4-Nitrobenzyl carbamates	Quinones
Purine Nuceloside Phosphorylase	6-Methylpurine deoxyriboside	Fludarabine		
Horse-Radish Peroxidase	**Indole-3-acetic acid**	5-Fluoroindole-3-acetic acid		
Carboxylesterase	Irinotecan	Anthracycline acetals		
Glycosidase Enzymes	HM1826	Anthracycline acetals		
Thymidine Phosphorylase	5′-Deoxy-5-fluorouridine			
Methionine-α, γ-Lyase	Selenomethionine			
Guanine Ribosyltransferase	6-Thioxanthine			
Cytosine Deaminase	**5-Fluorocytosine**			

Denny concluded that prodrugs of DNA alkylating agents, seem to be in general more active prodrugs and require shorter dosing schedules to be effective.[100] These prodrugs of DNA alkylating agents are also less cell cycle specific than some of the antimetabolite based prodrugs systems and are more effective against non-cycling tumour cells. This is important as the key criteria for a prodrug is their ability to be activated by the enzyme efficiently and selectively, they must also be metabolised to strong cytotoxins and be able to effectively kill cells regardless of the stage of the cell cycle they are in.[100] Both the prodrug and the metabolised activated product must have good distributive properties to allow for maximum efficiency of the bystander effect.

The six most common enzyme-prodrug combinations have been highlighted and include the following: herpes virus 1 thymidine kinase/ganciclovir, carboxypeptidase/ 4-[(2-chloroethyl)(2-mesyloxyethyl)amino]benzoyl-L-glutamic acid, CYP enzymes/ cyclophosphamide, NTR/CB1954, horseradish peroxidase/indole-3-acetic acid and cytosine deaminase/5-fluorocytosine.[97]

The thymidine kinase/ganciclovir system requires active DNA replication in order for the system to become cytotoxic, whereas the NTR/CB1954 and cytosine deaminase/5-flurocytosine systems require further metabolisation by endogenous enzymes present in the cells in order for them to exhibit cytotoxicity.[97]

The cytosine deaminase system produces an activated drug with a long half-life allowing it more time to work. The thymidine kinase system is disadvantaged by having to rely on cell to cell contact to initiate diffusion into neighbouring cells. Gap junctions are required in order for the activated metabolites of the prodrug, due to it being non-membrane permeable.[97]

The NTR/CB1954 system based on initial studies shows that it appears to react faster than most combinations, this was characterised by both Bridgewater *et al.*[101] and Cui *et al.*[102] who reported significant cytotoxic effects after 4 hours in vitro and 24 h in vivo respectively. This has been explained in part due to the fact that the cytotoxic activated drug is a DNA cross-linking agent and it is able to kill cells in both a non-proliferating and proliferating state, without the need for the DNA to enter an active replication phase.[103]

Initial research into these therapies proved promising and three notable areas of interest are; antibody-DEPT (ADEPT),[104,105] gene-DEPT (GDEPT)[106] and virus-DEPT (VDEPT).[107,108]

1.2.2 Antibody directed enzyme prodrug therapy

The main principle of ADEPT is the use of an antibody that can be directed towards a tumour associated antigen to immobilise an enzyme to a tumour site.[104] The selectivity of a target tumour is achieved using specific antibodies (Ab) that can form Ab-enzyme conjugates that will preferentially bind to antigens that are expressed on the surface of the tumour cells.[54] This in turn enables the enzyme to be retained at tumour sites even after it has been allowed time to clear the blood and other normal tissue systems.[104] The next step is to administer a non-toxic prodrug which when reacted with the tumour immobilised enzyme will produce a high cytotoxic agent.[104] An advantage of this system of delivery is that a relatively small cytotoxic agent can be created within a tumour site which is much easier to diffuse than an antibody molecule which is much larger in size comparison.[104] Another main advantage of the system is that it can undergo an amplification, meaning that just a single molecule of enzyme will catalyse the conversion of multiple molecules of prodrug into the desired cytotoxic agent.[105] The cytotoxic agent can also diffuse to neighbouring cells due to the prodrug being reduced extracellularly, killing the cells *via* the bystander effect.[109] The main disadvantage to ADEPT systems is the immunogenicity of the antibody-enzyme conjugate; this is a problem because it can seriously limit multiple cycles of treatment.[110] Other disadvantages include the difficulty and cost associated with the development of antibodies and ensuring their purity.[110]

1.2.3 Gene directed enzyme prodrug therapy

Gene directed therapy otherwise known as suicide gene therapy, this is where the enzyme that is required for the conversion of the prodrug is actually produced within the targeted cell this is done by encoding the enzymes to the target cells.[106] For non-viral delivery there is a variety of methods that generally include either chemical methods such as being aided by cationic liposomes or physical methods such as electroporation, ultrasound utilization and magnetofection among others, see Nayerossadat, 2012 for more in depth discussion.[111] This allows the gene when expressed to locally reduce the administered non-toxic prodrug to its cytotoxic product. This in turn allows for the therapeutic effect to not only occur in the tumour cells but in surrounding cells due to the by-stander effect.[106] The main advantages of the GDEPT approach is that it allows the use of prodrugs which have no activity in unmodified human cells.[106] It also allows for much higher concentrations of prodrug to be used due to reduction to its cytotoxic product only occurring in the target cells or within close proximity.[106] The suicide gene and prodrug combinations can also be designed to either increase tumour specificity/selectivity.[106,112] The prodrugs can also be designed to be preferentially active in hypoxic cells which will limit toxicity toward non-target cells.[106,113] Where the prodrug is reduced extracellularly the main disadvantage is the potential re-diffusion of the cytotoxic drug into the general circulation system.[114]

1.2.4 Virus directed enzyme prodrug therapy

Virus directed therapy is in principle the same as GDEPT however; it uses a viral vector to deliver the gene instead of relying on genes alone.[107] This again enables the production of enzyme to convert a non-toxic prodrug to its cytotoxic product within tumour cells.[107,108] There are currently several viruses which have been used in VDEPT systems such as; retroviruses,[115] adenoviruses[116,117] and Epstein-Barr virus (EBV).[118] The advantages are similar to those in GDEPT with the main advantages being the ability to administer higher concentrations of prodrug to create higher concentrations of the cytotoxic drug within the microenvironment of the tumour. Due to the bystander effect VDEPT does not have to rely on full transfer of the genes to all tumour cells.[108] The main disadvantages of VDEPT are that by using retroviral vectors the retrovirus can only target dividing cells, which most human tumour cells are slow dividing which results in a low transduction rate.[119] Another disadvantages associated with retroviral vectors but also with adenoviral vectors is that they can lead to immunogenicity. Replication-competent retroviruses have the potential to be regenerated to wild type viruses by recombining with helper functions.[120] This problem has been addressed in later generations of retro and adenoviruses; with the use of nonmurine cells that carry fewer endogenous retroviral sequences, enabling the decrease the frequency of recombination.[120]

1.2.5 Prodrug reduction by nitroreductases

The interaction of the nitroreductase (NTR) class of enzymes with nitro-aromatic prodrug compounds such as 5-(1-aziridinyl)-2,4-dinitrobenzamide (CB1954), which in its native form (compound **A**); see Figure 1.10, is minimally toxic but undergoes reduction by the NTRs to form its cytotoxic hydroxylamine derivatives has attracted considerable attention as a viable DEPT for the treatment of cancer. Principle investigations of this system carried out by *Knox et al*.[121,122] and subsequent studies and clinical trials have helped to drive the research into this methodology forward.[101,108,121–129] The prodrug CB1954 is reduced by nitroreductases to four cytotoxic derivatives and can undergo further reaction with thioester such as acetyl coenzyme A in physiological conditions. The NTR NfsB reduces the CB1954 to form 2- and 4-hydroxylamine derivatives (compounds **B** and **D** respectively) in equal proportions. It is the 4-hydroxylamine derivative that can undergo the further reaction with acetyl coenzyme A to form a potent DNA crosslinking agent as shown by compound (**F**) in Figure 1.10.

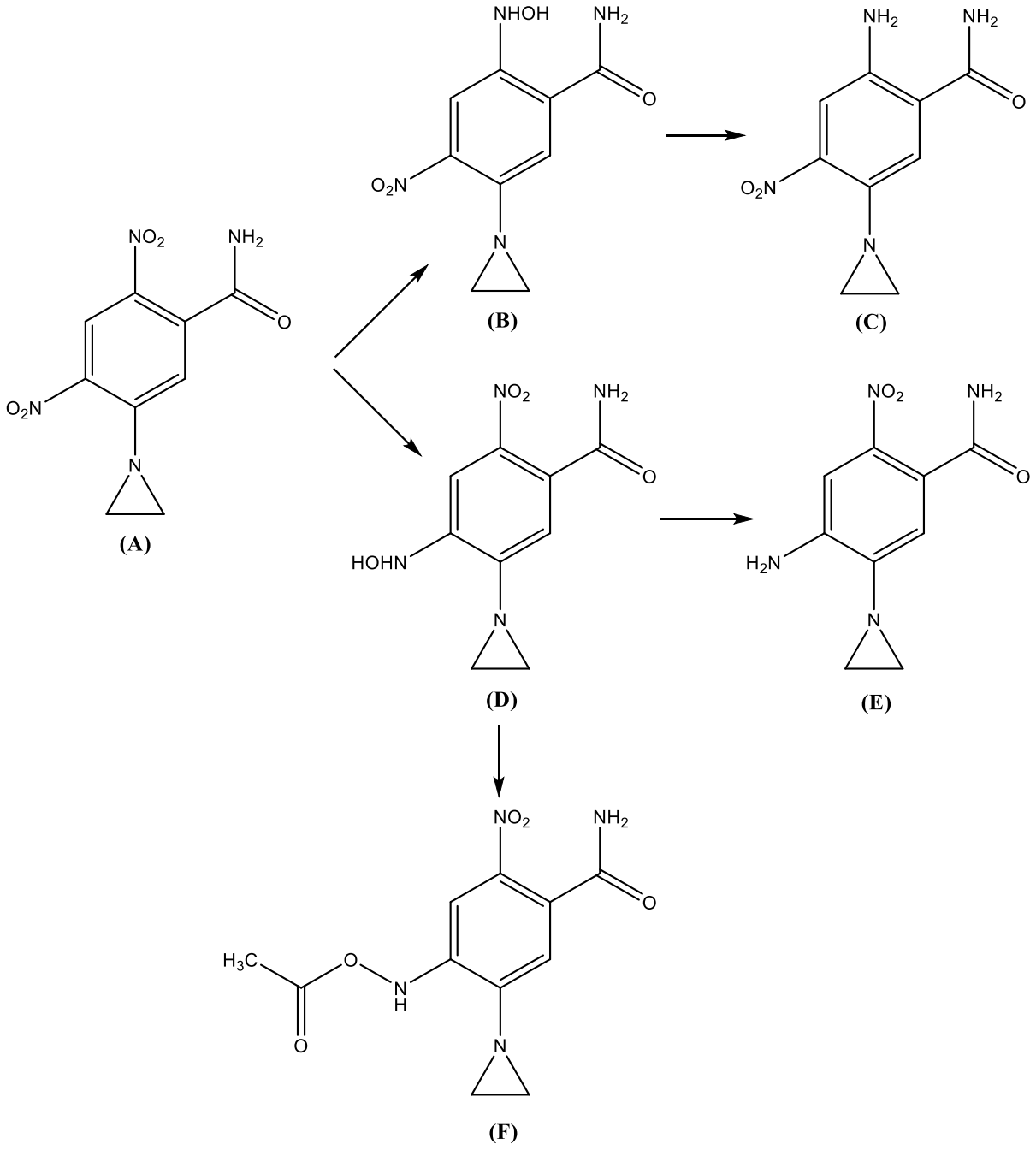

Figure 1.10 The reduction of 5-(1-aziridinyl)-2,4-dinitrobenzamide (CB1954) (A) to its hydroxylamine derivatives (B) and (D) and the further reduction to the amino derivatives (C) and (E). Compound (F) shows the potent DNA crosslinking agent formed from the reaction of 4-hydroxylamine product (D) with thioesters in a physiological environment.[124,130]

It is demonstrated that CB1954 can be reduced to four cytotoxic intermediates by NTRs prior to the reaction with a thioester.[124] The four products are the 2- and 4-hydroxylamines shown by compounds (**B**) and (**D)**; the hydroxylamine products can be further reduced to their corresponding amines shown by compounds (**C**) and (**E**), with the 4-hydroxylamine reduction product being the most cytotoxic of the four. Interestingly the 2-amino derivative (**C**) has a similar cytotoxicity to the compound (**D**).[130] The diffusion of the cytotoxic derivatives to

neighbouring cells which are not expressing the enzyme is an effect known as the "bystander effect" and is both highly important and well documented occurrence exhibited by DEPT.[131–133] It is believed that compound (**C**) the 2-amino derivative of CB1954 produces the greatest "bystander effect" *in vitro* due to its superior diffusion properties.[130] The "bystander effect" is of particular importance because it allows a transduced cell to produce cytotoxic compounds that can kill multiple cells by diffusing through a tumour and killing multiple neighbouring cells.[130] This is also a potential disadvantage if left to occur in an uncontrolled manner.[130]

Prodrugs are now being researched and developed to allow increased potency *in vitro* and a faster efficacy.[126,130] Prodrugs for the various DEPT treatments being created need to be constantly improving to provide better suitability to cancer therapy, stable when in contact with naturally occurring enzymes, be as quickly reduced by the NTR as possible and have a large increase in cytotoxicity between the reduced and oxidised forms of the prodrug.[134] They should also be very soluble in physiological conditions and the cytotoxic products it produces should have high diffusion rates.[125] All these properties should lead to increased efficiency of DNA crosslinking.[134] It is believed that DNA crosslinking occurs *via* the reaction of the N-acetoxy group (compound (**F**)). It is reported that this compound can cross link with DNA at the N7 position of the guanine on opposite strands forming an interstrand crosslink.[124,135]

Many different analogues of CB1954 have been synthesised in order to improve these properties; both with singular and multiple/combinations of alterations. This often leads to some properties being improved with others weakened, it is a fine balance to get the best compound overall.[136,137]

There are some promising alternative prodrugs to CB1954 in development and under study.[138,139] Below we will discuss some of these that have displayed greater efficiencies than CB1954 when used in combination with NTRs.

Dinitrobenzamide mustard prodrugs are a class of prodrugs that provide great interest. They contain a latent nitrogen mustard moiety, this becomes the active part of the prodrug when either of the nitro groups is reduced to the hydroxylamine product.[126] This process allows for the generation of reactive nitrogen mustard metabolites that is a selective process occurring in hypoxic cells; cells with a lack of oxygen. This allows these class of prodrugs to have hypoxia selective cytotoxicity.[140] The two main features of the dinitrobenzamide mustard prodrugs are that it undergoes activation at very low oxygen concentrations allowing for improved selectivity

towards hypoxic tumours which are classed as severely hypoxic. Its other main feature is that the activated metabolites exhibit a significant and efficient bystander effect due to their ability to locally diffuse in tumour tissues.[130,131]

One of the novel NTR prodrugs that has been developed and studied is the 3,5-dinitrobenzamide-2-bromomustard, SN 27686 (Figure 1.11). This was necessitated by the poor tolerance of humans to CB1954 and as such is an analogue of CB1954. The dinitrobenzamide mustard prodrug class are of interest as they have been determined to be a great substrate for nitroreduction by NTRS, particularly the 3,5- dintiro isomer structure.[134,136,137] It has been shown that only the 3-nitro group position of SN27686 is reduced to the corresponding cytotoxic hydroxylamine product, which has also been demonstrated by the reduction of a related compound PR-104 in hypoxic tumour cells.[141] This backs up studies into other analogues in the dinitrobenzamide mustard series and is consistent with NTR active site constraints that have been observed in the series.[126,142]

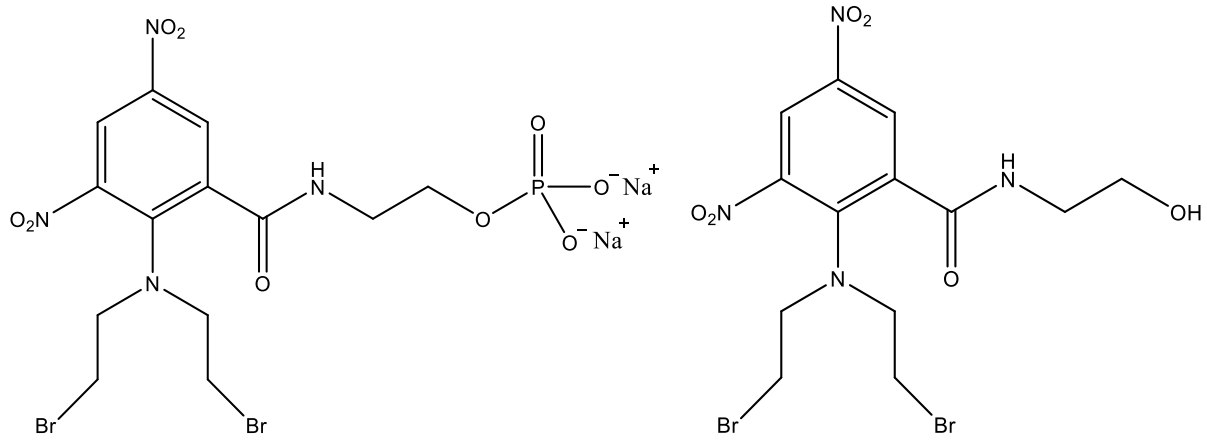

Figure 1.11 Structures of SN 27686 (right) and its water soluble phosphate ester SN 28343 (left).

This has been shown to provide a number of advantages over CB1954.[138] Singleton *et al.* compared SN 27686 to CB1954 by determining their growth inhibition across a selection of cell lines.[138] The study showed that SN 27686 was on average 12.8x more dose potent than CB1954 and possess an increased bystander effect alongside increase selectivity.[138]

To ascertain whether SN 27686 is a better substrate than CB1954 *in* vivo; Singleton *et al.* prepared a water soluble pre-prodrug which was the phosphate ester of SN 27686, this compound was classified as SN 28343 and its structure can be seen in Figure 1.11.[138] The SN 28343 exhibited a 3.75x greater maximum tolerated dose than CB1954 as when tested with CD-1 nude mice the SN 28343 was capable of reaching a maximum dosage of 750 μmol kg^{-1} compared to 200 μmol kg^{-1} for CB1954.[138] It also exhibited no loss of activity towards tumour growth inhibition when tested again tumours containing relatively small amounts of NTR; this

was conducted as it was perceived as more comparable to the levels of NTR present in exogenous delivery of NTRs *via* VDEPT. This was in comparison to CB1954 which was minimally active.[138] The use of SN 28343 is termed a two-stage system; initially the compound undergoes phosphatase mediation which produces the SN 27686 compound, this is then in turn reduced by NTRs to form the cytotoxic alkylating products which have a great diffusion quality and allow for a localized bystander effect.[138]

PR-104, Figure 1.12, is a 3,5-dinitrobenzamide-2-mustard that can be readily reduced in hypoxic cells and the nitrogen mustard group is asymmetrical and has bromide and mesylate leaving groups which are very reactive. As with the case of SN 28343, PR-104 is a water soluble phosphate pre-prodrug. Undergoing the similar phosphatase mediation it produces its corresponding alcohol, PR-104A. This product is a cytotoxic, DNA crosslinking and hypoxia selective product. The reduction of PR-104 to the cytotoxic product is a two-stage process in replication of that of SN 28343. The alcohol product formed after the 1st stage is lipophilic at such a level to be able to penetrate multiple layers of tumour cells, a trait required to reach hypoxic cells.

Patterson *et al.* studied PR-104 and its associated metabolites and concluded that PR-104 successfully satisfy the two key features that the dinitrobenzamide mustards.[141] They found PR-104A exhibited cytotoxicity at significantly lower concentrations of oxygen than other hypoxia selective prodrugs.[143] They concluded that the effective inhibition of cytotoxicity at normal tissue oxygen levels along with a strong bystander effect provides a smart system for taking advantage of the hypoxic conditions associated with tumour hypoxia.

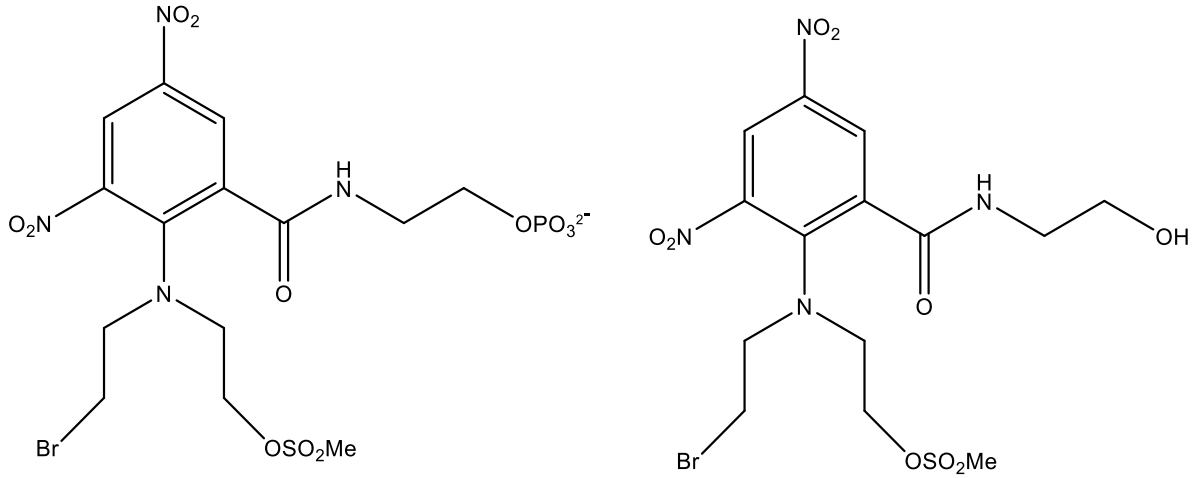

Figure 1.12 Structure of PR-104 (left) and PR-104A (right)

There are many other promising compounds being developed; Hu *et al.* has synthesised and tested a 4-nitrobenzyl phosphoramide mustard, see Figure 1.13.[144] It has been determined as being a substrate of NTR that is 19x greater than CB1954 and that it exhibited better selectivity and better activity when compared to CB1954 in cell culture assays.[144]

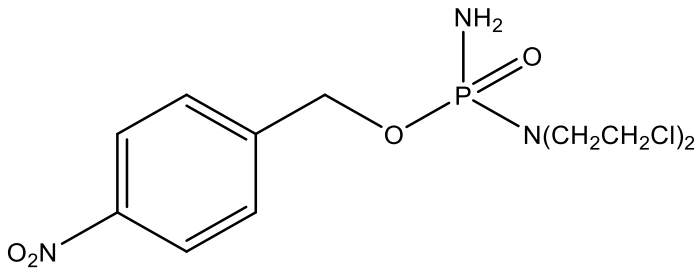

Figure 1.13 Structure of 4-nitrobenzyl phosphoramide mustard

Magnetic nanoparticle enzyme prodrug therapy (MNDEPT) hopes to overcome the problems in determining the best compound/combination for effective treatment and is being developed with genetically modified NTRs as an enzyme prodrug therapy. In this study CB1954 is being used as the prodrug simply because it is commercially available.

1.3 Nitroreductases

Nitroreductases are a class of enzymes which reduce organic nitro groups.[145] They are produced by a range of organisms; many of which produce more than one type of NTR. The enzymes come in two specific classes; type I and type II,[145,146] with type I being oxygen insensitive and type II which are oxygen sensitive. Type II NTRs are believed to be involved in a single electron process. Type I NTRs are flavoproteins; which undergo a two electron transfer process, producing hydroxylamine derivatives. Type I NTRs are further divided into two groups; NfsA and NfsB. NfsA proteins reduce nitro compounds in the presence of a nicotinamide adenine dinucleotide phosphate, reduced (NADPH), whereas NfsB uses both NADPH and nicotinamide adenine dinucleotide, reduced (NADH) as an electron source. Directed enzyme prodrug therapies are involved in the delivery of prodrug activating enzymes or their encoding genes to the tumour before administering the prodrug and DEPT is helped by type I NTRs and their ability to produce hydroxylamine derivatives.[129] Figure 1.14 shows the redox cycle of a type I NTR which; as a homodimeric flavoprotein contains flavin mononucleotide (FMN) this FMN is bound to the active site of NTR. A redox cycle is formed due to the FMN reversibly oxidising in the reduction of a nitro group and it is then reduced by the NAD(P)H.

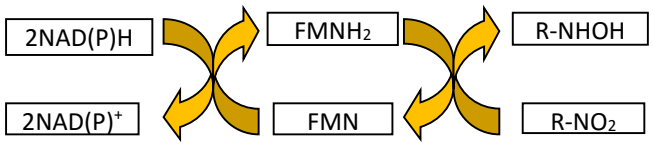

Figure 1.14 Redox cycle of Nitroreductase (NTR) with cofactor and substrate

The nitro reducing group of enzymes first established their use in application for a DEPT treatment when Knox *et al.* applied CB1954 to Walker carcinoma cells in 1988.[122] DT-diaphorase (DTD) was found to be the responsible enzyme for the generation of a DNA cross-linking agent from the CB1954. Walker carcinoma cells are rat breast carcinoma cell lines and the equivalent DTD that is produced in humans is shown to be less efficient at activating these prodrugs than the rat DTD.[147,148] The NTR NfsB from *Escherichia coli* was subsequently found to be substantially more active with CB1954 than the Walker rat DTD *in vitro*[123] with a turnover rate; the rate defining how much substrate is converted to product per second, of over 80x greater.[125] Nitroreductases such as NfsB have the potential to be introduced into unreactive cells that contain no native NTRs significantly increasing their sensitivity towards the prodrug.

The NTR *nfsB* was successfully incorporated into a virus and tumours in mouse studies showed a doubling of the median survival with the administration of CB1954.[116] In a different study the percentage of the population of mice that showed long term remission stood at 80% with *nfsB*

gene transduction, meanwhile 0% of the mice that were not given the NfsB VDEPT showed any signs of remission.[108] Some preliminary phase I human clinical trials have been conducted and have shown that the patients were able to tolerate the NTR, virus and administration of CB1954.[127,128]

The reaction of CB1954 and an NTR proceed *via* a mechanism known as the ping-pong Bi-Bi pathway.[149] This mechanism occurs whereby the FMN of the NTR is first reduced by the cofactor, NAD(P)H. This reduction releases NAD(P)+ and allows the FMN to donate two electrons to the prodrug, which allows the reduction of one of the nitro groups to a nitroso group.[149] The NAD(P)H and CB1954 cannot occupy the space where the FMN is bound at the same time as one another due to there being only one available pathway to the active site. It is for this reason that this reaction must proceed by the ping-pong Bi-Bi mechanism.[150] The nitroso group of the reduced prodrug can then undergo further reduction to form the hydroxylamine derivatives of the CB1954. This can only occur after it has left the active site, this means the reaction rate is held up by the rate at which the nitro group is reduced at the FMN site.[149]

1.4 Nanoparticle overview and significance

1.4.1. Gold nanoparticles

Michael Faraday is accredited with the first scientific study of gold colloids in the early 19th century.[151] However, gold nanoparticles (GNPs) have been used in dyes and stains since around 500 BC.[152] Since his studies research into gold nanoparticles has grown to a phenomenal size; with GNPs being researched for all kinds of applications ranging from diagnostics[153] to electronics.[154] Gold nanoparticles are also being researched for cancer therapies[155–157] and their use as hyperthermia agents[158–160] as well as cell labelling[161,162] and drug delivery.[161,162] One of the main focuses of research into GNPs is to be able to fully control the synthesis of the particles and a review conducted by Grzelczak *et al.* summarises the wide array of methods and research.[163] This control is imperative as many of the properties of the particles such as shape, size and surface chemistry have an effect on both the chemical and physical properties of the nanoparticle colloids which will have an impact on their potential use.[164]

For this study the research and use of GNPs within both the biological and medical fields is the main interest. The particles can be synthesised and then functionalised with biologically active compounds.[158] *In vitro* studies have found that in the majority of circumstances GNPs are non-toxic[165] and proceed to cell uptake *via* endocytosis.[166,167] GNPs with immobilised proteins

are taken up by this method.[168–170] Spherical gold nanoparticles that are 50 nm in size have been shown to be taken up into mammalian cells at a higher concentration and faster rate than GNPs that are smaller (14 nm) or larger (74 nm).[171]

Gold by its very nature is deep yellow in its colouration of the elemental form. However, GNPs have a distinct deep pink/red colouration. The reason for this difference in colour is surface plasmon resonance (SPR). This is a property displayed by various metal nanoparticles and is the process whereby electromagnetic radiation excites conducting electrons over a nanoparticles surface at a defined wavelength, see Figure 1.15.

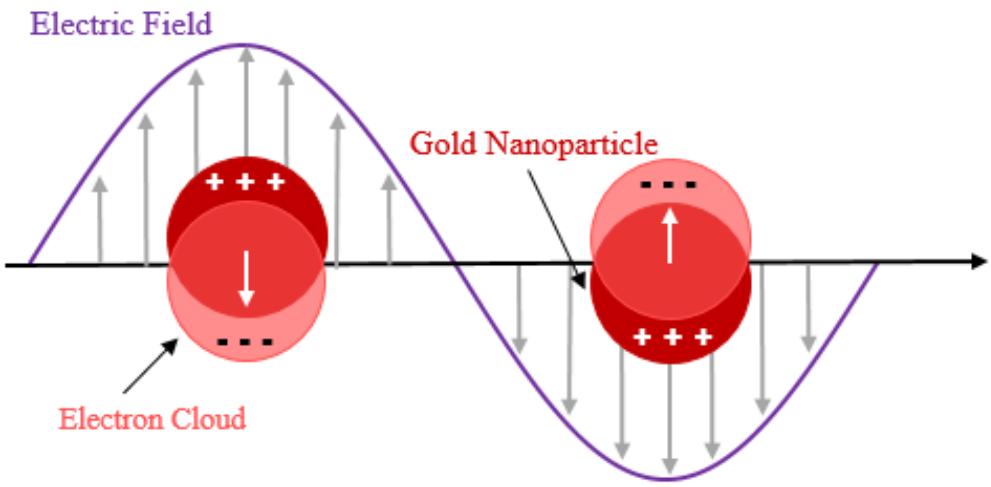

Figure 1.15 A graphic showing the principal behind surface plasmon resonance (SPR)[172,173]

For GNPs the wavelength at which SPR occurs and is observed is typically 520 nm.[172] This is an important property of gold nanoparticles which aids in the characterisation of synthesised gold coated magnetic nanoparticles (Au-MNPs).[174] The SPR of gold nanoparticles allows, *via* ultra-violet visible spectroscopy, the spherical nature of the particle to be determined by observing the distinct absorption peak at 520 nm; spherical particles and particles such as gold nanorods exhibit differences in their optical absorption.[175] Aggregation/agglomeration of GNPs can be indicated by a colour change from red to blue.[176]

Surface plasmon resonance is a very sensitive phenomenon and is easily effected by change at the nanoparticle surface; these changes can occur due to conjugation of ligands and other compounds to the surface, the properties of the solvent in which the nanoparticle is suspended and both the nanoparticle shape and size.[177–179] The role of ligands and other compounds conjugated to the surface of the nanoparticles play an important role in how the particle is taken into a cell.[166,171,180] As previously mentioned GNPs typically undergo cellular uptake by

endocytosis into vesicles, however the surface chemistry can be modified with different hydrophobic and anionic compounds enabling the particles to pass directly through the cell membrane with little or no damage to the membrane.[180]

The differences between *in vivo* and *in vitro* studies of gold nanoparticles is typified by the observation that GNPs between 8-37 nm caused severe damage to mice and even fatality after just 3 weeks whereas 3, 5, 50 and 100 nm particles caused no discernible issues in the mice over a period of 8 weeks.[181] The particles in the mice which suffered health issues and death had accumulated predominately in the lungs, spleen and liver;[181] Renal excretion is considered the most typical excretion route for particles < 8 nm.[182] De Jong *et al*.[176] studied the bio-distribution of GNPs in mice and concluded that 10 nm had the widest distribution across the samples test; the highest were the blood, liver and spleen.[176] Whereas 50 nm GNPs were found to accumulate predominately in the blood, liver, spleen and lungs, with the highest concentration present in the lungs.[176] For particles larger than 50 nm; 100 nm and 250 nm were tested and these accumulated in the liver, blood and spleen with concentrations in the liver nearly double that found in the blood and spleen.[176] It has been suggested that whilst the mechanism for the abnormalities and fatalities is unclear the particles themselves are not cytotoxic; it is in fact the interactions that occur when the particles are in the complex conditions of a physiological environment which leads to their toxicity.[183]

There is an abundance of research being conducted with gold nanoparticles of various shapes and sizes and in combination with a wide array of animal models and cell lines that is helping to piece together the reason for inconsistent toxicity of the particles.[184,185] One thing is however clear throughout is that having control of the surface chemistry of the particles is of paramount importance to ensure the particles are biocompatible.[186]

1.4.2. Magnetic nanoparticles

Magnetic nanoparticles play a significant role in cancer therapy, they have been approved by the Federal Drug Agency (FDA) for use against certain solid tumours.[187,188] They have been approved for use both on their own and in combination with conventional radiotherapy.[189] The MNPs and their application for biological purpose have consequently been the subject of numerous review articles.[190–194] To ensure that the MNPs that will be used in an MNDEPT system are suitable for purpose it is a desired preference that the MNPs must be superparamagnetic, have a strong magnetic response, be biocompatible and must maintain stability in a physiological environment. Superparamagnetic iron oxide nanoparticles have emerged as a strong contender in the field of MNPs. Their prominence is due to their

superparamagnetism, high magnetic saturation and their subsequent approval by the Medicines and Healthcare Products Regulatory Agency (MHRA); the European Medical Agency (EMA) and the FDA for their use in medical applications.[190] Other MNPs are being researched with potentially higher magnetic saturation and improved properties.[195] However, the issue of their biocompatibility and toxicity casts doubt over their use.[196,197] Some of the MNPs under study contain platinum to form a superparamagnetic iron platinum nanoparticles;[198] Iron platinum nanoparticles have often been used in various magnetic storage devices by high temperature annealing of superparamagnetic iron platinum particles (SIPPs).[199,200] These superparamagnetic particles have been studied for use as an MRI contrast agent.[201–203] The reported high volume magnetizations of SIPPs has led to the possibility of them being optimised to provide better contrast agents for MRI.[204,205] SIPPs have been compared to SPIONs for use as T_2 weighted MRI contrast agents. They have shown an increased r_2 and r_2/r_1 than that of commercially available SPIONs leading to the conclusion that SIPPs may be greater contrast agents for T_2 weighted MRI.[198]

Cobalt nanoparticles have also come under study.[194,206] They appear to have significant advantage of SPIONs due to having a 3.5 fold higher room temperature saturation magnetization.[187] This increase gives rise to cobalt nanoparticles possessing an improved magnetic resonance contrast, it also allows for the use of much smaller particles than that of already approved iron nanoparticle agents without compromising the sensitivity obtained.[187] One of the main drawbacks of cobalt nanoparticles is the difficulty of synthesising them in aqueous solvents, producing water soluble particles, this is mainly due to the fact they are particularly prone to oxidation.[187] There has however been a breakthrough in the ability to produce water stable cobalt nanoparticles which has allowed for them to be evaluated as a potential MRI agent.[207,208]

Fe_3O_4 and γ-Fe_2O_3 are two forms of iron oxides which are of interest in nanotherapeutics.[143] These MNPs must be surface functionalised for their application as a MNDEPT treatment, without modification the particles are have a greater risk of flocculation.[209,210] Gold is a preferred material for this with its ability to be bound to the cysteine modified NTRs; using strong covalent gold-sulfur (Au-S) thiol bonds, it is biocompatible in the body, provides stability for the colloid and it is nearly inert in its chemical reactivity.[211,212] For the particles to work in these various applications one of the most important properties of the particles is their magnetic properties and the applied magnetic fields used to manipulate them. Magnetic materials are split into different classes and are characterised by their magnetic susceptibility.

It is a measure of the parallel and anti-parallel alignment of the magnetic moments contained within a specified material and the magnitude of its magnetisation when present in an applied magnetic field that causes an amplification of the applied field. The relationship between magnetic susceptibility (χ), magnetisation (M) and H-field (H) is shown in Equation 1.1.[213]

$$\chi = \frac{M}{H}$$

Equation 1.1. The relationship between magnetic susceptibility(χ), magnetisation (M) and an H-field (H)[213]

If the magnetic susceptibility of a material is less than zero than it is classified as a diamagnetic material.[195] A diamagnetic material will weaken an applied field due to its magnetic moments opposing the external field. Diamagnetic materials can be sub-divided further; if a material has a susceptibility χ of ~ -10^{-6} then it can be classified as non-magnetic and if it possess a susceptibility of exactly -1 then it can be termed a superconductor.[213,214] When a material's magnetic susceptibility is greater than zero it can be classified as paramagnetic, this means that when placed in an applied field the material will actually amplify the magnetism. Paramagnets when removed from an external field will no longer exhibit a net magnetic moment as its magnetic moments become disordered.[195] When the magnetic moments remain aligned after the removal of the external field the material can be classified ferromagnetic.[213] Due to these properties both paramagnets and diamagnets are unsuitable for use as an *in vivo* nanoparticle system. This is because paramagnets have low magnetic saturation and a poor response to an applied field and diamagnets have a much greater response but due to the retention of a permanent magnetic field it is considered they would flocculate and aggregate rather than exist as a stable colloid.[213]

To characterise magnetic materials a hysteresis loop gives the best visual representation of the different magnetic classifications. A hysteresis loop is seen in Figure 1.16 below. The saturation is the point when all the magnetic domains in a material are aligned and increase in the H-field whilst no longer increasing in the B-field. H-field is defined as the magnetic field strength whereas B-field is defined as magnetic induction or magnetic flux density. The remanence magnetisation shows the proportion of magnetic domains that have remained aligned when the applied field is removed. Finally the coercive field show us the strength of the H-field that is required to return the B-field to zero.[213,214]

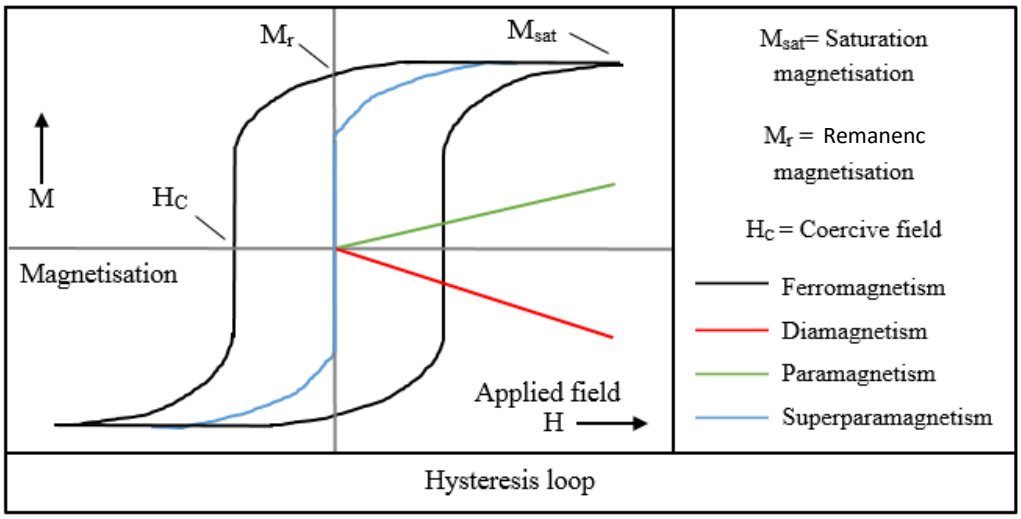

Figure 1.16 A hysteresis loop of the various classes of magnetic materials; ferromagnets in black, diamagnets in red, paramagnets in green and superparamagnets in blue.[214]

It can be determined from Equation 1.2 that materials that have a higher number of aligned magnetic domains within a smaller volume will show a greater response when exposed to an external applied magnetic field.[214] The early domain theory offers an initial explanation to the large difference in magnetisation that is observed between paramagnets and ferromagnets.[213]

$$M = \frac{N}{V}m$$

Equation 1.2. M represents magnetisation, N is the number of magnetic moments, m is the magnetic moment and V the volume of the material.[214]

For magnetic nanoparticles to have a significant response to an applied field then they must by virtue of Equation 1.2 contain a large number of aligned magnetic domains. Ferromagnetic materials exhibit such a property, however they suffer the disadvantage of particle aggregation to the remanence magnetisation. To avoid this disadvantage the MNPs must be single order domains so that when the applied magnetic field is removed they retain very little or no remanence magnetisation allowing them to stay stable in solution. An overview of magnetic domains and alignment can be seen in Figure 1.17.[213,214]

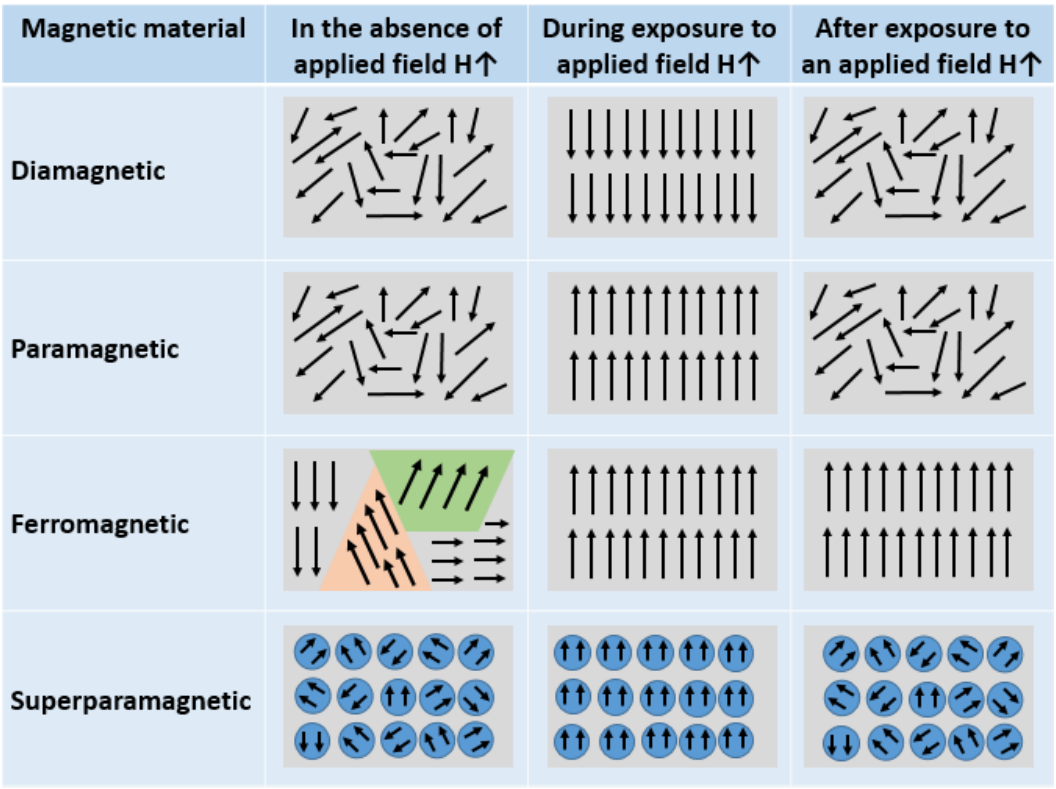

Figure 1.17 A graphical illustration of the ideal responses of various magnetic materials before, during and after exposure to an applied magnetic field H↑. The arrows are representative of magnetic moments.[213,214]

The chemical stability of a magnetic metal nanoparticle is of grave importance, especially in a physiological environment and the majority of metals will oxidise changing both their physical and chemical properties.[215] Due to this it can be an advantage to use a metal that is already oxidised or partially oxidised but yet still stable and biocompatible.

The rapid oxidation of magnetite (Fe_3O_4) to maghemite (γ-Fe_2O_3) due to magnetite nanoparticles small size and high surface area to volume ratio means it is more applicable to term them iron oxide nanoparticles rather than specifically maghemite or magnetite.[215]

To be stable as a colloidal suspension at physiological pH's, those of around pH 7, then the iron oxide nanoparticles must be functionalised.[216] Both polyethylene glycol (PEG) and dextran are popular surface coating compounds due to their stability and biocompatibility within physiological systems.[217–220] The ability of PEG to supress a response from the reticuloendothelial system (RES) and therefore give nanoparticles that have been coated with PEG a longer permeation and retention effect in the body is an added advantage over the use of dextran.[218] To conclude iron oxide magnetic nanoparticles have a promising application for use in MNDEPT but their surface chemistry needs to be suitable for enzyme immobilisation. The use of gold for this surface modification will be discussed in the next section.

1.4.3. Gold coated magnetic nanoparticles

Due to its desirability the coating of superparamagnetic iron oxide nanoparticles (SPIONs) with gold is an area of intense interest, considerable research has been conducted to synthesise core/shell magnetic/gold nanoparticles.[221] However if gold coated magnetic nanoparticles are to be successfully utilised for use in an MNDEPT treatment then the colloid needs to exhibit a significant response to an applied magnetic field, possess an NTR which can efficiently reduce a prodrug and be successfully immobilised to the Au-MNPs. Given that MNPs and NTRs have in their respective fields been trialled in humans and approved for use,[222,223] the key behind this study is in developing a MNDEPT by binding a modified protein NTR to gold coated magnetic nanoparticles.[224] The first stage of this research is the modification of the surface of iron oxide nanoparticles which is essential in biomedical application.[209,225] The iron oxide nanoparticles will provide the response to an applied magnetic field that is desired for the MNDEPT treatment, but without surface modification the possibility for particle flocculation is highly likely.[210] The research activity in the area is mainly due to the fact that gold is biocompatible, provides good stability to a colloidal solution is nearly inert in its chemical reactivity but ultimately provides a strong binding surface for biological compounds *via* gold thiol (Au-S) bonds.[226] Thus the synthesis and development of Au-MNPs is a stepping stone to allow the conjugation of genetically modified NTR to Au-MNPs for use in a MNDEPT for cancer.

An approach to synthesis of Au-MNPs that seems to exhibit the greatest control over size and morphology of the particles is the use of a reverse micelle system.[227] This methodology allows for significant control over the nanoparticle formation because of the number of parameters that can be changed/modified to determine the outcome of the final nanoparticle.[228] Solvent type, concentration of reagents, the ratios of surfactant to solvent and the type of surfactant or co-surfactant can all be adjusted to effect the final nanoparticles produced.[228,229] A reverse micelle process has been established to create iron-gold core-shell nanoparticles using iron sulphate ($FeSO_4$).[230] This system first creates the iron oxide nanoparticles in a cetyltrimethylammonium bromide (CTAB) solution that also contains 1-butanol and octane. This solution of the micelle is reduced by the same micellar solution containing sodium borohydride ($NaBH_4$). Once this process is complete chloroauric acid ($HAuCl_4$) is added almost immediately after the addition of $NaBH_4$ to prevent the growth of the iron nanoparticles.[230] The use of this reverse micelle process allows for some control over the thickness of the Au shell that forms on the surface and the morphology of the particles.[231–233] The overall particle size is controlled simply by the speed of the addition of $HAuCl_4$.[230]

Although this process offers greater control over the particles there is a major disadvantage to the system and that is the use of harsh organic solvents and surfactants such as octane and CTAB. For the Au-MNPS to be biocompatible[234] and to be used for enzyme immobilisation then the particles must be removed from the organic solvents and into an aqueous system.[235]

It is paramount that the gold surface of the particle is available for the self-assembly of cysteine residues.[236]

For the MNDEPT application this study focuses on, the drawback of the extra work and processes required for washing and transferring the phase of the particles formed in the micelle process, the most desirable of all the systems is developed to create hybrid nanoparticles are those that are carried out in aqueous solution.[237]

There are two main procedures which work in aqueous solution, one of them uses chloroauric acid that heated until boiling with sodium citrate to directly reduce the gold salt onto synthesised iron oxide cores.[238] The second is an iterative hydroxylamine seeding approach which uses the hydroxylamine to reduce the gold salt onto the surface of the iron oxide nanoparticle and iteratively grow the thickness of the gold coating.[239] Due to the aqueous nature of both of these methods they are highly suited for use in a DEPT system. Several of the synthesis methods to create the Au-MNPs use capping agents to bind to the particle surface and help the control of the particle morphology and size.[240] One of the commonly used capping agents for Au-MNPs are thioalkanes, these can control both particle growth and increase the stability of the colloidal sols.[241–243] The control of the size and morphology is again an advantage for the production of Au-MNPs along with the increased stability. However, for their use in a DEPT system, if the Au-MNPs are already thiolated from the use of thioalkane capping agents, then self-assembly immobilisation for the cysteine modified NTRs will be hindered and may not be possible at all.[244] This is due to the surface already having a layer of bound cysteine residues from the thioalkane preventing the modified NTRs from accessing the gold surface to allow the formation of the NTR on the surface *via* self-assembly with control of the enzymes orientation.

1.5 Immobilisation of nitroreductase

The main focus in the production of a MNDEPT system is to create a successful pathway to allow the binding of the NTRs to the nanoparticles. There are some interesting and significant advantages to immobilising enzymes onto nanoparticles such as the fact the particles often show increased stabilities and the immobilised enzymes show either similar or improved enzymatic activities.[245–249] Over the last decade there has been significant research into the subject of biotechnologies,[250] and their potential applications and the sheer scale and diversity of the wide range of nanomaterials and biological compounds that are of interest has been well reviewed in detail by Sapsford *et al*.[251]

The activity of an enzyme with a given substrate is controlled by the amino acid structure that surrounds the active site of the enzyme. Due to this fact any amino acid sequence that needs to be added to the enzyme in order to bond it to an inorganic surface is typically added to the end

of a polypeptide chain, minimising the impact of the modification on the active site.[252] Amino acid immobilisation is regularly utilised, the most common method is the His_6 method, whereby six consecutive histidine units are added to the enzyme.[253,254] This was developed by E. Hochuli *et al.*[255] at Roche Ltd. in the 1980's. The six consecutive histidine residues are added to either the C-Terminus or N-Terminus of the amino acid sequence, this is achieved by inserting a genetic code to the end of the gene sequence.[255] The advantage of using the His_6-tag method is that this allows the specified sequence to be purified from other proteins using a Ni^{2+} chelating column. The His-tags bind to the nickel (Ni) purification column and isolates the required protein from the others by competitively eluting the sample with imidazole at varying concentrations. The sequences without the histidine modification will be eluted at weak concentrations as they will not bind to the column properly, the modified sequence will elute at a higher imidazole concentration due to it being bound more tightly onto the nickel column.[256] Another advantage to the His_6-tagged proteins is that the bonding to nickel and subsequently nickel oxide nanoparticles is done *via* self-assembly.[257,258] Nickel oxide nanoparticles are however an unsuitable material for use in bio-applications due to their defined toxicity.[259] This method of self-assembly however has led onto further research and has shown that it can occur when working with gold surface and gold nanoparticles.[260] In other words the His_6-tagged proteins can bind to gold surfaces and nanoparticles *via* self-assembly just like they can with nickel.[260,261] The bond strength of a self-assembled thiol bond on an Au surface is in the region of 210 $kJmol^{-1}$.[262] When this is compared to that of a Ni-S bond which has a bond strength of 163 $kJmol^{-1}$, it indicates that Au has stronger binding and is therefore more desirable.[263]

Gold is a desirable material for biomedical application and as previously described it has undergone extensive research as a bio-nanomaterial given its ease of controlled synthesis, biocompatibility and its chemical stability.[262,264] The strength of this bonding coupled with the ease of thioalkane modification of gold makes the combination a preferred choice when selecting a self-assembly system for biological application.[262] The introduction of the use of cysteine residues as a functional bonding sequence allowing enzymes and proteins to be immobilised to gold has been well studied[154,236,265–269] and has also seen an important review compiled by J.C Love *et al.*[262] into its use in nanosystems. Cysteine is non-toxic and both S-H and S-S groups bond to Au.[267] The di-sulphide bridges formed by the S-S bonds allows for the bond strength to increase to nearly 400 $kJmol^{-1}$. It has been shown that the introduction of cysteine tags can improve enzymatic activity compared to the corresponding unmodified enzyme.[270–272] The presence of naturally occurring cysteine amino acids in the protein sequence

could lead to self-assembly of the proteins to an Au surface. This could lead to the orientation being effected as both the natural cys-tags and the added modified cys-tags could both form self-assembled immobilisation. In order to ensure the modified cys-tag is the preferential binding site for immobilisation to an Au surface Gwenin *et al.*[224] introduced a series of six cysteine sequences in consecutive order into a NTR sequence mimicking the His_6-tag immobilisation. This was shown to be an effective route in controlling the immobilisation of proteins onto an Au surface in the development of a biosensor used to detect explosive compounds using amperometric potential.[224]

This led to the development of a similar approach in the successful immobilisation of NTRs onto inorganic substrates. This was developed and patented as a potential application to be utilised in a novel directed enzyme prodrug therapy.[15,273] Figure 1.18 details how the six cysteine residues present in each monomer sequence of a dimeric NTR allow controlled orientation of the enzyme onto an Au surface *via* Au-S thiol bonds.[224] This illustration depicts the enzyme immobilising to a flat gold surface but the same approach should be applicable for conjugating the enzyme to a curved surface of a nanoparticles for example. It also shows that the addition of the cys-tags to the N-terminus allows the amino acids to access and bind to the gold surface without in theory altering the native enzyme's structure.

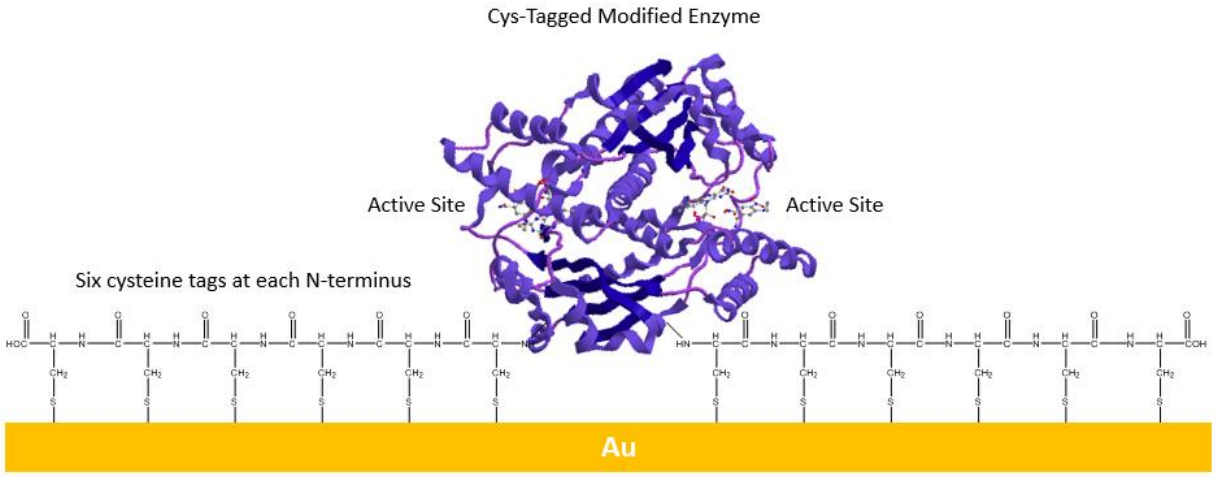

Figure 1.18 An illustration detailing the six consecutive cysteine tag residues included at the N-terminus in each monomer unit of a NTR allowing the dimeric enzyme to successfully immobilise onto an Au surface via Au-S bonds with controlled orientation.[224]

Nitroreductases have been used to reduce a large range of nitroaromatics and hold an interest in not only biomedicine but also the aforementioned nitroaromatic detection alongside bioremediation and biocatalysis.[274] The kinetic efficiency (k_{cat}/K_m); sometimes referred to as

the specificity constant of a NTR with the nitroaromatic compound CB1954 is a very important parameter to be considered when developing an MNDEPT system. There has recently been three novel NTRs isolated from *Bacillus lichenformis* which have a similar amino acid structure including their structure around the FMN site of the enzymes to that of the NTRs which have a known activity to nitroaromatic compounds.[275] These previously uncharacterized enzymes have shown activity towards a range on nitro containing explosives; they also showed the ability to retain this activity after both His_6-tag and cys-tag modification.[275] Amongst these enzymes is *yfkO* which will be used in this study to determine its activity towards the prodrug CB1954 and compared to the activity of the enzyme *nfsB.*

1.6 Selection of cancer cells

To allow the largest comparison of a potential MNDEPT system the cell line chosen for study in this project is the HeLa cell line. The HeLa cell employed in the work is a cell line that has been utilised for both research and industrial settings to establish cancer cell biology and processes.[276] HeLa is the oldest and most commonly used cervical cancer cell line.[277] The cell line is derived from cervical cancer cells that were isolated from the glandular cervical cancer of an African-American women named Henrietta Lacks.[278] Unfortunately she died from the disease on the 4th October 1951 but the preservation of her cells has enable research to continue.[278] HeLa cells; see

Figure 1.19, have been used to obtain knowledge about nearly every process that occurs in human cells, in combination with subsequent cells line that have now been isolated.[279] HeLa cells have been used for 60 years, from their first use in William F. Scherer's study[280] of the first polio vaccine in the 1950's to the present day.[281] It is estimated that more than 65,000 scientific research articles have been published using HeLa cells as the investigated cell line and this number is continually increasing.[280,282]

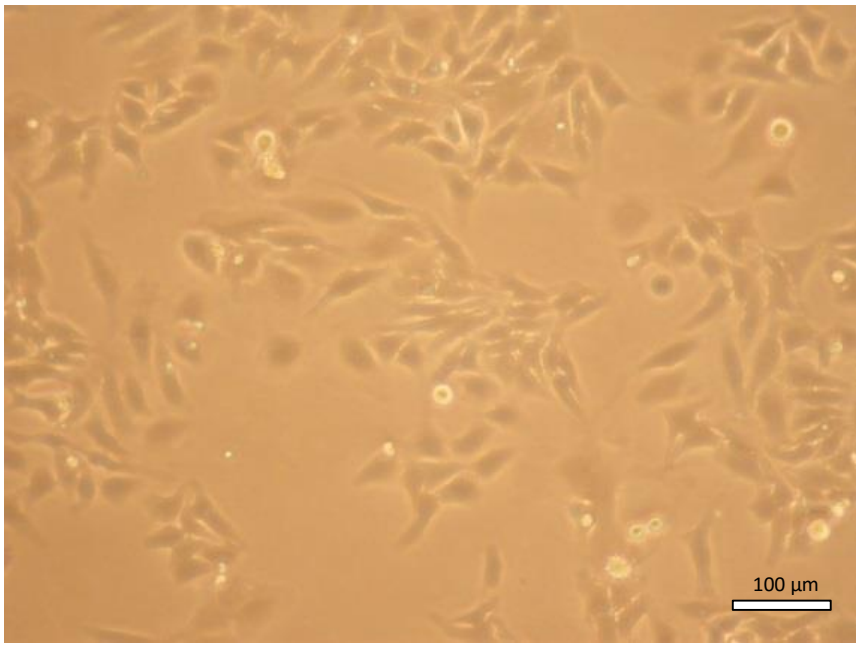

Figure 1.19 HeLa cell morphology shown with an image obtained of confluent HeLa cells growing in vitro, scale bar 100 µm

The importance of the HeLa cell line can also be further contributed to the fact that cervical cancer is the seventh most prevalent cancer overall and the third most common in women. It is estimated that approximately 530,000 women are being diagnosed with cervical cancer every year and that approximately 50% of the diagnosed cases lead to death.[283] Of the top 4 most prevalent cancers; breast and prostate cancer are most prevalent in women and men respectively, alongside lung and colon cancer.[284] Alongside the HeLa cell line it is hoped that the MCF-7 cell line can be studied. MCF-7 has been isolated from the breast cancer suffered by a 69 year old Caucasian women and is named after the Michigan Cancer Foundation, the institute where the breast cancer cell line was first established in 1973.[285] An advantage of using MCF-7 is that it is a robust cell line with a long passage life being able to maintain for over 90 weekly passages.[285] Compare this to HeLa cells being able to be passaged approximately 40 times before they lose their viability.

1.7. Conclusion

1.7.1 Conclusion

Many DEPTs are currently being trialled[128] with the efficacy of those being tested being low and needing further research and modifications to improve them.[128] One of the main drawbacks of the therapies is the reliance of the reduction of CB1954 by NfsB and as such different enzymes need to be identified and tested to increase the efficacy of the treatment.[275] The NTR YfkO from *B. Licheniformis* has been identified as a potential candidate for the therapy.[275]

In this study YfkO will be expressed, purified, assayed with CB1954 and compared to the NTR NfsB. Both of these NTRs will then be tested for their activity and enzymatic kinetics when immobilised to both gold nanoparticles (~50 nm) and synthesised 50 nm gold coated magnetic nanoparticles. The final step in the study is to determine the cell toxicity of the both the enzymes free in solution, the enzyme-gold nanoparticle bioconjugate and the enzyme-gold magnetic nanoparticle bioconjugates *via* cell viability assays initially tested on the HeLa cell line and followed by further cell lines. These assays will also hopefully give an initial indication to the cell uptake of the NTR/Au-MNPs and help set the basis for a multi enzyme screening process for MNDEPT to determine which NTRs have the highest efficacy and best potential for use in the treatment.

Sosnovik *et al.* specify that the FDA approved dosage for iron oxide nanoparticles is 3 mg Fe/kg.[286] A 50 nm Au-MNP that has a 10 nm Fe core calculates as ~1.10×10^{15} particles/kg; which when combined with the previously determined and published optimal ratio of NTR-Au-MNP conjugation[15] equates to 2.97×10^{17} particles of NTR/kg. An FDA approved antibody drug conjugate call Kadcyla® is used in clinical applications to treat patients with metastatic breast cancer and its recommended dosage is 3.6 mg/kg which is comparable to the dosage enabled to FDA approved iron oxide nanoparticles.[287] Francis *et al* reported that when using A5CP antibody-enzyme conjugate in combination with a bi-iodo phenol mustard prodrug; ZD2767P, in a phase I clinical trial, the maximum tolerated dose was reached at 15.5 mg/m^2. Based on an average body surface area (1.8 m^2)[288] for a human this dose equates to 27.9 mg. The average weight of a human has been calculated at 62 kg[289] so this gives the A5CP/ZD2767P system an effective dose of 450 µg/kg which is ~ 7-fold lower than for the proposed Au-MNP system.

Magnetic nanoparticles have been approved for use as MRI contrast agents with applications as both bowel contrast agents and liver/spleen contrast agents.[290] Lumiren® and Gastromark® are two commercially approved and available contrast agents for use in imaging the bowel. Endorem® and Feridex IV® are examples of magnetic nanoparticle products that have been

commercialised for use in liver/spleen imaging.[290] Magnetic nanoparticles have also found use in magnetic hyperthermia; this utilises MNPs under a time-varying magnetic field to induce heating of tumour cells and subsequently damaging the cells. This has been approved for use as a clinical therapy in the European Union.[291] Both of these applications have led to the use of magnetic nanoparticles in the proposed Au-MNP DEPT system. The ability of the MNPs to both be localised to the tumour site and the potential for the system to undergo magnetic hyperthermia; which could act as a secondary attack for the system has cemented the use of MNPs going forward in this study.

1.7.2. Aims of this study

The primary objective in this study is to ensure that the immobilisation of NTRs to MNPs is achieved in such a way that the enzymes do not subsequently dissociate from the nanoparticle surface. A covalent bond is the obvious choice to bind a particle to an enzyme which therefore leads to the use of gold to surface functionalise the MNPs. The production of Au-MNPs is therefore another important aim of the study along with the immobilisation of NTRs to these Au-MNPs. The control over size and morphology of the particles is required for the successful development of Au-MNPs for MNDEPT, with 50 nm in size and a spherical morphology the desired target. The kinetic and cell viability testing is important as it will help to characterise their enzymatic activity and cell toxicity and prove that it is retained as close as possible to that of NTRs reacting free in solution. This study also hopes to explore the possibility that the genetic modification of the enzymes and the surface functionally of the magnetic nanoparticles may even increase the activity of the enzymes when they are controllably immobilised.

Chapter 2

Experimental Methods

The majority of the work discussed in this chapter is published in the following paper.

YfkO nitroreductase immobilised with controlled orientation onto superparamagnetic nanoparticles; towards a direct enzyme cancer therapy approach. *Publication suited to Biomacromolecules,* **(in DRAFT)**

Chapter 2 – Experimental Methods

All Chemicals used were obtained from Fisher Scientific (UK) or Sigma-Aldrich (UK), unless specified otherwise.

2.1 Enzymes

2.1.1 Transformation of nitroreductase plasmid into competent cells

In order to transform the nitroreductase plasmids, eppendorf tubes of prepared competent cells (200 µL) were taken from cold storage (-20°C) and placed on ice. Typically DH5α is used for plasmid preparation and *Rosetta* is used for protein expression. The *Rosetta* competent cells are an efficient bacterium for the expression of heterologous genes; this is because it overexpresses rare tRNAs that are uncommon in other *E. coli* strains. This ensures that any heterologous gene carrying such rare codons will be expressed efficiently.[292] The prepared pET28a plasmid containing the NTR gene (2 µL) was added to the eppendorf's of competent cells and the samples where then left on ice for 30 minutes. The samples are then heat shocked at 42°C for exactly 50 seconds before being returned to ice for a further 2 minutes. The samples are then mixed with sterile Lysogeny broth (LB) ((500 µL) (Yeast (2.5 g), tryptone (5 g), NaCl (5 g) makes 500 mL)) before being incubated for 45 minutes at 37°C. To labelled, sterile agar plates (containing kanamycin (50 µg/mL)) the incubated plasmid/LB sample is added (125 µL) and spread across the plate using a sterilised glass spreader. The agar plates are then inverted and left to incubate at 37°C overnight. The agar plates are checked for colony growth and then removed from the incubator and stored for future use.

2.1.2 DNA plasmid digestion and DNA agarose gel

To perform a DNA plasmid restriction digest, purified pET28a plasmids containing the NTR gene (7 µL) were carefully transferred to a sterile eppendorf. To the eppendorf restriction enzymes (1 µL) were added; these correspond to the restriction enzyme sites present at the either end of the NTR insert (typically BamHI or HindIII) along with the appropriate restriction enzyme buffer (1 µL). The samples were then incubated at 37°C for 60 minutes. Whilst the samples are incubating the agarose gel can be prepared; first the gel mould is cleaned with industrial methylated spirit (IMS) and prepared by taping the ends of the cast closed. A 1% agarose gel is made by dissolving agarose (1 g) in 100 mL of 0.5% TBE (540 mg trisbase, 275 mg boric acid and 200 µl 500 mM Ethylenediaminetetraacetic acid (EDTA)). The solution is then heated gently to allow the agarose to completely dissolve before cooling; but not setting, to allow the addition of ethidium bromide (2.5 µL, 10 mg/mL). The gel can then be poured into the casting unit and the loading well comb added before being left to set. Once the gel has set

the loading comb and end tape can be removed. The gel should then be transferred into the running tank which contains 0.5% TBE buffer doped with ethidium bromide (2.5 μL, 10 mg/mL). Next 2 μL of 6x DNA gel loading dye was added to the 10 μL of digested plasmid and 5 μL of the resulting solution was added to the wells present in the agarose gel. 5 μL of DNA ladder was added into the wells contained at either end of the agarose gel to provide a reference point for the samples. The gel was then run for 45 minutes at 100 V before being removed from the running tank and placed on a UV transilluminator (UVP Benchtop transilluminator, UK) and an image of the resulting gel was taken.

2.1.3 Protein expression

Previously prepared and sequenced NTR plasmids were expressed using a method that has been previously described.[224] In brief; the bacteria containing the plasmids were picked and transferred to a mixture of LB media (5 mL) containing kanamycin (50 μg/mL), then grown overnight. The 5 mL of solution was mixed with 500 mL of LB solution (made as described above and autoclaved to sterilise) and kanamycin (50 μg/mL), and then the bacteria was grown at 37°C (shaken at 200 rpm) until a measured optical density ($O.D._{600\ nm}$) of 0.6 was achieved. The solutions was inoculated with isopropyl-beta-D-thiogalactopyranoside (IPTG) (2 mL, 100 mM, 0.4 mM (final)). The cells were then harvested by centrifuging (8000 rpm, 4°C for 10 min) and the resulting pellets were placed on ice and re-suspended in imidazole solution (10 mM, 10 mL); consisting of phosphate buffer (PB) (pH 7.4, 6.25 mL, 100 mM), and imidazole (2 M, 250 μL), made up to 50 mL with distilled water. The resulting suspensions were then placed in a beaker containing ice to avoid overheating the solution whilst they were sonicated four times for 30s, to break open the cells. The solutions were then centrifuged (20,000 rpm, 4°C, for 1h). The resulting solution contains the NTR and the pellet contains the cell debris. The solutions were then run on a sodium dodecyl sulphate-polyacrylamide gel electrophoresis (SDS-PAGE) to check that the protein was overproduced and that its molecular weight was as expected.

2.1.4 SDS–PAGE analysis

The glass plates were cleaned with ethanol and the 12% acrylamide sodium doecyl sulfate polyacrylamide gel electrophoresis (SDS-PAGE) resolving gel was prepared with doubly deionised (DDI) H_2O (3.4 mL), degassed acrylamide (30%, 4.0 mL), Tris-Cl pH 8.8 (2.5 mL), and SDS (10%, 100 μL). The stacking gel was prepared in the same way except that the pH of the Tris-Cl used was lower measuring pH 6.8. Immediately prior to the gel being poured; ammonium persulfate (APS) (10%, 100 μL) was added, followed by finally adding N,N,N',N'-tetramethylethylene diamine (TEMED) (10 μL) to the appropriate solution, initiating gel polymerisation once swirled. The resolving gel was poured into the plate until it

was 1 cm from the top, then water-saturated ethanol was poured on top of the gel to prevent the gel from contact with the air and possible contamination. When the resolving gel was set, the ethanol was washed away with distilled water, the stacking gel was poured onto the resolving gel, and a comb was pushed into the stacking gel. The samples were mixed with loading buffer, made up with: electrophoresis buffer (1 mL), glycerol (3 mL), 0.5% bromophenol blue (200 µL), and deionised water (5.8 ml), and then heated to 95°C for 5 min to denature the protein. These samples were then loaded onto the gel, which was run at 200 V for 45 min in an electrolyte solution of 1 x SDS. The gel was then stained with coomassie solution for 30 min made up with Coomassie Blue (1.25 g), methanol (500 mL), and acetic acid (100 mL), made up to 1 L with distilled water. The gel was then de-stained with a mixture of acetic acid (50 mL) and IMS (100 mL), made up to 500 mL with distilled water.

2.1.5 Enzyme purification

The imidazole solutions and the binding buffer were prepared as stated in Table 2.1 seen below, with filtered (450 nm filter) distilled water.

Table 2.1 Imidazole purification

PB 8x stock solution pH 7.4 (mL)	Imidazole (conc.)(mM)	Filtered dH_2O (mL)	Imidazole (2M) pH 7.4 (mL)
30	10 (binding buffer)	208.8	1.2
6.0	50	40.8	1.2
6.0	100	39.6	2.4
6.0	150	38.4	3.6
6.0	200	37.2	4.8
6.0	300	34.8	7.2
6.0	500	30.0	12.0
6.0	800	22.8	19.2
6.0	1000	18.0	24.0

A syringe (5 mL, plastipak) was filled with distilled water, and then connected to the column through a Luer adaptor. The nickel-agarose column (HiTrap chelating column, Amersham Biosciences, UK) was washed out with distilled water (5 mL) at approx. 1 drop/sec. The syringe was then filled with nickel salt solution ($NiSO_4$, 500 µL, 100 mM), which was applied to the column, followed by a further wash with filtered distilled water (5 mL). The column was then equilibrated with binding buffer (10 mL), the protein expression samples were then applied to the column and the flow-through collected. The column was then washed again with binding buffer (10 mL) and the flow-through collected. Increasing concentrations of imidazole were passed through the column and collected in 1 mL samples (5 for each concentration) to avoid

dilution. Finally, the column was washed with the remaining binding buffer (4 mL) and stored below 5°C ready for reuse. The second 1 mL aliquot of each elute was subjected to SDS-PAGE analysis; see section 2.1.4 for method, along with both of the sample flow-through's, an unpurified sample and an induced unpurified sample.

2.1.6 Removal of imidazole from the protein

In order to remove the imidazole from the resulting purified NTR the solution was passed down a PD-10 column (Amersham Biosciences). The PD-10 column is a polypropylene column that is gravity operated and contains 8.5 ml of Sephadex™ G-25 medium this is used for desalting and buffer exchange. The sealed column needs to be prepared before the NTR is passed through it. The top and bottom cap of the column were removed and the end of the column tip cut. Once this had been done the column was washed and equilibrated with PB (25 mL, 50 mM, pH 7.4). Then the NTR sample to be purified (2 mL) was applied to the column and eluted with 10 mL of PB. The enzyme was collected in a centrifuge tube (~2.5 mL) as a clear yellow band eluted from the column. The rest of the clear liquid was discarded as this contained the imidazole salt.

2.1.7 Determination of cys-tagged modified nitroreductases using cyclic voltammetry

All measurements were performed using an Autolab PGSTAT 30 computer-controlled electrochemical measurement system (Eco Chemie, Holland). The analysis was carried out with a three-electrode cell; using a saturated calomel reference electrode and a platinum counter electrode. Prior to use; the cell (Figure 2.1), was cleaned using ddH_2O followed by IMS and then acetone. The working electrode was an enzymatically-modified gold coated glass slide. A seal was made between the working electrode and the electrolyte solution with O-rings defining a geometric area of 0.6 cm^2.

The solution in the cell contained sodium hydroxide (20 mL, 100 mM), all the chemicals used were of an analytical grade. Prior to the formation of the enzyme layer, the gold (111)-coated glass slides (Winkler GmbH, Germany) were flame annealed in a Bunsen burner until they glowed red around the corners of the slides 3 times. This procedure produces a flat gold surface with strong Au (111) characteristics.[293] After cooling in air for a short time, 2 gold slides were placed glass back to glass back and transferred to a centrifuge tube containing the purified desalted NTR. The gold surface was modified by leaving the slides immersed in this solution for 48h at 5°C.

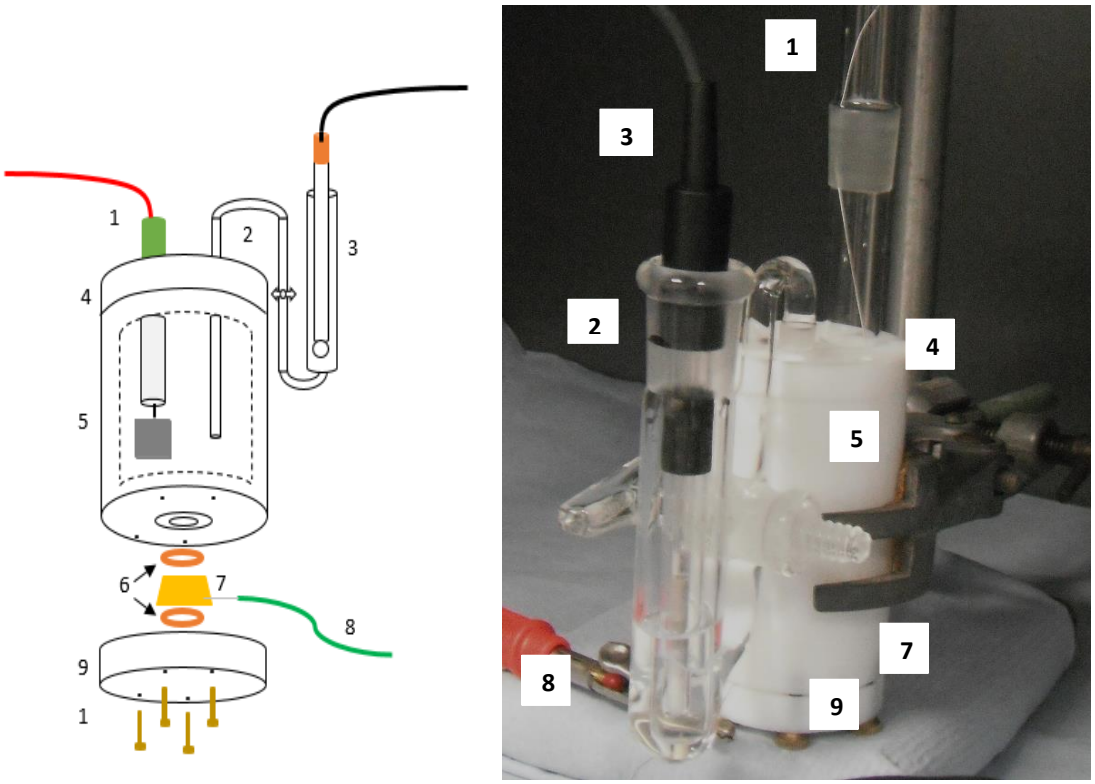

Figure 2.1 Diagram to show the set-up of cyclic voltammogram electrode cell. (1) Platinum counter electrode; (2) Salt bridge, (3) Saturated calomel electrode, (4) PTFE cell lid, (5) PTFE cell, (6) Rubber O-rings, (7) Au (111) gold coated glass slide working electrode, (8) Working electrode connection, (9) PTFE cell base.

After the electrode cell was assembled nitrogen was purged through the system for 20 minutes to remove all bubbles which could affect the scanning of the electrode. The cell was then placed in the faraday cage and the software was run using the following parameters (scan 0.0 V to -1.1 V, 50 mV/s, and scanned twice). The data was then collected and processed using Ecochemie GPES software and presented using Microsoft excel.

2.1.8 Using Bradford assay for protein quantification

To calculate the concentration of protein the method employed was using the Bradford reagent assay. The purified and desalted protein was compared to a set of bovine serum albumin (BSA) standards. The BSA standards are tested and a calibration graph was compiled; the unknown concentration of protein is them tested in triplicate and using the equation of the straight line from the calibration graph the protein concentration can be quantified from the gradient. The protocol for the Bradford reagent assay is as follows; Bradford reagent (BIO-RAD, UK) is removed from the fridge and allowed to equilibrate to room temperature (approx. 25°C), the BSA standards are prepared as per Table 2.2. A volume of 20 µL of BSA standard is pipetted into a cuvette along with 1mL of the Bradford solution, the same is done for the 3 samples of protein whose concentration is unknown. A reference cuvette is also prepared by adding 20 µL

of PB (50 mM, pH 7.4) to 1 mL of the Bradford reagent. All of the cuvettes are left to react for 5 minutes. The cuvettes are then tested for their optical density at a wavelength of 595 nm and each reading is recorded, the results are then analysed by plotting concentration against optical density and a calibration graph is produced. Using the straight line of the graph the unknown concentrations can be calculated.

Table 2.2 BSA standard solution calculation

Volume BSA stock solution (µL)	BSA stock concentration (µg/mL)	50 mM PB Volume (µL)	Final Protein Concentration (µg/mL)
70	2000	0	2000
75	2000	25	1500
70	2000	70	1000
35	1500	35	750
70	1000	70	500
70	500	70	250
70	250	70	125

2.2 Synthesis of superparamagnetic iron oxide nanoparticles

Due to its prominence in the literature, co-precipitation of iron ions in aqueous solution was chosen as the route to produce superparamagnetic iron oxide nanoparticles. Depending on the reagents and reaction conditions used both the size and morphology of the particles can be altered.[187,192,209] In a non-oxidising, basic environment, the reaction will proceed as Equation 2.1 to produce magnetite.

$$2Fe^{3+} + Fe^{2+} + 8HO^{-} \rightarrow Fe_3O_4 + 4H_2O$$

Equation 2.1 Formation of magnetite from aqueous iron ions in a non-oxidising environment

The co-precipitation method used for the synthesis of SPIONs is an adaptation of the methods previously described by Massart[216] and Lyon *et al.*[239] A 2:1 molar ratio of Fe^{3+}:Fe^{2+} was dissolved in HCl (10 mM, 25 mL) and added to NaOH (1.5 M, 250 mL) under vigorous stirring and in an Argon protected environment. The magnetite particles were then magnetically separated; washed with water, dispersed in HNO_3 (100 mM, 250 mL) and centrifuged (Thermo Scientific Heraeus Primo R, UK) at 5000 rpm for 45 mins. The precipitate was then redispersed in HNO_3 (10 mM, 250 mL) and heated to 90-100°C whilst stirring vigorously. During heating the solution changes colour from black/brown to brown/red. After 30 mins the heat was removed and the solution was allowed to return to room temp. The particles were then isolated *via* centrifugation at 5000 rpm for 45 mins. The precipitate was then redispersed and isolated

using centrifugation twice more, first using ddH_2O and then followed by Tetramethylammonium hydroxide (TMAOH) (100 mM, 100 mL). The supernatants were discarded and the final precipitate was suspended in TMAOH (5 mM, 250 mL).

2.3 Gold coating of the SPIONs

Two methods were investigated due to their success in the literature, the iterative hydroxylamine seeding method which was principally investigated by Lyon *et al.*,[239] and the pre-seeding method adapted from the principles in Brown *et al.'s* work.[294] The Lyon *et al.*,[239] method was conducted using the following procedure; to coat the iron particle cores with Au; Fe_3O_4 SPION cores (7.5 mL, 20.5 mM) were diluted to 1.1 mM using 140 mL water and this was stirred with Na citrate (100 mM, 7.5 mL) for 10 minutes. Upon successful reaction with Na citrate; $NH_2OH.HCl$ (200 mM) and $HAuCl_4$ (1% w/v) were then added incrementally, see table 2.3 on the following page for addition volumes.

Table 2.3 Composition of the incremental additions of $HAuCl_4$ and NH_2OH

Addition	200 mM $NH_2OH.HCl$ (µL)	1% $HAuCl_4$ (µL)
1	750	625
2	281	500
3	188	500
4	188	500
5	281	500

The final solution was subjected to magnetic separation by placing it in a conical flask with a 1T magnet (e-magnetsUK, NiCuNi plated Nd magnet) attached to the base. The solution was left overnight and then the resulting supernatant was decanted. The remaining magnetic particles were then washed with a citrate/ddH_2O solution (100 mM, 7.5 mL citrate, 140 mL ddH_2O), and magnetically separated again, the resulting particles were resuspended in ddH_2O stabilised with Na citrate (100 mM) and subjected to UV/Visible analysis (200-800 nm scan at a rate of 1000 nm/s, 200 µL sample: 800 µL ddH_2O against a blank of 1 mL ddH_2O). A 50 nm Au colloid standard was also subjected to the same UV/Visible analysis. Finally aliquots taken out during the course of the reaction; between iterations, were subjected to the UV/Visible spectrometer for analysis. The Lyon *et al.*[239] method was then adapted and combined with the principles of Brown *et al.'s* method.[294] The methodology is exactly the same as the above procedure with the only change coming in the composition of the incremental additions, see

Table 2.4. This 2nd method was created to try and avoid the potential for the Au^{3+} to nucleate and grow to become non-magnetic particles.

Table 2.4 Composition of the incremental additions of 5 nm Au Colloid, $HAuCl_4$ & NH_2OH

Addition	200 mM $NH_2OH.HCl$ (µL)	5 nm Au Colloid (µL)
1	750	625
	200 mM $NH_2OH.HCl$ (µL)	1% $HAuCl_4$ (µL)
2	281	500
3	188	500
4	188	500
5	281	500

2.3.1 Modification of Au-MNP synthesis

The gold coating procedure, section 2.3, was further adapted to optimise the production of fully coated monodispersed Au-MNPs. Fe_3O_4 SPION cores (3.5 mL, 3.3 mg/mL) were diluted with dH_2O (144 mL) and sodium citrate (5 mL, 100 mM). The solution was placed into a round bottom flask and degassed by bubbling argon through the solution for 30 minutes. To this solution 5 nm Au colloid was added (1 mL) and the solution was then heated to 30°C and vigorously stirred using a mechanical overhead stirrer (IKA, 8500 rpm) for 1 hour. A chloroauric acid solution (5 mL, 1% w/v) was then added to the reaction and the stirring continued for the duration of the experiment, the colour of the reaction at this point is observed as being orange. After the addition of the chloroauric acid; hydroxylamine (NH_2OH) (1.5 mL, 200 mM) was added at a drop rate of 1 mL/min. During this addition a colour change in the reaction is observed; as the first few drops of NH_2OH are added the colour changes from orange to a dark blue, as the addition of NH_2OH reaches 500 µL the reaction solution turns purple and after the remaining NH_2OH is added the solution is dark red in colouration. This is indicative of spherical gold particles.[295,296] The resulting solution is heated to 50°C and remains stirring vigorously for 1 hour. A 1:1 ratio solution of sodium citrate and ascorbic acid (5 mL, 100 mM:100 mM) is then added to the reaction. The solution is then left to continue to stir vigorously for 1 hour. The solution is then removed from the heat and the stirring is stopped. The resulting solution is then placed in a conical flask placed over a 1T magnet (e-magnetsUK, NiCuNi plated Nd magnet) and left to magnetically separate overnight. The supernatant of the solution is then decanted and the resulting Au-MNPs that are left attached to the magnetic attachment area are washed with dH_2O (5 mL) 3 times with a short magnetic separation period between washes ~1 hour. After the final wash the Au-MNPs are resuspended to an optical density of 1 $OD_{525\,nm}$ in 100 mM Na citrate stabilised ddH_2O and are stored in glass vials at 4°C for analysis and further use.

2.4 Immobilisation of NTR onto Au colloid and Au-MNPs

Purified and desalted NTRs were immobilized onto Au colloid by the formation of a self-assembled monolayer due to the cysteine tags present in the protein. According to previous research[15] the optimum ratio for Au-NTR conjugation is 270:1, To an Eppendorf tube containing Au colloid (50 nm, 15OD, Bioassay Works, 1 mL) the calculated volume of NTR was added and this Au-NTR solution was left to conjugate (1h, 25°C).

Immobilisation of NTRs onto Au-MNPs was achieved using the same optimised ratio. The calculated volume of NTR was added to the Au-MNPs (1 mL) and allowed to conjugate (1h, 25°C). After conjugation the Au-MNP immobilised NTRs were subjected to magnetic separation and then resuspended in ddH_2O.

2.5 Kinetics of NTR, Au-NTR and Au-MNP-NTR conjugates

2.5.1 Activity testing - enzyme reactivity to CB1954

Purified recombinant NTR were added to two solutions (one test and one reference solution) and made up to 1 mL using PB (50 mM, pH 7.4); see Table 2.5 for exact composition.

Table 2.5 Composition of reference and test cuvettes for activity testing.

	NTR activity		Au-NTR activity		Au-MNP-NTR activity	
Chemical	Volume (Reference) (µL)	Volume (Test) (µL)	Volume (Reference) (µL)	Volume (Test) (µL)	Volume (Reference) (µL)	Volume (Test) (µL)
CB1954 (10 mM)	-	10	-	10	10	10
NADH (10 mM)	60	60	60	60	60	60
PB (50 mM, pH 7.4)	925	925	890	890	830	830
NTR	5	5	-	-	-	-
Au-NTR	-	-	40	40	-	-
Au-MNP-NTR	-	-	-	-	-	100
Au-MNP	-	-	-	-	100	-
DMSO	10	-	10	-	-	-

To each solution, NADH (10 mM) was added and then to the reference solution dimethyl sulfoxide (DMSO) was added. The test and the reference sample were both heated to 37°C for 3 minute in a digital heat block (Stuart Heat block SBH130D, UK); before being transferred to the UV/Visible spectrophotometer (Jasco V-550, UK) one scan was completed before CB1954 (10 mM) was added to the test solution and then both solutions absorbance spectra (800 nm - 200 nm) was recorded every 1 minute for 15 minutes. The results were then analysed.[15] This was then repeated for Au-NTR with the amount of PB being used adjusted as

the volume of Au-NTR was increased. To test the Au-MNP-NTR activity the prodrug is added to both reference and test cuvettes, meaning no DMSO is added to either cuvette.

2.5.2 Determination of enzyme kinetics

The initial determination of the enzyme kinetics follows similar principles as the enzyme activity testing (section 2.5.1 above), but the focus is on the specific wavelength 420 nm. This wavelength is associated with the formation of the cytotoxic hydroxylamine products from the reduction of the prodrug CB1954. Varying concentrations of CB1954 were prepared and the change of absorbance at 420 nm was determined using time course management on UV/Visible spectrometer. A reference sample was prepared; PB (50 mM, pH 7.4), NADH (10 mM) DMSO (10 µL) and NTR. A test sample was also prepared in the same way with the omission of DMSO, see Table 2.8 for exact composition. Both the reference and test samples were incubated at 37°C for 3 minutes. The CB1954 was added last to the test cuvette just before commencing the UV/Visible scan and after inversion the cuvette was inserted into the UV/Visible spectrometer along with the reference cuvette and the 60 second analysis at 420 nm is started. Each concentration of CB1954 was tested in triplicate and at least 7 concentrations of prodrug were tested. The results are then compiled using Microsoft Excel and analysed using Sigmaplot®.

2.5.2.1 Modification to kinetic protocol for 96-well plate analysis

The final enzymatic kinetics were run using a 96-well plate microplate reader (Thermo Scientific Varioskan, USA). The methodology follows a similar principle to the kinetic analysis conducted above; just in a scaled down form, to reduce the quantity of compounds used and the cost. This method was developed by Dr. J. Halliwell, a fellow research group member. The microplate reader was turned on and the protocol loaded in advance of sample preparation to allow the microplate reader to heat up to 37°C. The protocol was set so that the microplate reader would measure the kinetic reaction over a time period of 60 s at a fixed wavelength of 420 nm. The microplate reader would take a reading at 4 defined time points which were; 1, 5, 25 and 60 seconds. To prepare the samples and ensure consistent experimentation a standard plate layout was created (see Figure 2.2). The procedure below was followed; the concentrations and volumes of the chemicals can be found in Table 2.6.

Table 2.6 Composition of the sample wells on the 96 well plate assay

Chemical	Volume (µL)
Prodrug CB1954	5
NADH (20 mM)	20
PB (50 mM, pH 7.4)	100 – everything else = X
Nitroreductase	Y (to give 10 µg/mL final concentration)

Firstly the prodrug CB1954 was added to the bottom of the 96-well plates in the wells indicated in Figure 2.2, then NADH was added to the wells. After the addition of both of these chemicals PB was added. The 96-well plate was then incubated (37°C, Stuart Incubator, UK) for 10 minutes along with a microcentrifuge tube containing the purified and desalted NTR. After 10 minutes the 96-well plate is removed from the incubator and positioned in the instrument tray of the microplate reader. Nitroreductase is then added to each of the wells and then the protocol is started for analysis. The results obtained from the 96-well plate assay had to be adjusted to account for the smaller path length utilised in the 96-well plates (3 mm) to allow for direct comparison to assays run using the traditional 10 mm path length in a UV/Visible spectrometer. This was done using photometric pathlength correction in the SkanIt software that is used to run the microplate reader.

	1	2	3	4	5	6	7	8	9	10	11	12
A		Blank										
B		2	4	8	12	16	24	32	40	64	100	
C		2	4	8	12	16	24	32	40	64	100	
D		2	4	8	12	16	24	32	40	64	100	
E		2	4	8	12	16	24	32	40	64	100	
F		2	4	8	12	16	24	32	40	64	100	
G												
H												

Figure 2.2 Plate layout for 96-well plate kinetic analysis, numbers correspond to concentration of prodrug added (mM)

The data imported into Sigmaplot® is the calculated product formed (µMol/L.s), see equation 2.2 for methodology and table 2.7 for an example set of values. The change in absorbance at 420 nm is measured typically between 5 and 25s, as long as this section is linear.

Table 2.7 Example set of data calculated in excel, prior to non-linear regression analysis in Sigmaplot®.

Final Substrate Concentration CB1954 (µmol/L)	420 nm Absorbance at 5s (**A**)	420 nm Absorbance at 25s (**B**)	Change in Absorbance (a.u.) (**C**)	Difference in time (s) (**D**)	Product (µmol/L)	Product (µmol/L.sec)
3000	0.53505	0.56526	0.03021	20	25.175	1.259

Molar extinction coefficient of hydroxylamine products of CB1954 = 1200 $Lmol^{-1}cm^{-1}$

420 nm absorbance at time (**B**) – 420 nm absorbance at time (**A**) = Change in absorbance (**C**)

Time (**B**) – Time (**A**) = Difference in time (**D**)

$$\text{Product formed (µmol/L)} = \frac{(0.03021)}{1200} \times 1 \times 10^6 = 25.175$$

$$\text{Product formed (µmol/L.sec)} = \frac{25.175}{20} = 1.259$$

Equation 2.2 Example calculation to illustrate how the product formed (µMol/L.s) is calculated from the UV/Visible spectroscopy data for later use in Sigmaplot®.

This data in triplicate is then inputted into Sigmaplot® along with the final prodrug concentrations tested. A nonlinear regression is applied to the data which produces a Michaelis-Menten hyperbolic curve (Figure 2.3) and a report containing the key kinetic parameters, see table 2.8 for example set of data.

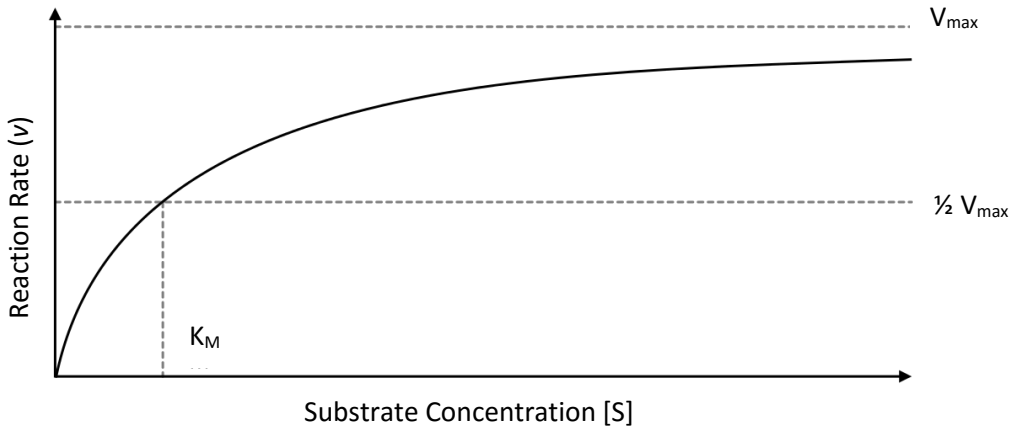

Figure 2.3 Typical Michaelis-Menten hyperbolic curve showing the relation between the substrate concentration [S] and the reaction rate (v), and defining the kinetic parameters V_{max} and ½ V_{max}.[297]

The data is derived from the Michaelis-Menten equation[297] (Equation 2.3).

$$v = \frac{Vmax[S]}{Km + [S]}$$

Equation 2.3 Michaelis-Menten equation

The reaction rate (*v)* is plotted along the y-axis and along the x-axis the substrate concentration [S] is plotted. The value V_{max} represents the maximum rate achieved by the system, at maximum (saturating) substrate concentrations. The Michaelis constant (K_m); defines the substrate concentration at ½ V_{max}. k_{cat} is the turnover number and defines the maximum number of substrate molecules that are converted to product per enzyme molecule per second. Finally $[E]_0$ is the enzyme concentration.[297]

Table 2.8 Example set of kinetic data obtained from Sigmaplot (V_{max} and K_m) k_{cat} is calculated using V_{max}/Et.

V_{max} ($\mu molL^{-1}s^{-1}$)	K_m ($\mu molL^{-1}$)	k_{cat} (s^{-1})	$[E]_0$ (μM)	k_{cat}/K_m ($M^{-1}s^{-1}$)
3.42	5755.30	58.01	0.0588	10,080

The procedure was then repeated for Au-NTR conjugate adjusting the volume of PB due to an increase in volume of Au-NTR; seen in table 2.9.

Table 2.9 Composition of reference and test cuvettes for enzyme kinetics testing

	NTR activity		Au-NTR activity	
Chemical	Volume (Reference) (µL)	Volume (Test) (µL)	Volume (Reference) (µL)	Volume (Test) (µL)
Prodrug CB1954	-	10	-	10
NADH (10 mM)	60	60	60	60
PB (50 mM, pH 7.4)	925	925	890	890
NTR	5	5	-	-
Au-NTR	-	-	40	40
DMSO	10	-	10	-

2.5.3 pH and temperature profile kinetics

The same protocol as described in the previous above was followed. However for the temperature profile, samples were heated for 3 mins at 20, 30, 40, 50, and 60 °C respectively. The CB1954 was then added to the test cuvette and then 60 second time drive analysis was conducted on the UV/Visible spectrophotometer at 420 nm. The samples were only tested at one concentration of CB1954 and this was set as the Km concentration obtained from the initial kinetic testing. The pH profile was conducted again using the same protocol and parameters from section 2.5.2 but the PB (50 mM, 925 µL) was prepared at the following differing pH's; pH 4, pH 6, pH 7, pH 8 and pH 10. The samples were then left for 5 minutes before the CB1954 was added and the UV/Visible analysis conducted.

2.6 HPLC analysis of DNA cross-linking hydroxylamine products

Samples were prepared for analysis *via* High performance liquid chromatography *(*HPLC) to determine the products formed from the enzymatic reaction of the NTRs with the prodrug CB1954 along with the co-factor NADH. To create a sample for HPLC (Thermo Scientific, Dionex UltiMate 3000 HPLC System, USA) analysis the following compounds; 120 µL NADH (10 mM), 20 µL CB1954 (50 mM), a calculated volume of NTR to give a final concentration of 116 µg/mL in 1080 µL, and PB (50 mM) were added to give a final sample volume of 1080 µL. The reaction is then left for 30 minutes and kept wrapped in foil throughout the reaction to prevent degradation of the light sensitive components. The sample is then degassed for 15 minutes using N_2 to remove any dissolved oxygen from the electrolyte. This is done by removing the lid of the falcon tube and creating a parafilm seal to which a glass pasteur pipette is then inserted through the film to allow the sample to be degassed. Once de-gassed, 600 µL of the reaction mixture is removed and transferred to a Chromacol Select 2 mL vial this is also wrapped in foil to prevent light degradation and then the sample is taken to the HPLC. The sample vial was loaded into the machines auto sampling tray and the machine was prepared for

analysis. A C18 column was used for the analysis (Waters Spherisorb® 5 µm ODS2 4.6 mm x 250 mm C18 Column, UK). The sample was run using the following protocol; 50 µL sample injection volume, ambient temperature (~21°C), 30 minute duration and the UV wavelengths used for detection were 260, 350, 400, 420 nm. The solvent gradients and composition can be seen in Table 2.10 below. This methodology was developed by George Robinson, a research technician within the research group.

Table 2.10. Overview of solvent gradient for HPLC analysis

	0 mins	20 mins	22 mins	24 mins	26 mins	30 mins
Water (A)	90%	70%	0%	0%	90%	90%
Acetonitrile (B)	10%	30%	100%	100%	10%	10%

2.7 Cell culturing and cell viability assay

All experiments relating to the viability assay were carried out in a class II tissue culture lab and all experiments were conducted in the tissue culture fume hood with aseptic practices in place.

2.7.1 Cell preparation and culturing

HeLa and MCF-7 cells (Public Health England, UK) were grown, maintained and cultured in preparation for testing in a cell viability assay, Figure 2.4, seen below provides a flow diagram of the procedure for the cell viability assay.

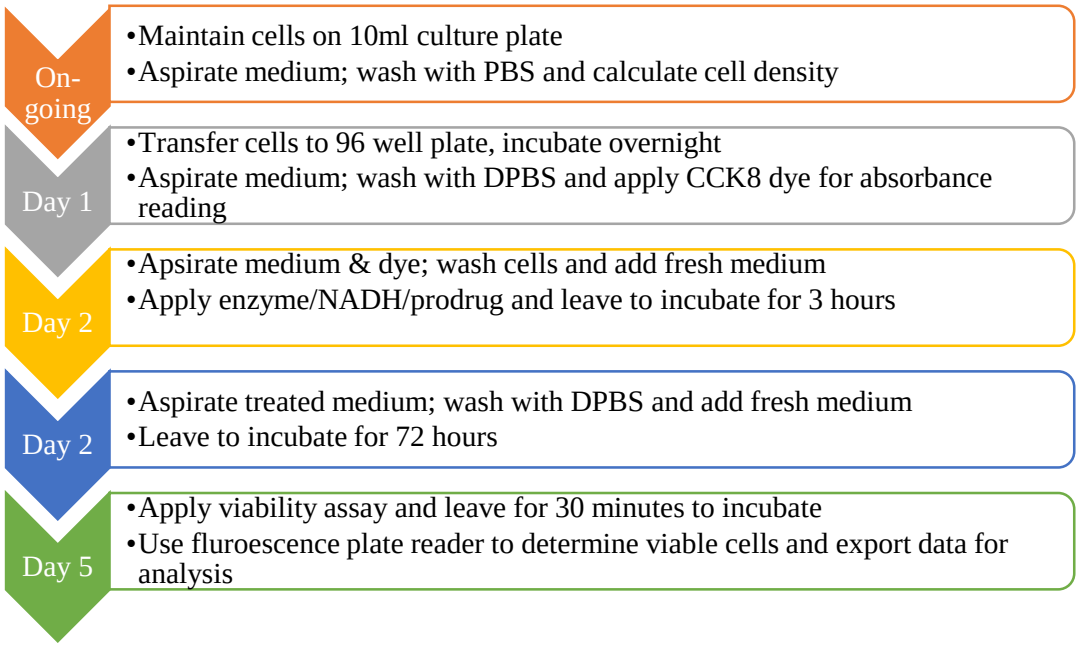

Figure 2.4 A condensed overview flow diagram of the procedure for cell viability assay[298]

The frozen cell lines were thawed by removing the vial of cells form vapour phase liquid nitrogen storage and allowed to thaw quickly at 37°C in a temperature controlled water bath. Just before the cells are completely thawed they are transferred to a 10 mL culture dish containing 9 mL of complete growth medium. For HeLa cells the complete medium contains; Dulbecco's modified eagle's medium (DMEM) containing 10% Foetal bovine serum (FBS) and 1% penicillin/streptomycin. For MCF-7 cells the complete medium consists of; DMEM containing 10% FBS, 1% penicillin/streptomycin, 1% Non-essential amino acid (NEAA) and L-glutamine (2 mM). The culture dish is then allowed to incubate for 2-4 hours at 37°C in a 5% CO_2 incubator (Thermo Scientific Heracell™ 150i CO_2 Incubator, UK); The medium is then removed and replaced with 10 mL of fresh medium and the cells are further incubated overnight. After 24 hours the cell again have the medium removed and replaced and are then re-incubated until the cells are ~80% confluent.

2.7.2. Cell freezing for long term storage

The cells should be approximately 80% confluent before preparation for freezing. Appropriate storage vials, e.g. cryovials should be used and labelled prior to use along with the preparation of the freezing medium. Freezing medium should be freshly produced before each set of freezing experiments. To make the freezing medium 900 µL of fresh complete cell medium and 100 µL anhydrous DMSO should be mixed for every 1 mL of freezing medium needed. The freezing medium should be kept on ice until used and any remaining medium should be discarded immediately using the appropriate disposal methods.

To prepare the cells for freezing the medium should be vacuum aspirated and the cells washed once with 5 mL Dulbecco's phosphate-buffered saline (DPBS). The DPBS should then be aspirated and 1 mL of trypsin-EDTA (5.0 g/l porcine trypsin and 2.0 g/l EDTA•4Na in 0.9% sodium chloride, 10X, cell culture tested) should be applied to the culture dish before replacing the culture into the CO_2 Incubator at 37°C for 5 minutes. Cell culture dishes are then removed from the incubator and 4 mL of complete medium is added to stop trypsinisation; the solution is then gently pipetted to ensure no clumping of the cells occurs. The cell solution is then transferred to sterile 15 mL centrifuge tubes and pelleted at 250 xg for 5 minutes at room temperature. Once pelleted the resulting supernatant medium is aspirated from the tubes. The freezing medium is then pipetted into the centrifuge tubes; 1 mL per tube and the cells resuspended in the freezing medium. The solutions are then transferred to cryovials and are transferred to a manual controlled freezing container, containing isopropyl alcohol and placed in a -80°C ultra-low temperature freezer (Thermo Scientific, USA) for 24 hours to allow the cells to cool by 1 °C per minute. After 24 hours the cryovials containing the frozen cells are transferred to the vapour phase liquid nitrogen for long term storage at -196°C.

2.7.3 Cell viability assay

Once the cells have reached the desired level of confluence the medium is removed from the culture dish by vacuum aspiration; the cells are then washed with 5 mL of DPBS to remove any excess medium or serum. The DPBS is then removed and 1 mL of trypsin/versene® is added to the culture dish and it is then incubated for 5 minutes. This process is done to allow the cells to detach from the bottom of the culture dish ready for resuspension. To stop the trypsinisation, 9 mL of the complete growth medium is added to the culture dish. To use the cells for the cytotoxicity assay the cells need to be resuspended to a certain density; to do this take 10 µL of the resuspended cell solution, apply it to the top side of a haemocytometer and then repeat for the bottom half. The number of cells present in the 4 x 4 grid outlined by 3 bright lines need to be counted for both the top and bottom half and then the 2 readings need to be averaged, if the average is below 25 then incubate the cells for a further 24 hours to allow further growth.

After the cell density is calculated the solution for the 96 well plate preparation is adjusted to the required cell density by diluting with complete DMEM, then carefully 100 µL of cell culture solution is added to each well and they are left to incubate overnight. On day two the cells need to be checked for their growth before the treatment step. The medium is aspirated from the plates, DPBS is used to wash the cells and then 100 µL of fresh medium is added. CCK-8 dye (NBS Bio, UK) is used to measure the absorbance of the cells so that based on a calibration graph conducted with cells only and the CCK-8 dye the plates can always be grown to the same starting point (OD_{650nm} 0.2). The dye is placed into the wells of the plate (10 µL) and the plate is then left to incubate for 2 hours. The absorbance of the plate is then read and analysed (Thermo Scientific Varioskan, USA) at 450 nm for the background reading (this is the region in which the phenol red from the growth media absorbs) and 650 nm. The two values are then subtracted from one another and when the absorbance has reached 0.2 then the plates proceed to the treatment stage. In the treatment stage 2.5 µL NADH (final conc. 250 µM), 2.5 µL CB1954 (final conc. 10 µM) and 1 µL enzyme (final conc. 2 µg) are added to the wells in various combinations; and then the plate is left to incubate for 3 hours (37°C, 5% CO_2).

After incubation the medium is removed, the cells washed with DPBS (100 µL) and fresh growth medium (100 µL) added to the plates. The plates are the incubated (37°C, 5% CO_2) for a further 72 hours. After this period of incubation the cells are then tested for their viability using the acetomethoxy derivative (AM) Calcein dye. Firstly the Calcein buffer is prepared using 5 mL of a 10x Calcein AM dilution/wash (DW) buffer (Trivegen, UK) and 45 mL of ddH_2O. To a tube containing one pellet of the Calcein AM dye (E-Biosciences, UK) 25 µL

anhydrous DMSO is added to make a 2 mM stock; for one 96 well plate take 5 µL of this stock and dilute it in 5 mL of the 1x Calcein AM DW buffer. The next step is to aspirate the media from the 96 well plates and then wash the cells with 100 µL of the 1x Calcein AM DW buffer. Remove the buffer and replace with 50 µL of the 1x Calcein AM DW buffer and 50 µL of the Calcein AM dye solution to each well.[298] The plate is then incubated for 30 mins (37°C, 5% CO_2); after this time the plate is removed and taken to the fluorescence reader (Thermo Scientific Varioskan, USA) for analysis. The plate is read using a pre-saved protocol which measures the excitation at 490 nm and the emission at 520 nm. The plate is then analysed and the data exported for further analysis. This assay was used in preliminary experimentation and was subsequently replaced by the assay detailed in section 2.7.4.

2.7.4 Modification to cell viability assay

The 3-[4,5-dimethylthiazol-2-yl]-2,5-diphenyltetrazolium bromide; thiazolyl blue (MTT) cell viability assay was performed following the method previously developed by Mossman, 1983 with some slight modification.[299] In brief; the cell lines were seeded at a density of $1x10^4$ cells per well, in 100 µL of complete DMEM medium and were allowed to attach to the bottom of the wells overnight (37°C, 5% CO_2). At the end of this period the media was carefully aspirated from the wells. Complete DMEM medium containing differing concentrations of NTR (50 µL) were added to the wells along with complete media (50 µL) containing the prodrug CB1954 (final concentration 10 µM) and NADH (200 µM). After 4h, the media was carefully aspirated, and the wells washed with 100 µL DPBS. This was then again carefully removed by aspiration and the cells were replenished by adding 100 µL of complete DMEM medium to the wells. After a period of 48h, 20 µL of MTT (5 mg/mL) was added to each well and the 96 well plate was incubated for 4h (37°C, 5% CO_2). The media was carefully aspirated from the wells with caution taken to not disturb or remove any of the resulting purple formazan crystals that formed. The formazan crystals were dissolved by adding 100 µL of DMSO to each of the wells. The 96 well plate was then placed in a microplate reader (Thermo Scientific Varioskan, USA) and the data was analysed at a wavelength of 570 nm.

Chapter 3

Nitroreductase Production and Determination of Kinetics

The majority of the work discussed in this chapter is published in the following paper.

YfkO nitroreductase immobilised with controlled orientation onto superparamagnetic nanoparticles; towards a direct enzyme cancer therapy approach. *Publication suited to Biomacromolecules,* **(in DRAFT)**

Chapter 3 – Nitroreductase production and determination of kinetics

3.1 Introduction

Previous work by Gwenin et al.,[15] has seen recombinant DNA techniques used to insert NTR genes into pET-28(+) vectors and be genetically modified to obtain a cysteine tag residue. Agarose gel, SDS-PAGE analysis and UV/visible spectroscopy were used to evaluate the enzymes along with 96-well plate enzymatic kinetic assays. This chapter details these experiments and their interpretation, comparing and contrasting the similarities and differences between NfsB and YfkO for their application in a magnetic nanoparticle directed enzyme prodrug therapy (MNDEPT). Appendix 7.1 shows the amino acid alignments of the two gene sequences which were compared and their divergences were chosen to enhance the chance of obtaining NTRs with a variety of reaction pathways, this comparison presented as a percentage of similarity is seen in Table 3.1. The complex nature of these genetically modified NTRs leads to a range of differences observed in kinetic properties for even the most similar NTRs.[300] This problem arises due to many different reasons as even enzymes with very similar structures can have varying kinetics properties to a given substrate or prodrug.[301]

Table 3.1 Amino acid sequence alignment comparisons

Sequence	***nfsB***	***yfkO***
nfsB	100%	25%
yfkO	-	100%

Previous worked conducted by Gwenin *et al.*[15]; concluded that the addition of 12 cysteine tag residues to a dimeric NTR; enabled maximum thiol-gold linkage which was confirmed using cyclic voltammetry.[224]

3.2 Plasmid digestion

Restriction endonucleases for *yfkO-cys* from *Bacillus Lichenformis* were used to digest the genes from the pET-28a(+) vector following the experimental procedure set out in section 2.1.2. Confirmation of successful cloning of the *yfkO-cys* gene into the plasmid can be seen in Figure 3.1 (left). Figure 3.1 (right); shows the resulting agarose gel from the use of restriction endonucleases for *nfsB-cys* from *Escherichia coli K12* to digest the genes from the pET-28a(+) vector.

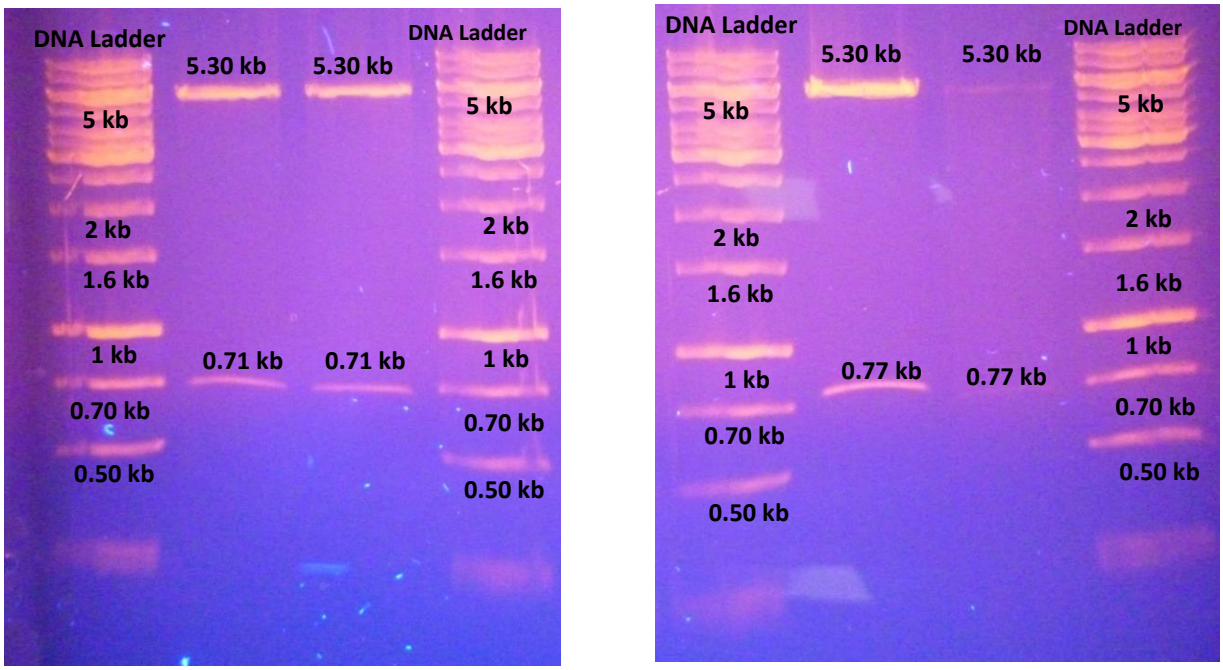

Figure 3.1 Agarose gel stained with ethidium bromide under exposure to UV light; showing (Right) the yfkO-cys genes after digestion form the from pET-28a(+) vectors; observed at 5.30kb (Left) the nfsB-cys gene after digestion from the pET-28a(+) vectors; observed at 5.30kb, both using the restriction enzymes BamHI and HindIII see Appendix 7.2.

The NTR gene sizes and protein weights for all the enzymes are shown in Table 3.2.

Table 3.2 The sizes of the genes and resulting proteins of the generated NTRs

NTR	Gene size (bp)	Monomer Mw (kDa)
yfkO-his	693	29.74
yfkO-cys	711	30.38
nfsB-his	750	27.46
nfsB-cys	770	28.1

3.3 SDS-PAGE analysis

The NTRs were expressed and then purified; next the cell free extracts analysed by SDS-PAGE to determine the molecular weight of the NTR protein monomer. The protocol for this can be found in section 2.1.4.

The NfsB-cys monomer was expressed and has an expected mass of 28.1 kDa this is due to the incorporation of the 6 cys- tags as without these the his-tagged NfsB monomer has an expected mass of 27.46 kDa. Figure 3.2, shows the successful induction process of the protein by comparison on the induced and uninduced samples.

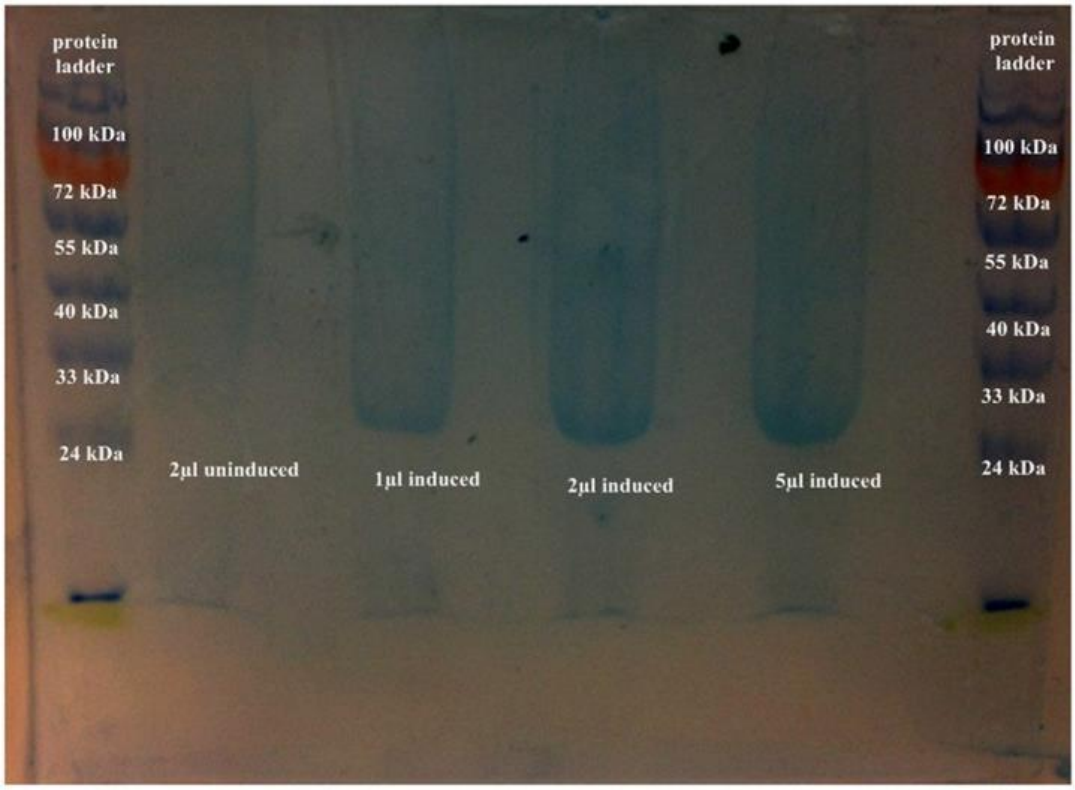

Figure 3.2. SDS gel showing the induced and uninduced expressed NfsB-cys samples

The proteins were then purified using the method set out in 2.1.5. By passing imidazole buffer (IB) through the nickel-agarose column at concentrations of 50 mM and 100 mM the imidazole displaces the naturally occurring proteins which have adsorbed to the nickel column, while the more strongly bound *NfsB-cys* remains immobilised to the column.

At concentrations of 200 mM IB the NfsB-cys elutes. Figure 3.3, below shows that the increasing imidazole concentrations used in the purification process are necessary for an effective elution of the NTR. The 200 mM imidazole run eluted the largest amount of NTR whilst the lower concentrations elute other fragments bound to the column.

Figure 3.3. SDS gel showing the crude, flowthrough & 50-200 m*M imidazole purification for* NfsB-cys

The 200 mM sample was then run on a separate SDS gel in 5 x 1 ml samples (Figure 3.4) along with the induced and uninduced crude samples. The gel in Figure 3.4 shows that the 2nd ml aliquot of the sample contains the largest amount of protein and therefore needs to be the only sample used and tested in future expressions. The other aliquots have a decreased clarity on the gel.

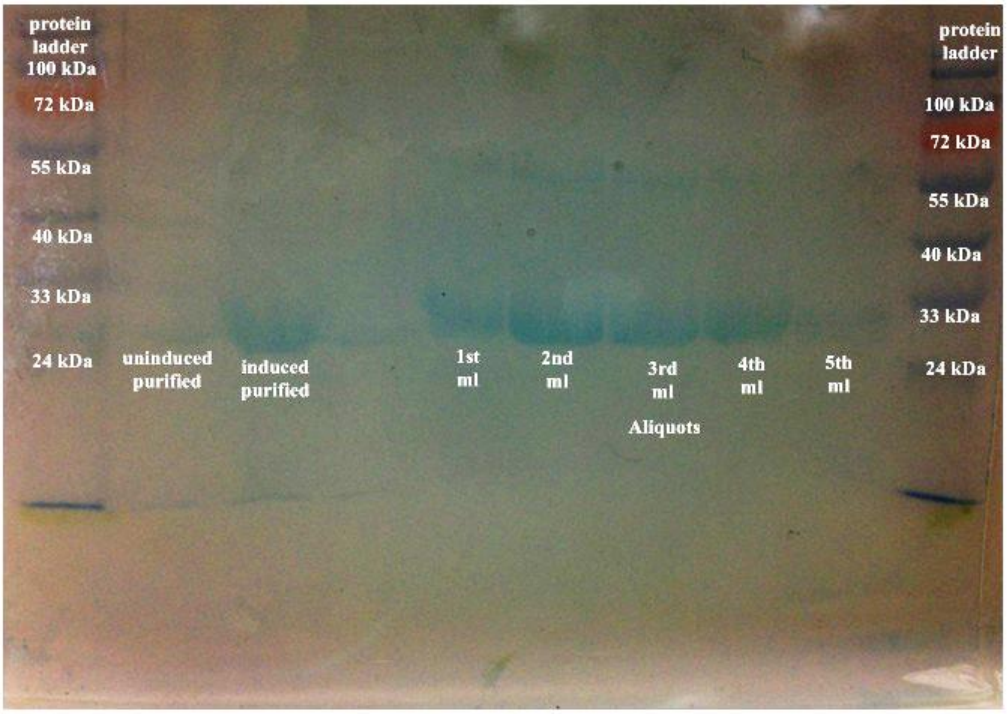

Figure 3.4. SDS gel showing the 5 sequential 1 mL aliquots of the 200 mM imidazole purification fraction for NfsB-cys

The YfkO-cys monomer was expressed and has an expected mass of 30.38 kDa this is due to the incorporation of the 6 cys-tags as without these the his-tagged YfkO monomer has an expected mass of 29.74 kDa. Figure 3.5 (left), shows that the increasing imidazole concentrations used in the purification process are necessary for an effective elution of the NTR. The 500 mM imidazole run eluted the largest amount of NTR whilst the lower concentrations possibly elute other fragments bound to the column.

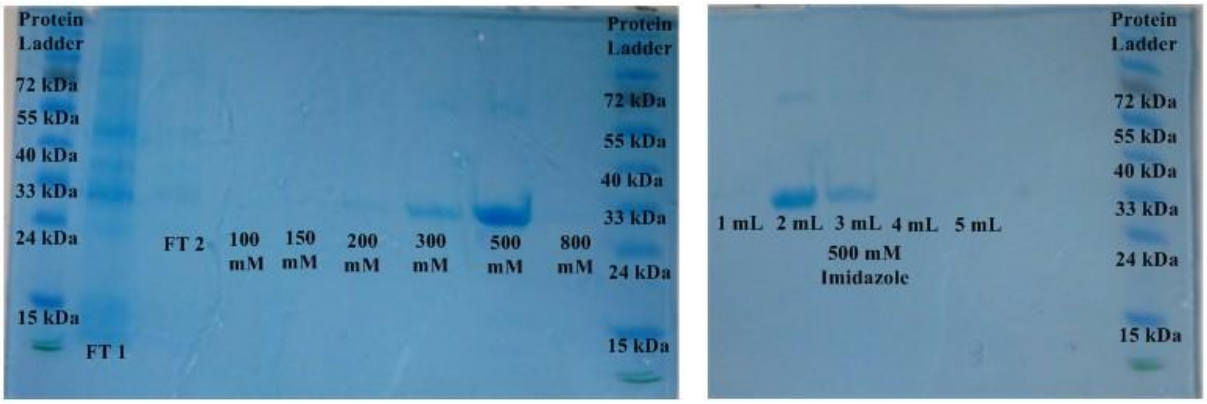

Figure 3.5. SDS gel showing (left) the flowthrough and 100 mM-800 mM imidazole purification runs for YfkO-cys *(right) the 1-5 mL aliquots of the 200 mM imidazole purification fraction for* YfkO-cys.

The 500 mM eluted sample was then run on a separate SDS gel; from the sequential 1 mL aliquots, 12 µL were loaded into separate wells on the gel (Figure 3.5 (right)). The gel shows that the 2nd ml aliquot of the 500 mM IB elution contains the largest concentration of protein indicated by the strength of the band present. The other aliquots have a decreased band intensity on the gel.

3.4 Enzyme assay using ultraviolet-visible spectroscopy

UV-Visible spectroscopy was used to measure the activities of the purified and desalted NTRs. The prodrug to be tested was CB1954 and in aqueous solution it has poor solubility and as such a 1 M master stock in DMSO was initially created and subsequent dilutions of the prodrug were made using PB (50 mM, pH 7.4). This was done to allow the concentration of DMSO present in the prodrug samples to stay below 5%. At concentrations above 5% DMSO has shown to inhibit the activity of NTR with the prodrug and would therefore affect the results obtained.[302]

The concentration and therefore absorbance of the cofactor NADH and CB1954 are expected to decrease during the enzymatic activity reaction, whilst at the same time an increase in absorbance of NAD+ and the hydroxylamine reduced derivatives of CB1954 should be observed. The reaction scheme for the production of the hydroxylamine derivatives of CB1954 is shown in Figure 1.10 in the introduction section of this study. The UV-Visible spectra of the reaction between YfkO-cys, NADH and CB1954 over 10 minutes is shown in Figure 3.6, with respective increases and decreases in absorbances at wavelengths corresponding to the different reaction species present.

Peak (**1**) of Figure 3.6 at approximately 280 nm is indicative of the absorbance region of NTRs. This region is also the area in which NAD+ and NADH absorb, they have a λ_{max} = 260 nm.[303] During the course of the reaction NADH is oxidised to NAD+, which solely absorb at ~260 nm meaning that as the reaction proceeds the peak will decrease due to oxidation of NADH but increase due to the formation of NAD+. This means that the concentrations of the oxidised and reduced forms of the cofactor cannot be quantified and therefore related directly to the reduction of the prodrug. The noise that is observed below 270 nm can be attributed to the cuvettes used in the activity scans having a transmission range of 230-900 nm, alongside the cancelling out of NADH due its presence in both the test and reference cuvette.

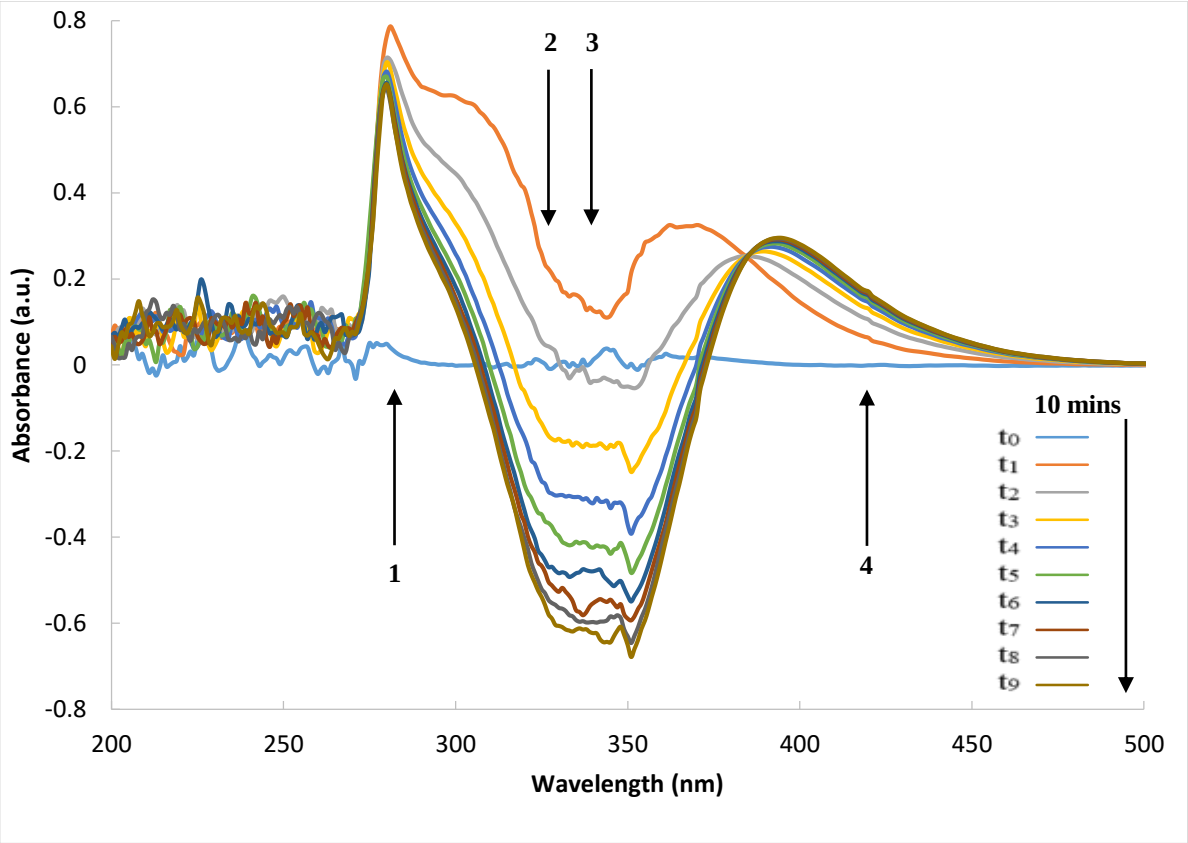

*Figure 3.6. UV-Visible spectra of yfkO-cys (10 µg/mL) showing the enzymatic activity assay. **(1)** NTR absorbance ~ 290 nm. **(2)** Reduction of CB1954 λ_{max} = 327 nm. **(3)** Oxidation of NADH λ_{max} = 340 nm. **(4)** Production of CB1954 reduction products λ_{max} = 420 nm.*

The broad peak observed at ~340 nm overlaps the λ_{max} of both CB1954 (**2**); see Appendix 7.3 and NADH (**3**), see Appendix 7.4, because of this overlap in this region the concentrations cannot be quantified of both the CB1954 and the NADH. The peak prevalent at 420 nm as indicated by peak (**4**) directly correlates to the λ_{max} of the two common reduction products of CB1954; the 2- and 4-hydroxylamine derivatives. These have a molar extinction coefficient (ε) = 1200 L $mol^{-1}cm^{-1}$. This is the only region that can determine the kinetic parameters of the NTRs by allowing the rate of product formation to be quantified in direct correlation with the absorbance.[301] Figure 3.7 shows the course of the reaction over the full 10 minute scan and plots absorbance vs time at 420 nm. It shows that the reaction is only truly linear for the 1st few minutes of the reaction, meaning that caputuring the data early in the reaction is paramount for kinetic analysis. For completeness the reaction of NfsB-cys is shown in Figure 3.8.

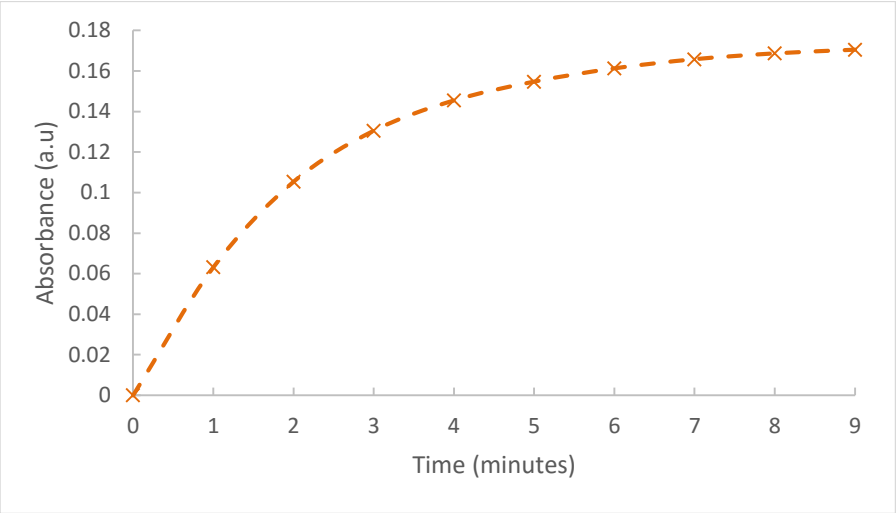

Figure 3.7 Plot of absorbance at 420 nm vs time for YfkO-cys (10 µg/mL), CB1954 (100 µM), NADH (600 µM) and PB (50 mM, pH 7.4).

The change in absorbance at 420 nm where the hydroxylamine reduction products are formed allows the rate of formation to be observed.[302] This region of the spectra is free from any interference from the other resulting absorbance peaks. Kinetic parameters can be determined by monitoring the change in absorbance at 420 nm; this should be done over a short time period allowing for accurate quantification of the rate of product formation.[302]

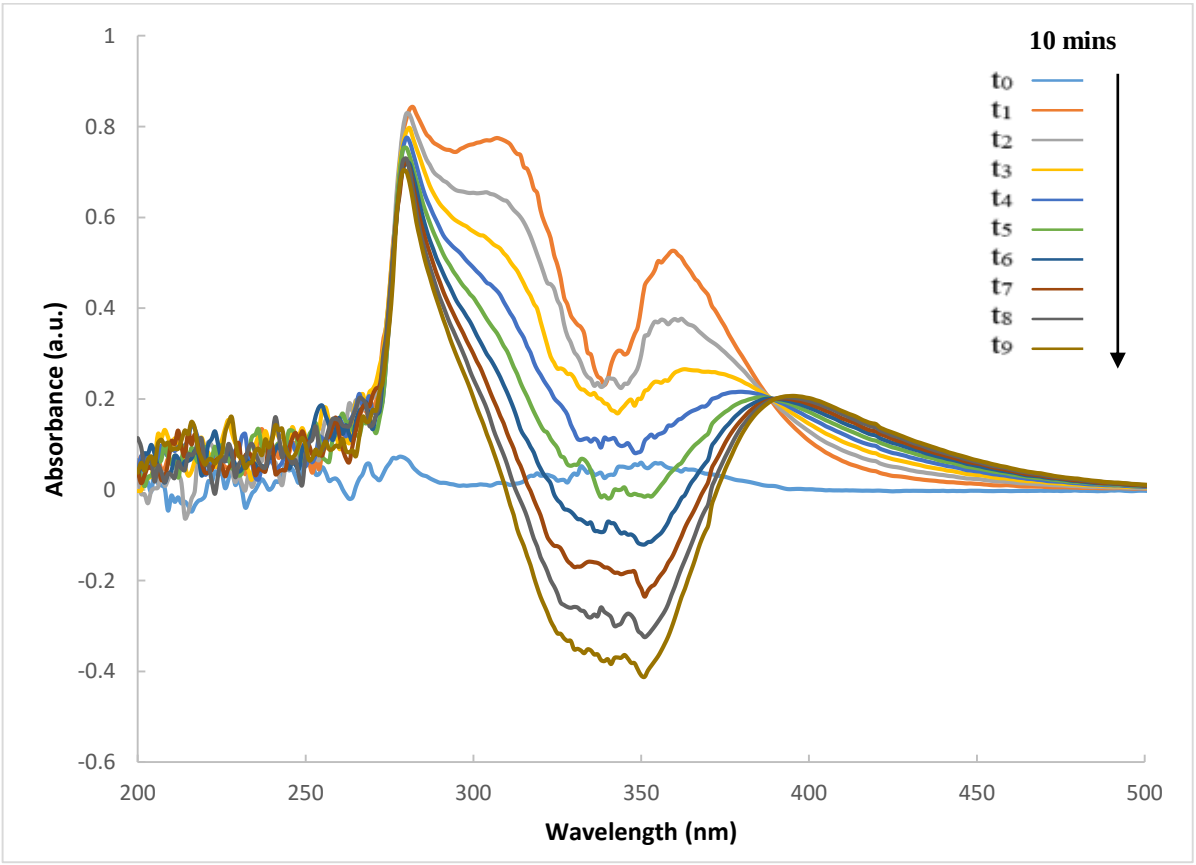

Figure 3.8. UV-Visible spectra of nfsB-cys (10 µg/mL) showing the reduction of the prodrug CB1954 and oxidation of the cofactor NADH.

Figure 3.9 shows the course of the reaction over the full 10 minute scan and plots absorbance vs time at 420 nm. This alongside Figure 3.7 for YfkO-cys again highlights the need for kinetic parameters to be determined over a short period of time as outside of the first 2 minutes of the reaction, the rate of hydroxylamine product formation begins to tail off and is no longer linear. The quantification of the kinetic parameters of the NTRs enables a comparison to be made between the NTRs and therefore identify the most ideal candidate for MNDEPT.[301] Each NTR was characterised with CB1954 and the amount of hydroxylamine derivatives generated were calculated. This data is discussed in the following sections; 3.5.1 and 3.6.1.

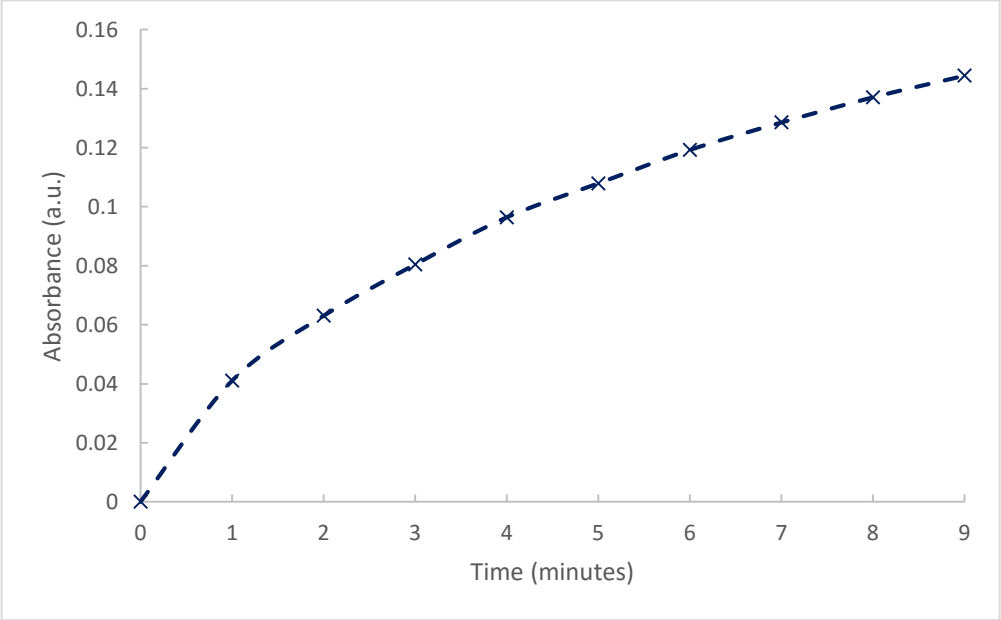

Figure 3.9 Plot of absorbance at 420 nm vs time for NfsB-cys (10 µg/mL), CB1954 (100 µM), NADH (600 µM) and PB (50 mM, pH 7.4).

3.5 Characterisation of NfsB-his and NfsB-cys

The ability of both NfsB-his and NfsB-cys to reduce CB1954 utilising NADH as a cofactor were analysed by monitoring the production of the hydroxylamine derivatives during the reaction. The optimal pH and temperature parameters were also determined for enzyme using UV-Visible spectroscopy. To distinguish the ratios of the 2- and 4-hydroxylamine derivatives produced from the reaction of CB1954 and the NTRs HPLC analysis of the enzymatic assay reaction was conducted and the compounds quantified.

3.5.1 K_m and V_{max} of NfsB-his and NfsB-cys

To calculate the K_m and V_{max} of the NfsB and NfsB-cys NTRs the kinetic enzymatic activity was measured at an increasing range of concentrations of CB1954. All kinetic experiments were conducted in triplicate and the average was plotted and analysed.

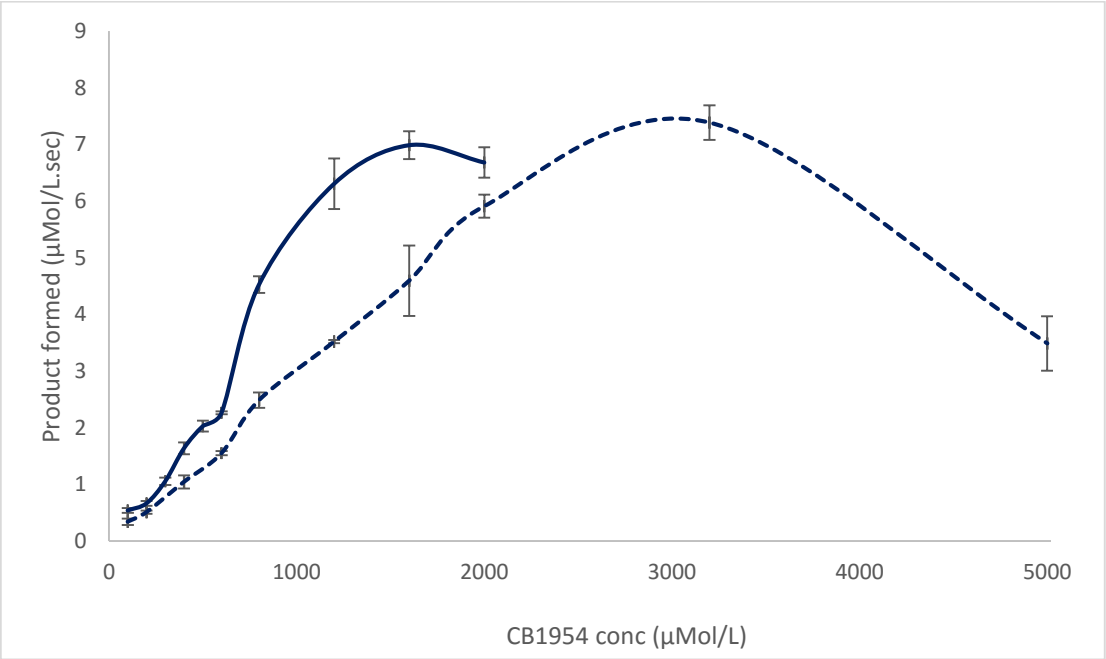

Figure 3.10. A graph quantifying the rate of the hydroxylamine reduced prodrug derivative formation (λ_{max} = 420 nm, ε = 1200 L mol^{-1}cm^{-1}) for the NfsB-his (Blue) *and* NfsB-cys (Dashed blue) *NTRs at increasing CB1954 concentrations. The error bars represent ± 1 SD.*

Figure 3.10 shows the rate of reaction increases with increasing concentration of CB1954 until the reaction reaches its $V_{max,}$ there is an observed drop in the product formation because at higher concentrations the vast majority of the prodrug and NADH has been consumed, this leads to one or both of these becoming a limiting factor when the measurement is taken between 5-25s. The prodrug at high concentrations can also bind to itself leading to it being too large and the wrong shape to fit into the active site of the enzyme. At high prodrug concentrations the CB1954 can also bind to other areas around the active site of the enzyme cause a change in the conformation of the enzymes active site, preventing the normal reduction of the prodrug. All of these cases result in a decrease of the efficiency of the NTR to the CB1954 and manifests as a drop in product formation. The data obtained for kinetic analysis is subjected to non-linear regression fitting to a hyperbolic curve in Sigmaplot®; for NfsB-cys see Figure 3.11, and for NfsB-his see Figure 3.12. The R^2 values obtained for these two hyperbolic curves are 0.93 and 0.92 respectively, this falls below the standard range of >0.97 but is attributed to the difficulty in measuring the true initial rate of reaction. The microtiter plate assay used to determine the data is difficult to execute in a short time frame and takes ~30-60s to prepare the plate from start to finish. The reaction occurs at a linear rate after addition of the CB1954 for at least 60s; based on the absorbance vs time plot for NfsB-cys shown in Figure 3.13.

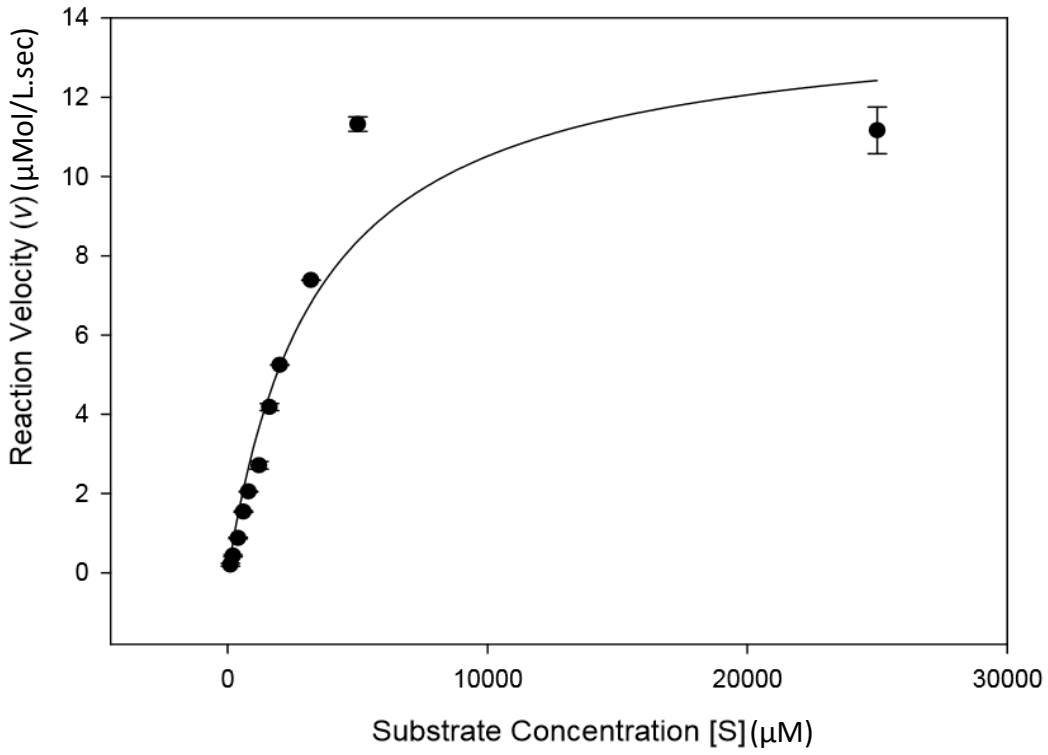

Figure 3.11 Michaelis-Menten hyperbolic curve obtained from Sigmaplot® showing the rate of the hydroxylamine reduced prodrug derivative formation. (λ_{max} = 420 nm, ε = 1200 L mol^{-1}cm^{-1}) for NfsB-cys (10µg/mL) at increasing CB1954 concentrations (µM). Error bars represent standard error of estimate.

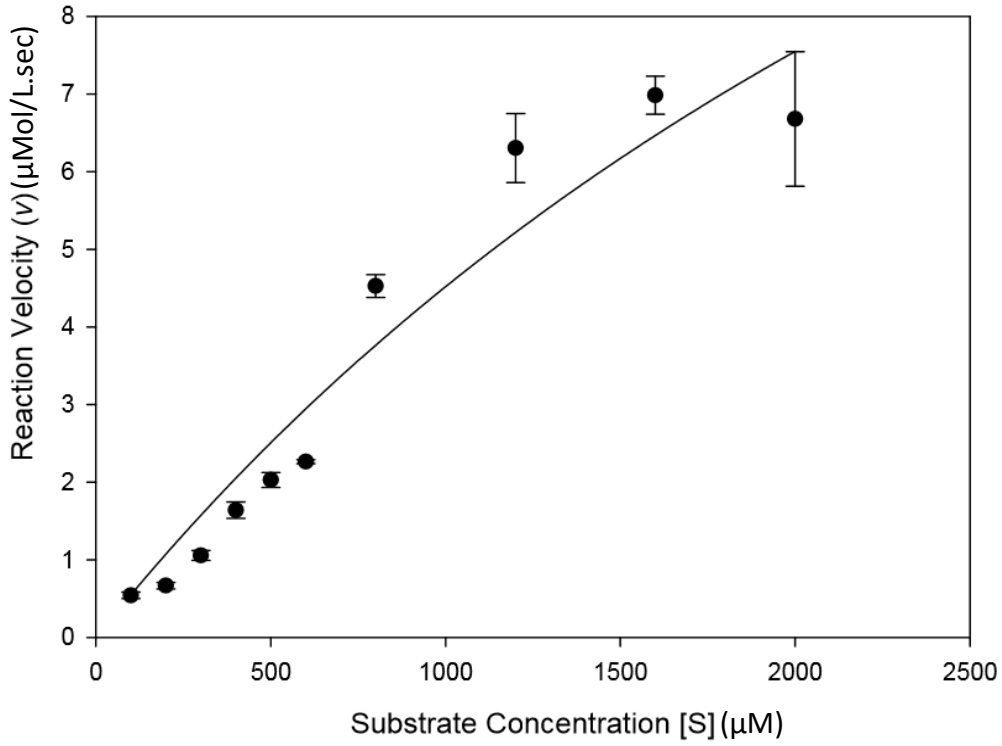

Figure 3.12 Michaelis-Menten hyperbolic curve obtained from Sigmaplot® showing the rate of the hydroxylamine reduced prodrug derivative formation. (λ_{max} = 420 nm, ε = 1200 L mol^{-1}cm^{-1}) for NfsB-his (10µg/mL) at increasing CB1954 concentrations (µM). Error bars represent standard error of estimate.

The data shown in Figure 3.13 shows that the reaction does remain linear in the 60s that the microtiter assay is conducted and as such the formation of the hydroxylamine reduced prodrug products are defined during the difference between 5-25 seconds. It is the initial set-up time that is most likely to affect the tightness of fit for the data to the hyperbolic curve, but without a more automated procedure the setup time cannot be realistically reduced. The kinetics are discussed in further detail and comparison between the enzymes is conducted in section 3.7.

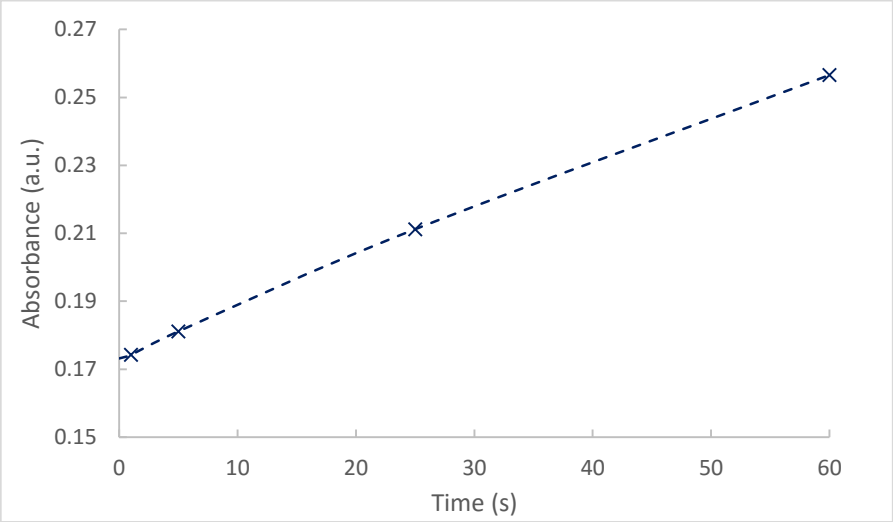

Figure 3.13 Plot of absorbance at 420 nm vs time for NfsB-cys (10 µg/mL), CB1954 (1 mM), NADH (4 mM) and PB (50 mM, pH 7.4).

3.5.2 Effect of pH on NfsB-his and NfsB-cys activity

To determine the optimum pH for NfsB-his and NfsB-cys the enzymes were assayed at 420 nm with the prodrug at various pH's as detailed in section 2.5.3. The results are seen below in Figure 3.14.

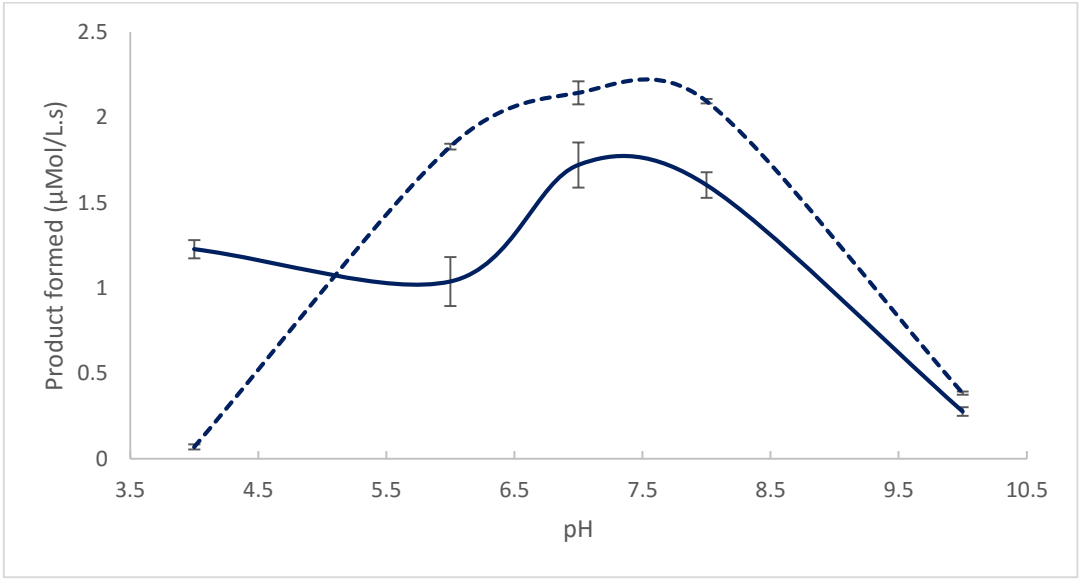

Figure 3.14. A graph detailing the effect of pH on the production of the hydroxylamine derivatives (λ_{max} = 420 nm, ε = 1200 L mol^{-1}cm^{-1}) of NfsB-his *(Blue) and* NfsB-cys *(Dashed blue) with 100 µM CB1954 and 600 µM NADH. The error bars represent ± 1 SD.*

Both of the his and cys tagged enzymes need to retain optimum activity at the human body's physiological pH of 7.38-7.42 also known as the body's acid-base homeostasis.[304] NfsB-his as seen above in

Figure 3.14 retains optimum activity within a range of pH 7-8 so will be optimally active at the body's physiological pH. NfsB-cys retains a wider range of optimum activity compared to NfsB-his with its optimum range increased at both higher and lower pH's to pH 6.5-8.5 allowing for a slightly wider optimal activity allowing for more variation in the body's physiological pH. Both enzymes rapidly decrease in activity above pH 8.5 and although NfsB-cys decreases rapidly below pH 6, NfsB-his declines in activity at a much slower rate below pH 4. The rates for the pH profiles suggest that all of the substrate would be used in a very short period of time, this can be attributed to the fact that for the pH profiles the exact concentration of NTR used was not calculated and was therefore potentially in excess for the concentration of prodrug used allowing the reaction to proceed a fast rate.

3.5.3 Effect of temperature on NfsB-his and NfsB-cys activity

To determine the optimum temperature parameters for NfsB-his and NfsB-cys the enzymes were assayed at 420 nm with the prodrug after incubation at a range of temperatures in PB as detailed in 2.5.3. The results can be seen in Figure 3.15 below.

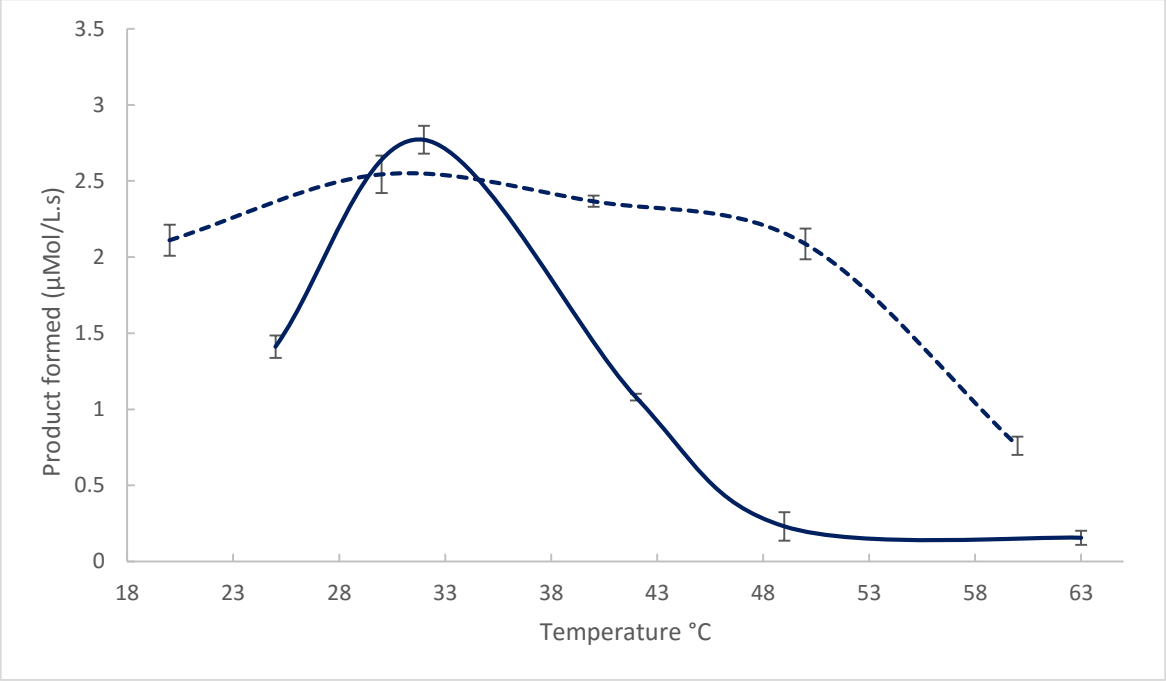

Figure 3.15. A graph detailing the effect of temperature on the production of the hydroxylamine derivatives (λ_{max} = 420 nm, ε = 1200 L mol^{-1}cm^{-1}) of NfsB-his *(Blue) and* NfsB-cys *(Dashed Blue) with 100 µM CB1954 and 600 µM NADH. The error bars represent ± 1 SD.*

As the temperature is increased up to 37^{o}C the reaction increases for NfsB-his until the enzyme activity begins to decrease above 40^{o}C, by the time it reaches 50°C there is no resulting enzyme activity, indicating that the enzyme structure is denaturing due to the increased temperature resulting in a loss of activity of the enzymes toward the prodrug. For NfsB-cys the enzyme exhibits a higher level of activity across a wider range of temperatures than NfsB-his, with significant activity being observed from 20^{o}C-50^{o}C before the activity finally starts to decrease as the enzyme starts to denature.

The enzymes need to retain optimum activity at the human body's physiological temperature of 37°C. NfsB-his has an optimal activity range between 25-40°C; with the highest activity achieved at approximately 34°C. Again as with the pH profiles these temperatures profiles were ran without a defined concentration of NTR, leading to the observation being made that almost all of the substrate would be exhausted within first few minutes of reaction.

3.5.4 HPLC analysis of reaction products: NfsB-cys

HPLC analysis of the products formed from the enzymatic reaction of NfsB-cys with the cofactor NADH and the prodrug CB1954 was conducted following the procedure outlined in section 2.6. The 2- and 4-hydroxylamine derivatives are the compounds of interest with emphasis on the importance of the 4-hydroxylamine compound, as this undergoes further reduction to form a highly cytotoxic DNA cross linker as pictured in Figure 1.10. The 4-hydroxylamine compound elutes from the HPLC column at approximately 5 minutes and the 2-hydroxylamine compound elutes at approximately 10 minutes.[300] Figure 3.16 shows both of these peaks determining that NfsB-cys produces both the 2- and 4- hydroxylamine derivatives when it reduces CB1954. From the spectra it can also be concluded that the enzyme has not fully reduced the prodrug due to the presence of peaks in the range where CB1954 is expected to elute.[300] There are also some additional peaks which can be attributed to compounds resulting in the reduction/degradation of the prodrug.[305] All of the peaks that have been defined have been determined from HPLC spectra generated by the testing of the compounds as standards; see appendices Appendix 7.6-7.9.

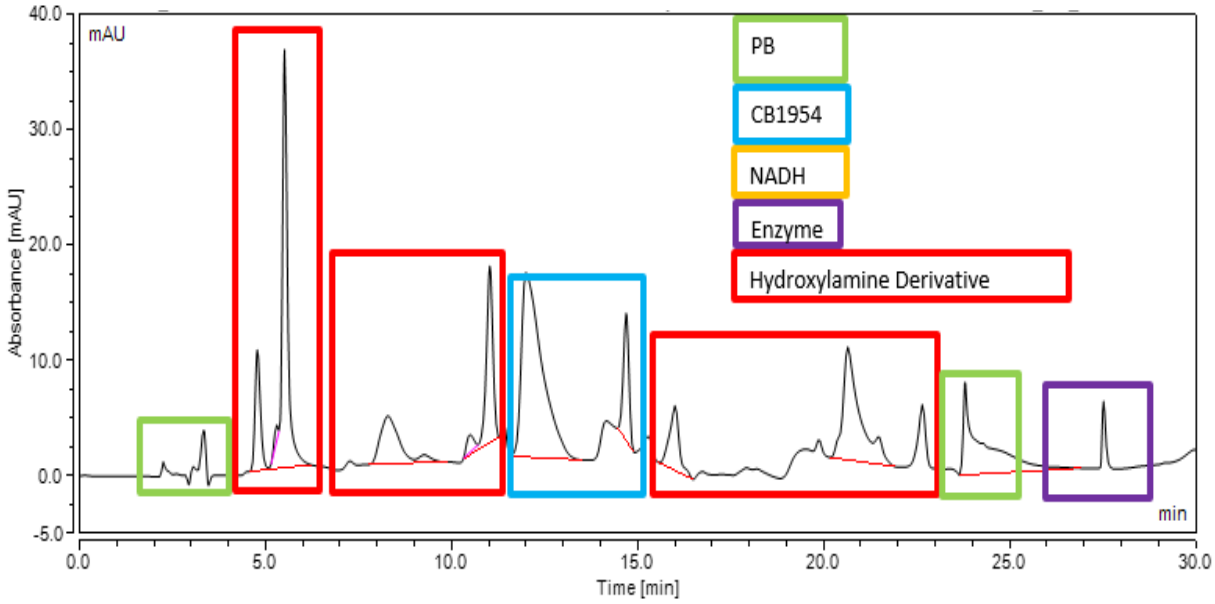

Figure 3.16. HPLC spectra identifying the components present after enzymatic reaction of CB1954, NADH and nfsB-cys, conducted at 420 nm wavelength

3.6 Characterisation of YfkO-his and YfkO-cys

The ability of both YfkO-his and YfkO-cys to reduce CB1954 utilising NADH as a cofactor were analysed by monitoring the production of the hydroxylamine derivatives produced during reaction. The optimal pH and temperature parameters were also determined for enzyme using UV-Visible spectroscopy. To distinguish the ratios of the 2- and the 4-hydroxylamine derivatives of CB1954 that are produced by the enzyme HPLC analysis of the enzymatic assay reaction was conducted and the compounds quantified.

3.6.1 K_m and V_{max} of YfkO-his and YfkO-cys

To calculate the K_m and V_{max} of the YfkO-his and YfkO-cys NTRs the kinetic enzymatic activity was measured at various increasing concentrations of CB1954. All kinetic experiments were conducted in triplicate and the average was plotted and analysed.

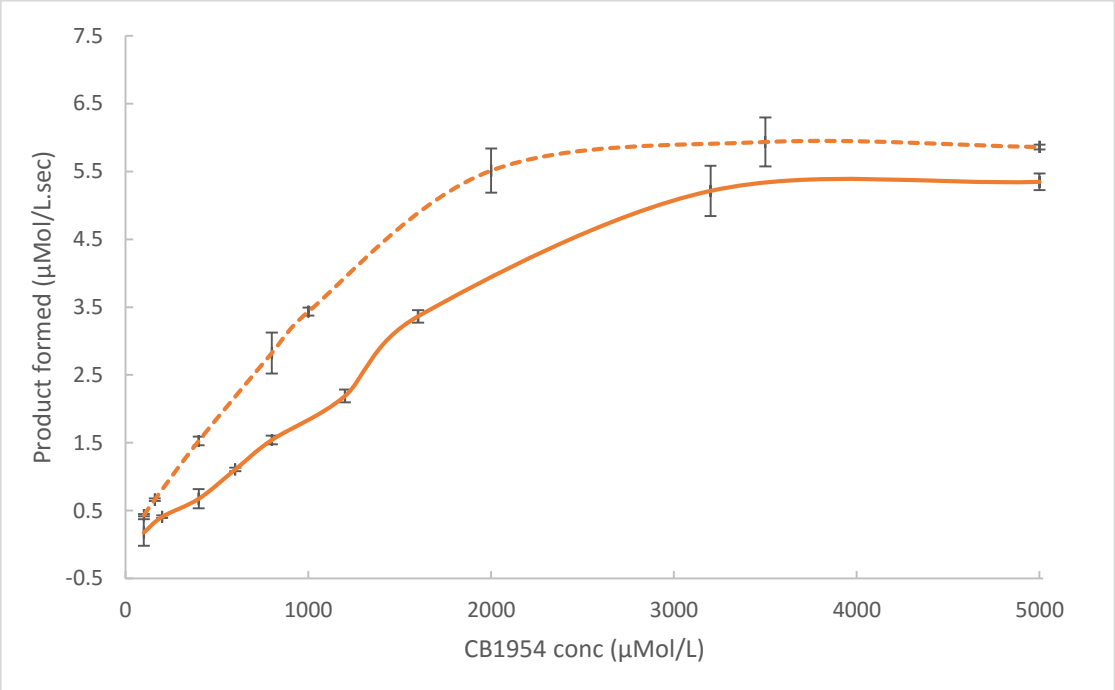

Figure 3.17. A graph quantifying the rate of the hydroxylamine reduced prodrug derivative formation. (λ_{max} = 420 nm, ε = 1200 L $mol^{-1}cm^{-1}$) for the YfkO-his *(Orange) and* YfkO-cys *(Dashed Orange) NTRs at increasing CB1954 concentrations. The error bars represent ± 1 SD.*

The rate of the reaction increases in correlation with the increase in CB1954 concentration until Figure 3.17 shows the reaction reaches its V_{max}. Both YfkO-his and YfkO-cys follow very similar trends with them both plateauing at similar prodrug concentrations. It can be observed that the his tagged YfkO has a slightly higher V_{max} than that of its cys tagged counterpart. The main difference that can be observed between the two enzymes is that the his tagged YfkO has a steeper rise in product formation.

The data obtained for kinetic analysis is subjected to non-linear regression fitting to a hyperbolic curve in Sigmaplot®; for YfkO-cys see Figure 3.18, and for YfkO-his see Figure 3.19. The R^2 values obtained for these two hyperbolic curves are 0.93 and 0.97 respectively. The value for YfkO-cys again as with the kinetic determination for NfsB, falls below the standard range of >0.97, however, the value for YfkO-his borders the low side of the standard range. The explanation can once again be attributed to the difficulty in measuring the true initial rate of reaction. The microtiter plate assay used to determine the data is difficult to execute in a short time frame and takes approximately 30-60s to prepare the plate from start to finish. The reaction occurs at a linear rate after addition of the CB1954 for approximately 60-120s; based on the absorbance vs time plot for YfkO-cys shown in Figure 3.7. The data shown in Figure 3.20 shows that the reaction does remain linear in the first 30s that were observed of the microtiter assay, This led to the define the difference period observed to allow for kinetic determination as 5-25 seconds. This still means however that the time taken to set up the microtiter assay is still the bottleneck for the largest error in measurement to occur and therefore the most likely to affect the tightness of fit for the data to the hyperbolic curve. This could be potentially solved using a more automated system for setup to reduce the time taken between starting the experiment and running the assay. The kinetics are discussed in further detail and comparison between the enzymes is conducted in section 3.7.

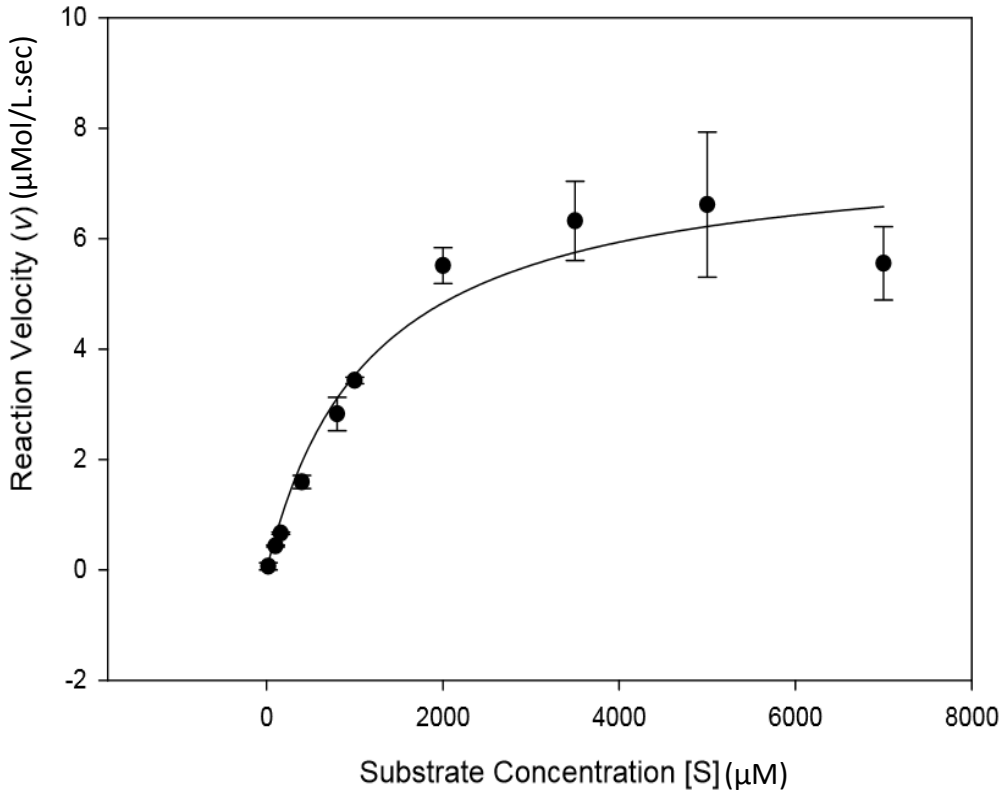

Figure 3.18 Michaelis-Menten hyperbolic curve obtained from Sigmaplot® showing the rate of the hydroxylamine reduced prodrug derivative formation. (λ_{max} = 420 nm, ε = 1200 L mol^{-1}cm^{-1}) for YfkO-cys at increasing CB1954 concentrations. Error bars represent standard error of estimate.

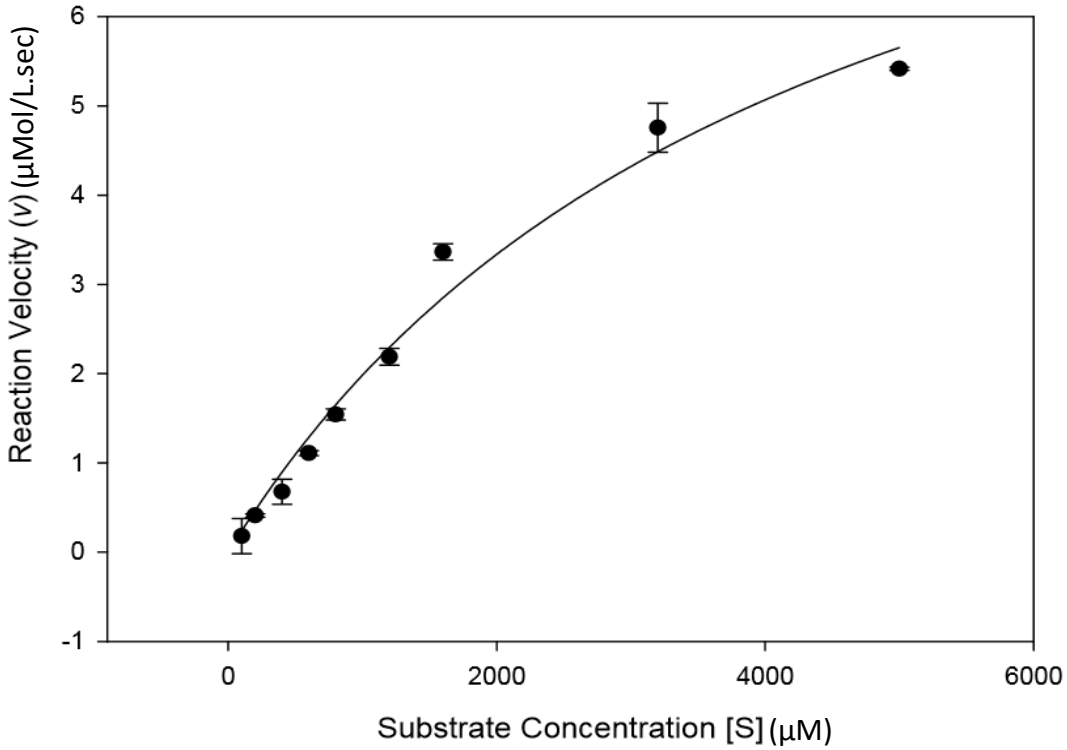

Figure 3.19 Michaelis-Menten hyperbolic curve obtained from Sigmaplot® showing the rate of the hydroxylamine reduced prodrug derivative formation. (λ_{max} = 420 nm, ε = 1200 L mol^{-1}cm^{-1}) for YfkO-his at increasing CB1954 concentrations. Error bars represent standard error of estimate.

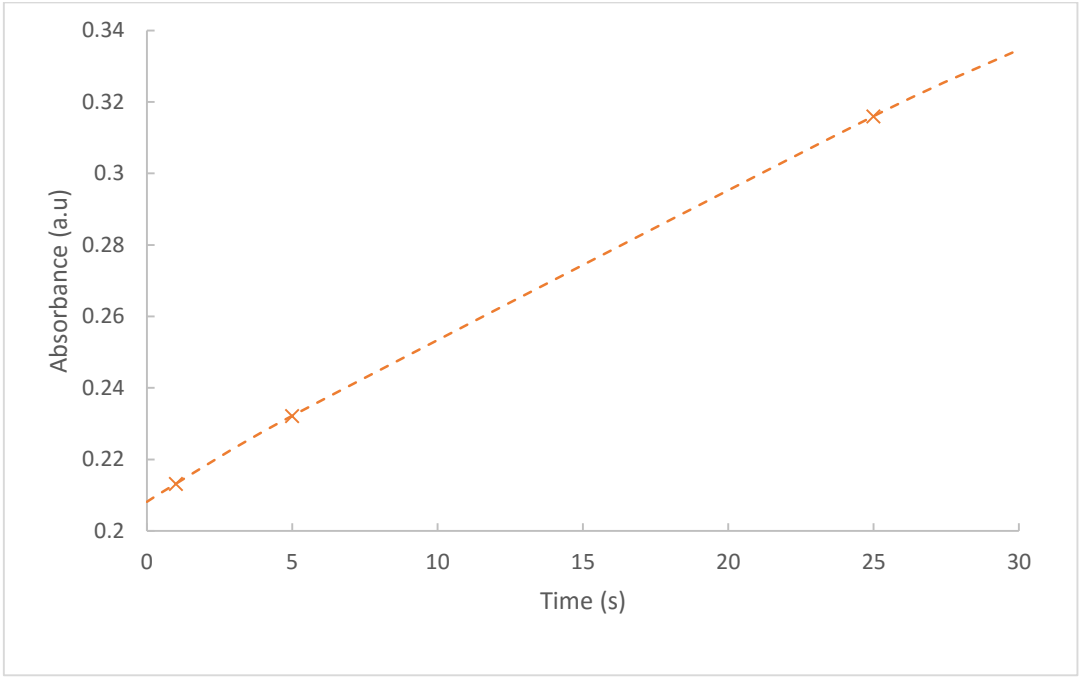

Figure 3.20 Plot of absorbance at 420 nm vs time for YfkO-cys (10 µg/mL), CB1954 (1 mM), NADH (4 mM) and PB (50 mM, pH 7.4).

3.6.2 Effect of pH on YfkO-his and YfkO-cys activity

To determine the optimum pH for YfkO-his and YfkO-cys; the enzymes were assayed at 420 nm with the prodrug at various pH's as detailed in section 2.5.3.

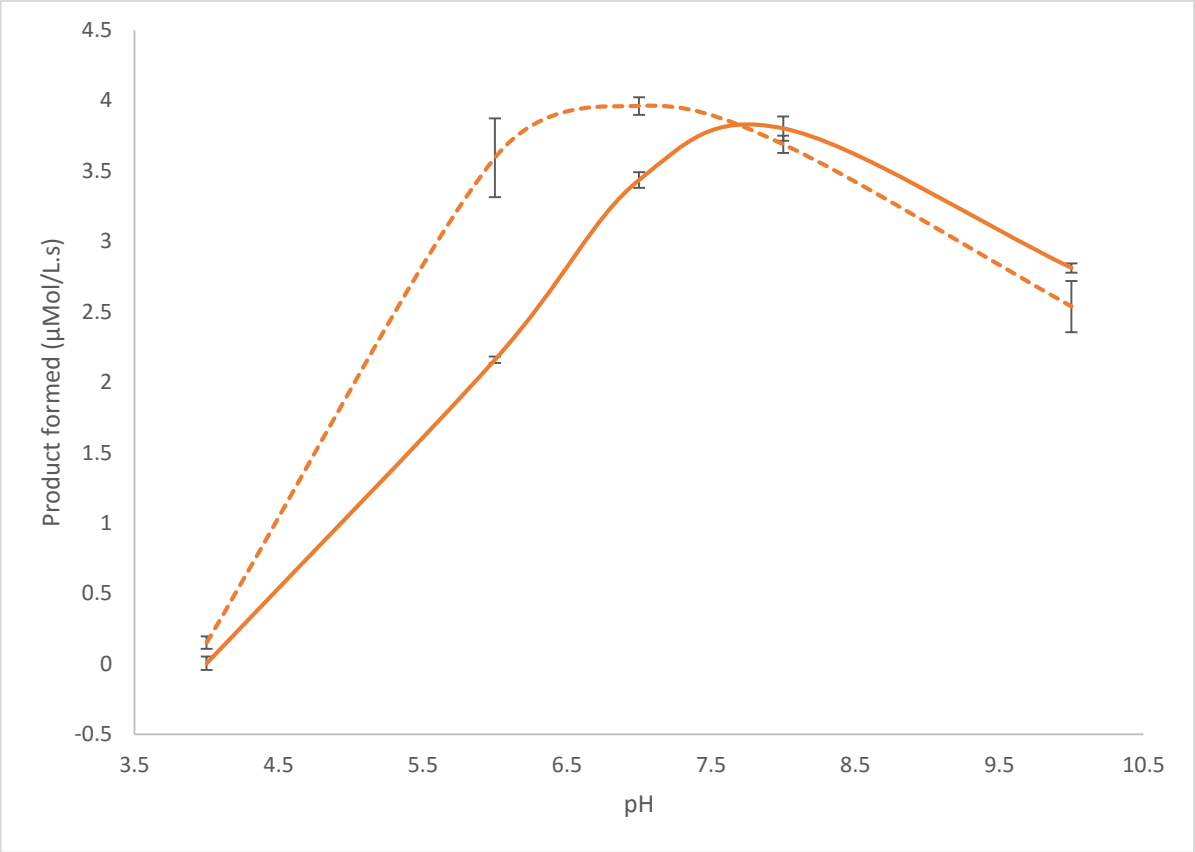

Figure 3.21. A graph detailing the effect of pH on the production of the hydroxylamine derivatives (λ_{max} = 420 nm, ε = 1200 L mol^{-1}cm^{-1}) of YfkO-his *(Orange) and* YfkO-cys *(Dashed orange) with 100 µM CB1954 and 600 µM NADH. The error bars represent ± 1 SD.*

Figure 3.21 shows that The YfkO-cys exhibits significant activity between pH 6.5 and 8. The physiological pH of 7.4 that is observed in the human body lies within this range indicating that YfkO-cys will be suitable for use in the body. YfkO-his follows a very similar trend to YfkO-cys with it exhibiting optimal activity between pH 6-8. Both enzymes shows a slow decline in activity above pH 8 still retaining sufficient activity at pH's approaching 10. However, both enzymes also show a rapid decrease in activity at pH's < 6 with no discernible activity observed at pH 4. The rates for the pH profiles for both YfkO-cys and YfkO-his suggest that all of the substrate would be exhausted in a very short space of time. This can be attributed to the NTR potentially being present in excess in these profiles and for the concentration was not defined for the pH and temperature profile experiments.

3.6.3 Effect of temperature on YfkO-his and YfkO-cys activity

To effect of temperature on the enzymes needs to be determined, in order to determine the optimum temperature parameters for YfkO-his and YfkO-cys the enzymes were assayed at 420 nm with the prodrug after incubation at a range of temperatures in PB as detailed in section 2.5.3. The results can be seen in Figure 3.22 below.

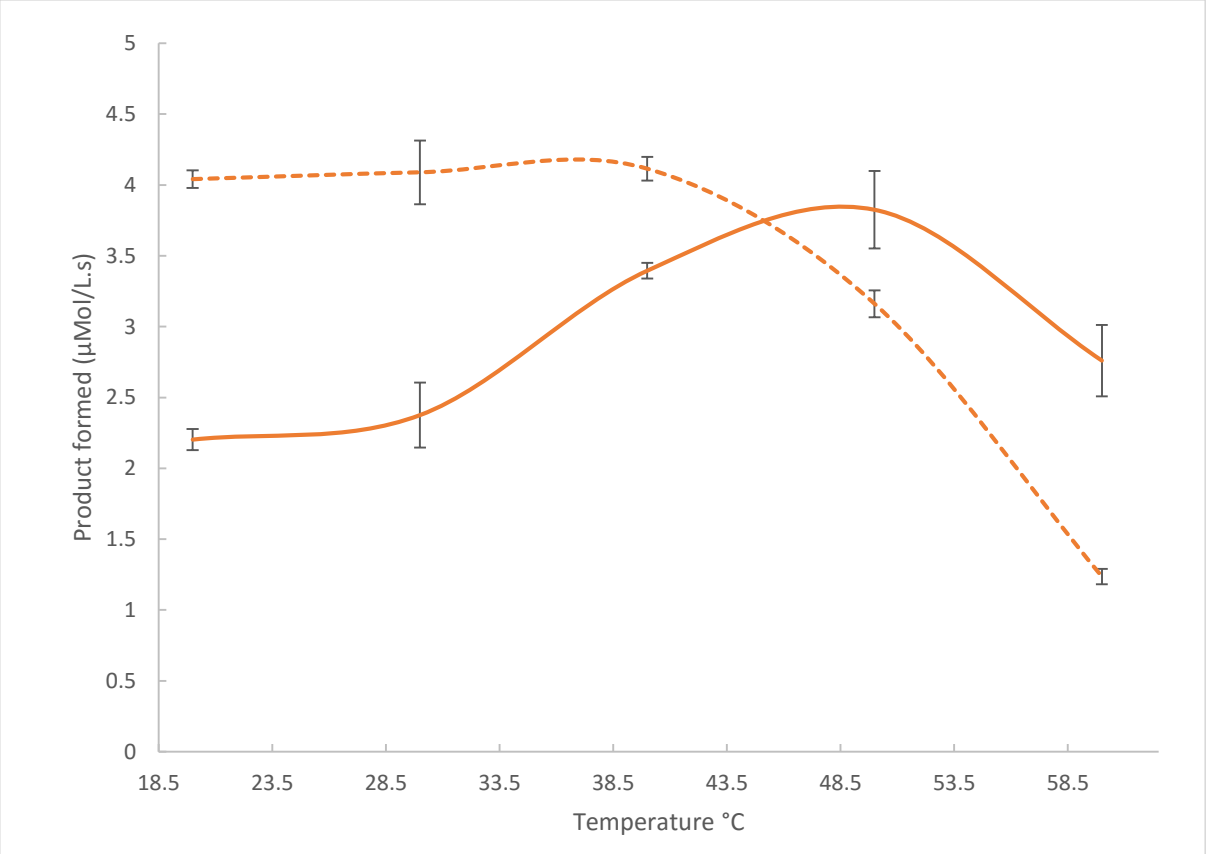

Figure 3.22. A graph detailing the effect of temperature on the production of the hydroxylamine derivatives (λ_{max} = 420 nm, ε = 1 200 L mol^{-1}cm^{-1}) of YfkO-his *(Orange) and* YfkO-cys *(Dashed orange) with 100 µM CB1954 and 600 µM NADH. The error bars ± 1 SD.*

In Figure 3.22 it is observed that as the temperature is increased up to 37ºC the reaction remains stable until the enzyme activity begins to decrease above 45 ºC indicating that the enzyme structure is denaturing due to the increased temperature resulting in a loss of activity of the enzymes toward CB1954.

The enzymes need to retain optimum activity at the human body's physiological temperature of 37°C, the enzyme retains optimal activity up until 45 °C. Again as with the pH profiles in the previous section the concentration of both YfkO-cys and –his wasn't defined.

3.6.4 HPLC analysis of reaction products: YfkO-cys

To determine the formation of the required cytotoxic DNA linker products HPLC analysis of the products formed from the enzymatic reaction of YfkO-cys with the cofactor NADH and the prodrug CB1954 was conducted following the procedure outlined in section 2.6. The 2- and 4-hydroxylamine derivatives are the compounds of interest. Identifying the 4-hydroxylamine compound is of significant importance as this undergoes further reduction to form a highly cytotoxic DNA cross linker. The 4-hydroxylamine compound elutes from the HPLC column at approximately 5 minutes and the 2- hydroxylamine compound elutes at approximately 10 minutes.[300]

Figure 3.23, seen below, shows an absence of the 2-hydroxylamine peak which corresponds with Emptage et al.'s[306] study which concludes that YfkO-cys from bacillus lichenformis is an exclusive 4-NO_2 reducer.[306] From the spectra it can also be concluded that the enzyme has not fully reduced the prodrug due to the presence of peaks in the range where CB1954 is expected to elute.[300] There is also a residual peak signal at ~16-18 minutes which can be attributed to further reduction products from the prodrug. For a full set of standard HPLC spectra ran on the individual compounds as standards in PB see appendices Appendix 7.6-7.9

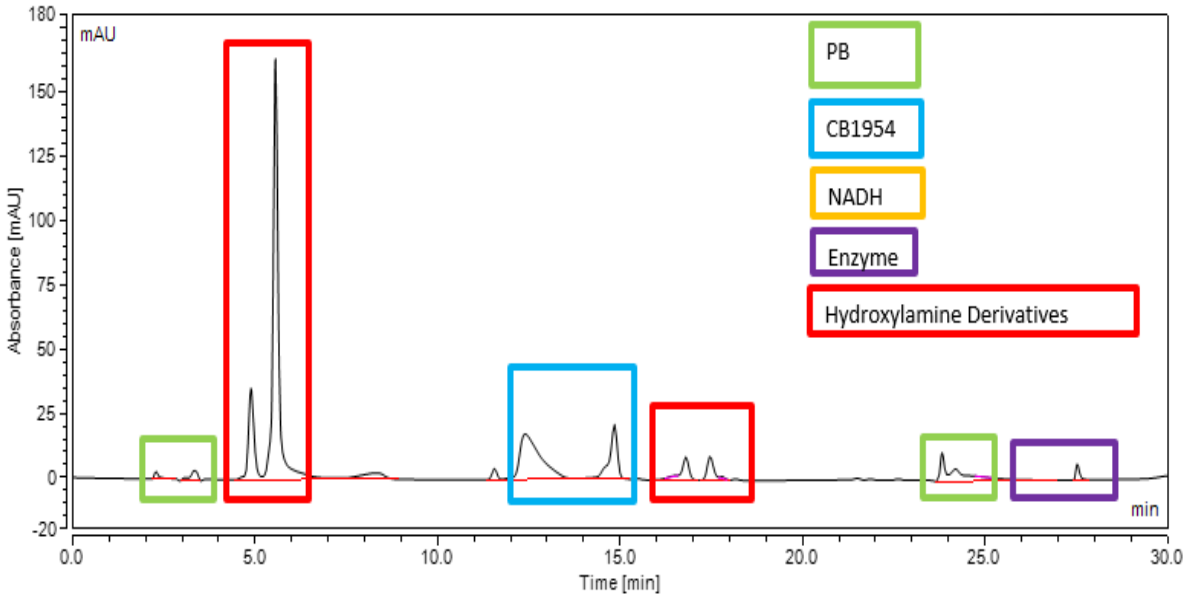

Figure 3.23. HPLC spectra identifying the components present after enzymatic reaction of CB1954, NADH and YfkO-cys, conducted at 420 nm wavelength.

3.7 Discussion of nitroreductase kinetic properties

Each of the his and cys tagged NfsB and YfkO NTRs were able to reduce the prodrug CB1954 to the 2- and 4-hydroxylamine derivatives. Kinetic enzymatic assays were conducted as per section 2.5.4 and the results shown in sections 3.5.1 and 3.6.1 respectively. An overview of the data obtained from both the kinetic enzyme activity scans and the pH and temperature profiling for all of the enzymes in this study can be seen summarised in Table 3.3 below.

Table 3.3. Kinetic parameters and optimum conditions of the four NTRs NfsB-his, NfsB-cys, YfkO-his and YfkO-cys *with CB1954.*

NTR	V_{max} ($\mu molL^{-1}s^{-1}$)	Std Error	K_m ($\mu molL^{-1}$)	Std Error	k_{cat} (s^{-1})	k_{cat}/K_m ($M^{-1}s^{-1}$)	pH	Temp. (°C)
YfkO-his	9.96	0.9377	3767.87	619.71	59.24	15,723	7.50	45.0
YfkO-cys	7.69	0.4666	1179.19	218.25	46.72	39,624	7.50	37.5
NfsB-his	22.90	7.0149	4064.43	1660.87	125.77	30,943	7.25	34.0
NfsB-cys	15.75	1.0062	3882.29	566.08	88.52	22,800	7.50	30.0-50.0

It is apparent in all the assays that genetic modification of the NTRs to include a sequence of 6 consecutive cysteine residues to each monomer reduces enzyme activity towards CB1954. For YfkO-his and YfkO-cys the difference is significant, with YfkO-cys showing significantly lower activity towards the prodrug and shows lower activity when exposed to the same differing environmental conditions. Figure 3.24, show overlays of the assays used to determine the K_m and V_{max} values for each of the NTRs, highlighting the different kinetic profiles of the different NTRs.

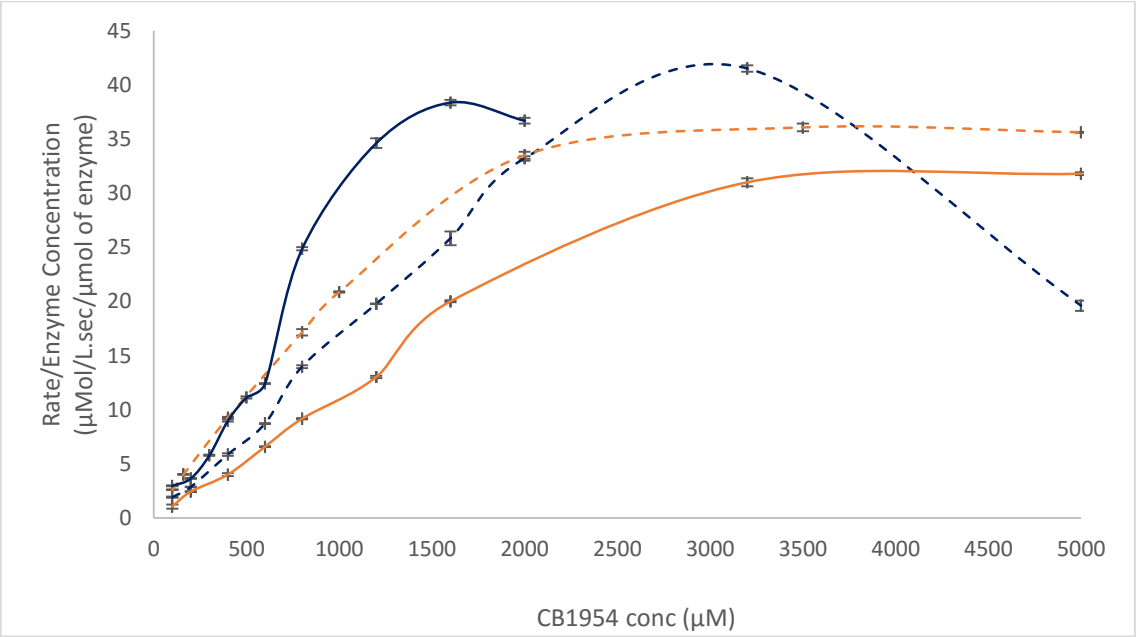

Figure 3.24. A graph showing the rate of hydroxylamine derivative generation (λ_{max} = 420 nm, ε = 1200 L $mol^{-1}cm^{-1}$) with increasing prodrug concentration up to 5 mM CB1954 for the four studied NTRs; NfsB-*cys (dashed blue),* NfsB-*his (solid blue),* YfkO-*cys (dashed orange) and* YfkO-*his (solid orange). Error bars represent ± 1 SD.*

The reaction rates for all of the his and cys NTRs varies significantly. YfkO-cys displays the fastest reaction rate, this can be seen in Figure 3.24 as it has the largest k_{cat}/K_m. NfsB-cys has nearly double the turnover rate than that of YfkO-cys as indicated by the k_{cat} values.

k_{cat}/K_m referred to as catalytic efficiency is the best indicator of activity of the NTRs to the prodrug as it is independent of cofactor concentration.[307] K_m and k_{cat} can be difficult to reliably obtain due to the limited solubility of CB1954 which makes it hard to test the activity beyond initial rates. The predicted concentrations needed for the prodrug therapy treatment for its use in clinical applications are very low.[127,128] This reinforces that comparison of the specificity constant is the most reliable measure of the kinetic activity for comparison of the different NTRs.[308]

3.8 Concluding remarks

To decide if the NTRs are suitable for use in Au-MNP DEPT the enzymatic activities were determined. All of the NTRs show activity towards the reduction of CB1954. The his-tagged NTRs show increased levels of activity but without the cysteine tag genetic modification they are unsuitable for us in an immobilised MNDEPT system. The cysteine tagged modified NTRs still show significant activity concluding they can be put forward for testing when immobilised to Au-MNPs. The specificity constant of YfkO-cys coupled with the HPLC DNA linker analysis indicates that this enzyme would be preferential for use in the MNDEPT system, due to its exclusive production of the 4-hydroxylamine product. All of the NTRs studied also exhibit activity in environments mirroring the physiological conditions of the human body. This also indicates that not only are they suitable for use in MNDEPT but also other NTR based therapies such as GDEPT. Screening of a multitude of NTRs activity to reducing prodrugs to their hydroxylamine derivatives informs us of their suitability for further testing. The initial setup duration taken for the microtiter assays is a significant bottleneck in the determination of the kinetic properties of the NTRs. The setup of the assay hinders the ability to truly define the initial reaction from its point of origin. A more automated system could allow for a reduction in the assay setup and could potentially be something that could be explored in the future; dependant on equipment and funding.

Chapter 4

Particle Synthesis

The majority of the work discussed in this chapter is published in the following paper.

YfkO nitroreductase immobilised with controlled orientation onto superparamagnetic nanoparticles; towards a direct enzyme cancer therapy approach. *Publication suited to Biomacromolecules,* **(in DRAFT)**

Chapter 4 – Particle synthesis

4.1 Superparamagnetic nanoparticles

4.1.1 Introduction to superparamagnetic iron oxide nanoparticles

Using the co-precipitation of Fe ions in aqueous solution, SPIONs can be produced in various sizes and morphologies. The size and morphology of the resulting nanoparticles depends upon not only the reaction conditions; such as temperature, but also the reagents used. SPIONs have a wide range of possible uses with the most common and important being their potential use in biomedicine; the area in which they would be used as part of an MNDEPT system.[187,192,209,225] Magnetite (Fe_3O_4) is the form of iron oxide nanoparticle formed when the reaction is conducted in a non-oxidising and basic environment, see Equation 4.1. If the magnetite nanoparticles are transferred to an acidic environment or are produced/stored in an oxidising environment then maghemite (γ-Fe_2O_3) can be synthesised, see Equation 4.2.

$$2Fe^{3+} + Fe^{2+} + 8HO^- \rightarrow Fe_3O_4 + 4H_2O$$

Equation 4.1 Formation of magnetite from aqueous iron ions in a non-oxidising environment.

$$Fe_3O_4 + 2HCl \rightarrow \gamma Fe_2O_3 + FeCl_2 + H_2O$$

Equation 4.2 Formation of maghemite (γ-Fe_2O_3) from magnetite (Fe_3O_4).

Iron oxide nanoparticles that are less than 10 nm in size are generally classified SPIONs due to the rapid oxidation of magnetite to maghemite.[215] Massart provides the simplest route to synthesising SPIONs using a co-precipitation reaction.[216] This method utilises iron chlorides; Fe^{3+} and Fe^{2+} in a 2:1 molar ratio that have been dissolved in a mildly acidic solution. Typically sodium hydroxide or ammonium hydroxide is used as the base.[216] The iron chloride solution is added drop wise to the basic solution and a black precipitate is formed which is magnetically separated from the solution using a 1T magnet. The resulting particles are then washed with dH_2O and stabilised in a solution of TMAOH. The particles exhibit a stability between pH 5 to pH 9.[216]

SPIONs produced using the Massart method are shown in Figure 4.1, and the method is described in more detail in section 2.2.

Figure 4.1 SPION produced from the Massart method[6] (Left) SPIONS after initial co-precipitation, (Right) SPIONs after magnetic and centrifugal separation and final stabilisation in TMAOH.

4.1.2 Characterisation of synthesised superparamagnetic iron oxide nanoparticles

Transmission electron microscopy was used to evaluate the SPIONs produced using Massart's co-precipitation method and the resulting image is shown below in Figure 4.2 alongside some energy-dispersive X-ray analysis (EDAX) taken from the same sample as seen in Figure 4.3. From Figure 4.2 the majority of the particles are ~10 nm in size, there is some evidence of aggregation of the particles in the top left hand corner.

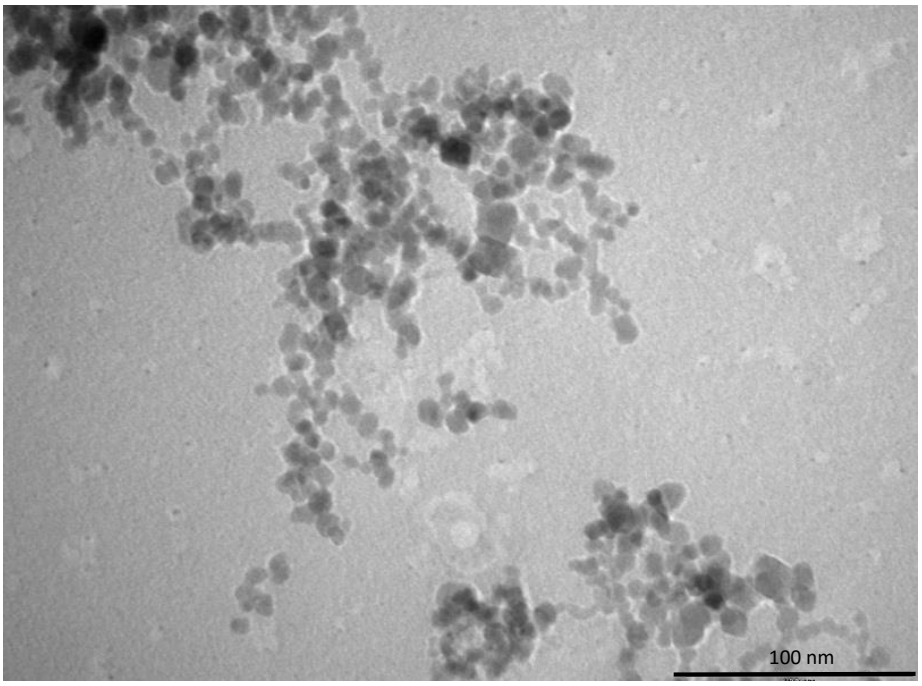

Figure 4.2 Image from TEM analysis of the synthesised SPION. The scale bar is 100 nm.

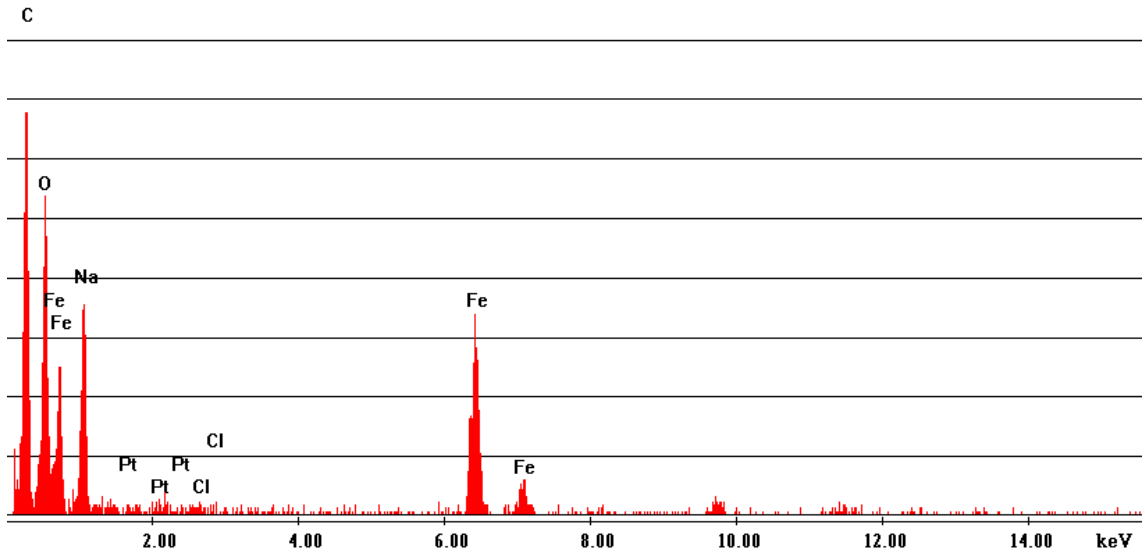

Figure 4.3 EDAX spectra obtained during TEM analysis of synthesised SPIONs.

EDAX taken during TEM seen in Figure 4.3, contains predominately iron. This is to be expected as the sample under test was synthesised SPIONs. There are traces of carbon and sodium due to surface bound citrate. The platinum is a response exhibited from the TEM grid.

Powder X-ray diffraction (XRD) (Philips X-Pert PANalytical diffractometer, USA, at 45 kV and 35mA between 20 and 60° 2θ using Ni-filtered Cu-$K_{\alpha 1}$ radiation (λ = 1.5405 Å)) was conducted to further assess the crystal structure of the particles and compare the synthesised SPION to magnetite/maghemite standards and the literature.[309] Figure 4.4 shows the XRD pattern with respective diffraction planes assigned. The accompanying data seen in table 4.1 gives full details into the detailed XRD spectra, along with peak assignments and the standard 2θ positions, relative peak intensities and corresponding diffraction planes.

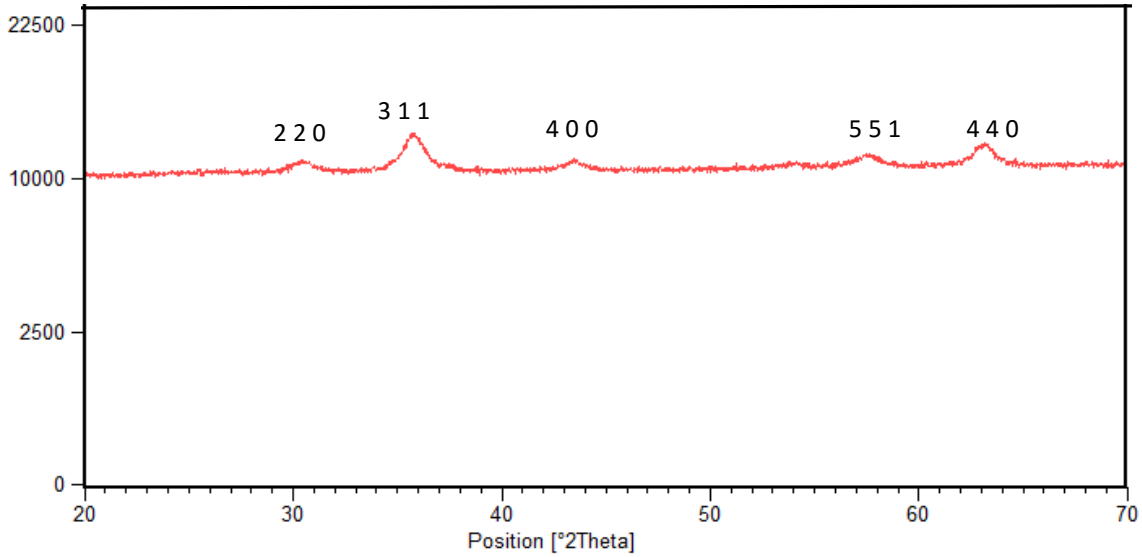

Figure 4.4 XRD pattern of synthesised SPION. Full details shown in Table 4.1.

Table 4.1 Table detailing the full XRD pattern of synthesised SPIONs.

Position [°2θ]	Height [cts]	FWHM [°2θ]	d-spacing [Å]	Rel. Int. [%]	hkl
30.4229	786.66	1.0706	2.93822	28.81	2 2 0
35.7588	2730.45	0.7360	2.51107	100.00	3 1 1
43.4474	731.06	1.6059	2.08288	26.77	4 0 0
57.5303	1164.38	1.6059	1.60205	42.64	5 1 1
63.1297	1985.21	0.8160	1.47154	72.71	4 4 0

The XRD pattern for the synthesised SPIONs following Massart's co-precipitation match the reference patterns; for magnetite/maghemite as expected. PANalytical X'Pert HighScore (Phillips, USA) was used to analyse the diffractograms. It was also used to identify the peaks and measure the peak widths. The calculation of peak widths were used to calculate the crystallite size.

$$D = \frac{K\lambda}{\beta \cos \theta}$$

Equation 4.3 The Scherrer equation.[310]

The crystallite size of the sample (*D)* is calculated using the Scherrer equation, Equation 4.3. The shape factor (K) is typically in the range $0.89 < K > 1$ for spherical crystals.[311] λ is the incident x-ray wavelength; β refers to the θ value of the peak at the full width half maximum (FWHM) in radians. θ is the Bragg angle of the peak, which is a measure of the scattering caused by the material. The Scherrer equation is limited by calculating crystallite size and not particle size. Crystallite size is typically smaller than particle size by ~10%.[312]

Both TEM and XRD have been used to confirm the synthesised SPIONs are approximately 10 nm in size; with D_{XRD} of 11.3 nm and TEM of 7.15 nm ± 1.2 nm respectively and exhibit a reasonably spherical morphology.

The SPIONs display a superparamagnetic response in the presence and absence of a magnetic field, as shown in Figure 4.5. Superconducting quantum interference device (SQUID) analysis is currently being conducted on the samples and should confirm in more detail the magnetic characteristics of the SPIONs.

Figure 4.5 SPIONs in the absence of a magnetic field (left); in the presence of a 1T magnet (middle) and in the absence of a magnetic field after magnetic exposure (right).

The synthesised SPION sample was subjected to UV/Visible spectroscopy and shows the corresponding peak at ~260 nm as expected for iron oxide nanoparticles in the spectrum seen below in Figure 4.6.[313]

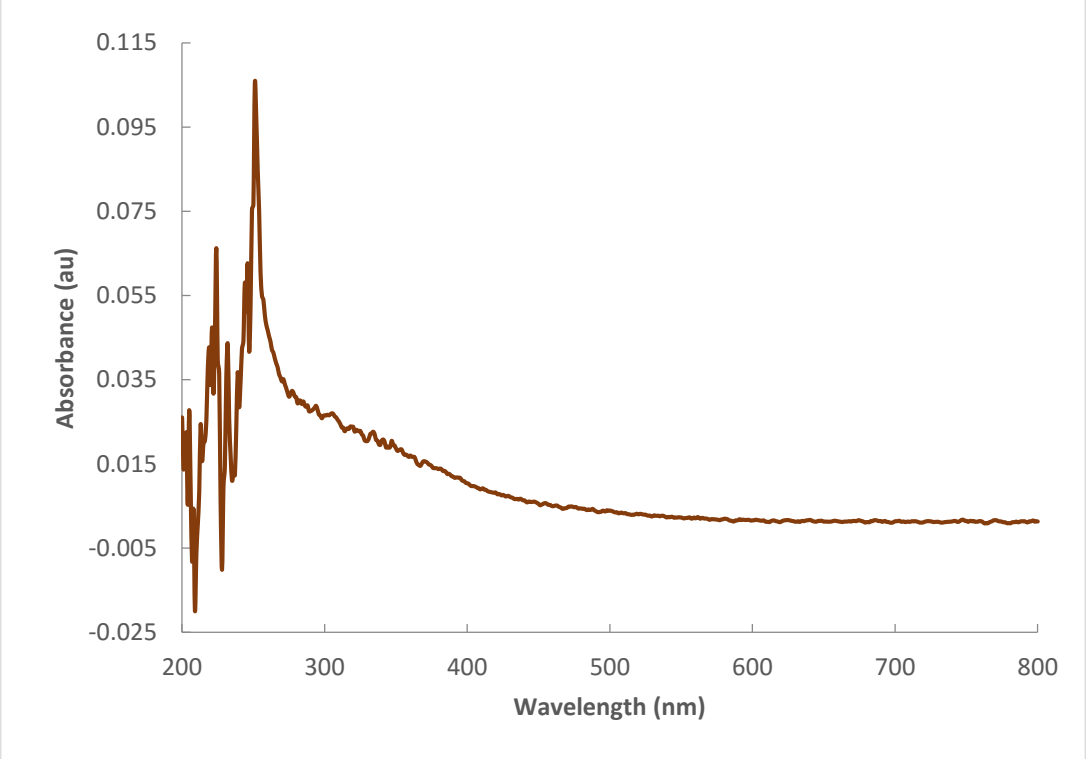

Figure 4.6 UV/Visible spectrum of synthesised SPIONs.

4.2 Hydroxylamine coating of superparamagnetic iron oxide particles with chloroauric acid

Chloroauric acid ($HAuCl_4$) and hydroxylamine (NH_2OH) were added to synthesised SPION suspensions in a citrate solution, this methodology was based on a reproduction of the synthetic route described by Lyon *et al.*[239] The procedure is reported to utilise the direct reduction of Au^{3+} onto the synthesised SPION surface to create Au-MNPs. These are created by iteratively adding $HAuCl_4$ and NH_2OH to the citrate stabilised SPIONs, see Figure 4.7.[239] After 5 iterations Lyon *et al.* report particles of ~60 nm in size with almost spherical morphology.[239]

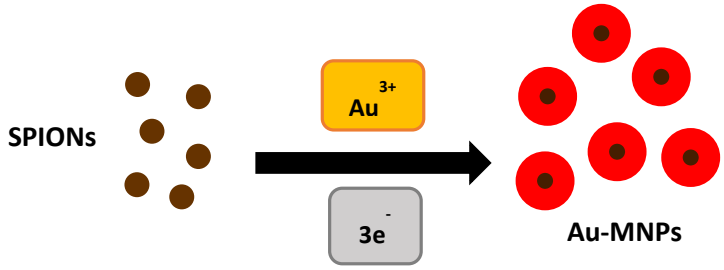

Figure 4.7 A diagram detailing the hydroxylamine coating of SPIONs to form of Au-MNPs.

Lyon *et al.*[239] comment in their report that for direct surface reduction of Au^{3+} to occur the SPIONs must be oxidised from magnetite to maghemite, without doing so results in aggregation of the reaction occurring during the initial additions of $HAuCl_4$ and NH_2OH. To oxidise the particles they are heated to ~100°C in a solution of 10 mM HNO_3 for a duration of 30 minutes, the resulting maghemite particles are then washed and stabilised in 5 mM TMAOH. This method can be seen in more detail in section 2.3.

The reduction of chloroauric acid using hydroxylamine as described by Lyon *et al.*[239] was repeated with stabilising the particles in 5 mM TMAOH. The results were a dark purple/grey sol which indicates the particles have started to aggregate. The resulting sol was characterised *via* UV/Visible spectroscopy, seen in Figure 4.8. The UV/Visible spectra shows a red shift and a broadening of the peak which is observed when the particle sizes increase, for instance in aggregation.[176]

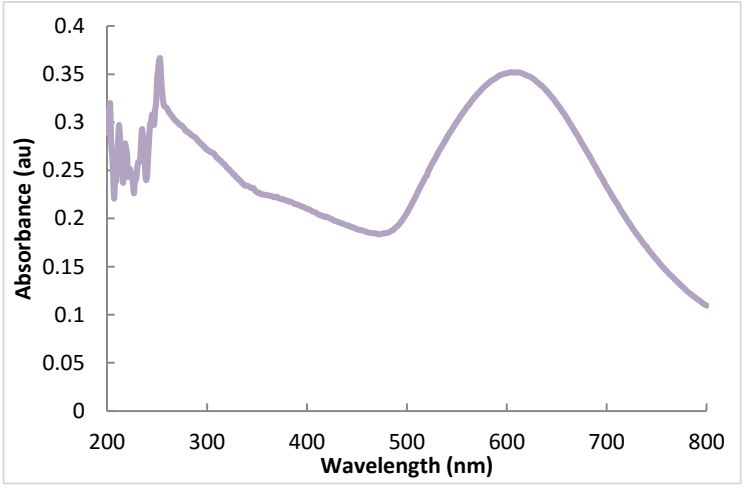

Figure 4.8 UV/Visible spectra of Au-MNPs synthesised via the Lyon et al.[239] method.

4.3 Pre-seeding superparamagnetic iron oxide nanoparticles with 5 nm Au nanoparticles

Brown *et al.*[294] formulated a procedure of creating highly monodisperse gold colloids by reduction of Au^{3+} onto pre-existing Au particles.[294] In order to avoid Au^{3+} nucleating during the reaction and growing to become exclusively gold particles without magnetic cores, small Au seeds can be first attached to SPION before further Au^{3+} reduction. Separating the nucleation and growth stages of particle generation, Brown *et al.* were able to improve control of particle size and shape for Au colloids of larger particle size.[294] In the first step pre-synthesised gold nanoparticles were attached to the SPIONs. Au^{3+} was then reduced onto the seeded SPIONs to produce Au-MNPs, the pre-seeded SPIONs providing a nucleation point for the further reduction of Au^{3+}.[294] It is hoped that this will create a full coated Au shell over the SPION cores, see Figure 4.9. This method was repeated which slight modification and can be found described in more detail in section 2.3.

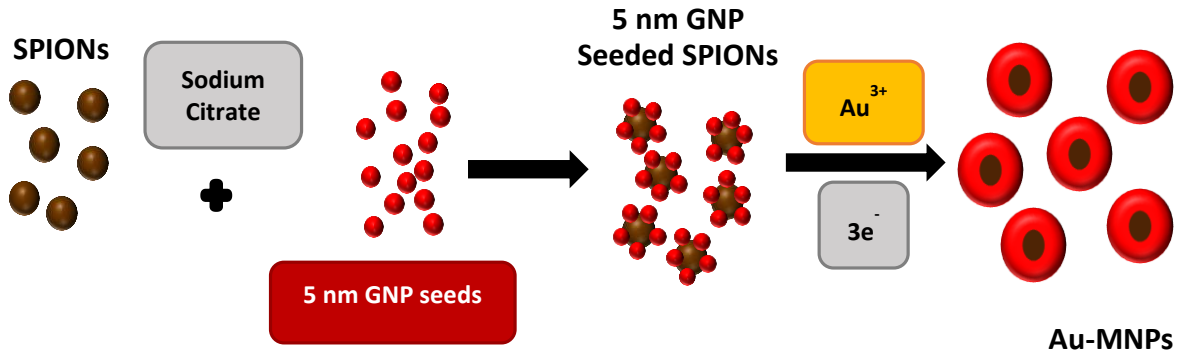

Figure 4.9 A diagram detailing the adapted pre-seeding & hydroxylamine coating of SPIONs to form Au-MNPs.

Figure 4.10 shows the change in absorbance profile for the SPIONs after seeding with 5 nm GNPs, with a broad peak spanning 525 nm to ~600 nm which is absent in the absorbance profile for the SPIONs. This corresponds to the SPR of the GNP seeds that are bound to the SPION surface. The sensitive nature of SPR causes a shift in λ_{max}; this is due to the change in the electron environment at the GNP surface which occurs due to the covalent bonding of the GNP seeds to the SPIONs.

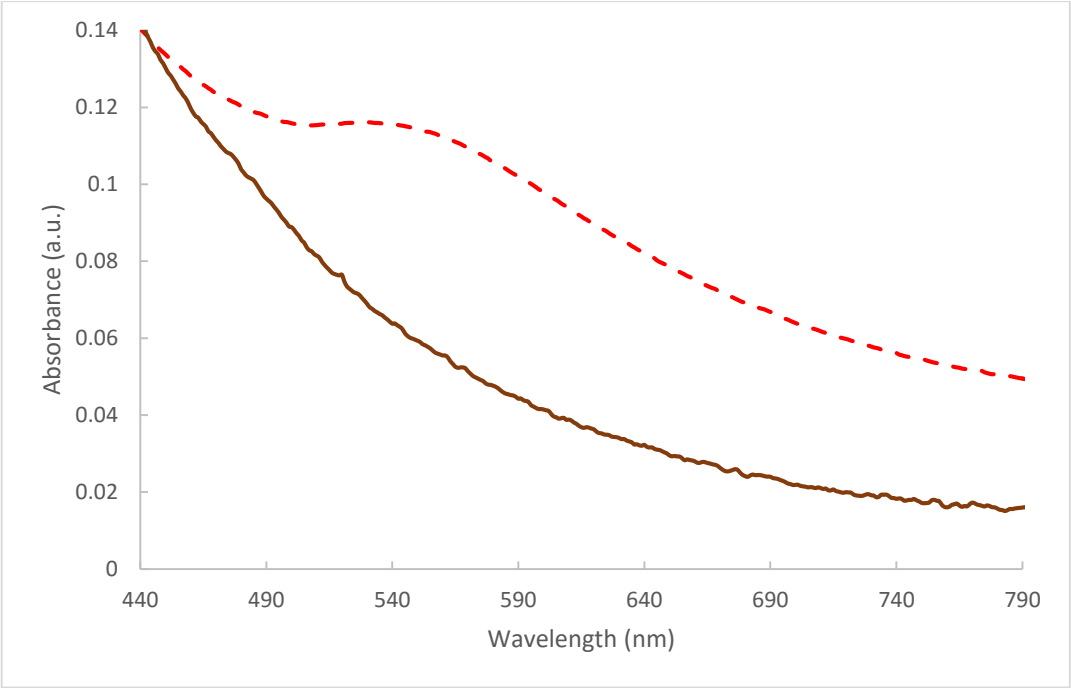

Figure 4.10 UV/Visible spectra taken of a sample of the Au-MNPs after the initial 5 nm Au seeding step (red dashed line) and bare SPIONs (brown line).

By reducing Au^{3+} onto the GNP seeded SPIONs using the sequential addition of $HAuCl_4$ and NH_2OH the surface bound GNP seeds act as a nucleation site for the Au^{3+} ions, causing the growth of Au at the surface of the GNP seed modified SPIONS, this in turn produces a complete surface covering of Au over the SPION core to form Au-MNPs. Figure 4.11 shows the UV/Visible spectra of the various addition stages of Au coating.

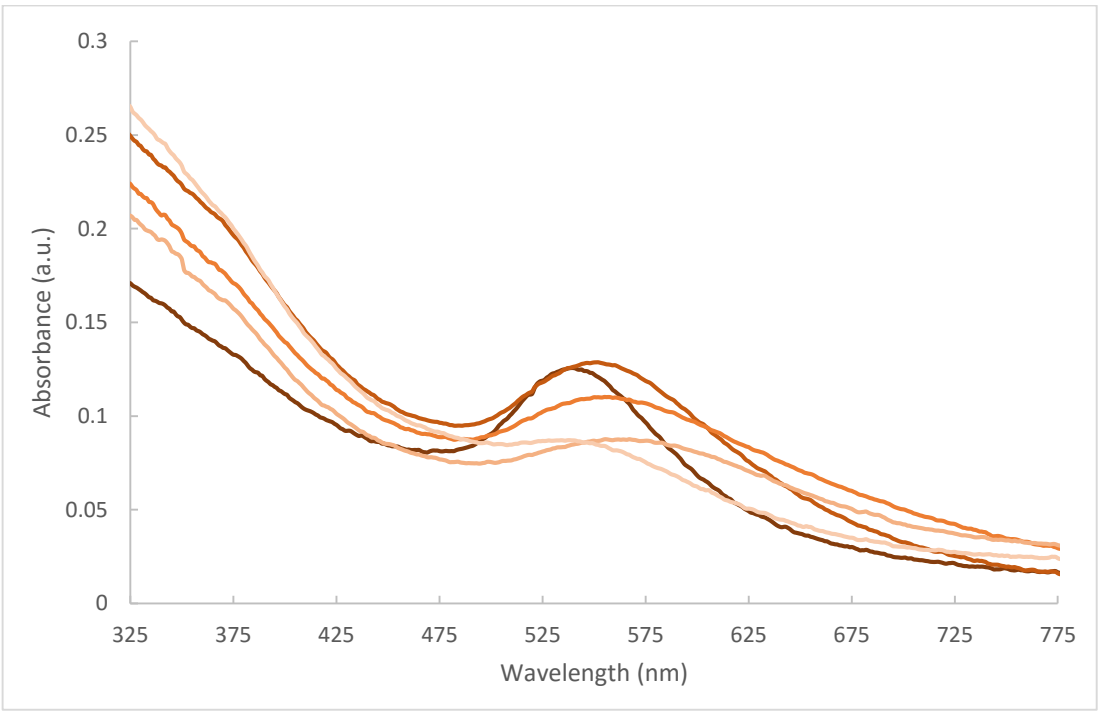

*Figure 4.11 UV/*visible *spectra showing the absorbance profile of the Au coated magnetite after sequential addition of $HAuCl_4$ and NH_2OH, 1-5 additions noted by change in colour from light to dark.*

The UV/Visible spectra of the Au coating process, Figure 4.11, shows an initial broad peak at ~ 575 nm. With each further reduction of Au^{3+} to the surface of the GNP seeded SPIONs this peak blue shifts and becomes sharper. After the 5th and final addition there is a distinct peak at λ_{max} = 540 nm. As the GNP seeds grow on the surface of the SPION they gradually coalesce to form a fully coated Au surface over the SPION core, the SPR returns and the now formed Au-MNPs exhibit similar behaviours to that of GNPs due to the similar surfaces.[314]

The Au-MNPs were analysed using TEM and were tested at the end of the GNP seeding stage along with TEM analysis of the final Au-MNPs. Figure 4.12, shows the 5 nm GNP seeded SPIONs and the particles appear to have a nodular like architecture at the surface of the SPIONs showing the 5 nm GNP seeds bound to the surface of the SPION. This nodular surface should provide a nucleation point to grow a form a gold shell around the particles.

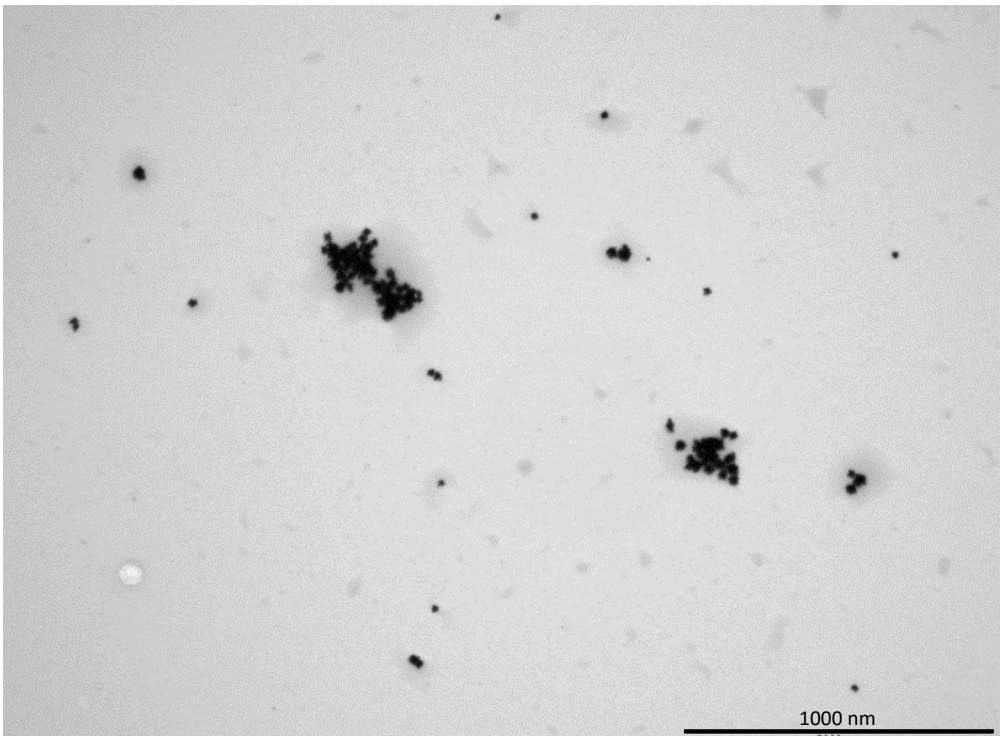

Figure 4.12 TEM image of the 5 nm Au seeded magnetite particles, Scale bar is 1000 nm.

EDAX taken during the TEM of the 5 nm GNP seeded SPIONs can be seen in Figure 4.13. The EDAX indicates that there is the presence of both Au and Fe which allows for the confirmation that the SPION cores have GNPs bound to their surface but there is exposed SPION being observed at the surface of the particles.

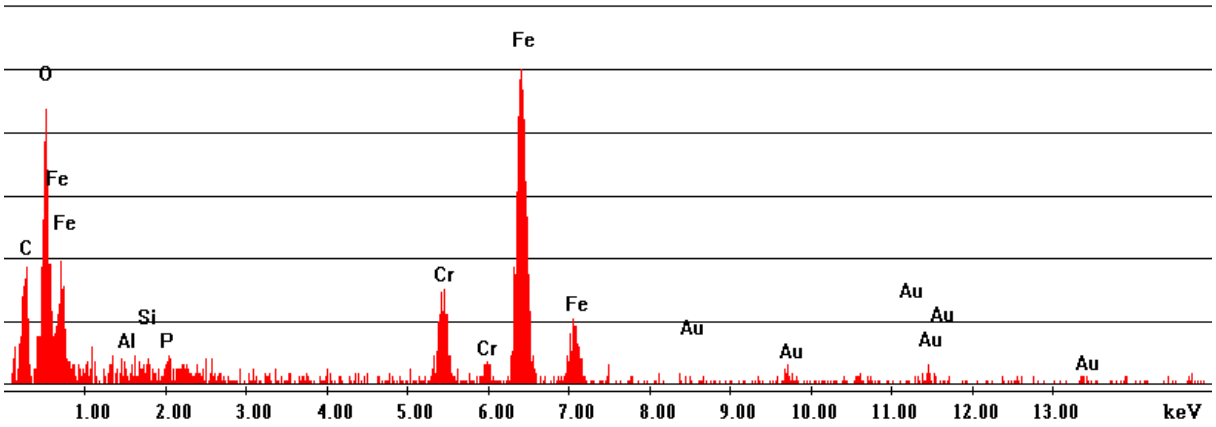

Figure 4.13 EDAX spectra obtained during TEM analysis of 5 nm Au seeded magnetite particles.

Figure 4.14, shows the TEM image obtained from the analysis of the final synthesised Au-MNPs, after they have undergone both the 5 nm GNP seeding stage and the hydroxylamine and chloroauric acid sequential additions. The size of the particles can be determined to be largely ~50 nm in size. It appears in the image that there are some smaller and lighter in intensity particles that can be assumed are uncoated SPIONs. On the left hand side of the image there is a tube/needle like structure, these may be present from the SPIONs and their presence has been described by Kang *et al.*[315] along with the suggested remediation of them by adjusting the pH of the SPION solution.[315]

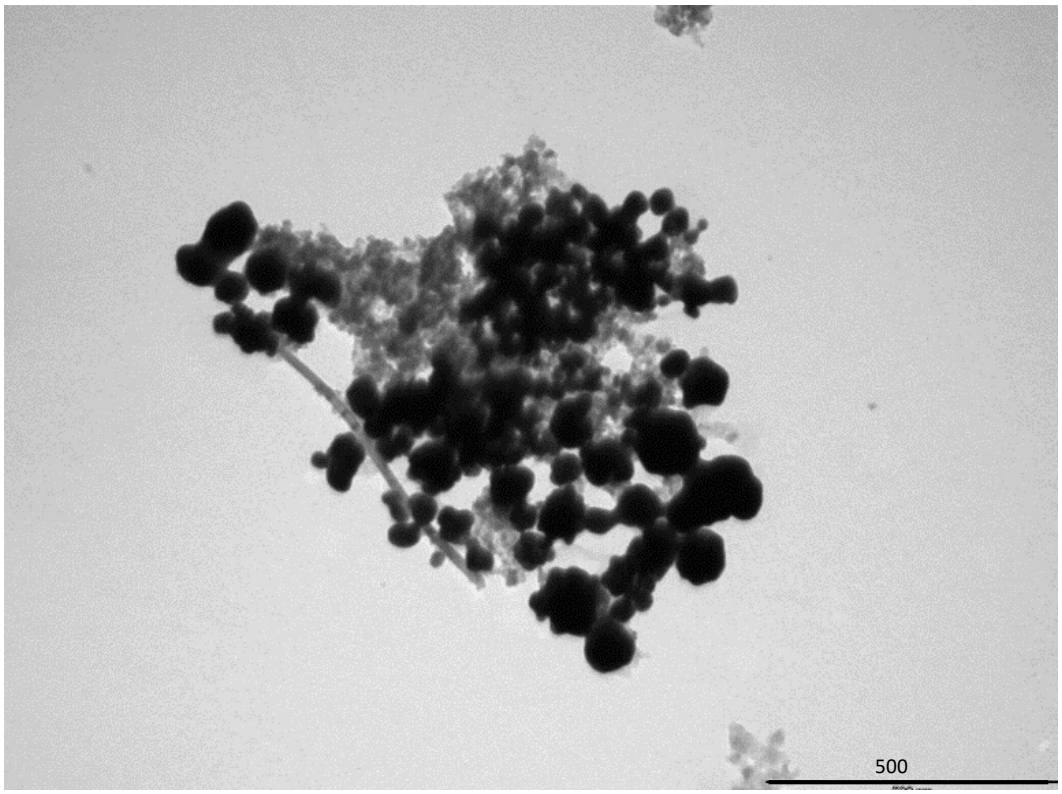

Figure 4.14 TEM image of the final Au-MNPs after sequential coating, Scale bar is 500 nm.

EDAX taken during TEM of the final synthesised Au-MNPs can be seen in Figure 4.15 below; contains only very small traces of iron, and is predominately composed of Au. This indicates that the particles are not quite fully coated with gold. If the particles were fully coated in gold then there should be no response to iron shown, it could also indicate that there is a small amount of completely uncoated iron particles. As previously mentioned the carbon and sodium peaks are due to surface bound citrate.

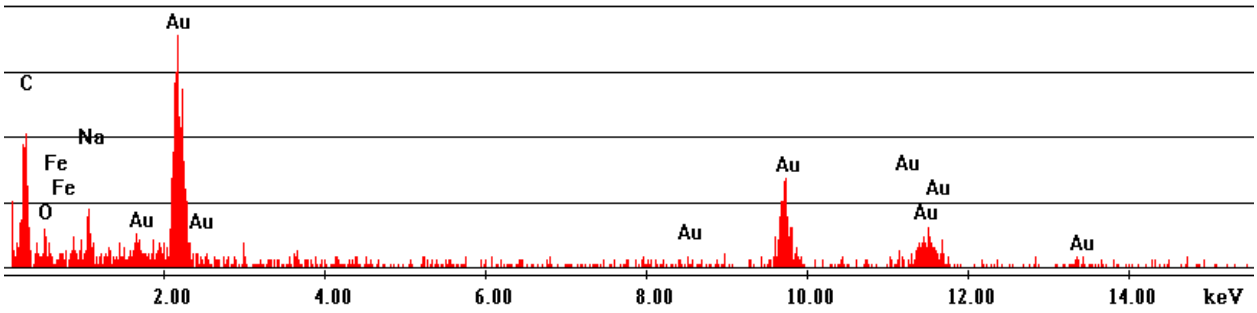

Figure 4.15 EDAX spectra obtained during TEM analysis of Au-MNPs.

The Au-MNPs were also subjected to particle size measurement using Nanosight®. The particle size of the seeded and coated Au-MNPs was confirmed to be have an average size of 58 nm as seen in Figure 4.16.

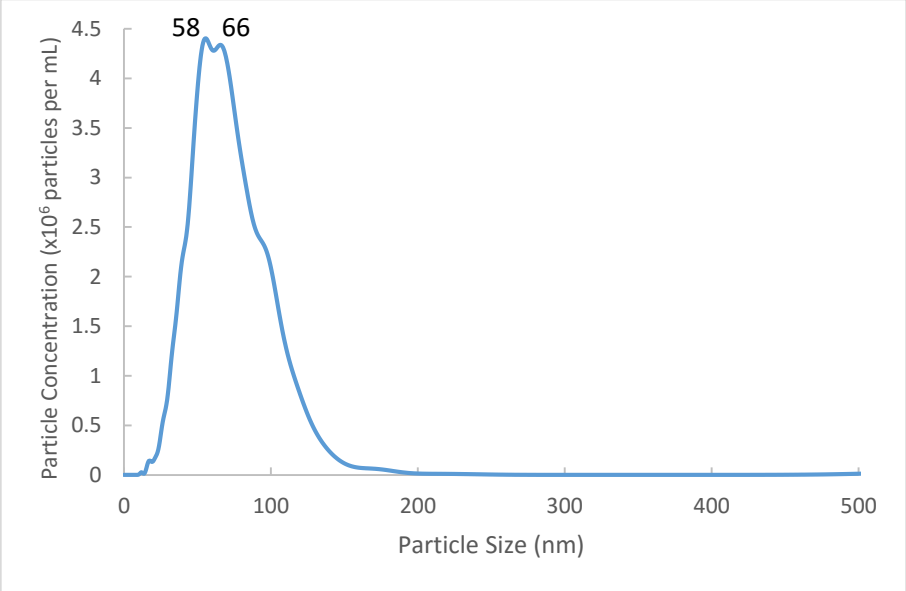

Figure 4.16 Size report recreated from data obtained from Nanosight® analysis of Au-MNPs.

The Au-MNPs have been successfully synthesised; however from the TEM analysis it would appear that there is not the desired fully coated spherical particles that this study set out to make. Further investigation is needed to optimise the coating process to allow the Au-MNPs to be successfully used in an MNDEPT approach. The TEM and size analysis allows us to define the size of the particles as ~50 nm which was the size that the study was aiming for and the desired size for cell uptake.[171]

4.4 Modified gold coated magnetic nanoparticle synthesis

Following the initial success in achieving ~50 nm Au-MNPs, the synthesis was adapted to optimise the surface coverage of the Au coating and also the morphology of the Au-MNPs to provide more spherical particles. The methodology for this can be found in more detail in section 2.3.1. The UV/Visible spectra of the particles, Figure 4.17 seen below, shows a peak indicative of Au at ~525 nm.[176] The overlaid spectra of the Au-MNPs obtained using the Lyon method[239] compared to the modified Au-MNP synthesis particles,; shows a much broader peak between 525-725 nm for the Lyon method Au-MNPs, indicating that the gold present in the sample is aggregating. This aggregation causes the shift in colour from the distinctive red colour to a blue-grey colour.[176]

The particles were sized using analysis of the TEM image, Figure 4.18, to give an average size of 47.35 nm ± 11.2 nm, the TEM images also enable the morphology of the particles to be defined. The particles seen in the TEM image appear nearly spherical in their morphology, there is also the absence of any light grey areas of particulate matter which would indicate the presence of SPIONs/SPION surfaces. This implies that the particles have a full coating of Au around the SPION core. Further analysis of the particles *via* EDAX; like that obtain for the other particles samples would further aid the definition of the particle coating.

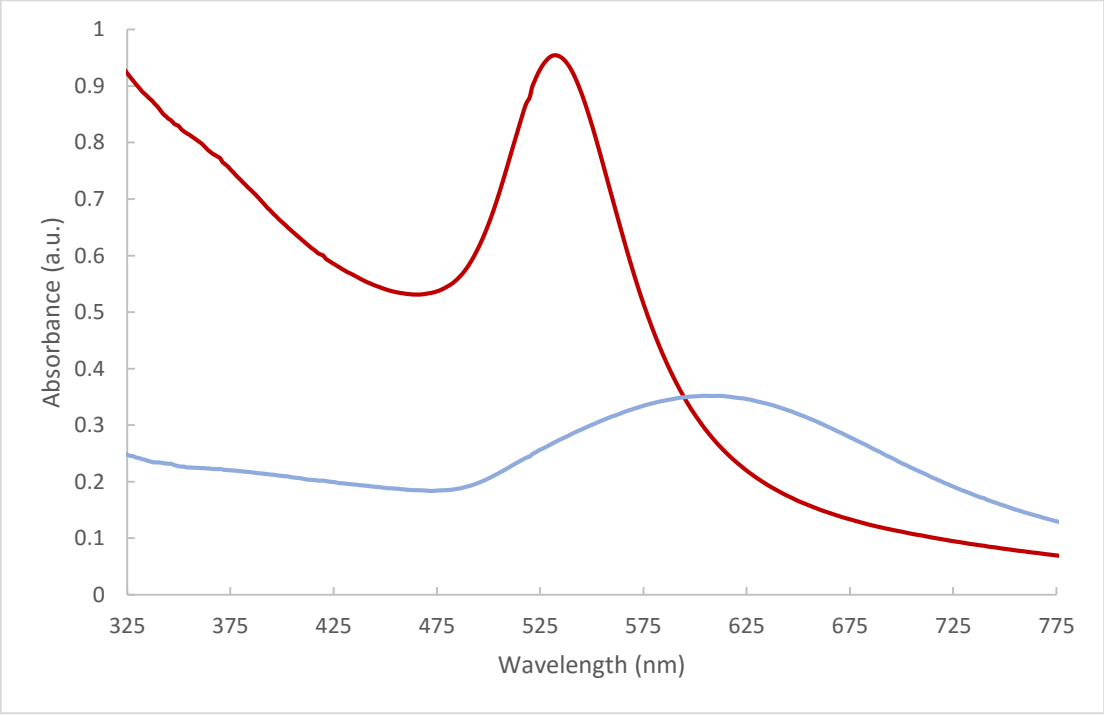

Figure 4.17 UV/Visible spectra comparing Au-MNPs synthesised using Lyons method [239] (Blue) and the modified gold coating route (Red).

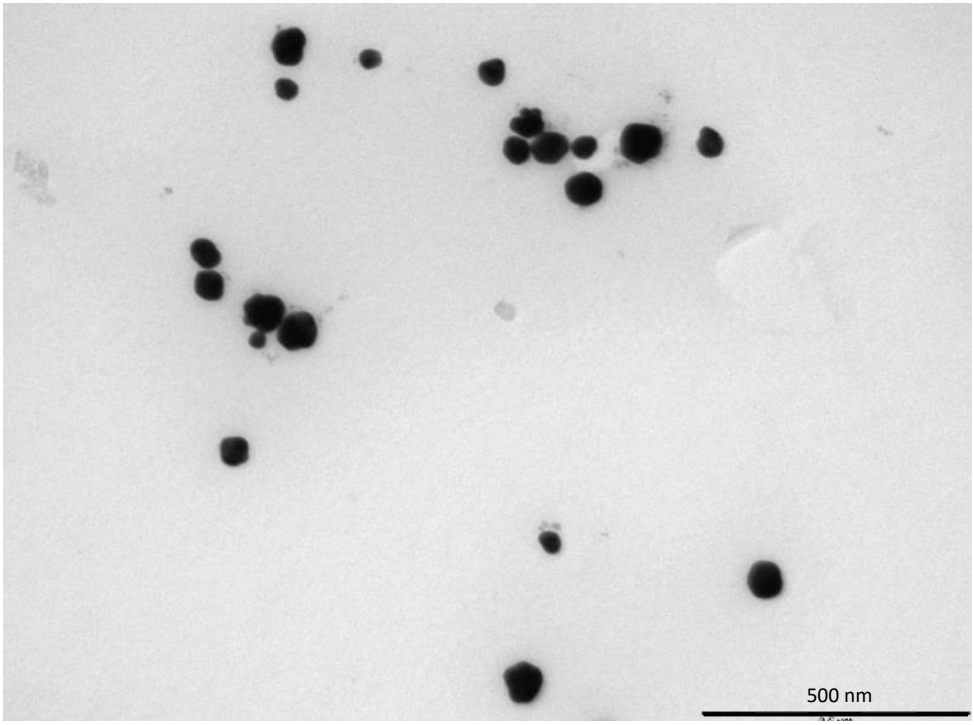

Figure 4.18 TEM image of the Au-MNPs synthesised using modified Au coating synthesis, Scale bar is 500 nm.

Details of the size properties as determined by TEM are compiled in Table 4.2 and compared to those obtained by Lyon *et al.*[239] and to another study from Jeong *et al.*[316] The particles that have been produced in this study are not only smaller in size but they possess a slightly narrower size distribution than the particles produced from both of the previous reports.

Table 4.2 A table showing the relative particle sizes of synthesised Au-MNPs from this study and from the studies conducted by Lyon et al.[239] *and Jeong et al.*[316]

Synthesis	Average size (nm)	Distribution (nm)
Lyon *et al.*	57	± 14
Jeong *et al.*	70	± 20
Au-MNP synthesis (4.3)	58	± 24
Modified Au-MNP synthesis (4.4)	47	± 14

The particle sizes for the synthesised particles were obtained by TEM analysis using an automated particle image analysis and the sizes provided in the form of a table. The average particle size was then calculated and the distribution given by defining the range between the smallest measure particle and the largest; e.g. 58 nm average particle size with distribution of ±24 nm defines that the smallest particle size is 34 nm and the largest 82 nm. For each synthesised samples there were measures of ~100 particles provided and the averages and distributions were calculated from these.

The experimental overview that expands on the 3 methods that were explored for the synthesis of Au-MNPs can be seen in Appendix 7.10. The initial iterative hydroxylamine seeding method as initially followed from the work of Lyon *et al.*[239] and as discussed in previous section did not produce any Au-MNPs that's exhibited magnetic behaviours and possessed the properties in the correct UV/Visible region matching that of a 50 nm Au colloid standard (λmax = 525 nm). The initial approach noted by step 1 led to the production of a blue/grey aggregated solution that wasn't observationally indicative of a gold colloid solution, back up by the shift in λmax of 80 nm. Steps 2-8 set about varying the concentration of the chloroauric acid and the hydroxylamine. Step 7 with half the original concentrations suggested by Lyon *et al* [239] but twice the number of additions resulted in the closest λmax at 578 nm, this is still a shift of 53 nm suggesting that aggregation is occurring. It is interesting to not however that the both step 7 and step 8 resulting in the same overall concentration of reagents added.

The next modification to the iterative seeding method made was the introduction of a heating step during the addition of the reagents; 50 and 75°C this resulted in a reduction in the shift of λmax observed for both of the heating steps using the original 5 additions stated by Lyon *et al* [239] but was still a shift of ~ 30-35 nm. The addition of a heating step with 10 additions of reagents resulted in a much greater shift indicating that that the particles were aggregating/ the gold formation was too large and/or the wrong morphology. The next step was to introduce a pre-seeding step whereby the SPIONs were mixed with 5 nm Au colloid prior to further iterative hydroxylamine seeding, this was suggesting using a methodology put forward by Brown *et al*.[294] This step was introduced in the hope that the 5 nm seeds would provide a nucleation point on the surface of the SPIONs in which to grow the gold coating. Following the reduction in the shift of λmax observed when the concentrations of the hydroxylamine seeding were reduced the pre-seeding method started with steps 15 and 16, although this in general showed a reduction in the shift it was still >80 nm and the same blue/grey sol was observed.

Steps 17 and 18 went back to the original concentrations used by Lyon *et al* but with the addition of the pre-seeding step suggested by Brown.[294] When only 5 additions were used; with the first chloroauric acid addition substituted for the 5 nm Au colloid the particles exhibited a λmax of 535 nm which was the closest achieved to that of the 50 nm Au colloid standard. But after analysis of the particles by TEM it was observed that the particles didn't possess the desired spherical morphology but a nodular type surface and there was a large presence of uncoated SPIONs. Further additions of the reagents were carried out but this resulted in the solution becoming bluer in colour and aggregation was observed. It was at this point that all the variables

that had contributed to a positive outcome in the first steps lead to step 19 whereby a larger volume of 5 nm gold colloid seeds were added in the first part of the reaction and this was coupled with an increased volume of chloroauric acid than was used by Lyon *et al.*[239] The amount of hydroxylamine was also slightly reduced to keep the pH of the solution more balanced. And the addition of heating the reaction mixture to 50°C which provided benefit in some of the earlier steps was retained. This lead to the production of particles with a λmax of 535 nm the closest match to the Au standard; along step 17, but this time with TEM analysis the morphology and size of the particles were the required spherical ~ 50 nm particles.

4.5 Concluding remarks on magnetic nanoparticles

The reproduction of Au-MNPs following previously described methods in the literature[239,316] proved problematic and did not produce any useable Au-MNPs. This was due to a number of reasons, some reproductions produced a grey/blue sol which was indicative of an aggregated Au particle solution.[176] Another reason was that although some particles could be magnetically separated the majority of the Au-MNPs in initial syntheses did not respond to an external magnetic field. The use of the pre seeding method adapted from Brown *et al's.*[294] produced Au-MNPs that exhibited magnetic behaviour to an external magnetic field and both UV/Visible and TEM analysis of the particles confirmed the presence of a gold coating. These particles however did display a remaining presence of iron in the EDAX analysis which suggests that the particles are either not fully coated or fully separated from uncoated SPIONs. For industrial and commercial use a process requiring further separation is undesirable as is a process whereby the yield of fully coated particles is not ≥ 99%. The morphology of the particles observed in the TEM analysis does not show the desired spherical nature needed to allow the genetically modified cys tagged NTRs to immobilise to the surface in a controlled manner allowing retention of a fully open active site.

Whilst the direct reduction of $HAuCl_4$ onto SPION cores did not produced the desired Au-MNPs as found in the study by Lyon *et al.*[239] A modified synthesis produced Au-MNPs that were 47 nm ± 14 nm and from the TEM analysis appear spherical in their morphology, and there is no presence of the lighter grey particulate matter; that from the EDAX analysis of previous samples could be defined as the SPION particle material. These Au-MNPs possessed a magnetic response allowing them to be easily separated using a 1 T magnet. These particles also meet the desired size that the study set out to synthesis and is required for their use in an *in vivo* MNDEPT application.

This modified synthesis has a very low yield; ~ 6.7%; see equation 4.4 based on the number of iron cores present at the start of the gold coating compared to final particle count of the Au-MNPs. The iron particle count was determined using Nanosight® and the Au-MNP particle count was determined by Dr von Ruhland using TEM.

$$\frac{5.04 \times 10^{9}}{7.54 \times 10^{10}} \times 100 \ = 6.68\%$$

Equation 4.4 Experimental yield of Au-MNPs

They are suitable to undergo further study to determine if they can be immobilised to cys tagged NTRs and retain the NTRs activity towards the prodrug CB1954. If activity is successfully retained then further experimentation will be conducted to determine the viability of an MNDEPT approach *in vitro*.

Chapter 5

Immobilisation and Cell Viability of Nitroreductases

The majority of the work discussed in this chapter is published in the following paper.

YfkO nitroreductase immobilised with controlled orientation onto superparamagnetic nanoparticles; towards a direct enzyme cancer therapy approach. *Publication suited to Biomacromolecules,* **(in DRAFT)**

Chapter 5 – Immobilisation and cell viability of nitroreductases

5.1 Characterising Au-S bonding and nitroreductase immobilisation

The self-assembly of enzymes onto a gold surface arises due to interactions between the proteins functional groups in the amino acids.[317] By introducing a repeated series of cysteine amino acid residues into a NTR a thermodynamically preferential bonding site between the enzyme and the gold surface can occur. To determine the presence of Au-S thiol bonding in the cysteine tagged genetically modified NTRs, cyclic voltammetry is used. The protocol for this cyclic voltammetry characterisation can be found in section 2.1.7. In brief Au(111) coated glass slides (Winkler GmbH, Germany) were incubated at 4°C for 48 hours with the purified cysteine tagged NTRs, these were then removed from the NTR solutions, washed with PB (50 mM, pH 7.4) and used as the working electrode in the electrochemical cell set-up. The NTRs were left for 48 hours to allow adequate time for the enzymes to self-assemble on the surface of the gold slides. The voltammogram showing the electrochemical desorption of NfsB-cys after 48 hour incubation is shown in Figure 5.1, with the desorption of a bare Au(111) coated glass slide shown as a control.

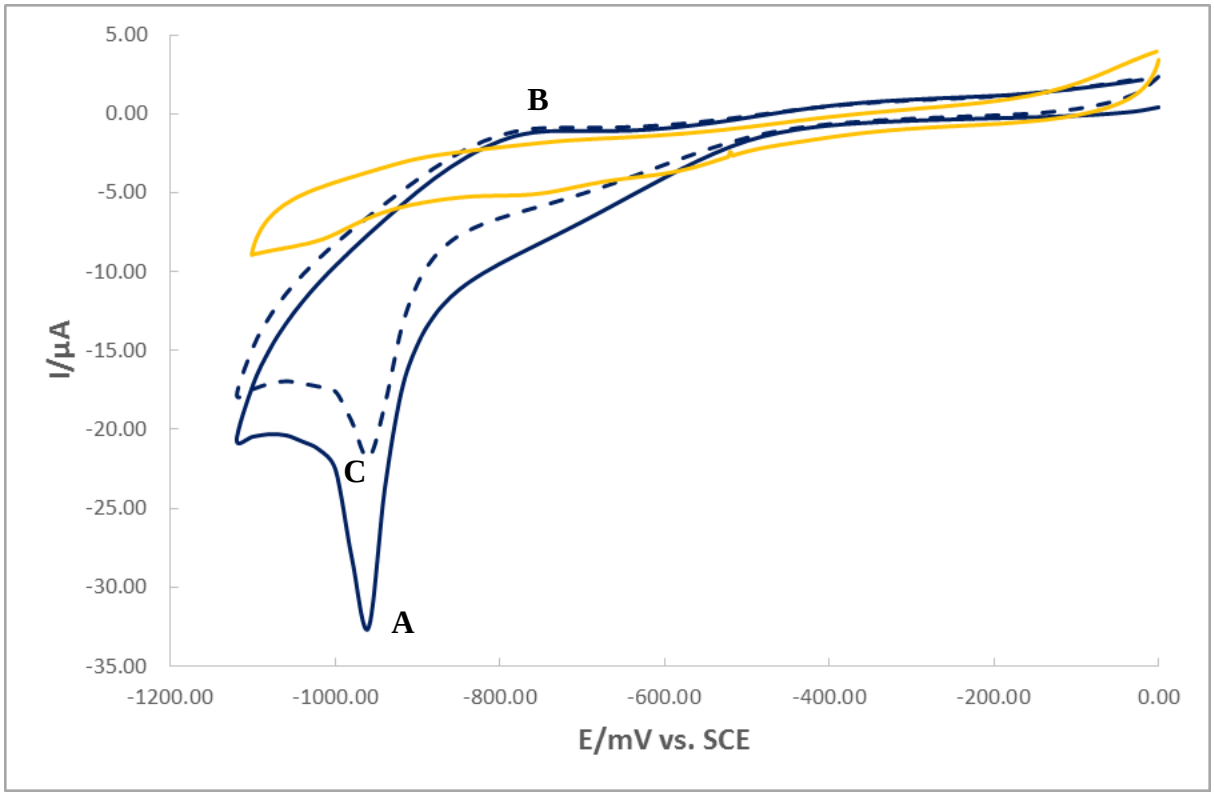

Figure 5.1 Voltammogram showing a sweep of a bare Au(111) coated glass slide (solid gold line) and two consecutive sweeps of an Au(111) coated glass slide after 48 hour incubation with NfsB-cys*: scan 1 (solid blue line) = -959.47 mV, -32.60 µA and scan 2 (dashed blue line) = -959.47 mV, -21.82 µA. The potential is vs. SCE in an electrolyte of 0.1 M NaOH, 50 mV/s sweep rate.*

A bare Au(111) coated slide was subjected to cyclic voltammetry and can be seen in Figure 5.1. This acts as a control allowing us to conclude that any reduction and oxidation that occurs in the scans conducted with the protein bound gold slides, is solely from the binding of the cysteine tagged NTRs to the gold working electrode. All cyclic voltammetry experiments were carried out between 0 and -1.1 V under basic conditions. During the first sweep (solid line) there is a distinct reduction peak (**A**) observed at -959.47 mV, -32.60 µA; this corresponds to the reduction of gold thiol bonds between the gold and the cysteine tagged residues of the genetically modified NfsB-cys.[262] These are within the typical range for the reductive desorption of thiols from Au and which have been well reported in the literature.[267,318] There is also a small shoulder peak (**B**) indicating the reabsorption of the cys tags onto the Au(111) slide, the magnitude of this peak is very small and this is due to the fact that the cysteine tags only have a few seconds for reabsorption. The second sweep cycle (dashed line) in Figure 5.1 shows a peak (**C**) at the same potential to that of peak (**A**) observed in the first sweep. The reduction peak in the second scan was observed at -959.47 mV, -21.82 µA. The presence of a second peak (**C**) indicates that after the desorption of the Au-S bonds in the first cathodic sweep some of the cysteine tag residues re-bind to the Au surface. The lower current required for the desorption in the second sweep indicates that the Au-S bonds are weakened due to only having a matter of seconds to reform after being broken in the first sweep. These weakened bonds require much less voltage to re-break them.

Figure 5.2, shows the voltammogram of an Au(111) glass working electrode that was subjected to a 48 hour incubation with the genetically modified NTR YfkO-cys.

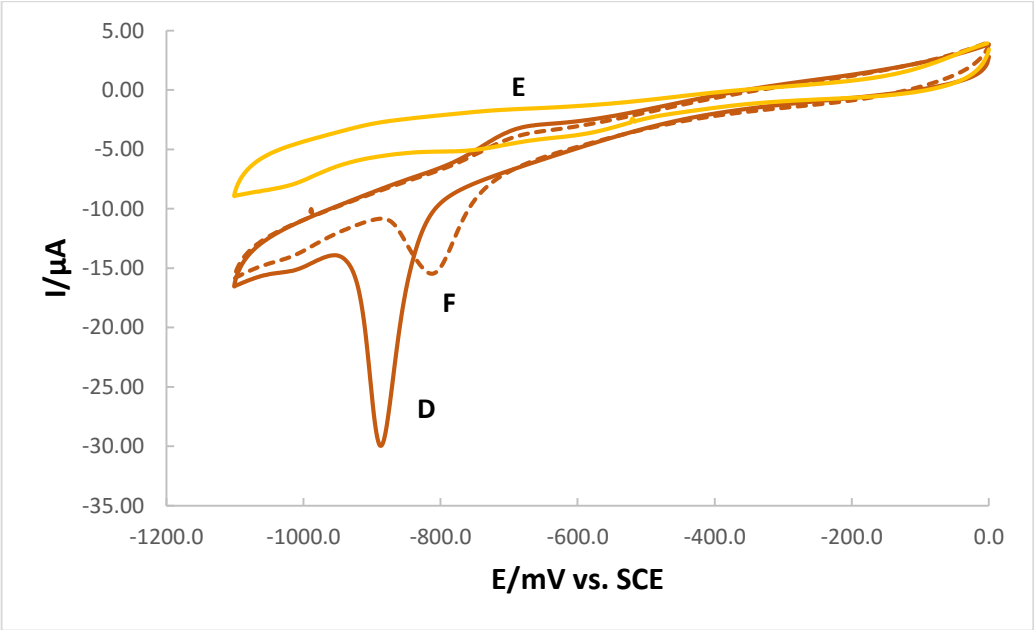

Figure 5.2 Voltammogram showing a sweep of a bare Au(111) coated glass slide(solid gold line) and two consecutive sweeps of an Au(111) coated glass slide after 48 hour incubation with YfkO-cys *scan 1 (solid orange line)= -886.2 mV, -29.94 µA and scan 2 (dashed orange line) = -808.1 mV, -15.40 µA. The potential is vs. SCE in an electrolyte of 0.1 M NaOH, 50 mV/s sweep rate.*

During the first sweep (solid orange line) there is a clear cathodic desorption peak (**D**) observed at -886.2 mV, -29.94 µA; this corresponds to the reduction of gold thiol bonds between the gold and the cysteine tag residues of the YfkO-cys enzyme. Peak (**F**) observed in the second cathodic sweep (dashed line) is observed at a lower voltage and also a lower current (-808.1 mV, -15.40 µA).

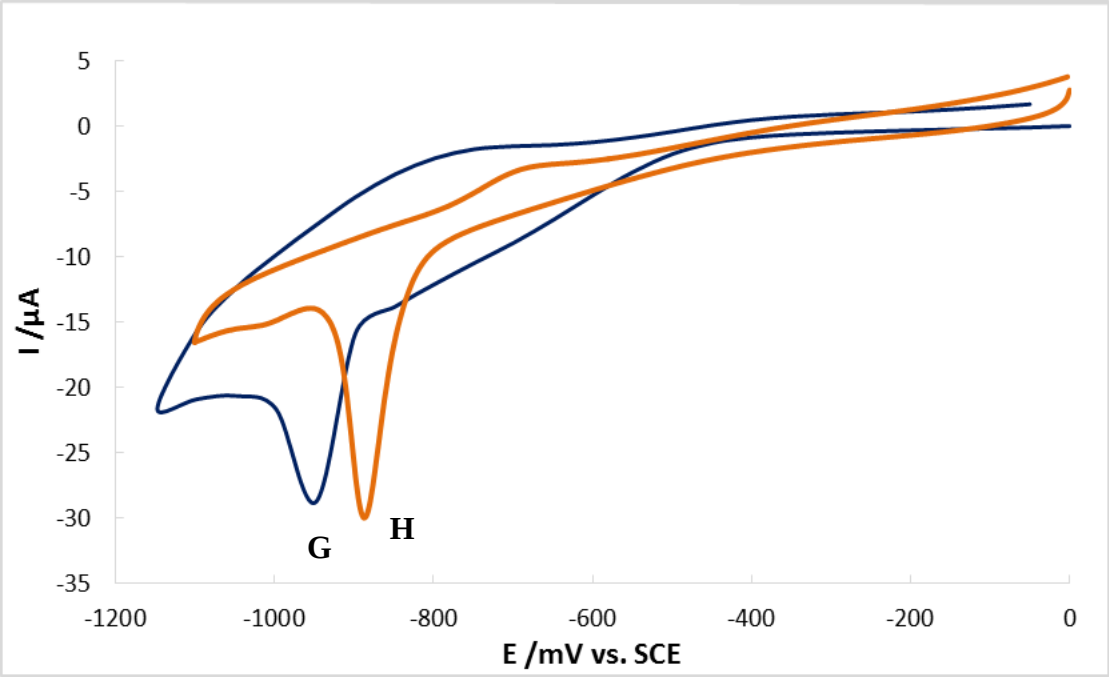

Figure 5.3 Voltammogram showing cathodic sweeps of an Au(111) coated glass slide after 48 hour incubation with YfkO-*cys (solid orange line)= -886.2 mV, -29.94 µA and* NfsB-*cys (solid blue line) = -959.47 mV, -32.60 µA. The potential is vs. SCE in an electrolyte of 0.1 M NaOH, 50 mV/s scan rate.*

A comparison of the first cathodic sweeps for both NfsB-cys and YfkO-cys immobilised onto an Au(111) can be seen in Figure 5.3. The reduction in current at peak (**H)** (-886.2 mV, -29.94 µA) compared to the observed peak G (-959.47 mV, -32.60 µA) indicates that fewer Au-S bonds are being reduced, but can also suggest that the configuration of the bonds has changed.[267] The cyclic voltammetry within this study was conducted using an NTR concentration of 2 mg/mL. The lower density can allow for a change in orientation and packing of the NTRs on the surface. This difference in potential and current of peaks (**A)** and (**C)** suggests that the number of Au-S bonds have both decreased and changed in nature.[224] The peaks present on the shoulders of the sweeps where the readsorption of the NTRs onto the gold surface occurs; indicate that after the desorption has occurred the NTRs bind so quickly back to the surface of the gold slide that the subsequent charge to desorb them in the second sweep is significantly decreased. This is most likely due to the orientation of the readsorption occurring with different functional groups of the NTR, changing the overall conformation and shape of the immobilised NTR affecting the Au-S reduction potential. The value and

prominence of peaks (**C**) and (**F**) are much smaller than the peaks (**A**) and (**D**) in the first reduction cycles of the two enzymes due to them corresponding to the reduction of Au-S bonds that have reformed between scans, meaning they have formed in a much faster time frame and will be weaker and present in a more disordered manner than the linear orientation expected from the 48 hour initial incubation with the original 12 cysteine tag residues.

Figure 5.3 confirms that the presence of cysteine residues in the genetically modified enzymes NfsB-cys and YfkO-cys enabling them to successfully bind to a gold surface *via* Au-S thiol bonds. This is paramount to the success of immobilising the enzymes to the gold coated nanoparticle system. The ability to determine how much cys-tagged NTR is bound to the slide is hindered by the large biological layer that forms on the slide; this leads to an increase in capacitance, which prevents the quantification of the volume of cys-tagged NTR bound to the surface of the slide. The ability to immobilise an NTR to a gold surface is vital in the development of an MNDEPT application. The modified NTRs will need to be bound to the gold coated nanoparticles. The density of the monolayer formed by the self-assembly of the genetically modified enzymes is important and could be potentially be determined by cross sectionally imaging with a scanning electron microscope. It may also be defined by analysing the surface of a slide that has intentionally not fully coated, e.g. masked using atomic force microscopy. The strength of the binding of the cys-tagged NTRs is also important and could be determined by conducting further stripping cyclic voltammetry experiments using a varying range of voltages to determine the level needed to break the cys-tagged bound NTR.

5.2 Activity of immobilised nitroreductases

UV-Visible spectroscopy was used to measure the activities of the immobilised NTR conjugates. CB1954 was the prodrug of choice for the activity assay because it has been studied extensively in the literature[125,301,308,319] and is one of only a few prodrugs which are commercially available. The prodrug has a poor solubility in aqueous solvents so a concentrated master stock was created using DMSO and diluted to various concentrations using 50 mM phosphate buffer (pH 7.4). At lower concentrations the prodrug is readily soluble in aqueous solvents. The dilutions were performed this way due to the need to keep the DMSO concentration present in the prodrug sample below 5%; this is due to higher concentrations of DMSO exhibiting inhibition of NTR activity towards the prodrug.[302]

The absorbance of both the cofactor and prodrug are expected to decrease during the immobilised enzyme conjugate activity reactions. This decrease in absorbance is indicative of a decrease in concentration; at the same time as the decrease in cofactor and prodrug an increase in the absorbance of NAD+ and the hydroxylamine reduced prodrug derivatives should be observed. The exact concentration of NTR bound to the Au-MNPs needs to be determined in future experiments; but could potentially be done by analysing; using the Bradford protein concentration assay (section 2.1.8) the decanted supernatant after the conjugate has undergone magnetic separation. This would allow for the amount added to the Au-MNP and the amount that is left unbound to the particles to be known, in turn the amount bound to the particles could be surmised.

5.2.1 Activity of Au colloid immobilised NfsB-cys

The activity of an Au colloid immobilised NfsB-cys was conducted using UV/Visible spectroscopy. There are four distinct peaks observed in the UV/Visible spectra of the immobilised NTR. Peak (**1**) of Figure 5.4, at approximately 290 nm is indicative of the absorbance region of NTRs. This region is also the area in which NAD+ and NADH absorb, both of these compounds have a λ_{max} = 259 nm. This means that the concentrations of the oxidised and reduced forms of the cofactor cannot be quantified, due to the interference in absorbance from the NTRs and therefore cannot be related directly to the reduction of the prodrug. The reduction of CB1954 and the oxidation of NADH have λ_{max} values that are very close to each other; 327 nm and 340 nm respectively, this can again give rise to interference and prevent quantitative analysis of the absorbance regions.

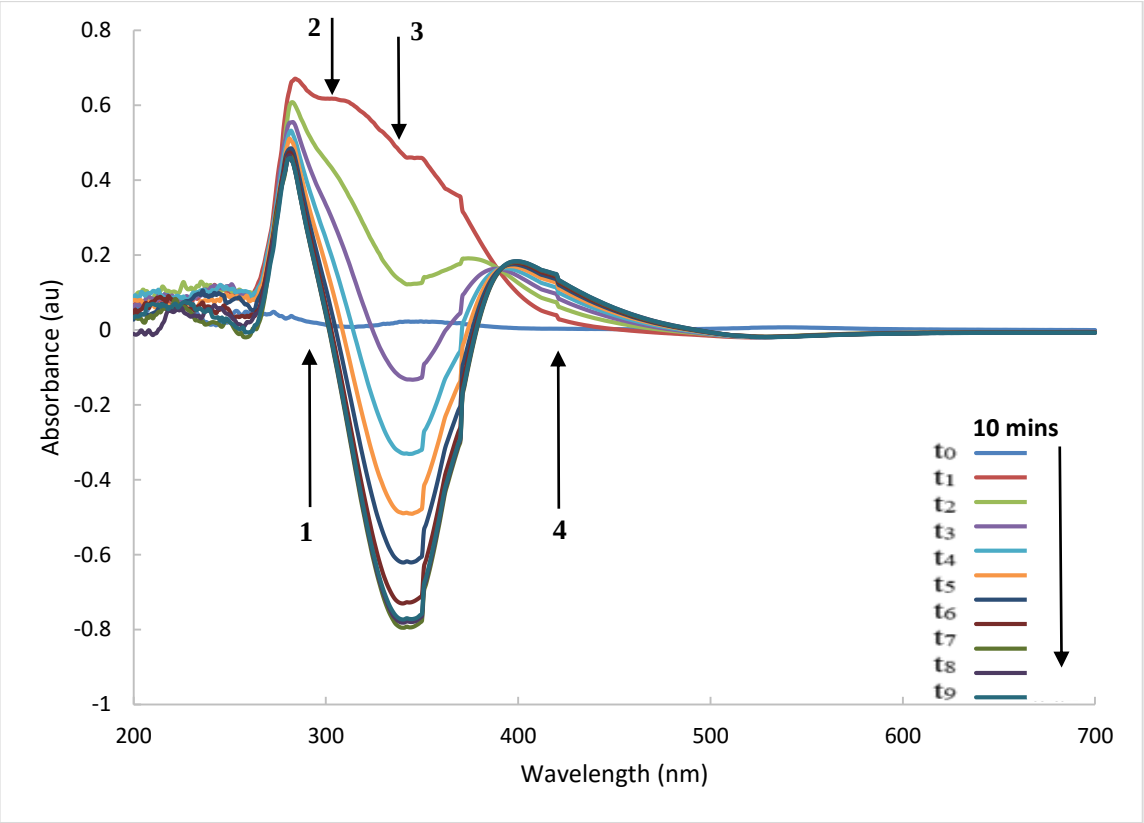

Figure 5.4 UV-Visible spectra of Au colloid immobilised NfsB-*cys showing the enzymatic activity assay. **(1)** NTR absorbance ~ 290 nm. **(2)** Reduction of CB1954 λ_{max} = 327 nm. **(3)** Oxidation of NADH λ_{max} = 340 nm. **(4)** Production of CB1954 reduction products λ_{max} = 420 nm.*

The broad peak observed at ~340 nm overlays the λ_{max} of both the prodrug CB1954 (**2**) and the cofactor NADH (**3**). This overlap prevents definitive quantification of the concentrations of both of these compounds. The peak observed at 420 nm as indicated by (**4**) directly correlates to the λ_{max} of the two common reduction products of CB1954; both the 2- and 4-hydroxylamine derivatives. These reduced hydroxylamine products have a molar extinction coefficient (ε) = 1200 L $mol^{-1}cm^{-1}$. Due to the overlaps present in the other regions of the scans this is the only region that can determine the kinetic parameters of the gold colloid immobilised NTR conjugates by allowing the rate of product formation to be quantified in direct correlation with the absorbance.[301]

Figure 5.5 is a plot to show the course of the reaction over the full 10 minute scan and plots absorbance vs time at 420 nm. The plot shows that the reaction only proceeds lineraly the 1st 1-3 minutes of the reaction, meaning that caputuring the data early in the reaction is paramount to be able to analyse the data to determine the kinetic properties of the Au-NfsB-cys conjugate.

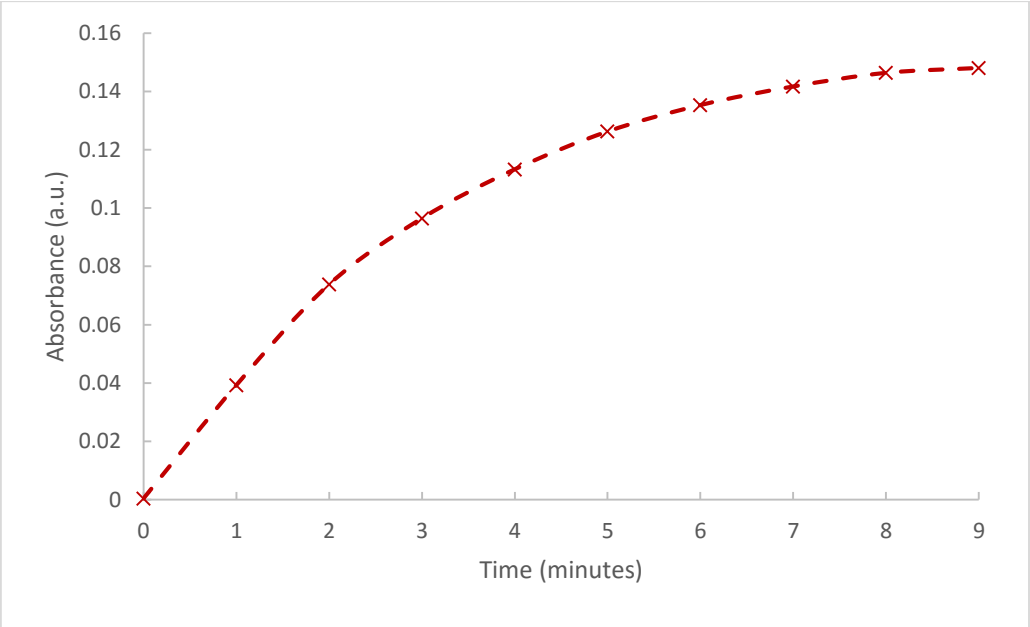

Figure 5.5 Plot of absorbance at 420 nm vs time for Au-NfsB-cys, CB1954 (100 µM), NADH (600 µM) and PB (50 mM, pH 7.4).

The broad peak observed at ~340 nm overlays the λ_{max} of both the prodrug CB1954 (**2**) and the cofactor NADH (**3**). This overlap prevents definitive quantification of the concentrations of both of these compounds. The peak observed at 420 nm as indicated by (**4**) directly correlates to the λ_{max} of the two common reduction products of CB1954; both the 2- and 4-hydroxylamine derivatives. These reduced hydroxylamine products have a molar extinction coefficient (ε) = 1200 L $mol^{-1}cm^{-1}$. Due to the overlaps present in the other regions of the scans this is the only region that can determine the kinetic parameters of the gold colloid immobilised NTR conjugates by allowing the rate of product formation to be quantified in direct correlation with the absorbance.[301]

5.2.2 Effect of pH on Au colloid immobilised NfsB-cys

The effect of pH on the gold colloid immobilised NfsB-cys conjugates ability to reduce the prodrug CB1954 has been previously determined by Gwenin *et al.*[15] It was determined in the study that the gold colloid immobilised enzyme conjugates were stable at pH's greater than pH 3 up until pH 11. This allows the conclusion to be drawn that the Au-NfsB-cys conjugates would remain stable in the physiological conditions the conjugate would experience in the human body. This would allow it to be a suitable agent in a DEPT treatment system.

5.2.3 Effect of temperature on Au colloid immobilised NfsB-cys

To determine the optimum temperature parameters for gold colloid immobilised NfsB-cys the enzyme conjugates were assayed at 420 nm with the prodrug CB1954 after incubation at a range of temperatures in phosphate buffer as detailed in section 2.5.3.

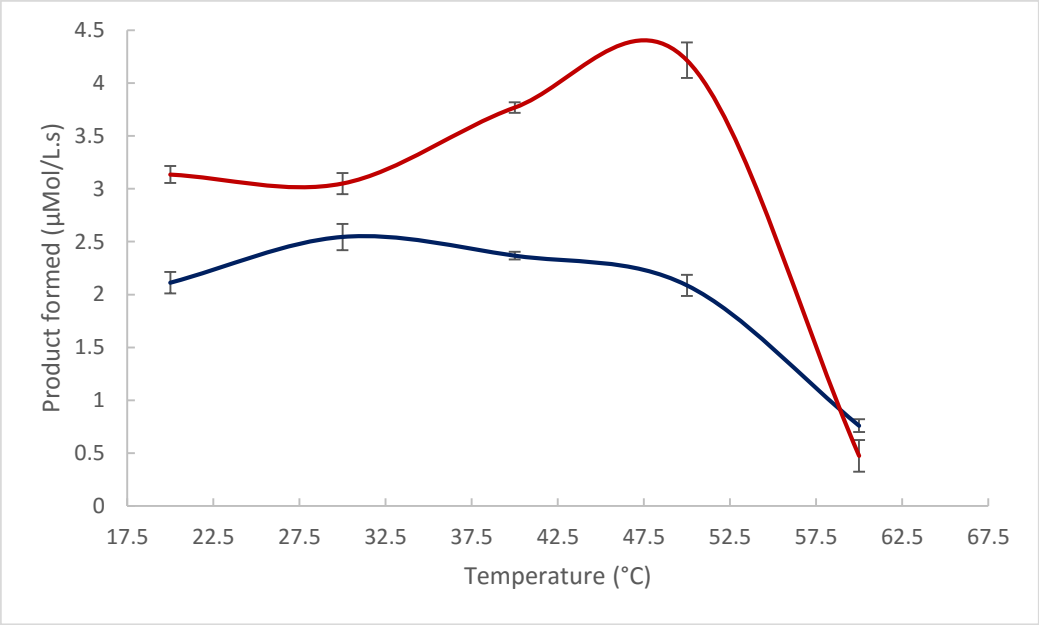

Figure 5.6 A graph detailing the effect of temperature on the production of hydroxylamine derivatives (λ_{max} = 420 nm, ε = 1200 L mol^{-1}cm^{-1}) of gold colloid immobilised NfsB-*cys conjugate (red line) and non-immobilised* NfsB-*cys (blue line) with 100 µM CB1954 and 600 µM NADH. Error bars represent ± 1 SD.*

It can be observed in Figure 5.6 that as the temperature is increased up to 50°C the reaction remains stable until the enzyme activity begins to decrease rapidly above 50°C indicating that the enzyme structure is denaturing due to the increased temperature resulting in a loss of activity of the enzyme conjugate toward CB1954. The immobilised enzyme conjugates need to retain optimum activity at the human body's physiological temperature of 37°C, the gold colloid immobilised NfsB-cys retains optimal activity up until ~50°C. The non-immobilised NfsB-cys, displays stability of a slightly larger temperature range with it only exhibiting a slight decrease in activity at ~ 50°C. However the activity of the non-immobilised NfsB-cys is less across the whole range of temperatures tested when compared with the Au-colloid immobilised NfsB-cys. At temperatures approaching 60°C both the immobilised and non-immobilised NTR exhibit little or no activity towards the prodrug CB1954. The Au-colloid immobilised NfsB-cys has a heightened optimal activity range of 37.5-50°C with an overall range of 25-50°C. The non-immobilised NfsB-cys has a similar range of 25-47.5°C but with no heightened activity observed.

5.2.4 Activity of Au colloid immobilised YfkO-cys

The activity of gold colloid immobilised YfkO-cys conjugate was tested using the same methodology briefly described in section 5.2 and detailed in full in section 2.5.1.

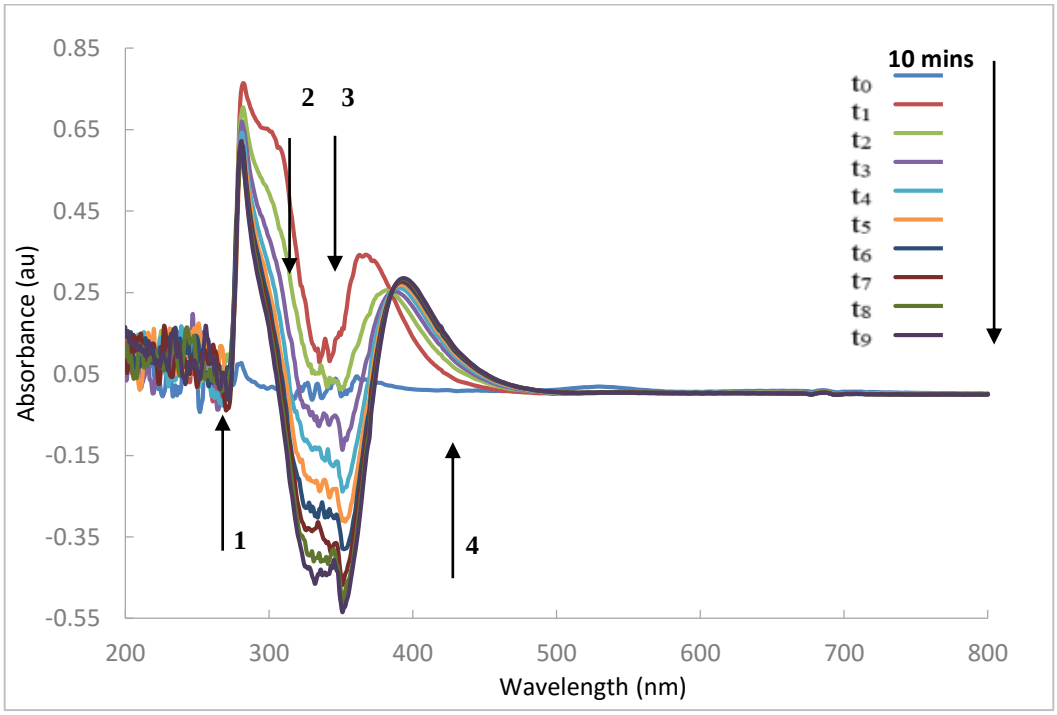

Figure 5.7 UV-Visible spectra of Au colloid immobilised yfkO-cys conjugate showing the enzymatic activity assay. ***(1)*** *NTR absorbance ~ 290 nm.* ***(2)*** *Reduction of CB1954 λ_{max} = 327 nm.* ***(3)*** *Oxidation of NADH λ_{max} = 340 nm.* ***(4)*** *Production of CB1954 reduction products λ_{max} = 420 nm.*

Figure 5.8 is a plot to show the course of the reaction over the full 10 minute scan and plots absorbance vs time at 420 nm. The plot shows that the reaction only proceeds lineraly the 1st 1-3 minutes of the reaction. This means the importance of capturing the formation of the hydroxylamine reaction products during the initial stages of the reaction is paramount. This will enable an accurate determination of the kinetic parameters of the Au-YfkO-cys conjugate.

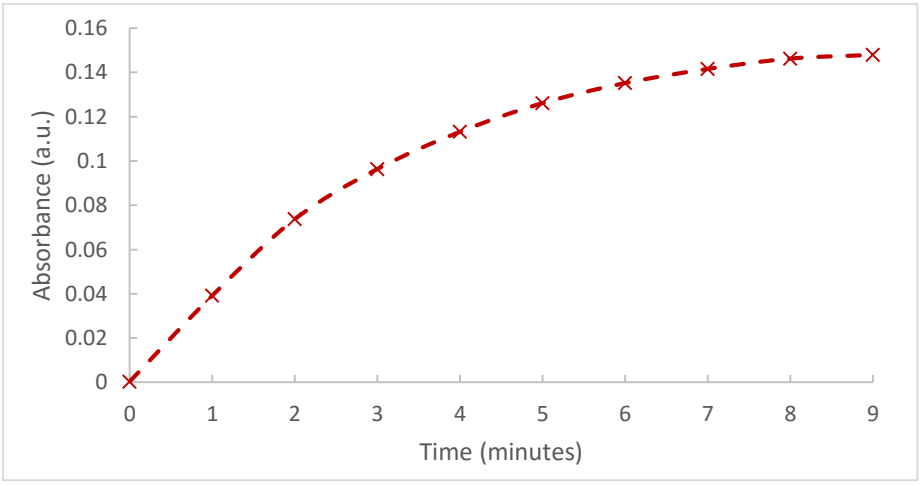

Figure 5.8 Plot of absorbance at 420 nm vs time for Au-YfkO-cys, CB1954 (100 µM), NADH (600 µM) and PB (50 mM, pH 7.4).

The change in absorbance observed at 420 nm (peak 4) in Figure 5.7 allows the rate of formation of the hydroxylamine reduced prodrug derivatives to be determined. This area of the spectra is the only area free from interferences from the other corresponding absorbance peak regions (Peak 1, 2 and 3). Kinetic parameters such as rate of formation and specificity constant can be determined by monitoring this increase change in absorbance at 420 nm (peak 4), this can be focused over a short period of time allowing for the most accurate quantification of the rate of product formation.[302] The quantification of these parameters of the immobilised NTR conjugates allows for the comparison of these systems to the kinetic ability of the NTRs used free in solution, this comparison allows the identification of the most suitable candidate for use in a MNDEPT application.[301] The data for this is discussed in sections 5.3.1, 5.3.2 and 5.3.3, briefly for each individual immobilised conjugate followed by a comparison in section 5.3.4.

5.2.5 Effect of pH on Au colloid immobilised YfkO-cys

The effect of pH on the gold colloid immobilised YfkO-cys conjugate ability to reduce the prodrug CB1954 was determined by assaying the conjugate at various pH's, with the prodrug and quantified at 420 nm as detailed in section 2.5.3.

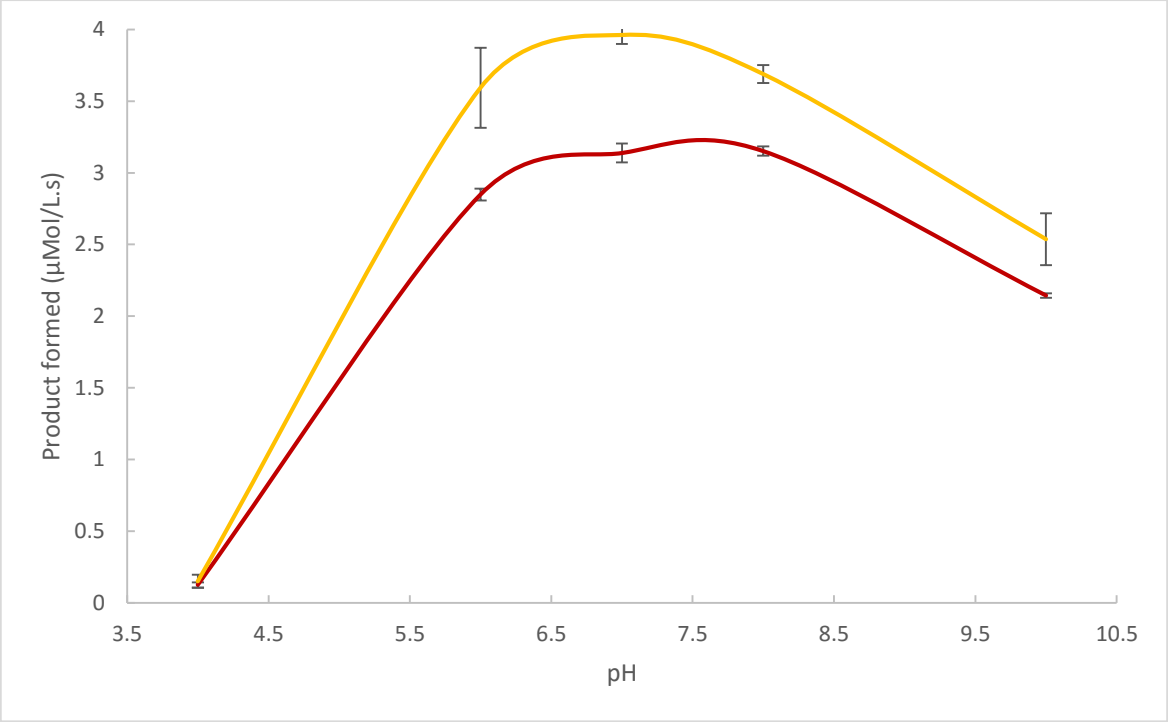

Figure 5.9 A graph detailing the effect of pH on the production of the hydroxylamine derivatives (λ_{max} = 420 nm, ε = 1200 L mol^{-1}cm^{-1}) of gold colloid immobilised YfkO*-cys conjugate (red line) and non-immobilised* YfkO*-cys (yellow line) with 100 µM CB1954 and 600 µM NADH. The error bars represent ± 1 SD.*

In Figure 5.9 the Au-colloid immobilised YfkO-cys conjugate shows significant activity between pH 6 and 8 before the activity begins to decline at pH's >10. The Au-colloid

immobilised conjugate displays slightly decreased activity compared to the non-immobilised YfkO-cys but follows the same trend for optimum activity. Both the immobilised and non-immobilised YfkO-cys exhibit a rapid decline in activity at pH's < 6 with neither of them displaying activity towards the prodrug CB1954 at pH 2. Exhibiting activity in the range of pH 6-8 means that the conjugate will retain optimum activity at the required pH of 7.4 which is the pH of human physiological conditions allowing for its suitability to be used a treatment system to be used in the human body.

5.2.6 Effect of temperature on Au colloid immobilised YfkO-cys

To determine the optimum temperature parameters for the gold colloid immobilised YfkO-cys conjugate, the conjugate was assayed at 420 nm with the prodrug CB1954 after a short incubation at a range of temperatures in phosphate buffer as detailed in section 2.5.3.

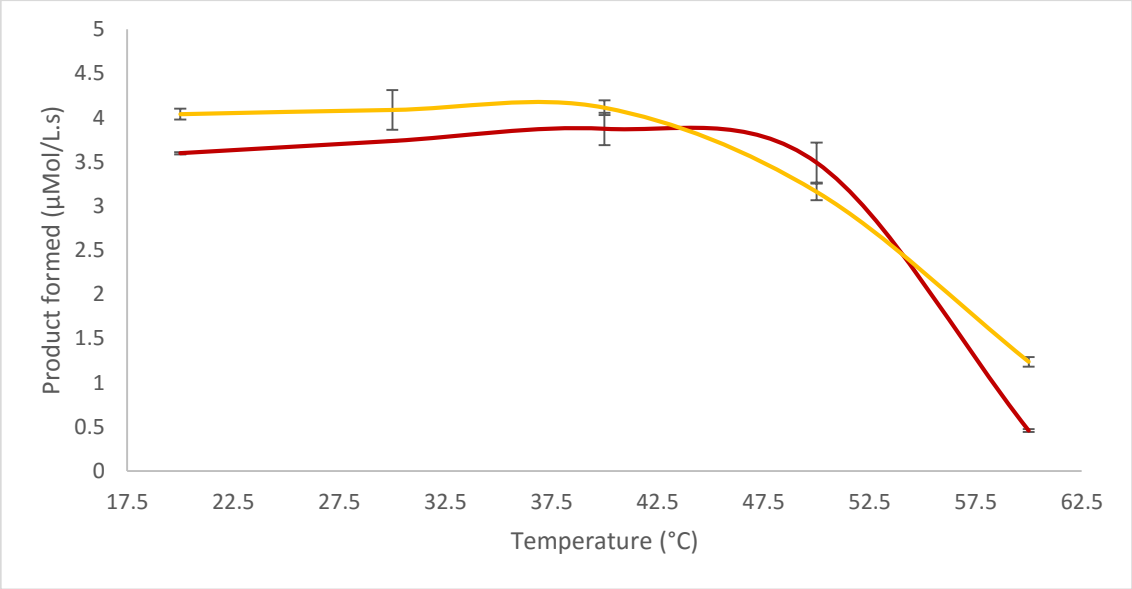

Figure 5.10 A graph detailing the effect of temperature on the production of the hydroxylamine derivatives (λ_{max} = 420 nm, ε = 1200 L mol^{-1}cm^{-1} of gold colloid immobilised YfkO*-cys conjugate (red) and non-immobilised* YfkO*-cys (yellow) with 100 µM CB1954 and 600 µM NADH. The error bars represent ± 1 SD.*

In Figure 5.10 the Au-colloid immobilised YfkO-cys retains optimum activity up to ~50°C. The non-immobilised enzyme retains similar levels of activity but begins to decrease in activity at a lower temperature than the Au-colloid immobilised enzyme at ~ 42.5 °C. As the temperature is increased further the ability of the conjugate to reduce the prodrug decreases rapidly. This rapid decrease indicates that the enzyme conjugate structure begins to denature resulting in a loss of activity of the conjugate towards the prodrug CB1954. Both the immobilised and non-immobilised YfkO-cys exhibit activity as temperatures lower than 37°C with both retaining significant activity at 20°C

For suitability in its use in a DEPT system the conjugate needs to retain optimum activity at the physiological temperature exhibited in the human body. The gold colloid immobilised enzyme conjugate retains optimal activity up to ~50°C so is therefore a suitable candidate for use in a DEPT system.

5.2.7 Activity of Au-MNP immobilised YfkO-cys

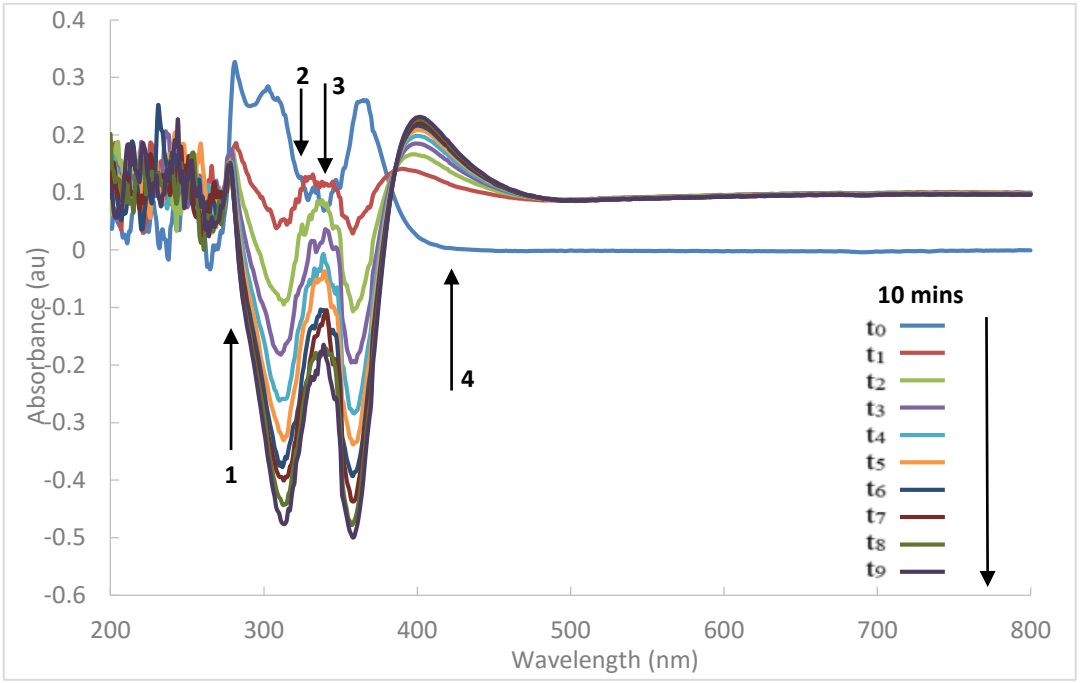

Figure 5.11 UV-Visible spectra of Au-MNP immobilised YfkO*-cys conjugate showing the enzymatic activity assay.* ***(1)*** *NTR absorbance ~ 290 nm.* ***(2)*** *Reduction of CB1954* λ_{max} *= 327 nm.* ***(3)*** *Oxidation of NADH* λ_{max} *= 340 nm.* ***(4)*** *Production of CB1954 reduction products* λ_{max} *= 420 nm.*

Figure 5.12 plots absorbance vs time at 420 nm over the course of the 10 minute activity assay. The plot shows that the reaction only proceeds lineraly the 1st 1-2 minutes of the reaction. Therefore to determine the kinetic properties of the Au-MNP-YfkO-cys conjugate the measurements will need to be conducted as close to the addition of prodrug as possible.

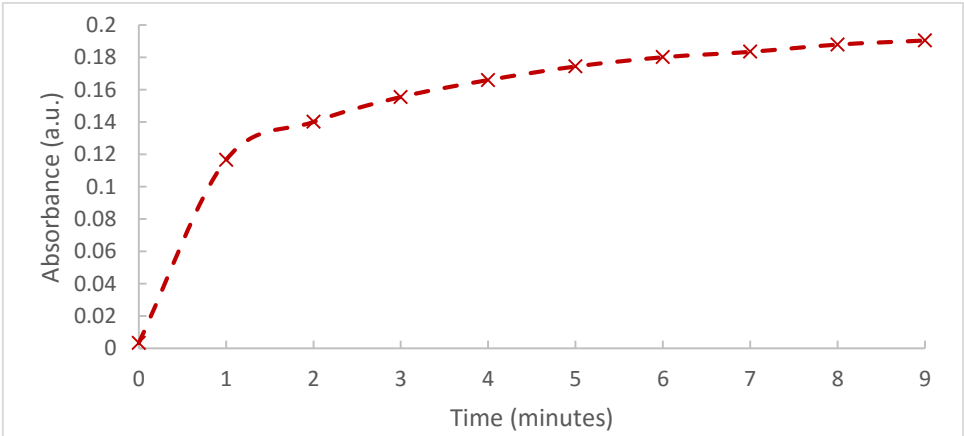

Figure 5.12 Plot of absorbance at 420 nm vs time for Au-MNP-YfkO-cys, CB1954 (100 µM), NADH (600 µM) and PB (50 mM, pH 7.4).

The activity of a cysteine tagged genetically modified NTR immobilised onto a synthesised gold coated magnetic nanoparticle was performed for what is believed to be the first time, seen in Figure 5.11. The increase in absorbance at 420 nm (Peak 4) can be used to determine the kinetic parameters of the conjugate to allow comparison between enzymes free in solution, gold colloid immobilised enzyme conjugate and the gold magnetic nanoparticle immobilised NTR conjugate. The increase in absorbance at peak 4 indicates the production of the cytotoxic hydroxylamine derivatives of the prodrug CB1954. This indication of activity allows the progress of the Au-MNP-NTR immobilised conjugate system to be moved forward for further testing to determine the kinetics of the system and also the cell viability. The ability of the genetically modified NTR to retain activity towards reducing the prodrug CB1954 after immobilisation onto a gold coated magnetic nanoparticle is a huge breakthrough in the possibility of forming a working MNDEPT treatment.

5.3 Enzymatic kinetics of immobilised nitroreductases

To calculate the K_m and V_{max} of immobilised NTR conjugates the kinetic enzymatic activity was measured at various increasing concentrations of CB1954 as detailed in section 2.5.4. All kinetic experiments were conducted in triplicate and the average was plotted and analysed.

5.3.1 Kinetics of Au colloid immobilised NfsB-cys

The kinetic parameters for the Au-colloid immobilised NfsB-cys were determined using the protocol laid out in section 2.5.4, in brief the cys tagged enzyme was conjugated to a 50 nm Au colloid for 1 hr at 25°C at a ratio of 270:1 as previously determined by Gwenin *et al.*[15]

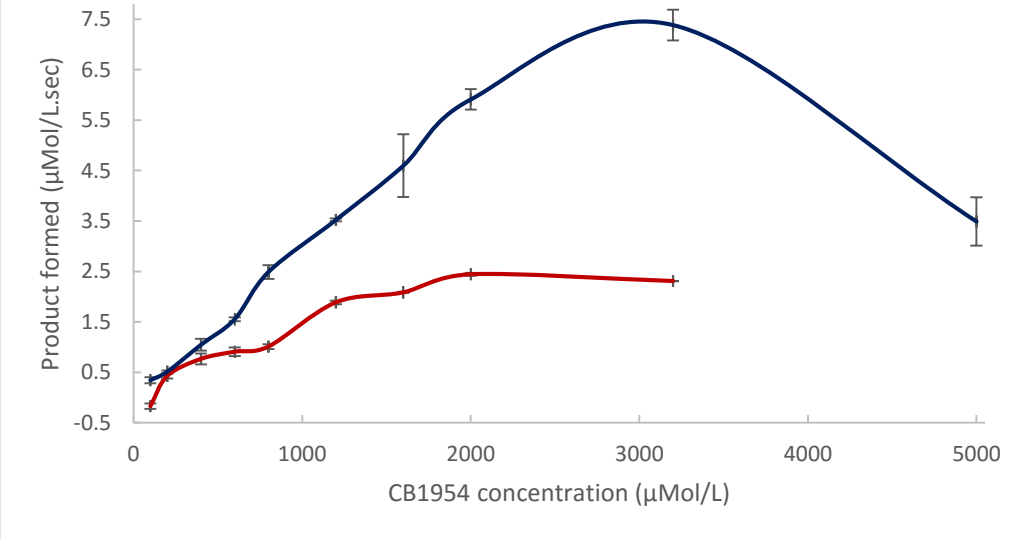

Figure 5.13 A graph quantifying the rate of the hydroxylamine reduced prodrug derivative formation. (λ_{max} = 420 nm, ε = 1200 L mol^{-1}cm^{-1}) for the gold colloid immobilised NfsB-*cys conjugate (red line) and non-immobilised* NfsB-*cys (blue line) at increasing CB1954 concentrations. The error bars represent ± 1 SD.*

Figure 5.13 shows the rate of reaction increases with increasing concentration of CB1954 until the reaction reaches its V_{max}. The overall rate increases until the plateau at V_{max} however the increase is not an entirely linear increase as has come to be expected from some of the other NTR kinetic determinations. The plateau at V_{max} also occurs at much lower concentrations for the gold colloid immobilised enzyme and therefore further testing with higher concentrations is not required. The kinetics are discussed in further detail and comparison between the immobilised enzyme conjugates is conducted in 5.3.4 along with comparison to the NTRs free in solution. Figure 5.13 does show that the NfsB-cys free in solution retains a higher formation of product compared to the Au-colloid immobilised NfsB-cys. The immobilised enzyme does exhibit a faster increase in turnover but an overall decreased product formation.

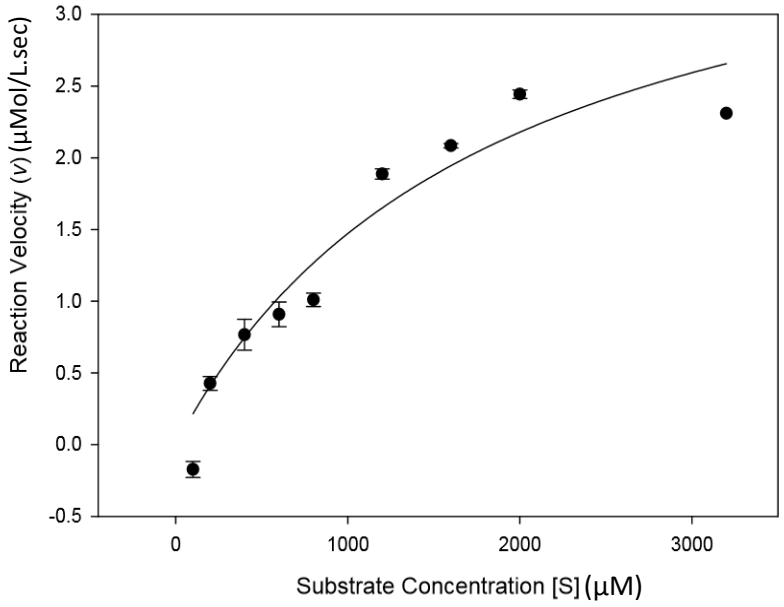

Figure 5.14 Michaelis-Menten hyperbolic curve obtained from Sigmaplot® showing the rate of the hydroxylamine reduced prodrug derivative formation. (λ_{max} = 420 nm, ε = 1200 L mol^{-1}cm^{-1}) for the gold colloid immobilised NfsB-cys conjugate at increasing CB1954 concentrations. Error bars represent standard error of standard error of estimate.

The data obtained for kinetic analysis of the Au-NfsB-cys conjugate is subjected to non-linear regression fitting to a hyperbolic curve in Sigmaplot®; see Figure 5.14. The R^2 value obtained from the data analysed to produce the hyperbolic curve was 0.92. This value falls below the standard required range of >0.97. The reason for the variance in fit of the data to the hyperbolic curve can be explained by difficulty in measuring the true initial rate of reaction. The microtiter plate assay used to determine the data is difficult to execute in a short time frame and takes approximately 30-60s to prepare the plate from start to finish. The reaction occurs at a linear rate for at least the first 30s of the reaction, see Figure 5.15 with the desired difference observed being 5-25s, this is however possibly more realistically 35-65s accounting for the setup time of the assay.

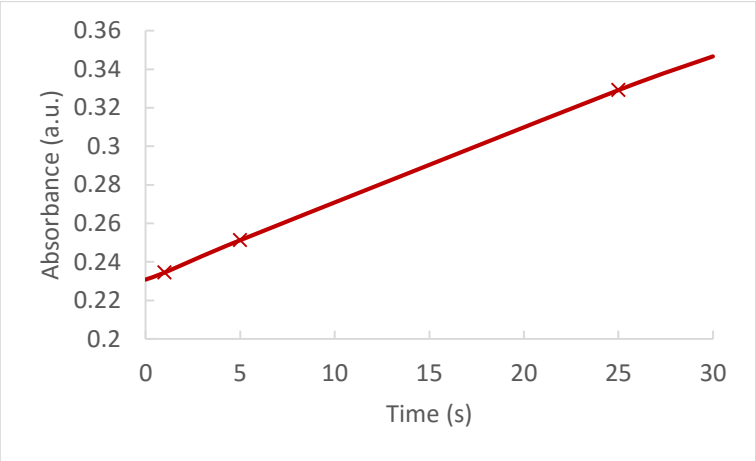

Figure 5.15 Plot of absorbance at 420 nm vs time for Au-NfsB-cys, CB1954 (1 mM), NADH (4 mM) and PB (50 mM, pH 7.4).

The plot of absorbance at 420 nm vs time for Au-NfsB-cys is shown in Figure 5.15. It shows that over the first 30 secs the reaction was measured the assay remains linear as such the formation of the hydroxylamine reduced prodrug products are defined during the difference between 5-25 seconds. The most likely cause for errors in the measurement is the initial set-up time required to perform the assay this will in turn affect the tightness of fit for the data to the hyperbolic curve. This could be solved in future experiments using a more automated procedure; therefore, decreasing the setup time, which cannot be realistically reduced any further using a manual setup.

5.3.2 Kinetics of Au colloid immobilised YfkO-cys

Following the same procedure for that of the NfsB-cys Au-colloid immobilised NTR, YfkO-cys underwent determination of its kinetic parameters.

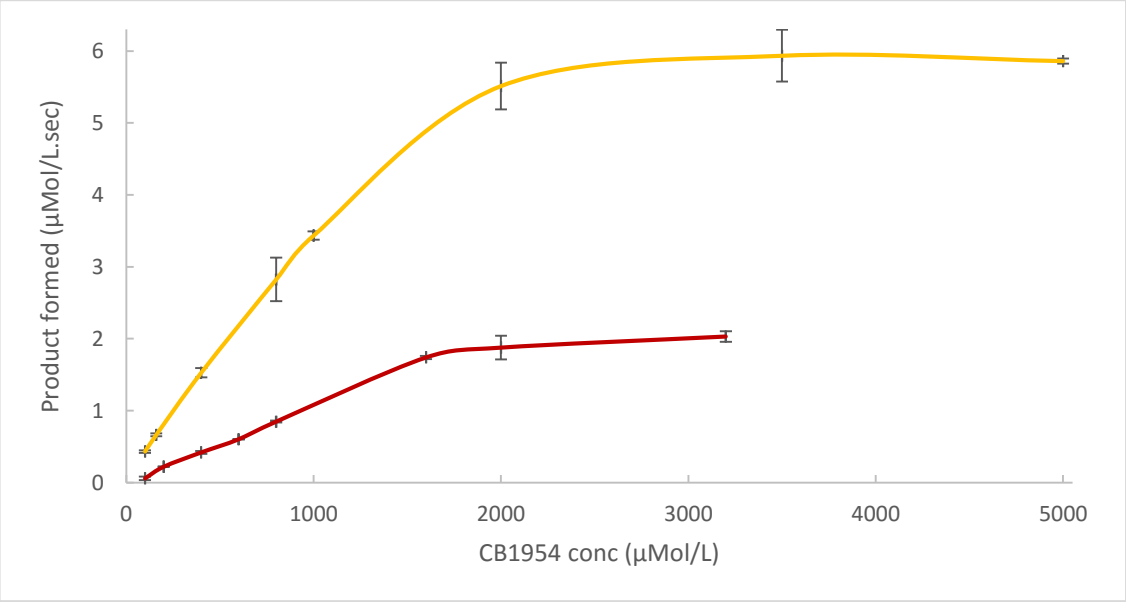

Figure 5.16 A graph quantifying the rate of the hydroxylamine reduced prodrug derivative formation. (λ_{max} = 420 nm, ε = 1200 L mol^{-1}cm^{-1}) for the gold colloid immobilised YfkO-cys *conjugate (red line) and the non-immobilised YfkO-cys (yellow line) at increasing CB1954 concentrations. Error bars represent ± 1 SD.*

Figure 5.16 shows the rate of reaction increases with increasing concentration of CB1954 until the reaction reaches its V_{max}. The increase is almost linear up until the point the kinetic reactions reach V_{max}. The reaction is conducted to a lower concentration for the gold colloid immobilised conjugate due to it reaching the V_{max} at a lower concentration, once the plateau is achieved the use of higher concentrations of prodrug is not required. The kinetics are discussed in further detail and comparison between the immobilised enzyme conjugates is conducted in 5.3.4 along with comparison to the NTRs free in solution.

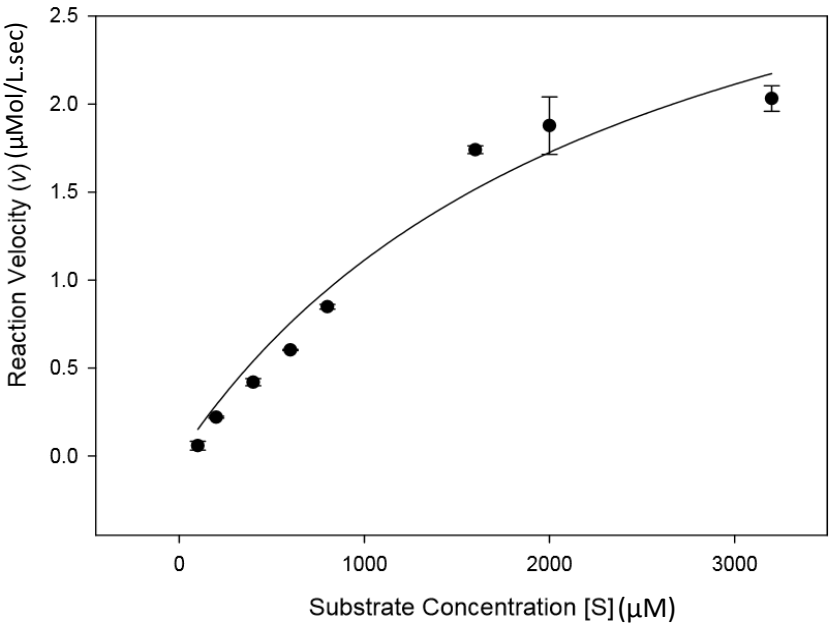

Figure 5.17 Michaelis-Menten hyperbolic curve obtained from Sigmaplot® showing the rate of the hydroxylamine reduced prodrug derivative formation. (λ_{max} = 420 nm, ε = 1200 L mol^{-1}cm^{-1}) for the gold colloid immobilised YfkO-cys conjugate at increasing CB1954 concentrations. Error bars represent

The data obtained for kinetic analysis of the Au-YfkO-cys conjugate is subjected to non-linear regression fitting to a hyperbolic curve in Sigmaplot®; see Figure 5.17. After fitting to the curve an R^2 value is determined to note how tight the fit of the data is to the hyperbolic curve. The R^2 obtained from the data produced and analysed for the Au-YfkO-cys conjugate was 0.96. This value falls just below the standard required range of >0.97. The reason for the variance in fit of the data to the hyperbolic curve can be explained by difficulty in measuring the true initial rate of reaction. The microtiter plate assay used to determine the data is difficult to execute in a short time frame. The reaction only proceeds linearly for approximately 1-2 minutes based on the absorbance vs time plot for the activity assay, see Figure 5.8 and defined definitively for the first 30s, see Figure 5.18. This means that to obtain a truly accurate account of the enzyme kinetics the difference in absorbance observed between 5-25 is very important and any delay due to the setup of the assay could account for an increase in error of the measurements.

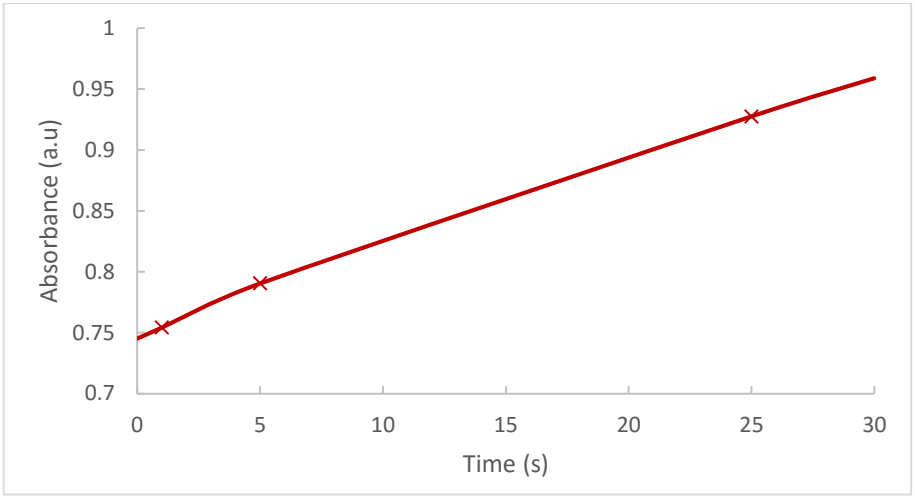

Figure 5.18 Plot of absorbance at 420 nm vs time for Au-YfkO-cys, CB1954 (1 mM), NADH (4 mM) and PB (50 mM, pH 7.4).

5.3.3 Kinetics of Au-MNP immobilised YfkO-cys

Following kinetic determination procedure detailed in section 2.5.4, synthesised Au-MNPs ~50 nm in size were conjugated with cys-tagged YfkO. This was prepared conjugating the YfkO to the synthesised Au-MNPs in a ratio of 270:1 and was tested against increasing concentrations of the prodrug CB1954. This is believed to be the first reported data on an NTR-Au-MNP immobilised conjugate system.

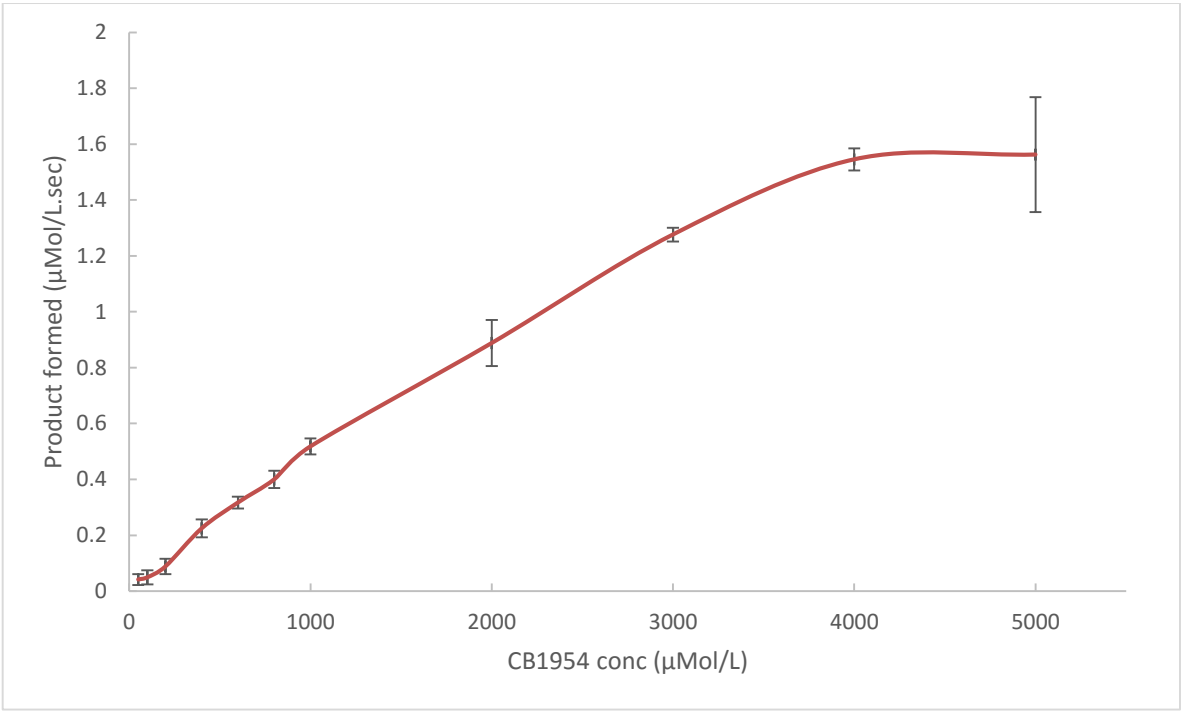

Figure 5.19 A graph quantifying the rate of the hydroxylamine reduced prodrug derivative formation. (λ_{max} = 420 nm, ε = 1200 L mol^{-1}cm^{-1}) for the Au-MNP immobilised YfkO-cys *conjugate at increasing CB1954 concentrations. The error bars represent ± 1 SD.*

Figure 5.19 shows the rate of reaction increases with increasing concentration of CB1954 until the reaction reaches its V_{max}. The gold magnetic nanoparticle conjugated YfkO-cys has a higher K_m than the enzyme free in solution or immobilised onto the gold colloid. And also reaches V_{max} slower, this is signified by the shallower slope of the graph. The Au-MNP-NTR immobilised conjugate requires a higher concentration of prodrug to complete its reaction. The kinetics are discussed in further detail and comparison between the immobilised enzyme conjugates is conducted in 5.3.4 on the following page, along with comparison to the NTRs free in solution.

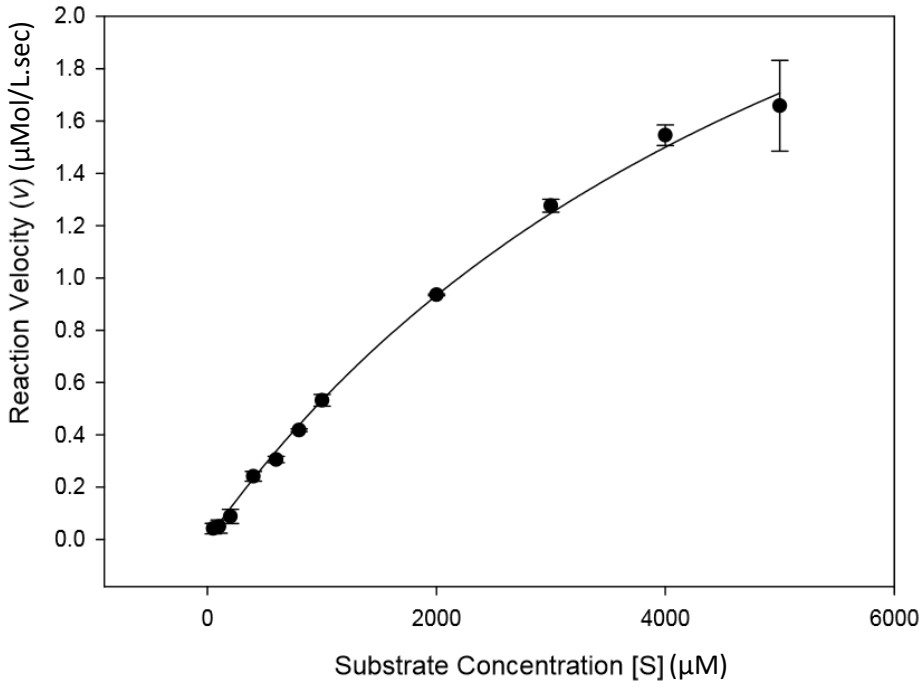

Figure 5.20 Michaelis-Menten hyperbolic curve obtained from Sigmaplot® showing the rate of the hydroxylamine reduced prodrug derivative formation. (λ_{max} = 420 nm, ε = 1200 L mol^{-1}cm^{-1}) for the Au-MNP immobilised YfkO-cys conjugate at increasing CB1954 concentrations. Error bars represent standard error of estimate.

The data obtained for kinetic analysis of the Au- MNP-YfkO-cys conjugate is subjected to non-linear regression fitting to a hyperbolic curve in Sigmaplot®; see Figure 5.20. The R^2 value obtained from the data analysed to produce the hyperbolic curve was 0.97. At this value the correlation and tightness of the data fit to the model is in line with the standard required range of >0.97. The data set could be tightened further by decreasing the setup time of the assay which would lead to a more accurate determination of the enzyme conjugate kinetic parameters for the variance in fit of the data to the hyperbolic curve can be explained by difficulty in measuring the true initial rate of reaction. The reaction does occur at a linear rate for at least the first 30s of the reaction, see Figure 5.21 with the plot taken during the activity assay, Figure 5.12 showing that this linearity last until approximately 2 minutes.

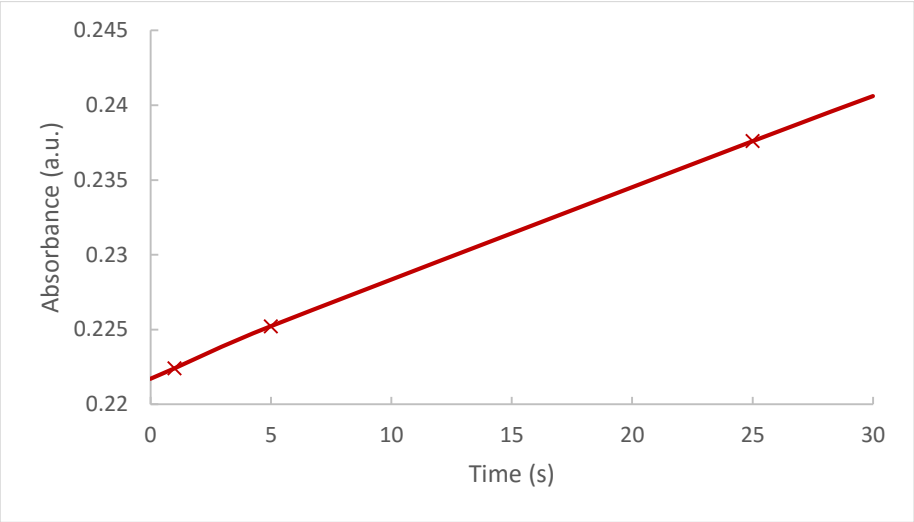

Figure 5.21 Plot of absorbance at 420 nm vs time for Au-MNP-YfkO-cys (10 µg/mL), CB1954 (1 mM), NADH (4 mM) and PB (50 mM, pH 7.4).

5.3.4 Comparison of immobilised kinetics

Each of the cys tagged NfsB and YfkO NTRs immobilised to the gold colloid and the gold magnetic nanoparticle immobilised YfkO-cys conjugate were able to reduce the prodrug CB1954 to its hydroxylamine derivatives. Kinetic enzymatic assays were conducted as per section 2.5.4 and the results shown in sections 5.3.1, 5.3.2 and 5.3.3 respectively. An overview of the data obtained from both the kinetic enzyme activity scans and the pH and temperature profiling for all of the immobilised enzyme conjugates and enzymes in this study can be seen summarised in Table 5.1.

Table 5.1 Kinetic parameters and optimum conditions of the four NTRs NfsB-*his*, NfsB-*cys*, YfkO-*his and* YfkO-*cys with CB1954.*

NTR	**V_{max}** ($\mu molL^{-1}s^{-1}$)	**Std Error**	**K_m** ($\mu molL^{-1}$)	**Std Error**	**k_{cat}** (s^{-1})	**k_{cat}/K_m** ($M^{-1}s^{-1}$)	**pH**	**Temp.** (°C)
YfkO-his	9.96	0.94	3767.87	619.71	59.24	15,723	7.50	45.0
YfkO-cys	7.69	0.47	1179.19	218.25	46.72	39,624	7.50	37.5
Au-YfkO-cys	4.20	0.56	2933.33	653.31	24.06	8,202	7.5	37.5-47.5
Au-MNP-YfkO-cys	3.42	0.43	5755.30	1147.48	58.01	10,080	ND	ND
NfsB-his	22.90	7.01	4064.43	1660.87	125.77	30,943	7.25	34.0
NfsB-cys	15.75	1.01	3882.29	566.08	88.52	22,800	7.50	30.0-50.0
Au-NfsB-cys	4.19	0.52	1853.05	435.77	4.61	2,488	4.00-11.00	20.0-50.0

It was assumed that the immobilisation of NTR to Au colloid/Au-MNP had a coupling efficiency of 100%, reduction in k_{cat} that can be observed for the conjugated NTRs could be explained by this coupling efficiency being lower than the assumed 100%, meaning less NTR is bound to the surface of the colloid/Au-MNP than theorised.

The genetic modification of the NTRs with a sequence of 12 consecutive cysteine residues decreases the enzyme activity towards the prodrug CB1954. For both NfsB and YfkO the V_{max} which is an indicator of the maximum rate that can be achieved by the system, is lower for the modified enzymes and the immobilised modified enzyme conjugates.

Figure 5.22-Figure 5.24 respectively, depict the K_m, V_{max} and k_{cat}/K_m values for each of the NTRs, the Au-colloid immobilised NTRs and the Au-MNP immobilised NTR. There is a distinct decrease in V_{max}, seen in Figure 5.22, moving from the his tagged NTRs through to the cys tagged and then onto the Au-colloid immobilised and Au-MNP immobilised NTRs.

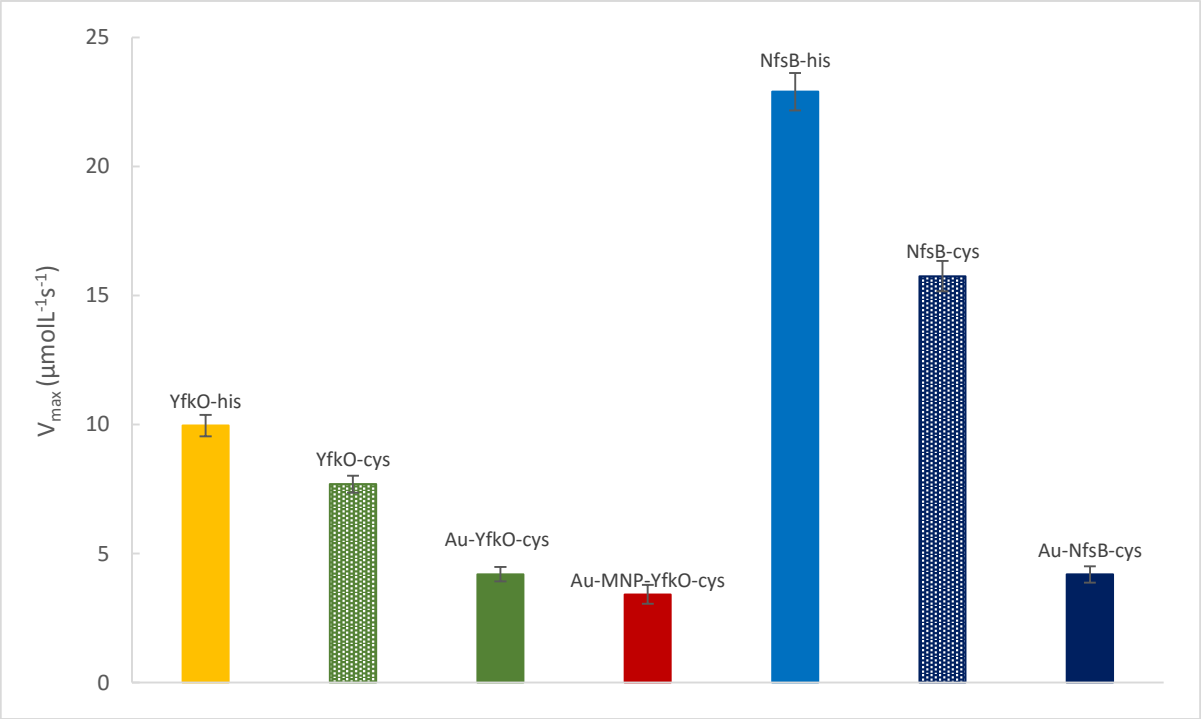

Figure 5.22 A bar chart illustrating the rate of reaction (V_{max}) for the four studied NTRs and the immobilised enzyme conjugates; Au-NfsB-cys (solid dark blue), NfsB-cys (dashed dark blue), NfsB-his (solid light blue), Au-MNP-YfkO-cys (solid red), Au-YfkO-cys (solid green) YfkO-cys (dashed green) and YfkO-his (solid yellow). Error bars represent standard error.

For all the cysteine modified enzymes their K_m (Figure 5.23) and k_{cat}/K_m (Figure 5.24) show improved activity towards CB1954. They exhibit a lower K_m meaning the concentration of substrate needed for the enzyme reaction to reach half the maximum rate of the system. The specificity constant k_{cat}/K_m indicates that for the cysteine tagged modified enzymes the specificity increases allowing them more effectively reduce the prodrug CB1954.

The reaction rates for all of the his and cys NTRs along with the gold colloid and gold magnetic nanoparticle immobilised NTR conjugates varies significantly. NfsB-his displays the fastest

reaction rate, this is indicated by it having the highest k_{cat} value. YfkO-cys displays the highest k_{cat}/K_m value, seen in Figure 5.24 indicating it has the highest specificity.

The gold colloid immobilised cysteine tagged NTRs display lower activity towards the prodrug CB1954, this may be due to the orientation in which the enzyme binds to the surface of the gold colloid nanoparticle. The gold coated magnetic nanoparticle immobilised YfkO-cys shows an increase in both reaction rate and specificity compared to the gold colloid immobilised YfkO-cys; but also displays a higher K_m value indicating it requires a higher concentration to reach its half V_{max} and exhibits a lower V_{max} rate than both the free in solution NTRs and gold colloid immobilised NTR.

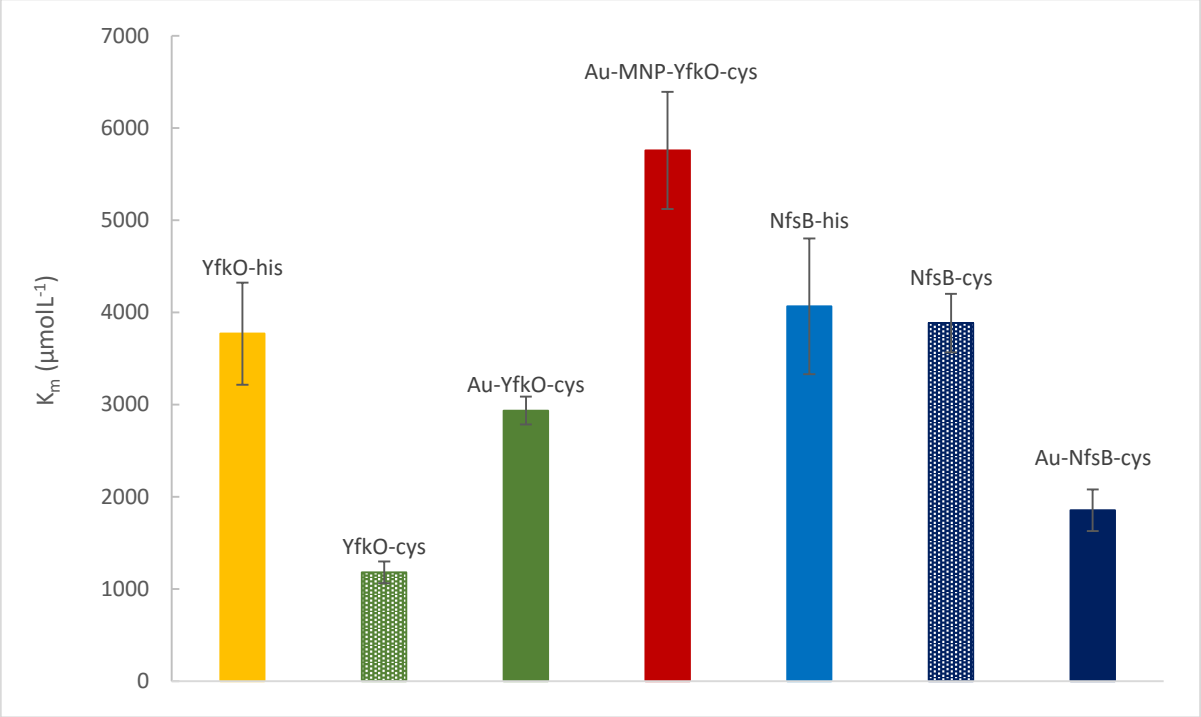

Figure 5.23 A bar chart illustrating the Michaelis constant (K_m) for the four studied NTRs and the immobilised enzyme conjugates; Au-NfsB-cys (solid dark blue), NfsB-cys (dashed dark blue), NfsB-his (solid light blue), Au-MNP-YfkO-cys (solid red), Au-YfkO-cys (solid green) YfkO-cys (dashed green) and YfkO-his (solid yellow). Error bars represent standard error.

k_{cat}/K_m seen in Figure 5.24, can often be referred to as catalytic efficiency and is considered the best indicator of activity of the NTRs to the prodrug as it is independent of cofactor concentration.[307] The disadvantages of using K_m and k_{cat} can be that they are difficult to reliably obtain due to the limited solubility of CB1954. This results in an increase in the difficulty of testing the activity past initial rates.

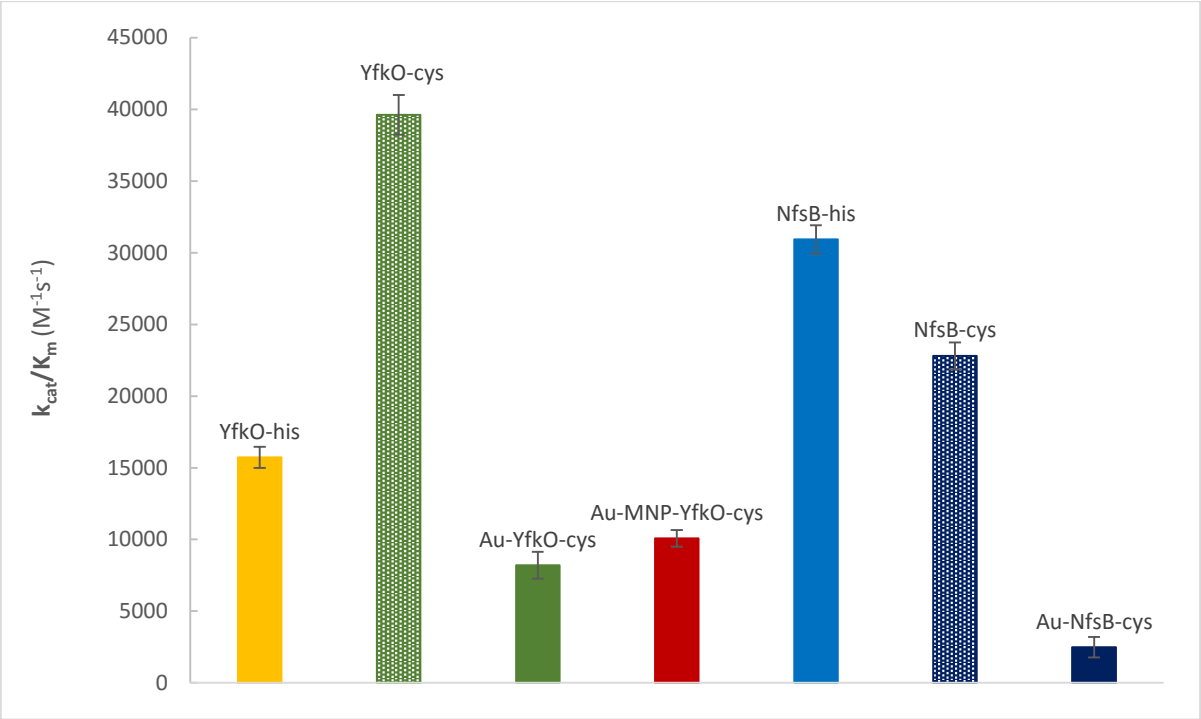

Figure 5.24 A bar chart illustrating the k_{cat}/K_m specificity constant for the four studied NTRs and the immobilised enzyme conjugates; Au-NfsB-cys *(solid dark blue),* NfsB-cys *(dashed dark blue),* NfsB-his *(solid light blue),* Au-MNP-YfkO-cys *(solid red),* Au-YfkO-cys *(solid green)* YfkO-cys *(dashed green) and* YfkO-his *(solid yellow). Error bars represent standard error.*

The predicted concentrations needed for the prodrug therapy treatment for its use in clinical applications are very low.[127,128] This reinforces that comparison of the specificity constant is the most reliable measure of the kinetic activity for comparison of the different NTRs.[308] The specificity observed for the immobilised enzyme conjugates shows a significant decrease compared to the enzyme free in solution. This could be affected for many reasons, in the case of the Au-MNP immobilised conjugate it is most likely due to the enzyme not being able to form a complete monolayer around the particle due to it only being partially coated. This partial coating can decrease the overall concentration of enzyme present on the surface of the particle but can also lead to non-optimal orientation of the enzymes meaning the active site where the prodrug reaction occurs could be obscured from the reaction.[308]

5.4 Cell Viability

5.4.1 Setup, design and implementation of cell culture facilities

Part of the aim in this project was to setup the first specialised cell culture laboratory to be situated in the School of Chemistry at Bangor University, see Figure 5.25. There was no provision of service for cell culture work to be carried out at the school prior to this project. The laboratory space was acquired once adequate funding was obtained and then the laboratory space was upgraded to comply with Class II regulations and the equipment needed to run a cell culture lab was procured. The facilities that are now available as the result of work from this study have enabled the cell viability work to be conducted in a more controlled environment. With any setup and implantation of a laboratory space such as this, the importance of setting up and preforming experiments to obtain a standardised protocol that could be used by multiple users to obtain results with minimal variation was paramount. After the lab setup was completed and the laboratory commissioned, a lengthy set of experimentations were conducted before the final viability assay protocol, reportable experimentation and data was finally achieved.

Figure 5.25 Bangor School of Chemistry Cell Culture Laboratory after final commission

5.4.2 Viability assay introduction

In order to test the efficiency of the NTR/CB1954 system in cell lines the MTT assay was performed following the method of derived by Mosmann, 1983 with slight modification.[299] The MTT assay works by the reduction of the tetrazolium dye 3-(4,5-dimethylthiazol-2-yl) -2,5-diphenyltetrazolium bromide (MTT) to its insoluble (*E,Z*)-5-(4,5-dimethylthiazol-2yl) -1,3-diphenylformazan (formazan) product, see Figure 5.26.[299]

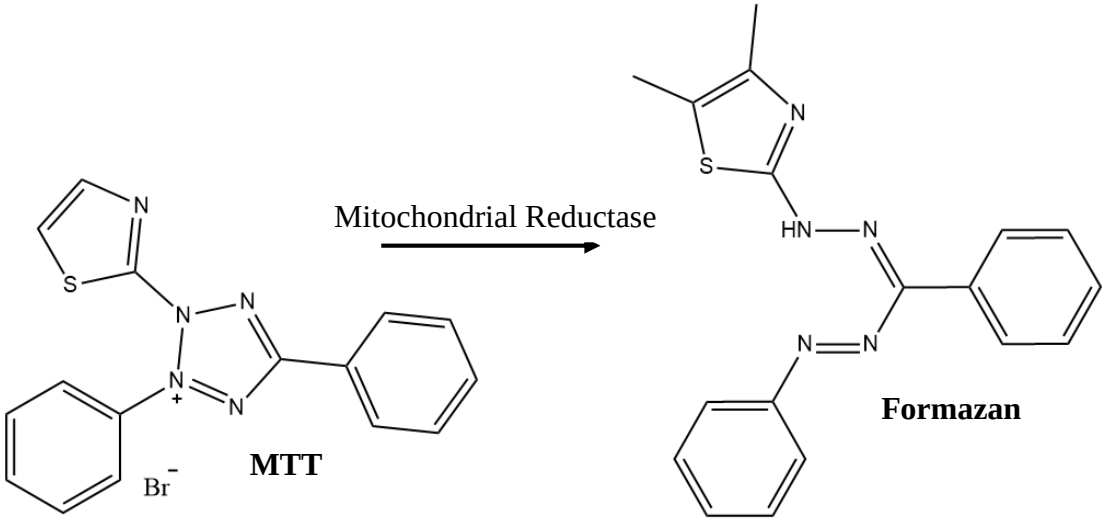

Figure 5.26 The formation of formazan from MTT in response to living cells.

The absorbance of the formazan product formed can be measured by dissolving it in DMSO and the resulting purple coloured solution can be quantified at 570 nm using a spectrophotometer.[320] The assay can be used to determine the degree of living cells, this is due to the active metabolism of cells converting the MTT to formazan. When cells die they no longer possess the ability to covert MTT to formazan. Therefore, the colour formation can serve as a useful marker for viable cells.[320] This can then be in turn used to determine the % of cell survival when compared to a non-treated cell line control.

In brief, the cells were seeded at a density of $1x10^4$ cells per well, in 100 µl DMEM medium containing 10% FBS and were allowed to attach overnight in a CO_2 incubator. After aspirating off the media carefully, 50 µl of the media containing CB1954 (10 µM) was added to the 96-well plate. To that 50 µl of media containing various concentrations of NTR (25-200 nM) was added to the plate. After 4 hours, the media was aspirated and the cells were replenished with 100 µl of complete media. After being incubated for 48 hours (37°C, 5% CO_2), 20 µl of MTT (5 mg/ml) was added to each well and the plate incubated for a further 4 hours (37°C, 5% CO_2). The purple formazan crystals formed were dissolved in 100 µl of DMSO after aspirating the media carefully and the 96-well plate was read at 570 nm in a 96-well plate microplate reader (Thermo Scientific Varioskan, USA).

5.4.3 Determination NfsB-cys cell viability

The cell viability MTT assay was conducted using the NTR NfsB-cys. The concentration of NTR was varied in the assay with a range from 25 nM to 200 nM. The concentration of NADH was kept constant at 200 µM alongside a constant concentration of the prodrug CB1954 (10 µM). The assay was also conducted using a set of MCF-7 cells treated only with NfsB-cys (200 nM) as a control alongside cells treated only with prodrug (10 µM). The cell viability assay was conducted using the methodology defined in section 2.7.4. The results were than analysed and normalised such that the control; which consisted of only cells in untreated growth media, were classed at 100% viability. Figure 5.27 below, shows the result of conducting the MTT assay. As the concentration of NTR increases up to 200 nM the percentage of remaining viable cells decreases to ~20%, this means when using the combination treatment at set concentrations of 200 µM NADH, 10 µM CB1954 and 200 nM NfsB-cys the treatment has an ~80% efficiency towards exhibiting a cytotoxic response and killing the cell line. In this assay additional controls were conducting using NfsB-cys alone without the presence of prodrug and NADH and also prodrug alone with the presence of NTR and NADH.

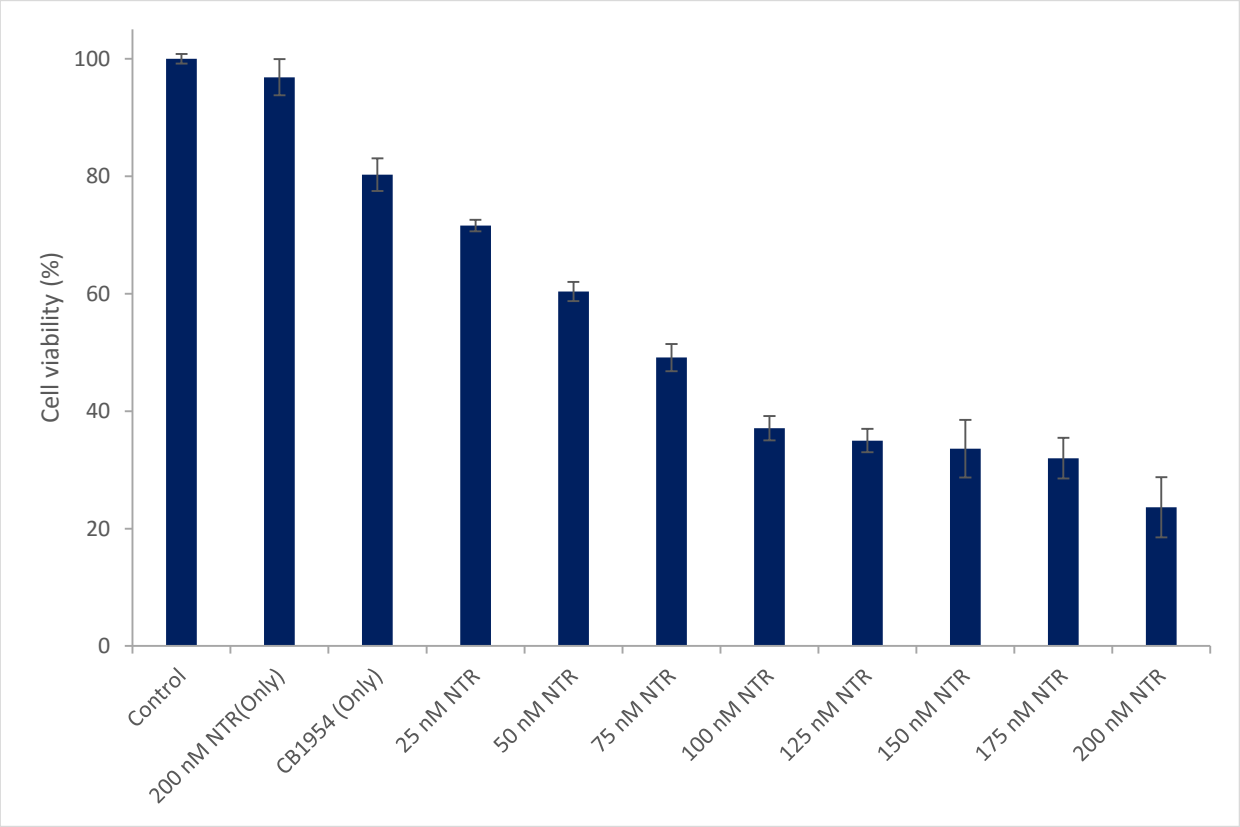

Figure 5.27 NfsB-cys in varying concentrations (25-200 nM) with CB1954 (10 µM) and NADH (200 µM) MTT cell viability assay results, Error bars represent standard error of the mean (SEM).

In the NfsB-cys alone control the cell viability measured 96% and within error it can be classed as 100 %, this means that when treated with NTR alone there is no cytotoxic response and the cells continue to grow unaffected. The control using the prodrug alone at a concentration of 10 μM, there was limited cell death; ~20% with the cells retaining 80% viability. This was most likely caused by the reagent used to dissolve the prodrug in solution. The solvent used was DMSO and it has been reported that at concentrations greater than 5% it has a significant effect on inducing cell death.[321] Due to this all prodrug solutions were diluted to ensure they contained less than 5% DMSO.

5.5 Concluding remarks

Cyclic voltammetry reveals that each of the two candidate cysteine tagged genetically modified NTRs bond to an Au surface *via* Au-S bonds. The bonding is such that naturally occurring cysteine residues throughout the enzyme are not involved in the immobilisation process meaning the enzyme binds with controlled orientation.

The immobilisation of enzymes onto nanoparticles typically improves the activity and stability of the enzymes.[322,323] However the nature of the immobilising bonds are critical to the effects to the enzymes kinetic properties.[324] It was hoped that by introducing a preferential cysteine immobilising sequence outside of the native NTR structure there would be a reduction in non-controlled immobilisation which could lead to limited accessibility of the active site. For MNDEPT it is important the enzyme orientation is controlled and a surface monolayer forms over the nanoparticles. The combination of a cysteine tag residue sequence introduced into the NTRs coupled with a gold coated surface modification of the magnetic nanoparticles, could provide a route to a controlled and complete surface monolayer formation of NTR on the Au-MNPs *via* Au-S self-assembly. For a true comparison to be made between the immobilised enzyme conjugates and the enzymes free in solution further quantification of the amount of enzyme bound to the Au colloid/Au-MNPs needs to be conducted; it may be possible to qualitatively define the amount of enzyme bound by testing the supernatant decanted from the conjugation mixture after magnetic separation. The concentration remaining in the supernatant could be deduced from the original concentration of enzyme added to the conjugation mixture and the total from this subtraction would determine the amount bound to the particles.

The viability assay conducted using a varying concentration of NTR showed that in a combination treatment using 10 μM CB1954 and NADH the reduction in cell viability was significant. Using concentrations of ≥ 100 nM NfsB-cys the cell viability was decreased to

below 40%, and when using a concentration of 200 nM the reduction in viability was reduced two fold to ~20%. Following the trend shown when assessing varying concentrations of NfsB-cys it could be predicted that a further increase in NTR concentration to > 200 nM could further decrease the cell viability to under 20%. This would prove advantageous as it would not require the increase of concentration for the CB1954 dosage applied to the treatment. At higher concentrations of CB1954 there is greater potential for adverse side effects to be observed.

The advantage of the combination system using NADH as the cofactor in the reduction of the prodrug to its cytotoxic derivatives is that this compound is found intracellularly within the human body. This helps to increase the safety of the system.[325]

The promise shown by the combination treatment with higher NTR concentrations paves the way for its within an MNDEPT system, aided in the system by the NTRs being conjugated to the MNPs in a 270:1 ratio which will allow for greater concentration of NTR in the treatment.

Chapter 6

Conclusions and Future Work

6. General Conclusions

6.1 Conclusion

Four NTRs were successfully grown from the recombinant plasmid pet28a; NfsB-his, NfsB-cys, YfkO-his and YfkO-cys. The NTRs were then subjected to protein expression, purification, and the enzymatic activity and kinetics were determined. The cys-tagged NTRs underwent immobilisation to a standard Au colloid and the YfkO-cys was also then immobilised to synthesised Au-MNPs. Cyclic voltammetry was conducted on the cys-tagged NTRs and allowed the conclusion that the cysteine tags on the modified NTRs are still present after expression. The presence of the cys tags enables the NTRs to undergo immobilisation *via* self-assembly to the gold surfaces of the colloid and the Au-MNPs *via* Au-S thiol bonds.

UV/Visible spectroscopy was carried out and confirms that the NTRs are active when reacted with a cofactor and prodrug and that it retains this activity after successful immobilisation onto Au colloid and Au-MNP. The kinetics of both the NTRs and the Au colloid immobilised NTRs were tested and proved that the Au colloid bound NTR still retains activity when compared to the enzyme free in solution. The kinetics of YfkO-cys bound to the Au-MNPs was successfully determined and demonstrated that the NTR-Au-MNP conjugate still retained activity towards the prodrug CB1954; this is believed to be the first report into the kinetic properties of an NTR-Au-MNP conjugate.

The Au-MNPs were successfully synthesised and the desired size of ~50 nm; the aim at the start of the project, has been achieved with both the pre-seeding method and the modified methodology, see table 6.1. The modified method has allowed the Au-MNPs to be synthesised with a more spherical morphology, due to a more prevalent coating. This will need further optimisation to achieve a commercially viable synthesis.

Table 6.1 Overview of synthesised Au-MNP sizes

Synthesis	Average size (nm)	Distribution (nm)
Au-MNP synthesis (4.3)	58	± 24
Modified Au-MNP synthesis (4.4)	47	± 14

The Au-MNPs were analysed using UV/Visible spectroscopy (Figure 6.1) and when compared to a 50 nm Au colloid standard the Au-MNPs synthesised using the modified synthesis show similar characteristics and it can be concluded that along with the size analysis data that the Au-MNPs synthesised are ~50 nm in size and have a predominate gold coating.

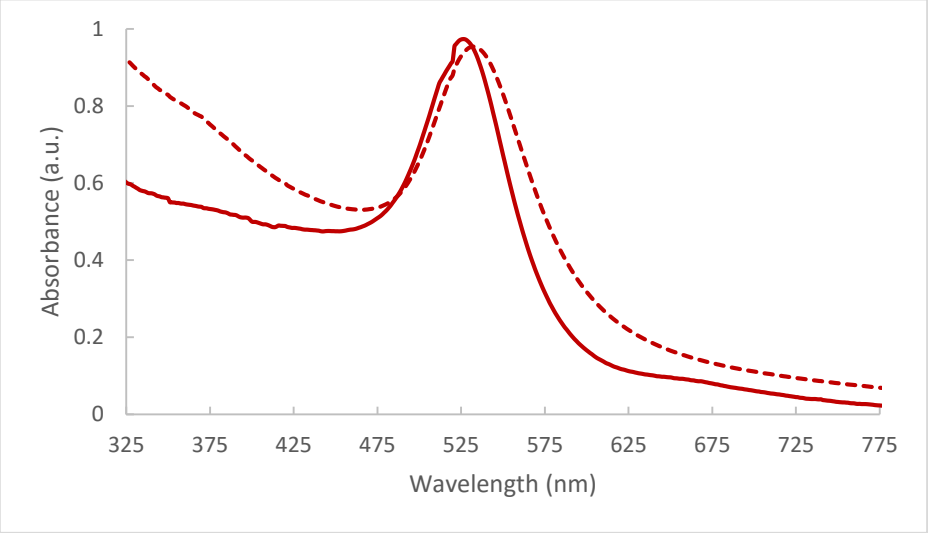

Figure 6.1 UV/Visible spectra comparing the synthesised Au-MNPs (dashed red line) to a 50 nm Au colloid standard (solid red line)

The procurement and setup of a Class II cell culture laboratory was achieved within this project, with the design and procurement of the equipment needed before its final commission which was a lengthy process. The laboratory space was converted to ensure all guidelines were met and then laboratory was commissioned for use by the University's biological health and safety department. This meant that Bangor University's School of Chemistry had its very first working cell culture laboratory enabling cell viability assays to be conducted. A lengthy set of protocol and parameter defining experimentation was carried out alongside the inevitable teething problems a new laboratory setup can incur.

The initial cell viability assays for the NfsB-cys NTR free in solution have been conducted using the MTT assay. Initial results show that the NTR free in solution in combination with the prodrug CB1954 (10 µM) and NADH (200 µM) exhibit a toxicity toward the cell lines with an ~50 % efficiency and this can be tuned to ~80 % using higher concentrations of enzyme. This leads a path to the investigation and screening of a wide range of modified NTRs and also to determine the optimum parameters for the treatment; with the concentration of prodrug and NTR being the main focus. The experimentation using Au-MNP-NTR immobilised conjugates for cell viability has not been carried out but it is believed that with the conjugates immobilised in a 270:1 ratio this should allow for increased NTR concentration and directed control with the

Au-MNP core. The initial aims of the project were to be able to successfully retain enzyme activity for a cys-tagged modified NTR that was immobilised onto a spherical 50 nm Au-MNP and for this to induce the formation of a cytotoxic reduction product from a prodrug. The retention of activity and production of ~ 50 nm Au-MNPs were achieved, however due to time constraints and experimental problems the investigation into the cell viability of the MNDEPT system against cell lines *in vitro* was not achieved. The successful retention of enzymatic activity for the cysteine modified NTRs has advanced the study of the proposed MNDEPT system forward and hopefully the next stage of determining the viability of the therapy *in vitro* can prove successful and help to determine the optimum parameters of the system that will enable it to be adapted to further investigation such trials with a mice model.

6.2 Future Work

This study has laid a foundation on which the further development of a viable MNDEPT system can be investigated. To continue this research there needs to be further determination of an optimum Au-MNP synthesis. The optimisation of this synthesis is paramount for research purposes and in liaison with industrial and commercial partnerships implementation of a viable synthesis that can be easily scaled and minimise costs is aimed to be obtained. To aid in the determination of an optimised synthesis there needs to be more in depth characterisation conducted on the Au-MNPs. Any changes to the synthesis will warrant the need for further particle size analysis and also composition of the particles needs to be fully identified, this can be achieved using techniques such as TEM, XRD and SEM/EDAX. There is also a need for quantitative analysis of the magnetic properties of the Au-MNPs, these have shown superparamagnetic behaviour at an observation stage but investigation into the exact magnetic properties and strength of magnetism needs to be determined. This can be done using techniques such as using a vibrating sample magnetometer (VSM) or with a superconducting quantum interference device (SQUID). XRD or SEM needs to be conducted on the Au-MNPs to confirm sole presence of gold and no residual iron to conclusively quantify full surface coverage and successful separation of the Au-MNPs from the reaction synthesis.

The cell viability work needs to be continued with a larger bank of modified NTRs to be screened and the optimal concentrations of all components in the combination treatment need to be investigated and defined. Following the screening of a wide range of modified NTRs the cell viability of the corresponding Au-MNP-NTR immobilised conjugates needs to be

investigated and again the concentrations and ratio of the components of the combination treatment need to be quantified. A control experiment comparing the immobilised particle conjugates to both Au-MNPs and SPIONs alone needs to be conducted to define control parameters.

The uptake of the Au-MNPs and Au-MNP-NTR conjugates into a cell line system *in vitro* needs to be investigated and analysed. This can hopefully be achieved using microscopy but also a modified viability assay could also lead to the determination of successful particle uptake. This will help to determine if the MNDEPT system will work intra- or extracellularly or possibly a combination of both.

The possibility of testing the efficiency of magnetic control over the Au-MNPs along with determination of their localisation could be done *in vivo* at the mouse trial stage of investigation. DeNardo *et al.*[326] studied athymic mice bearing human breast cancer xenografts. In brief, they were able to determine the location of MNPs by harvesting the tumours and also by using ultrastructural analysis of the inserted bioprobe location along with cancer cell viability and placing the scarified mice in Karnovsky's fixative. More detail can be found by referring to the study.[326]

Chapter 7

Appendix

7. Appendix

```
                10        20        30        40        50        60        70        80        90       100
        ....|....|....|....|....|....|....|....|....|....|....|....|....|....|....|....|....|....|....|....|
NfsB    -----MDIISVALKRHSTKAFDASKKLTPEQAEQIKTLLQYSPSSTNSQPWHFIVASTEEGKARVAKSAAGNYVFNERKML-DASHVVVFCAKTAMDDVW
YfkO    MADLKTQILDAYNFRHATKEFDPNKKVSDSDFEFILETGRLSPSSLGLEPWKFVVVQNPEFREKL-RE----YTWGAQKQLPTASHFVLILARTAKDIKY

                110       120       130       140       150       160       170       180       190       200
        ....|....|....|....|....|....|....|....|....|....|....|....|....|....|....|....|....|....|....|....|
NfsB    LKLVVDQEDADGRFATPEA-KAANDKGRKFFA-DMHRKDLHDDA-EWMAKQVYLNVGNFLLGVAALGLDAVPIEGF--D--AAILDAEFGLKEKG-YTSL
YfkO    NADYIKRHLKEVKQMPQDVYEGYLSKTEEFQKNDLHLLESDRTLFDWASKQTYIALGNMMTAAAQIGVDSCPIEGFQYDHIHRILEEE-GLLENGSFDIS

                210       220       230
        ....|....|....|....|....|....|.
NfsB    VVVPVGHHSVEDFNATLPKSRLPQNITLTEV
YfkO    VMVAFGYR-VRD---PRPKTRSAVEDVVKWV
```

Appendix 7.1 Full amino acid alignment of NfsB and YfkO.

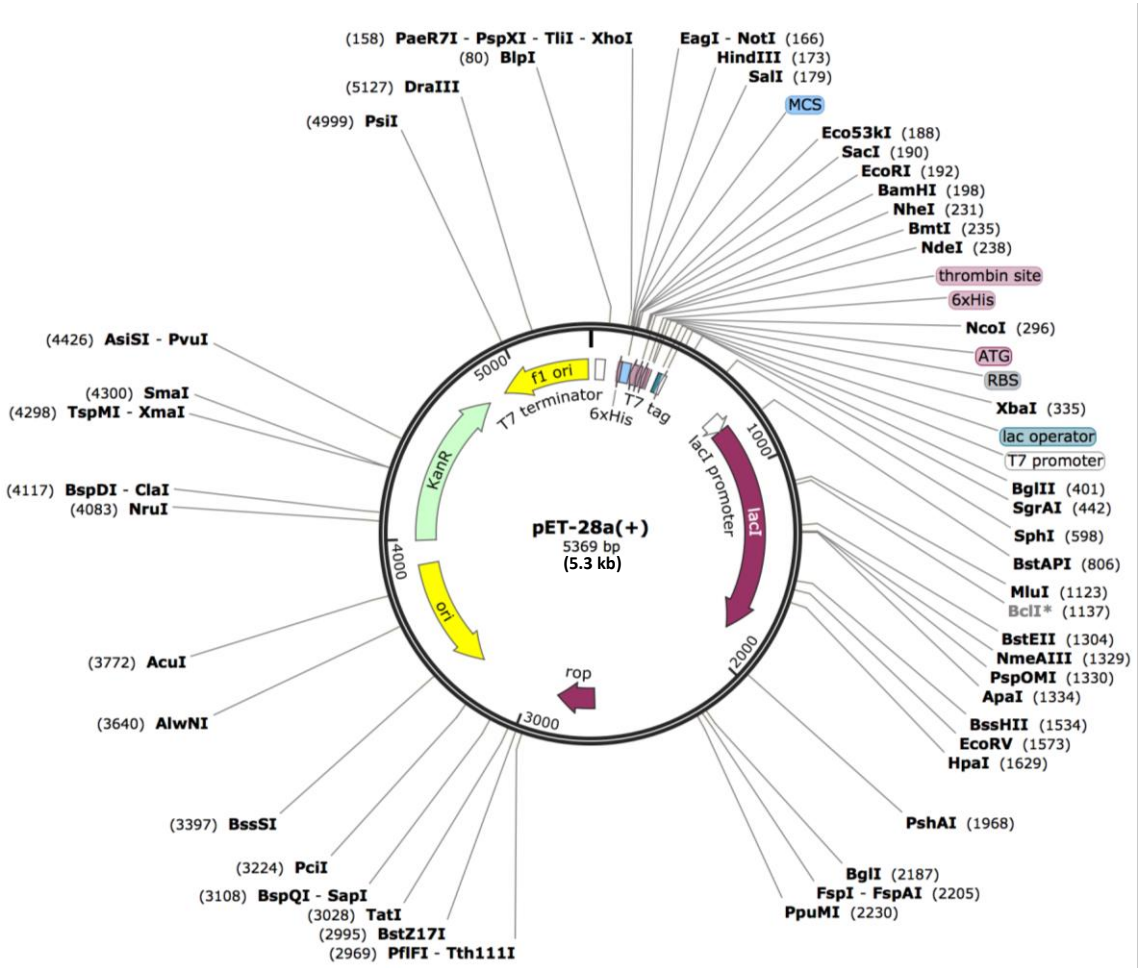

Appendix 7.2 pET-28a(+) plasmid map

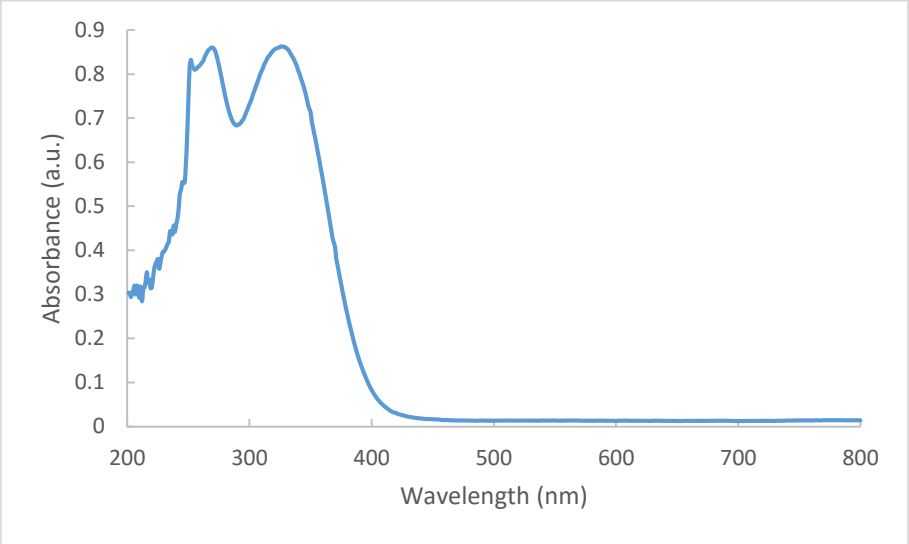

Appendix 7.3 CB1954 UV/Visible spectra background scan; CB1954 (100 µM) vs PB (50 mM, pH 7.4).

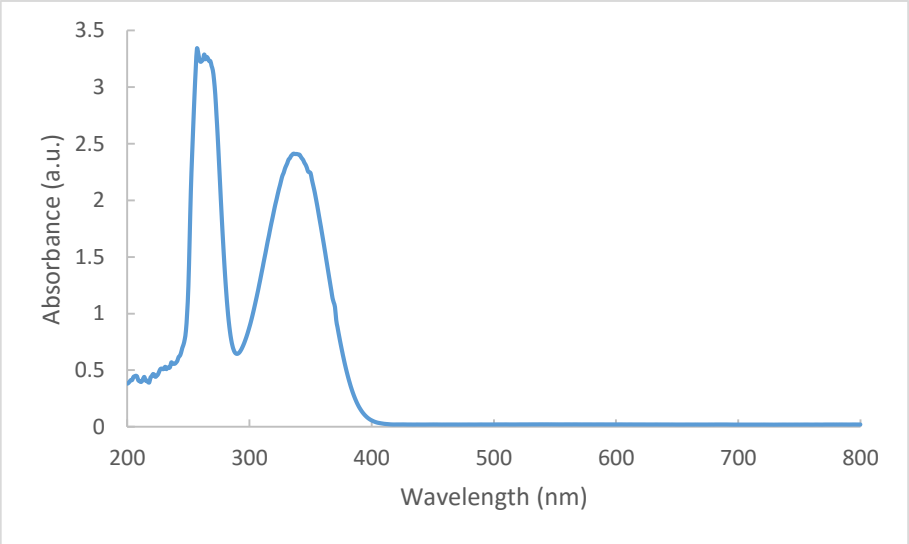

Appendix 7.4 NADH UV/Visible spectra background scan; NADH (600 µM) vs PB (50 mM, pH 7.4).

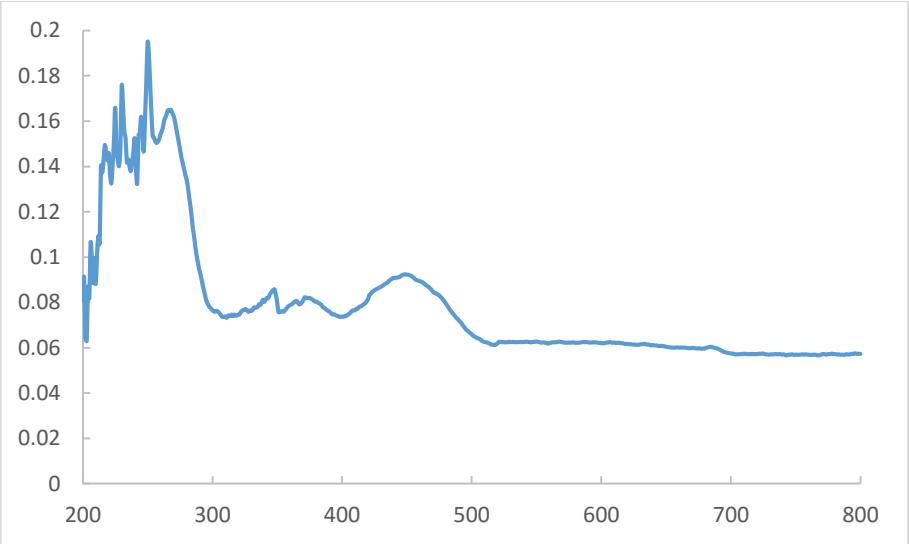

Appendix 7. 5 NTR UV/Visible spectra background scan; NTR (10 µg/mL) vs PB (50 mM, pH 7.4)

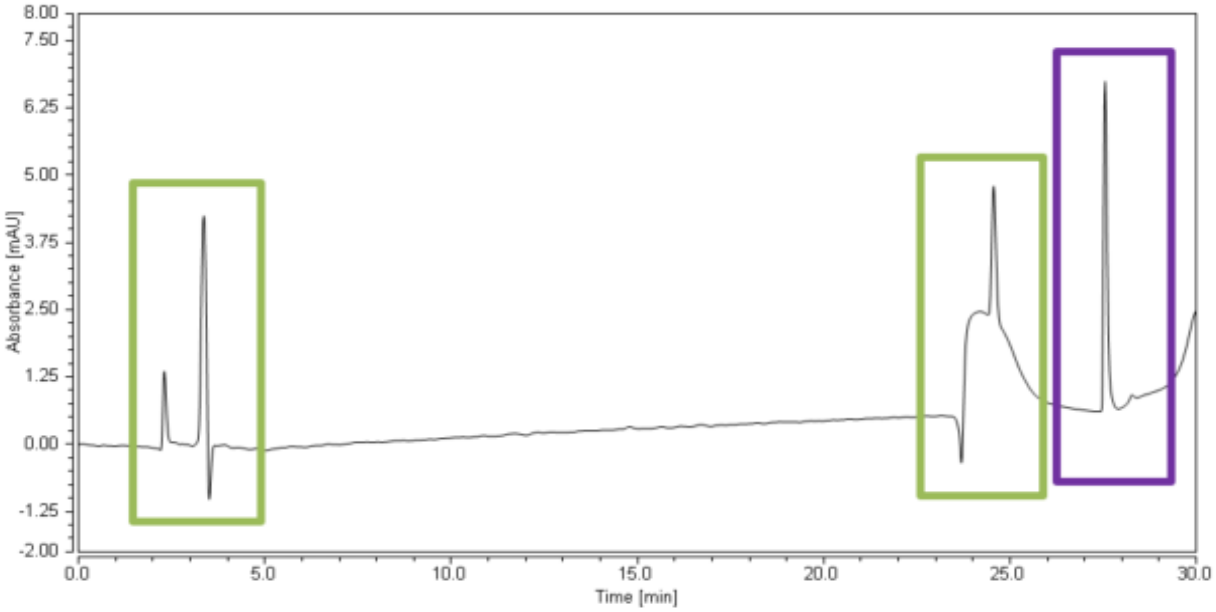

Appendix 7.6 HPLC spectra resulting from the determination of NTR [Purple] in PB [Green] (50 mM, pH 7.4), conducted at 420 nm wavelength.

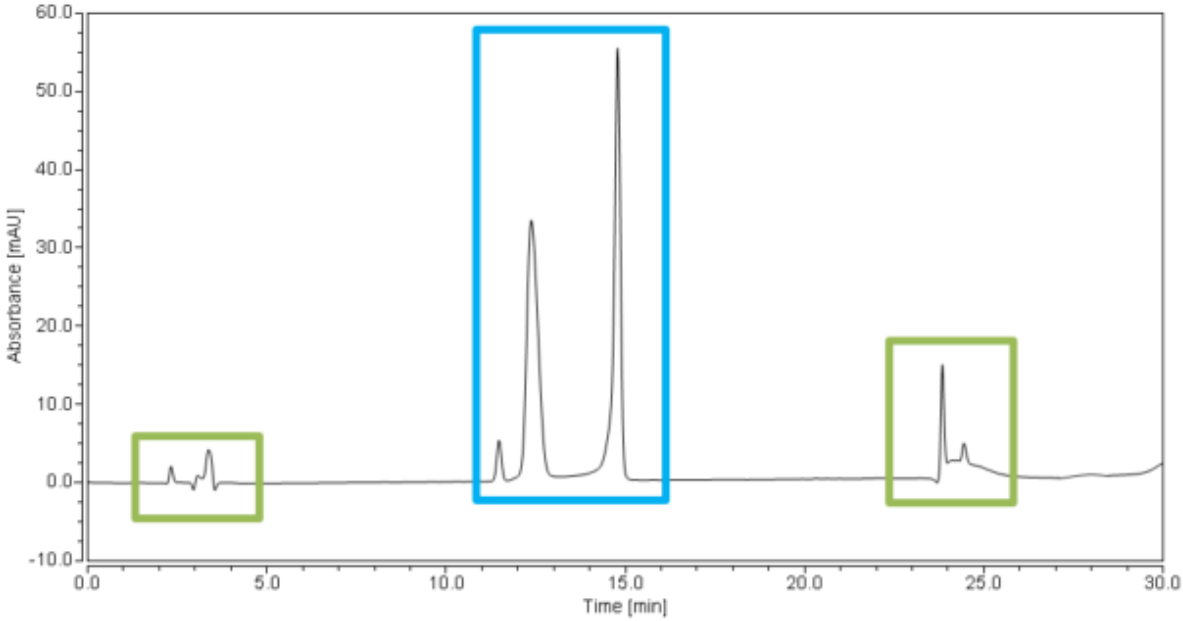

Appendix 7.7 HPLC spectra resulting from the determination of CB1954 [Blue] (50 mM) in PB [Green] (50 mM, pH 7.4), conducted at 420 nm wavelength.

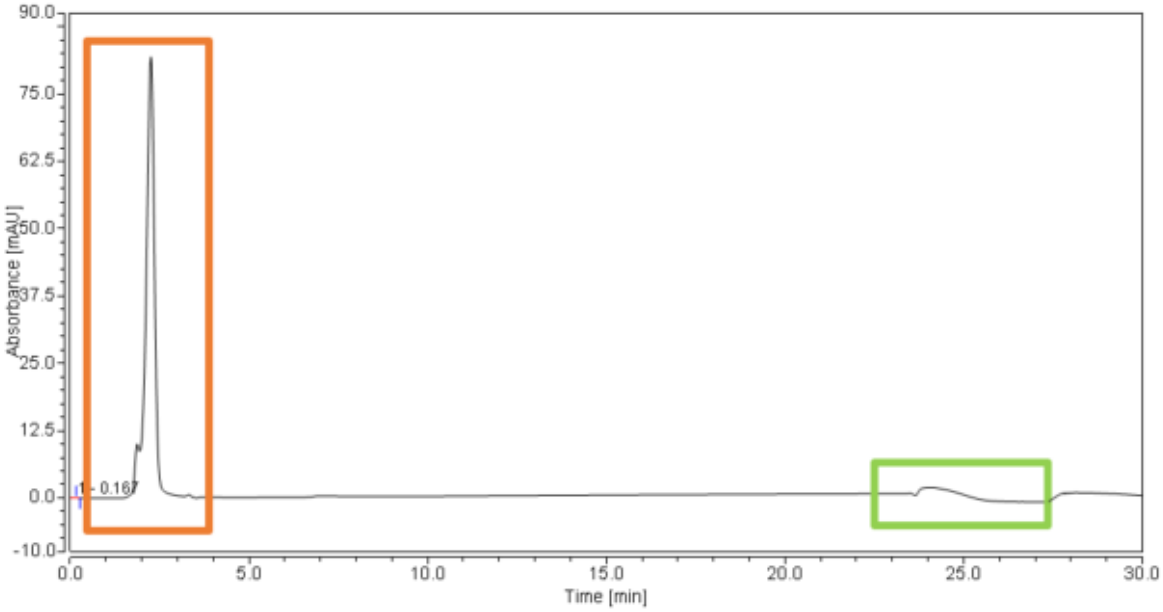

Appendix 7.8 HPLC spectra resulting from the determination of NAD+[Orange] in PB [Green] (50 mM, pH 7.4), conducted at 320 nm wavelength.

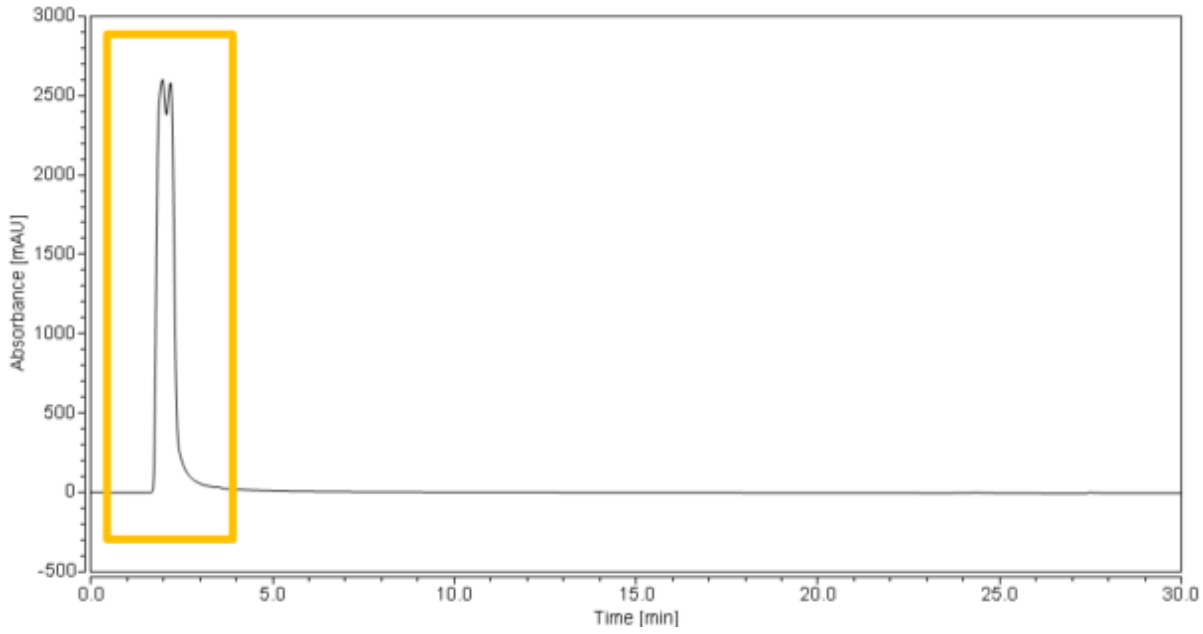

Appendix 7.9 HPLC spectra resulting from the determination of NADH [Yellow] in PB [Green](50 mM, pH 7.4), conducted at 320 nm wavelength.

	Reagent			Reaction Conditions		Total Additions of Reagents			Total Volume of Reagents (µL)			λmax (nm)
	$HAuCl_4$	NH_2OH	5 nm Au Colloid	Speed (rpm)	Heating (°C)	$HAuCl_4$	NH_2OH	5 nm Au Colloid	$HAuCl_4$	NH_2OH	5 nm Au Colloid	
Iterative Hydroxylamine Seeding												
1	1% wt/v	200 mM	N	8,000	X	5	5	X	2625	1688	X	605
2	1% wt/v	200 mM	N	8,000	X	10	10	X	5125	2721	X	621
3	2% wt/v	200 mM	N	8,000	X	5	5	X	2625	1688	X	613
4	0.5% wt/v	100 mM	N	8,000	X	5	5	X	2625	1688	X	ND
5	0.1% wt/v	100 mM	N	8,000	X	5	5	X	2625	1688	X	ND
6	2% wt/v	200 mM	N	8,000	X	10	10	X	5125	2721	X	653
7	0.5% wt/v	100 mM	N	8,000	X	10	10	X	5125	2721	X	578
8	0.1% wt/v	100 mM	N	8,000	X	10	10	X	5125	2721	X	ND
9	1% wt/v	200 mM	N	8,000	50	5	5	X	2625	1688	X	560
10	1% wt/v	200 mM	N	8,000	50	10	10	X	5125	2721	X	612
11	1% wt/v	200 mM	N	8,000	75	5	5	X	2625	1688	X	554
12	1% wt/v	200 mM	N	8,000	75	10	10	X	5125	2721	X	602
13	1% wt/v	200 mM	N	8,000	X	5	5	X	1312	845	X	583
14	1% wt/v	X	N	8,000	100	1	X	X	5000	X	X	675
5 nm Gold Colloid Pre-Seeded Iterative Hydroxylamine Seeding												
15	0.5% wt/v	100 mM	Y	8,000	X	4	5	1	2000	1688	625	605
16	0.5% wt/v	100 mM	Y	8,000	X	9	10	1	4500	2721	625	615
17	1% wt/v	200 mM	Y	8,000	X	4	5	1	2000	1688	625	535
18	1% wt/v	200 mM	Y	8,000	X	9	10	1	4500	2721	625	575
Modified Au-MNP Synthesis												
19	[a] 1% wt/v	200 mM	Y	8,500	50	1	1	1	5000	1500	1000	535

Appendix 7.10 Overview of experimental approach and pathway to the final modified Au-MNP synthesis.

References

1 S. Knox, **From 'omics' to complex disease: a systems biology approach to gene-environment interactions in cancer**, *Cancer Cell Int.*, 2010, **10**, 11.

2 A. Jemal, F. Bray, M. M. Center, J. Ferlay, E. Ward, et al., **Global cancer statistics**, *CA. Cancer J. Clin.*, 2011, **61**, 69–90.

3 C. La Vecchia, C. Bosetti, F. Lucchini, P. Bertuccio, E. Negri, et al., **Cancer mortality in Europe, 2000–2004, and an overview of trends since 1975**, *Ann. Oncol.*, 2010, **21**, 1323–1360.

4 M. Malvezzi, A. Arfé, P. Bertuccio, F. Levi, C. La Vecchia, et al., **European cancer mortality predictions for the year 2011**, *Ann. Oncol.*, 2011, **22**, 947–956.

5 B. K. Edwards, M. L. Brown, P. A. Wingo, H. L. Howe, E. Ward, et al., **Annual Report to the Nation on the Status of Cancer, 1975–2002, Featuring Population-Based Trends in Cancer Treatment**, *J. Natl. Cancer Inst.*, 2005, **97**, 1407–1427.

6 A. L. Vogel, B. A. Stipelman, K. L. Hall, L. Nebeling, D. Stokols, et al., **Pioneering the Transdisciplinary Team Science Approach: Lessons Learned from National Cancer Institute Grantees**, *J. Transl. Med. Epidemiol.*, 2014, **2**, 1027–1040.

7 S. Eckhouse, G. Lewison and R. Sullivan, **Trends in the global funding and activity of cancer research**, *Mol. Oncol.*, 2008, **2**, 20–32.

8 M. J. Thun, J. O. DeLancey, M. M. Center, A. Jemal and E. M. Ward, **The global burden of cancer: priorities for prevention**, *Carcinogenesis*, 2009, **31**, 100–110.

9 P. Boyle, **Favorable trends in cancer mortality in the European Union but no room for complacency**, *Ann. Oncol.*, 2008, **19**, 605–606.

10 M. J. Quinn, A. d'Onofrio, B. Møller, R. Black, C. Martinez-Garcia, et al., **Cancer mortality trends in the EU and acceding countries up to 2015**, *Ann. Oncol.*, 2003, **14**, 1148–1152.

11 R. S. Go and A. A. Adjei, **Review of the Comparative Pharmacology and Clinical Activity of Cisplatin and Carboplatin**, *J. Clin. Oncol.*, 1999, **17**, 409.

12 S. Quasthoff and H. P. Hartung, **Chemotherapy-induced peripheral neuropathy**, *J. Neurol.* 2002, **249**, 9–17.

13 V. Buxhofer-Ausch, L. Secky, K. Wlcek, M. Svoboda, V. Kounnis, et al., **Tumor-Specific Expression of Organic Anion-Transporting Polypeptides: Transporters as Novel Targets for Cancer Therapy**, *J. Drug Deliv.*, 2013, **v.2013**, 863539.

14 K. D. Bagshawe, S. K. Sharma, P. J. Burke, R. G. Melton and R. J. Knox, **Developments with targeted enzymes in cancer therapy**, *Curr. Opin. Immunol.*, 1999, **11**, 579–583.

15 V. V Gwenin, C. D. Gwenin and M. Kalaji, **Colloidal gold modified with a genetically engineered nitroreductase: Toward a novel enzyme delivery system for cacer prodrug therapy,** *Langmuir*, 2011, **27**, 14300–14307.

16 S. Parker, **Chapter 8 - Principles of surgical oncology,** *MCRS Applied Basic Science and Clinical Topics*, JP Medical Ltd, 2013, 99–109.

17 B. Vogelstein and K. W. Kinzler, **Cancer genes and the pathways they control**, *Nat. Med.*, 2004, **10**, 789–799.

18 P. Nowell, **The clonal evolution of tumor cell populations**, *Science*, 1976, **194**, 23–28.

19 M. B. Sporn, **The war on cancer**, *Lancet*, 1996, **347**, 1377–1381.

20 G. Christofori and H. Semb, **The role of the cell-adhesion molecule E-cadherin as a tumour-suppressor gene**, *Trends Biochem. Sci.*, 1999, **24**, 73–76.

21 S. S. Hecht, **Tobacco Smoke Carcinogens and Lung Cancer**, *J. Natl. Cancer Inst.*, 1999, **91**, 1194–1210.

22 E. Cardis, M. Vrijheid, M. Blettner, E. Gilbert, M. Hakama, et al., **Risk of cancer after low doses of ionising radiation: retrospective cohort study in 15 countries**, *BMJ*, 2005, **331**, 77.

23 A. Storey, M. Thomas, A. Kalita, C. Harwood, D. Gardiol, et al., **Role of a p53 polymorphism in the development of human papilloma-virus-associated cancer**, *Nature*, 1998, **393**, 229–234.

24 D. L. Mager, **Bacteria and cancer: cause, coincidence or cure? A review**, *J. Transl. Med.*, 2006, **4**, 14.

25 M. Wainwright, **Do fungi play a role in the aetiology of cancer?**, *Rev. Med. Microbiol.*, 2002, **13**, 37–42.

26 D. J. Slamon, G. M. Clark, S. G. Wong, W. J. Levin, A. Ullrich, et al., **Human breast cancer: correlation of relapse and survival with amplification of the HER-2/neu oncogene**, *Science*, 1987, **235**, 177–182.

27 F. McCormick, **Cancer therapy based on oncogene addiction**, *J. Surg. Oncol.*, 2011, **103**, 464–467.

28 V. Huff, **Wilms' tumours: about tumour suppressor genes, an oncogene and a chameleon gene**, *Nat Rev Cancer*, 2011, **11**, 111–121.

29 D. Hanahan and R. A. Weinberg, **The hallmarks of cancer**, *Cell*, 2000, **100**, 1, 57–70.

30 J. M. Bishop and R. A. Weinberg, **Scientific american molecular oncology,** Scientific American Inc., New York, 1996.

31 D. Hanahan and R. A. Weinberg, **Hallmarks of Cancer: The Next Generation**, *Cell*, 2011, **144**, 646–674.

32 N. E. Hynes and G. MacDonald, **ErbB receptors and signaling pathways in cancer**, *Curr. Opin. Cell Biol.*, 2009, **21**, 177–84.

33 M. A. Lemmon and J. Schlessinger, **Cell signaling by receptor tyrosine kinases.**, *Cell*, 2010, **141**, 1117–34.

34 N. Cheng, A. Chytil, Y. Shyr, A. Joly and H. L. Moses, **Transforming growth factor-beta signaling-deficient fibroblasts enhance hepatocyte growth factor signaling in mammary carcinoma cells to promote scattering and invasion.**, *Mol. Cancer Res.*, 2008, **6**, 1521–33.

35 N. A. Bhowmick, E. G. Neilson and H. L. Moses, **Stromal fibroblasts in cancer initiation and progression.**, *Nature*, 2004, **432**, 332–7.

36 C. J. Sherr and F. McCormick, **The RB and p53 pathways in cancer**, *Cancer Cell*, 2002, **2**, 103–112.

37 J. M. Adams and S. Cory, **The Bcl-2 apoptotic switch in cancer development and therapy.**, *Oncogene*, 2007, **26**, 1324–37.

38 S. W. Lowe, E. Cepero and G. Evan, **Intrinsic tumour suppression.**, *Nature*, 2004, **432**, 307–15.

39 J.-H. Chen, C. N. Hales and S. E. Ozanne, **DNA damage, cellular senescence and organismal ageing: causal or correlative?**, *Nucleic Acids Res.*, 2007, **35**, 7417–28.

40 M. A. Blasco, **Mice with bad ends: mouse models for the study of telomeres and telomerase in cancer and aging.**, *EMBO J.*, 2005, **24**, 1095–103.

41 J. W. Shay and W. E. Wright, **Hayflick, his limit, and cellular ageing.**, *Nat. Rev. Mol. Cell Biol.*, 2000, **1**, 72–6.

42 D. Hanahan and J. Folkman, **Patterns and Emerging Mechanisms of the Angiogenic Switch during Tumorigenesis**, *Cell*, 1996, **86**, 353–364.

43 G. Bergers and L. E. Benjamin, **Tumorigenesis and the angiogenic switch.**, *Nat. Rev. Cancer*, 2003, **3**, 401–10.

44 V. Baeriswyl and G. Christofori, **The angiogenic switch in carcinogenesis.**, *Semin. Cancer Biol.*, 2009, **19**, 329–37.

45 M. Raica, A. M. Cimpean and D. Ribatti, **Angiogenesis in pre-malignant conditions.**, *Eur. J. Cancer*, 2009, **45**, 1924–34.

46 J. E. Talmadge and I. J. Fidler, **AACR centennial series: the biology of cancer metastasis: historical perspective.**, *Cancer Res.*, 2010, **70**, 5649–69.

47 I. J. Fidler, **The pathogenesis of cancer metastasis: the 'seed and soil' hypothesis revisited.**, *Nat. Rev. Cancer*, 2003, **3**, 453–8.

48 G. Berx and F. van Roy, **Involvement of Members of the Cadherin Superfamily in Cancer**, *Cold Spring Harb. Perspect. Biol.*, 2009, **1**, a003129–a003129.

49 U. Cavallaro and G. Christofori, **Cell adhesion and signalling by cadherins and Ig-CAMs in cancer.**, *Nat. Rev. Cancer*, 2004, **4**, 118–32.

50 J. Luo, N. L. Solimini and S. J. Elledge, **Principles of cancer therapy: oncogene and non-oncogene addiction.**, *Cell*, 2009, **136**, 823–37.

51 S. Negrini, V. G. Gorgoulis and T. D. Halazonetis, **Genomic instability - an evolving hallmark of cancer.**, *Nat. Rev. Mol. Cell Biol.*, 2010, **11**, 220–8.

52 F. Colotta, P. Allavena, A. Sica, C. Garlanda and A. Mantovani, **Cancer-related inflammation, the seventh hallmark of cancer: links to genetic instability.**, *Carcinogenesis*, 2009, **30**, 1073–81.

53 Z. E. Stine, B. J. Altman, A. L. Hsieh, A. M. Gouw and C. V. Dang, **Derugulation of the cellular energetics of cancer cells,** *PATD*, 2014, 444-455.

54 M. W. L. Teng, J. B. Swann, C. M. Koebel, R. D. Schreiber and M. J. Smyth, **Immune-mediated dormancy: an equilibrium with cancer.**, *J. Leukoc. Biol.*, 2008, **84**, 988–93.

55 A. Pardee and G. Stein, **The biology and treatment of cancer: Understanding cancer,** *Wiley*, 2009.

56 National Cancer Institute, **National cancer institute factsheet: Understanding cancer prognosis,** *NIH*, 2014.

57 S. Edge, D. R. Byrd, C. C. Compton, A. G. Fritz, F. L. Greene, et al., **AJCC cancer staging manual,** Springer, 2010, 7th ed.

58 R. Doll, **The Pierre Denoix Memorial Lecture: Nature and nurture in the control of cancer**, *Eur. J. Cancer*, 2014, **35**, 16–23.

59 J. Brierley, **The evolving TNM cancer staging system: an essential component of cancer care**, *Can. Med. Assoc. J.*, 2006, **174**, 155–156.

60 M. S. Braun and M. T. Seymour, **Review: Balancing the efficacy and toxicity of chemotherapy in colorectal cancer**, *Ther. Adv. Med. Oncol.*, 2011, **3**, 43–52.

61 W. I. Onuigbo, **Historical trends in cancer surgery**, *Med. Hist.*, 1962, **6**, 154–161.

62 S. P. Luh and H. P. Liu, **Video-assisted thoracic surgery--the past, present status and the future**, *J. Zhejiang Univ.*, 2006, **7**, 118–128.

63 M. R. Diaz and P. E. Vivas-Mejia, **Nanoparticles as Drug Delivery Systems in Cancer Medicine: Emphasis on RNAi-Containing Nanoliposomes**, *Pharmaceuticals*, 2013, **6**, 1361–1380.

64 T. Lammers, F. Kiessling, W. E. Hennink and G. Storm, **Drug targeting to tumors: Principles, pitfalls and (pre-) clinical progress**, *Drug Deliv. Res. Eur.*, 2012, **161**, 175–187.

65 R. Langer, **Drug delivery and targeting**, *Nat. JID - 0410462*, 1998, **392**, 5–10.

66 S. Muro, **Challenges in design and characterization of ligand-targeted drug delivery systems**, *J. Control. Release*, 2012, **164**, 2, 125–137.

67 F. Yamashita and M. Hashida, **Pharmacokinetic considerations for targeted drug delivery**, *Adv. Drug Deliv.*, 2013, **65**, 139–147.

68 J. Dobson, **Cancer therapy: A twist on tumour targeting**, *Nat Mater*, 2010, **9**, 95–96.

69 J. M. Chacon and M. K. Gardner, **Analysis and Modeling of Chromosome Congression During Mitosis in the Chemotherapy Drug Cisplatin**, *Cell. Mol. Bioeng.*, 2013, **6**, 406–417.

70 C. Vogel, C. Hager and H. Bastians, **Mechanisms of Mitotic Cell Death Induced by Chemotherapy-Mediated G2 Checkpoint Abrogation**, *Cancer Res.*, 2007, **67**, 339–345.

71 B. Alberts, A. Johnson, J. Lewis, M. Raff, K. Roberts, et al., *Molecular Biology Of The Cell*, Garland Science, New York, 2002, vol. 4th, 983–1027.

72 V. T. DeVita and E. Chu, **A History of Cancer Chemotherapy**, *Cancer Res.*, 2008, **68**, 8643–8653.

73 P. G. Corrie, **Cytotoxic chemotherapy: clinical aspects**, *Oncology*, 2008, **36**, 24–28.

74 M. J. Lind, **Principles of cytotoxic chemotherapy**, *Medicine*, 2008, **36**, 19–23.

75 G. Damia and M. D'Incalci, **Mechanisms of resistance to alkylating agents.**, *Cytotechnology*, 1998, **27**, 165–73.

76 Z. H. Siddik, **The cancer handbook,** John Wiley & Sons, Ltd, Chichester, UK, 2005.

77 V. Malhotra and M. C. Perry, **Classical Chemotherapy: Mechanisms, Toxicities and the Therapeutc Window**, *Cancer Biol. Ther.*, 2003, **2**, 1–3.

78 P. Pourquier, **Alkylating agents**, *Bull. Cancer*, 2011, **98**, 1237–51.

79 W. B. Parker, **Enzymology of purine and pyrimidine antimetabolites used in the treatment of cancer.**, *Chem. Rev.*, 2009, **109**, 2880–93.

80 E. K. Rowinsky and R. C. Donehower, **The clinical pharmacology and use of antimicrotubule agents in cancer chemotherapeutics.**, *Pharmacol. Ther.*, 1991, **52**, 35–84.

81 Q.-X. Yue, X. Liu and D.-A. Guo, **Microtubule-binding natural products for cancer therapy.**, *Planta Med.*, 2010, **76**, 1037–43.

82 J. Goodman and V. Walsh, *The story of taxol: Nature and politics in the pursuit of an anti-cancer drug***,** Cambridge University Press, 2001.

83 World Health Organization, **19th WHO model list of essential medicinces (April 2015),** 2015.

84 O. Tacar, P. Sriamornsak and C. R. Dass, **Doxorubicin: an update on anticancer molecular action, toxicity and novel drug delivery systems.**, *J. Pharm. Pharmacol.*, 2013, **65**, 157–70.

85 F. A. Fornari, J. K. Randolph, J. C. Yalowich, M. K. Ritke and D. A. Gewirtz, **Interference by doxorubicin with DNA unwinding in MCF-7 breast tumor cells.**, *Mol. Pharmacol.*, 1994, **45**, 649–56.

86 R. L. Momparler, M. Karon, S. E. Siegel and F. Avila, **Effect of adriamycin on DNA, RNA, and protein synthesis in cell-free systems and intact cells.**, *Cancer Res.*, 1976, **36**, 2891–5.

87 J. M. Goldman and J. V Melo, **Chronic myeloid leukemia--advances in biology and new approaches to treatment.**, *N. Engl. J. Med.*, 2003, **349**, 1451–64.

88 C. Fausel, **Targeted chronic myeloid leukemia therapy: Seeking a cure.**, *Am. J. Health. Syst. Pharm.*, 2007, **64**, S9–15.

89 F. Stegmeier, M. Warmuth, W. R. Sellers and M. Dorsch, **Targeted cancer therapies in the twenty-first century: lessons from imatinib.**, *Clin. Pharmacol. Ther.*, 2010, **87**, 543–52.

90 E. Sala, L. Mologni, S. Truffa, C. Gaetano, G. E. Bollag, et al., **BRAF silencing by short hairpin RNA or chemical blockade by PLX4032 leads to different responses in melanoma and thyroid carcinoma cells.**, *Mol. Cancer Res.*, 2008, **6**, 751–9.

91 E. Maverakis, L. A. Cornelius, G. M. Bowen, T. Phan, F. B. Patel, et al., **Metastatic melanoma - a review of current and future treatment options.**, *Acta Derm. Venereol.*, 2015, **95**, 516–24.

92 G. Hatzivassiliou, K. Song, I. Yen, B. J. Brandhuber, D. J. Anderson, et al., **RAF inhibitors prime wild-type RAF to activate the MAPK pathway and enhance growth.**, *Nature*, 2010, **464**, 431–5.

93 R. Halaban, W. Zhang, A. Bacchiocchi, E. Cheng, F. Parisi, et al., **PLX4032, a selective BRAF(V600E) kinase inhibitor, activates the ERK pathway and enhances cell migration and proliferation of BRAF melanoma cells.**, *Pigment Cell Melanoma Res.*, 2010, **23**, 190–200.

94 C. A. Hudis, **Trastuzumab--mechanism of action and use in clinical practice.**, *N. Engl. J. Med.*, 2007, **357**, 39–51.

95 J. Albanell, J. Codony, A. Rovira, B. Mellado and P. Gascón, **Mechanism of action of anti-HER2 monoclonal antibodies: scientific update on trastuzumab and 2C4.**, *Adv. Exp. Med. Biol.*, 2003, **532**, 253–68.

96 G. M. Dubowchik and M. A. Walker, **Receptor-mediated and enzyme-dependent targeting of cytotoxic anticancer drugs**, *Pharmacol. Ther.*, 1119, **83**, 67–123.

97 O. Greco and G. U. Dachs, **Gene directed enzyme/prodrug therapy of cancer: historical appraisal and future prospectives**, *J. Cell. Physiol.*, 2001, **187**, 22–36.

98 F. Kratz, I. A. Muller, C. Ryppa and A. Warnecke, **Prodrug strategies in anticancer chemotherapy**, *ChemMedChem*, 2008, **3**, 20–53.

99 M. Rooseboom, J. N. Commandeur and N. P. Vermeulen, **Enzyme-catalyzed activation of anticancer prodrugs**, *Pharmacol. Rev.*, 2004, **56**, 53–102.

100 W. A. Denny, **Prodrugs for Gene-Directed Enzyme-Prodrug Therapy (Suicide Gene Therapy).**, *J. Biomed. Biotechnol.*, 2003, **2003**, 48–70.

101 J. A. Bridgewater, C. J. Springer, R. J. Knox, N. P. Minton, N. P. Michael, et al., **Expression of the bacterial nitroreductase enzyme in mammalian cells renders them selectively sensitive to killing by the prodrug CB1954**, *Eur. J. Cancer*, 1995, **31**, 2362–2370.

102 W. Cui, B. Gusterson and A. J. Clark, **Nitroreductase-mediated cell ablation is very rapid and mediated by a p53-independent apoptotic pathway.**, *Gene Ther.*, 1999, **6**, 764–70.

103 A. J. Clark, M. Iwobi, W. Cui, M. Crompton, G. Harold, et al., **Selective cell ablation in transgenic mice expression E. coli nitroreductase.**, *Gene Ther.*, 1997, **4**, 101–10.

104 K. D. Bagshawe, **Antibody-directed enzyme prodrug therapy (ADEPT) for cancer**, *Expert Rev. Anticancer Ther.*, 2006, **6**, 1421–1431.

105 I. Niculescu-Duvaz and C. J. Springer, **Antibody-directed enzyme prodrug therapy (ADEPT): a review**, *Deliv. Chemother. Drugs*, 1997, **26**, 151–172.

106 D. Portsmouth, J. Hlavaty and M. Renner, **Suicide genes for cancer therapy**, *Genes cure cancer*, 2007, **28**, 4–41.

107 J. I. Grove, P. F. Searle, S. J. Weedon, N. K. Green, I. A. McNeish, et al., **Virus-directed enzyme prodrug therapy using CB1954**, *Anticancer. Drug Des.*, 1999, **14**, 461–472.

108 I. A. McNeish, N. K. Green, M. G. Gilligan, M. J. Ford, V. Mautner, et al., **Virus directed enzyme prodrug therapy for ovarian and pancreatic cancer using retrovirally delivered E. coli nitroreductase and CB1954**, *Gene Ther.*, 1998, **5**, 1061–1069.

109 R. J. Francis, S. K. Sharma and C. Springer, **A phase I trial of antibody directed enzyme prodrug therapy (ADEPT) in patients with advanced colorectal carcinoma or other CEA producing tumours,** *Br. J. Cancer*, 2002, **87**, 6, 600-607.

110 G. Xu and H. L. McLeod, **Strategies for Enzyme/Prodrug Cancer Therapy**, *Clin. Cancer Res.*, 2001, **7**, 3314–3324.

111 N. Nayerossadat, T. Maedeh and P. A. Ali, **Viral and nonviral delivery systems for gene delivery.**, *Adv. Biomed. Res.*, 2012, **1**, 27.

112 K. Saukkonen and A. Hemminki, **Tissue-specific promoters for cancer gene therapy**, *Expert Opin. Biol. Ther.*, 2004, **4**, 683–696.

113 A. Yakkundi, V. McErlane, M. Murray, H. O. McCarthy, C. Ward, et al., **Tumor-selective drug activation: a GDEPT approach utilizing cytochrome P450 1A1 and AQ4N**, *Cancer Gene Ther.*, 2006, **13**, 598–605.

114 C. J. Springer and I. Niculescu-Duvaz, **Chapter 8: Gene-directed enzyme prodrug therapy,** *Anticancer Drug Development*, Academic Press, San Diego, 2002, 137–155.

115 N. K. Green, D. J. Youngs, J. P. Neoptolemos, F. Friedlos, R. J. Knox, et al., **Sensitization of colorectal and pancreatic cancer cell lines to the prodrug 5-(aziridin-1-yl)-2,4-dinitrobenzamide (CB1954) by retroviral transduction and expression of the E. coli nitroreductase gene**, *Cancer Gene Ther.*, 1997, **4**, 229–238.

116 S. J. Weedon, N. K. Green, I. A. McNeish, M. G. Gilligan, V. Mautner, et al., **Sensitisation of human carcinoma cells to the prodrug CB1954 by adenovirus vector-mediated expression of E. coli nitroreductase**, *Int. J. Cancer*, 2000, **86**, 848–854.

117 P. F. Searle, S. J. Weedon, I. A. McNeish, M. G. Gilligan, M. J. Ford, et al., **Sensitisation of human ovarian cancer cells to killing by the prodrug CB1954 following retroviral or adenoviral transfer of the E. coli nitroreductase gene**, *Adv. Exp. Med. Biol.*, 1998, **451**, 107–113.

118 E. M. Westphal, J. Ge, J. R. Catchpole, M. Ford and S. C. Kenney, **The nitroreductase/CB1954 combination in Epstein-Barr virus-positive B-cell lines: induction of bystander killing in vitro and in vivo**, *Cancer Gene Ther.*, 2000, **7**, 97–106.

119 D. A. Hamstra, D. J. Rice, S. Fahmy, B. D. Ross and A. Rehemtulla, **Enzyme/prodrug therapy for head and neck cancer using a catalytically superior cytosine deaminase**, *Hum. Gene Ther.*, 1999, **10**, 1993–2003.

120 H. Chong, W. Starkey and R. G. Vile, **A replication-competent retrovirus arising from a split-function packaging cell line was generated by recombinationevents between the vector, one of the packaging constructs and endogenous retroviral sequences**, *J. Virol.*, 1998, **74**, 4, 2663-2670.

121 R. J. Knox, M. P. Boland, F. Friedlos, B. Coles, C. Southan, et al., **The nitroreductase enzyme in Walker cells that activates 5-(aziridin-1-yl)-2,4-dinitrobenzamide (CB 1954) to 5-(aziridin-1-yl)-4-hydroxylamino-2-nitrobenzamide is a form of NAD(P)H dehydrogenase (quinone) (EC 1.6.99.2)**, *Biochem. Pharmacol.*, 1988, **37**, 4671–4677.

122 R. J. Knox, F. Friedlos, M. Jarman and J. J. Roberts, **A new cytotoxic, DNA interstrand crosslinking agent, 5-(aziridin-1-yl)-4-hydroxylamino-2-nitrobenzamide, is formed from 5-(aziridin-1-yl)-2,4-dinitrobenzamide (CB 1954) by a nitroreductase enzyme in walker carcinoma cells**, *Biochem. Pharmacol.*, 1988, **37**, 4661–4669.

123 R. J. Knox, F. Friedlos, R. F. Sherwood, R. G. Melton and G. M. Anlezark, **The bioactivation of 5-(aziridin-1-yl)-2,4-dinitrobenzamide (CB1954)--II. A comparison of an Escherichia coli nitroreductase and Walker DT diaphorase**, *Biochem. Pharmacol.*, 1992, **44**, 2297–2301.

124 R. J. Knox, F. Friedlos, T. Marchbank and J. J. Roberts, **Bioactivation of CB 1954: Reaction of the active 4-hydroxylamino derivative with thioesters to form the ultimate DNA-DNA interstrand crosslinking species**, *Biochem. Pharmacol.*, 1991, **42**, 1691–1697.

125 G. M. Anlezark, R. G. Melton, R. F. Sherwood, B. Coles, F. Friedlos, et al., **The bioactivation of 5-(aziridin-1-yl)-2,4-dinitrobenzamide (CB1954)--I. Purification and properties of a nitroreductase enzyme from Escherichia coli--a potential enzyme for antibody-directed enzyme prodrug therapy (ADEPT)**, *Biochem. Pharmacol.*, 1992, **44**, 2289–2295.

126 N. A. Helsby, S. J. Wheeler, F. B. Pruijn, B. D. Palmer, S. Yang, et al., **Effect of nitroreduction on the alkylating reactivity and cytotoxicity of the 2,4-dinitrobenzamide-5-aziridine CB 1954 and the corresponding nitrogen mustard SN 23862: Distinct Mechanisms of Bioreductive Activation**, *Chem. Res. Toxicol.*, 2003, **16**, 469–478.

127 G. Chung-Faye, D. Palmer, D. Anderson, J. Clark, M. Downes, et al., **Virus-directed, Enzyme Prodrug Therapy with Nitroimidazole Reductase: A Phase I and Pharmacokinetic Study of its Prodrug, CB1954**, *Clin. Cancer Res.*, 2001, **7**, 2662–2668.

128 P. Patel, J. G. Young, V. Mautner, D. Ashdown, S. Bonney, et al., **A Phase I/II Clinical Trial in Localized Prostate Cancer of an Adenovirus Expressing Nitroreductase with CB1984**, *Mol. Ther.*, 2009, **17**, 1292–1299.

129 R. J. Knox, F. Friedlos and M. P. Boland, **The bioactivation of CB 1954 and its use as a prodrug in antibody-directed enzyme prodrug therapy (ADEPT)**, *Cancer metastasis Rev.*, 1993, **12**, 195–212.

130 N. A. Helsby, D. M. Ferry, A. V Patterson, S. M. Pullen and W. R. Wilson, **2-Amino metabolites are key mediators of CB 1954 and SN 23862 bystander effects in nitroreductase GDEPT**, *Br. J. Cancer*, 2004, **90**, 1084–1092.

131 W. R. Wilson, S. M. Pullen, A. Hogg, N. A. Helsby, K. O. Hicks, et al., **Quantitation of Bystander Effects in Nitroreductase Suicide Gene Therapy Using Three-Dimensional Cell Cultures**, *Cancer Res.*, 2002, **62**, 1425–1432.

132 J. A. Bridgewater, R. J. Knox, J. D. Pitts, M. K. Collins and C. J. Springer, **The bystander effect of the nitroreductase/CB1954 enzyme/prodrug system is due to a cell-permeable metabolite**, *Hum. Gene Ther.*, 1997, **8**, 709–717.

133 A. H. Djeha, A. Hulme, M. T. Dexter, A. Mountain, L. S. Young, et al., **Expression of Escherichia coli B nitroreductase in established human tumor xenografts in mice results in potent antitumoral and bystander effects upon systemic administration of the prodrug CB1954**, *Cancer Gene Ther.*, 2000, **7**, 721–731.

134 G. M. Anlezark, R. G. Melton, R. F. Sherwood, W. R. Wilson, W. A. Denny, et al., **Bioactivation of dinitrobenzamide mustards by an E. coli B nitroreductase**, *Biochem. Pharmacol.*, 1995, **50**, 609–618.

135 F. Ali-Osman, A. Rairkar and P. Young, **Formation and repair of 1,3-bis-(2-chloroethyl)-1-nitrosourea and cisplatin induced total genomic DNA interstrand crosslinks in human glioma cells**, *Cancer Biochem. Biophys.*, 1995, **14**, 231–241.

136 F. Friedlos, W. A. Denny, B. D. Palmer and C. J. Springer, **Mustard Prodrugs for Activation by Escherichia coli Nitroreductase in Gene-Directed Enzyme Prodrug Therapy**, *J. Med. Chem.*, 1997, **40**, 1270–1275.

137 G. J. Atwell, S. Yang, F. B. Pruijn, S. M. Pullen, A. Hogg, et al., **Synthesis and structure-activity relationships for 2,4-dinitrobenzamide-5-mustards as prodrugs for the Escherichia coli nfsB nitroreductase in gene therapy**, *J. Med. Chem.*, 2007, **50**, 1197–1212.

138 D. C. Singleton, D. Li, S. Y. Bai, S. P. Syddall, J. B. Smaill, et al., **The nitroreductase prodrug SN 28343 enhances the potency of systemically administered armed oncolytic adenovirus ONYX-411NTR**, *Cancer Gene Ther.*, 2007, **14**, 953–967.

139 G. A. Prosser, J. N. Copp, A. M. Mowday, C. P. Guise, S. P. Syddall, et al., **Creation and screening of a multi-family bacterial oxidoreductase library to discover novel nitroreductases that efficiently activate the bioreductive prodrugs CB1954 and PR-104A.**, *Biochem. Pharmacol.*, 2013, **85**, 1091–103.

140 B. D. Palmer, W. R. Wilson, S. Cliffe and W. A. Denny, **Hypoxia-selective antitumor agents. 5. Synthesis of water-soluble nitroaniline mustards with selective cytotoxicity for hypoxic mammalian cells**, *J. Med. Chem.*, 1992, **35**, 3214–3222.

141 A. V Patterson, D. M. Ferry, S. J. Edmunds, Y. Gu, R. S. Singleton, et al., **Mechanism of action and preclinical antitumor activity of the novel hypoxia-activated DNA cross-linking agent PR-104.**, *Clin. Cancer Res.*, 2007, **13**, 3922–32.

142 E. Johansson, G. N. Parkinson, W. A. Denny and S. Neidle, **Studies on the nitroreductase prodrug-activating system. Crystal structures of complexes with the inhibitor dicoumarol and dinitrobenzamide prodrugs and of the enzyme active form.**, *J. Med. Chem.*, 2003, **46**, 4009–20.

143 P. Vaupel, **Tumor microenvironmental physiology and its implications for radiation oncology.**, *Semin. Radiat. Oncol.*, 2004, **14**, 198–206.

144 *, † Longqin Hu, † Chengzhi Yu, † Yongying Jiang, † Jiye Han, † Zhuorong Li, et al., **Nitroaryl phosphoramides as novel prodrugs for E. coli nitroreductase activation in enzyme prodrug therapy.**, *J. Med. Chem.*, 2003, **46**, 4818–21.

145 D. R. McCalla, C. Kaiser and M. H. Green, **Genetics of nitrofurazone resistance in Eschericihia coli***J. Bacteriol.*, 1978, **133**, 10–16.

146 D. W. Bryant, D. R. Mccalla, M. Leeksma and P. Laneuville, **Type I nitroreductases of Escherichia coli,** *Can. J. Microbiol.*, 1981, **25**, 81–86.

147 S. Chen, R. Knox, K. Wu, P. S.-K. Deng, D. Zhou, et al., **Molecular Basis of the Catalytic Differences among DT-diaphorase of Human, Rat, and Mouse**, *J. Biol. Chem.*, 1997, **272**, 1437–1439.

148 M. P. Boland, R. J. Knox and J. J. Roberts, **The differences in kinetics of rat and human DT diaphorase result in a differential sensitivity of derived cell lines to CB 1954 (5-(aziridin-1-yl)-2,4-dinitrobenzamide)**, *Biochem. Pharmacol.*, 1991, **41**, 867–875.

149 P. R. Race, A. L. Lovering, R. M. Green, A. Ossor, S. A. White, et al., **Structural and mechanistic studies of Escherichia coli nitroreductase with the antibiotic nitrofurazone. Reversed binding orientations in different redox states of the enzyme**, *J. Biol. Chem.*, 2005, **280**, 13256–13264.

150 G. N. Parkinson, J. V Skelly and S. Neidle, **Crystal Structure of FMN-Dependent Nitroreductase from Escherichia coli B: A Prodrug-Activating Enzyme,** *J. Med. Chem.*, 2000, **43**, 3624–3631.

151 M. Faraday, **The Bakerian Lecture: Experimental Relations of Gold (and Other Metals) to Light**, *Philos. Trans. R. Soc. London*, 1857, **147**, 145–181.

152 F. E. Wagner, S. Haslbeck, L. Stievano, S. Calogero, Q. A. Pankhurst, et al., **Before striking gold in gold-ruby glass**, *Nature*, 2000, **407**, 691–692.

153 A. J. Mieszawska, W. J. M. Mulder, Z. A. Fayad and D. P. Cormode, **Multifunctional Gold Nanoparticles for Diagnosis and Therapy of Disease**, *Mol. Pharm.*, 2013, **10**, 831–847.

154 P. K. Sudeep and T. Emrick, **Polymer • Nanoparticle Composites: Preparative Methods and Electronically Active Materials**, *Polym. Rev.*, 2007, **47**, 155–163.

155 S. Santra, D. Dutta, G. A. Walter and B. M. Moudgil, **Fluorescent nanoparticle probes for cancer imaging**, *Technol. Cancer Res. Treat.*, 2005, **4**, 593–602.

156 A. G. Cuenca, H. Jiang, S. N. Hochwald, M. Delano, W. G. Cance, et al., **Emerging implications of nanotechnology on cancer diagnostics and therapeutics**, *Cancer*, 2006, **107**, 459–466.

157 S. Rana, A. Bajaj, R. Mout and V. M. Rotello, **Monolayer coated gold nanoparticles for delivery applications**, *Biol. Interact. Nanoparticles*, 2012, **64**, 200–216.

158 Y. Su, X. Wei, F. Peng, Y. Zhong, Y. Lu, et al., **Gold nanoparticles-decorated silicon nanowires as highly efficient near-infrared hyperthermia agents for cancer cells destruction.**, *Nano Lett.*, 2012, **12**, 1845–50.

159 L. R. Hirsch, R. J. Stafford, J. A. Bankson, S. R. Sershen, B. Rivera, et al., **Nanoshell-mediated near-infrared thermal therapy of tumors under magnetic resonance guidance**, *Proc. Natl. Acad. Sci.*, 2003, **100**, 13549–13554.

160 R. Sharma and C. J. Chen, **Newer nanoparticles in hyperthermia treatment and thermometry**, *J. Nanoparticle Res.*, 2009, **11**, 671–689.

161 D. F. Emerich and C. G. Thanos, **The pinpoint promise of nanoparticle-based drug delivery and molecular diagnosis**, *Biomol. Eng.*, 2006, **23**, 171–184.

162 Z. P. Xu, Q. H. Zeng, G. Q. Lu and A. B. Yu, **Inorganic nanoparticles as carriers for efficient cellular delivery**, *Biomol. Eng.*, 2006, **61**, 1027–1040.

163 M. Grzelczak, J. Perez-Juste, P. Mulvaney and L. Liz-Marzan, **Shape control in gold nanoparticle synthesis**, *Chem. Soc. Rev.*, 2008, **37**, 1783–1791.

164 C. Burda, X. Chen, R. Narayanan and M. El-Sayed, **Chemistry and Properties of Nanocrystals of Different Shapes**, *Chem. Rev.*, 2005, **105**, 1025–1102.

165 E. C. Dreaden, A. M. Alkilany, X. Huang, C. J. Murphy and M. A. El-Sayed, **The golden age: Gold nanoparticles for biomedicine** *Chem. Soc. Rev.*, 2012, 2740–79.

166 B. D. Chithrani and W. C. W. Chan, **Elucidating the Mechanism of Cellular Uptake and Removal of Protein-Coated Gold Nanoparticles of Different Sizes and Shapes**, *Nano Lett.*, 2007, **7**, 1542–50.

167 R. Shukla, V. Bansal, M. Chaudhary, A. Basu, R. R. Bhonde, et al., **Biocompatibility of Gold Nanoparticles and Their Endocytotic Fate Inside the Cellular Compartment: A Microscopic Overview**, *Langmuir*, 2005, **21**, 10644–54.

168 A. Verma, O. Uzun, Y. Hu, Y. Hu, H.-S. Han, et al., **Surface-structure-regulated cell-membrane penetration by monolayer-protected nanoparticles**, *Nat Mater*, 2008, **7**, 588–595.

169 J. Lovrić, H. S. Bazzi, Y. Cuie, G. R. A. Fortin, F. M. Winnik, et al., **Differences in subcellular distribution and toxicity of green and red emitting CdTe quantum dots**, *J.Mol.Med.*, 2005, **83**, 377–385.

170 C. M. Goodman, C. D. McCusker, T. Yilmaz and V. M. Rotello, **Toxicity of Gold Nanoparticles Functionalized with Cationic and Anionic Side Chains**, *Bioconjug. Chem.*, 2004, **15**, 897–900.

171 B. D. Chithrani, A. A. Ghazani and W. C. W. Chan, **Determining the Size and Shape Dependence of Gold Nanoparticle Uptake into Mammalian Cells**, *Nano Lett.*, 2006, **6**, 662–668.

172 S. K. Ghosh and T. Pal, **Interparticle Coupling Effect on the Surface Plasmon Resonance of Gold Nanoparticles: From Theory to Applications**, *Chem. Rev.*, 2007, **107**, 4797–4862.

173 K. A. Willets and R. P. Van Duyne, **Localized Surface Plasmon Resonance Spectroscopy and Sensing**, *Annu. Rev. Phys. Chem.*, 2007, **58**, 267–297.

174 E. Katz and I. Willner, **Integrated Nanoparticle? Biomolecule Hybrid Systems: Synthesis, Properties, and Applications**, *Angew. Chemie Int. Ed.*, 2004, **43**, 6042–6108.

175 S. Link and M. El-Sayed, **Shape and size dependence of radiative, non-radiative and photothermal properties of gold nanocrystals**, *Int. Rev. Phys. Chem.*, 2000, **19**, 409–453.

176 W. H. De Jong, W. I. Hagens, P. Krystek, M. C. Burger, A. J. A. M. Sips, *et al*., **Particle size-dependent organ distribution of gold nanoparticles after intravenous administration**, *Biomaterials*, 2008, **29**, 1912–1919.

177 S. Underwood and P. Mulvaney, **Effect of the Solution Refractive Index on the Color of Gold Colloids**, *Langmuir*, 1994, **10**, 3427–3430.

178 P. Mulvaney, **Surface Plasmon Spectroscopy of Nanosized Metal Particles**, *Langmuir*, 1996, **12**, 788–800.

179 A. C. Templeton, J. J. Pietron, R. W. Murray and P. Mulvaney, **Solvent Refractive Index and Core Charge Influences on the Surface Plasmon Absorbance of Alkanethiolate Monolayer-Protected Gold Clusters**, *J. Phys. Chem. B*, 2000, **104**, 564–570.

180 R. Gref, A. Domb, P. Quellec, T. Blunk, R. H. Müller, *et al*., **The controlled intravenous delivery of drugs using PEG-coated sterically stabilized nanospheres.**, *Adv. Drug Deliv. Rev.*, 1995, **16**, 215–233.

181 Y.-S. Chen, Y.-C. Hung, I. Liau and G. Huang, **Assessment of the In Vivo Toxicity of Gold Nanoparticles**, *Nanoscale Res. Lett.*, 2009, **4**, 858–864.

182 M. Longmire, P. L. Choyke and H. Kobayashi, **Clearance Properties of Nano-sized Particles and Molecules as Imaging Agents: Considerations and Caveats**, *Nanomedicine*, 2008, **3**, 703–717.

183 E. E. Connor, J. Mwamuka, A. Gole, C. J. Murphy and M. D. Wyatt, **Gold Nanoparticles Are Taken Up by Human Cells but Do Not Cause Acute Cytotoxicity**, *Small*, 2005, **1**, 325–327.

184 N. Khlebtsov and L. Dykman, **Biodistribution and toxicity of engineered gold nanoparticles: a review of in vitro and in vivo studies**, *Chem. Soc. Rev.*, 2011, **40**, 1647–1671.

185 I. Fratoddi, I. Venditti, C. Cametti and M. V Russo, **How toxic are gold nanoparticles? the state-of-the-art**, *Nano Res.*, 2015, **8**, 1771–1799.

186 A. Alkilany and C. Murphy, **Toxicity and cellular uptake of gold nanoparticles: what we have learned so far?**, *J. Nanoparticle Res.*, 2010, **12**, 2313–2333.

187 Q. A. Pankhurst, N. T. K. Thanh, S. K. Jones and J. Dobson, **Progress in applications of magnetic nanoparticles in biomedicine**, *J. Phys. D. Appl. Phys.*, 2009, **42**, 224001.

188 M. Tang, P. J. Russell and A. Khatri, **Magnetic nanoparticles: prospects in cancer imaging and therapy**, *Discov. Med.*, 2007, **7**, 68–74.

189 K. Maier-Hauff, F. Ulrich, D. Nestler, H. Niehoff, P. Wust, et al., **Efficacy and safety of intratumoral thermotherapy using magnetic iron-oxide nanoparticles combined with external beam radiotherapy on patients with recurrent glioblastoma multiforme**, *J. Neurooncol.*, 2011, **103**, 317–324.

190 M. A. Adarsh Sandhu and Hiroshi Handa and, **Synthesis and applications of magnetic nanoparticles for biorecognition and point of care medical diagnostics**, *Nanotechnology*, 2010, **21**, 442001.

191 M. Colombo, S. Carregal-Romero, M. F. Casula, L. Gutierrez, M. P. Morales, *et al.*, **Biological applications of magnetic nanoparticles** , *Chem. Soc. Rev.*, 2012, **41**, 4306-4334.

192 S. Laurent, D. Forge and M. Port, **Magnetic iron oxide nanopaticles: Synthesis, stabilization, vectorization, physiochemical characterizations and biological applications,** *Chem. Rev.*, 2008, **108**, 2064–2110.

193 Y. Li, Z. Chen and N. Gu, **In vitro biological effects of magnetic nanoparticles**, *Chinese Sci. Bull.*, 2012, **57**, 3972–3978.

194 A. G. Roca, R. Costo, A. F. Rebolledo, S. Veintemillas-Verdaguer, P. Tartaj, *et al.*, **Progress in the preparation of magnetic nanoparticles for applications in biomedicine**, *J. Phys. D. Appl. Phys.*, 2009, **42**, 224002.

195 A. G. Kolhatkar, A. C. Jamison, D. Litvinov, R. C. Willson and T. R. Lee, **Tuning the Magnetic Properties of Nanoparticles**, *Int. J. Mol. Sci.*, 2013, **14**, 15977–16009.

196 P. V Asharani, Y. lianwu, Z. Gong and S. Valiyaveettil, **Comparison of the toxicity of silver, gold and platinum nanoparticles in developing zebrafish embryos**, *Nanotoxicology*, 2011, **5**, 43–54.

197 S. Chattopadhyay, S. K. Dash, S. Tripathy, B. Das, D. Mandal, et al., **Toxicity of cobalt oxide nanoparticles to normal cells; an in vitro and in vivo study**, *Chem. Biol. Interact.*, 2015, **226**, 58–71.

198 R. M. Taylor, D. L. Huber, T. C. Monson, V. Esch and L. O. Sillerud, **Structural and Magnetic Characterization of Superparamagnetic Iron Platinum Nanoparticle Contrast Agents for Magnetic Resonance Imaging**, *J. Vac. Sci. Technol. Nanotechnol. Microelectron. Mater. Process. Meas. Phenom.*, 2012, **30**, 101–106.

199 L. Han, U. Wiedwald, B. Kuerbanjiang and P. Ziemann, **Fe oxidation versus Pt segregation in FePt nanoparticles and thin films.**, *Nanotechnology*, 2009, **20**, 285706.

200 L. C. Varanda and M. Jafelicci, **Self-assembled FePt nanocrystals with large coercivity: reduction of the fcc-to-L1(0) ordering temperature.**, *J. Am. Chem. Soc.*, 2006, **128**, 11062–6.

201 S. Maenosono, T. Suzuki and S. Saita, **Superparamagnetic FePt nanoparticles as excellent MRI contrast agents**, *J. Magn. Magn. Mater.*, 2008, **320**, 79–83.

202 M. P. Morales, M. F. Bédard, A. G. Roca, P. de la Presa, A. Hernando, et al., **Relaxation times of colloidal iron platinum in polymer matrixes**, *J. Mater. Chem.*, 2009, **19**, 6381.

203 R. M. Taylor, D. L. Huber, T. C. Monson, A.-M. S. Ali, M. Bisoffi, *et al.*, **Multifunctional iron platinum stealth immunomicelles: targeted detection of human prostate cancer cells using both fluorescence and magnetic resonance imaging.**, *J. Nanopart. Res.*, 2011, **13**, 4717–4729.

204 F. Zhao, M. Rutherford, S. Y. Grisham and X. Peng, **Formation of monodisperse FePt alloy nanocrystals using air-stable precursors: fatty acids as alloying mediator and reductant for Fe3+ precursors.**, *J. Am. Chem. Soc.*, 2009, **131**, 5350–8.

205 C. Xu, Z. Yuan, N. Kohler, J. Kim, M. A. Chung, *et a*l., **FePt nanoparticles as an Fe reservoir for controlled Fe release and tumor inhibition.**, *J. Am. Chem. Soc.*, 2009, **131**, 15346–51.

206 E. Pollert, P. Veverka, M. Veverka, O. Kaman, K. Závěta, et al., **Search of new core materials for magnetic fluid hyperthermia: Preliminary chemical and physical issues**, *Prog. Solid State Chem.*, 2009, **37**, 1–14.

207 L. T. Lu, L. D. Tung, I. Robinson, D. Ung, B. Tan, et al., **Size and shape control for water-soluble magnetic cobalt nanoparticles using polymer ligands**, *J. Mater. Chem.*, 2008, **18**, 2453.

208 L. M. Parkes, R. Hodgson, L. T. Lu, L. D. Tung, I. Robinson, *et al*., **Cobalt nanoparticles as a novel magnetic resonance contrast agent-relaxivities at 1.5 and 3 Tesla**, *Contrast Media Mol. Imaging*, 2008, **3**, 150–156.

209 A. K. Gupta and M. Gupta, **Synthesis and surface engineering of iron oxide nanoparticles for biomedical applications**, *Biomaterials*, 2005, **26**, 3995–4021.

210 L. H. Reddy, J. L. Arias, J. Nicolas and P. Couvreur, **- Magnetic Nanoparticles: Design and Characterization, Toxicity and Biocompatibility, Pharmaceutical and Biomedical Applications**, - *Chem. Rev.*, 2012, **112**, 5818–5878.

211 G. Han, P. Ghosh and V. M. Rotello, **Chapter 4: Multifunctional gold nanoparticles for drug delivery,** *Bio-Applications Of Nanoparticles*, Springer Science, 2007, 48–56.

212 I. L. Medintz, H. T. Uyeda, E. R. Goldman and H. Mattoussi, **Quantum dot bioconjugates for imaging, labelling and sensing**, *Nat Mater*, 2005, **4**, 435–446.

213 D. Jiles, **Introduction to magnetism and magnetic materials,** Chapman and Hall, London; New York, 1991.

214 A. H. Morrish, **The physical principles of magnetism,** Wiley-IEEE Press, 2001.

215 A. S. Teja and P.-Y. Koh, **Synthesis, properties, and applications of magnetic iron oxide nanoparticles**, *Prog. Cryst. Growth Charact. Mater.*, 2009, **55**, 22–45.

216 R. Massart, **Preparation of aqueous magnetic liquids in alkaline and acidic media**, *Magn. IEEE Trans.*, 1981, **17**, 1247–1248.

217 E. Okon, D. Pouliquen, P. Okon, Z. V Kovaleva, T. P. Stepanova, et al., **Biodegradation of magnetite dextran nanoparticles in the rat. A histologic and biophysical study**, *Lab. Invest.*, 1994, **71**, 895–903.

218 A. S. Karakoti, S. Das, S. Thevuthasan and S. Seal, **PEGylated Inorganic Nanoparticles**, *Angew. Chemie Int. Ed.*, 2011, **50**, 1980–1994.

219 C. Tassa, S. Y. Shaw and R. Weissleder, **Dextran-Coated Iron Oxide Nanoparticles: A Versatile Platform for Targeted Molecular Imaging, Molecular Diagnostics, and Therapy**, *Acc. Chem. Res.*, 2011, **44**, 842–852.

220 S. L. Easo and P. V Mohanan, **Dextran stabilized iron oxide nanoparticles: synthesis, characterization and in vitro studies**, *Carbohydr. Polym.*, 2013, **92**, 726–732.

221 A.-H. Lu, E. L. Salabas and F. Schüth, **Magnetic Nanoparticles: Synthesis, Protection, Functionalization, and Application**, *Angew. Chemie Int. Ed.*, 2007, **46**, 1222–1244.

222 A. Eifler and C. S. Thaxton, **Nanoparticles therapeutics: FDA approval, clinical trials, regulatory pathways and case studies,** *Methods. Mol. Biol.*, 2011, **726,** 325-338.

223 P. F. Searle, M.-J. Chen, L. Hu, P. R. Race, A. L. Lovering, et al., **Nitroreductase: A prodrug-activating enzyme for cancer gene therapy**, *Clin. Exp. Pharmacol. Physiol.*, 2004, **31**, 811–816.

224 C. D. Gwenin, M. Kalaji, P. A. Williams and R. M. Jones, **The orientationally controlled assembly of genetically modified enzymes in an amperometric biosensor**, *Biosens. Bioelectron.*, 2007, **22**, 2869–2875.

225 A. K. Gupta and M. Gupta, **Cytotoxicity suppression and cellular uptake enhancement of surface modified magnetic nanoparticles**, *Biomaterials*, 2005, **26**, 1565–1573.

226 P.-L. Tran, T.-D. Tran, T. Vo and B.-J. Lee, **Promising iron oxide-based magnetic nanoparticles in biomedical engineering**, *Arch. Pharm. Res.*, 2012, **35**, 2045–2061.

227 M.-C. C. Daniel and D. Astruc, **Gold nanoparticles: assembly, supramolecular chemistry, quantum-size-related properties, and applications toward biology, catalysis, and nanotechnology**, *Chem. Rev.*, 2004, **104**, 293–346.

228 G. H. Bahmanrokh, M. Hashim, N. Soltani, I. Ismail, P. Vaziri, *et al*., **Magnetic-property enhancement of sized controlled cobalt-gold core-shell nanocrystals**, *Dig. J. Nanomater. Biostructures*, 2012, **7**, 1799–1810.

229 M. C. Daniel and D. Astruc, **Gold nanoparticles: assembly, supramolecular chemistry, quantum-size-related properties, and applications toward biology, catalysis, and nanotechnology**, *Chem. Rev.*, 2004, **104**, 293–346.

230 W. L. Zhou, E. E. Carpenter, J. Lin, A. Kumbhar, J. Sims, *et al*., **Nanostructures of gold coated iron core-shell nanoparticles and the nanobands assembled under magnetic field**, *EPJD*, 2001, **16**, 289–292.

231 J. Lin, W. Zhou, A. Kumbhar, J. Wiemann, J. Fang, *et al*., **Gold-Coated Iron (Fe@Au) Nanoparticles: Synthesis, Characterization, and Magnetic Field-Induced Self-Assembly**, *J. Solid State Chem.*, 2001, **159**, 26–31.

232 T. Kinoshita, S. Seino, K. Okitsu, T. Nakayama, T. Nakagawa, *et al*., **Magnetic evaluation of nanostructure of gold–iron composite particles synthesized by a reverse micelle method**, *J. Alloys Compd.*, 2003, **359**, 46–50.

233 Z. Xu, Y. Hou and S. Sun, **Magnetic Core/Shell Fe3O4/Au and Fe3O4/Au/Ag Nanoparticles with Tunable Plasmonic Properties**, *J. Am. Chem. Soc.*, 2007, **129**, 8698-8699.

234 M. Gonzales and K. M. Krishnan, **Phase transfer of highly monodisperse iron oxide nanocrystals with Pluronic F127 for biomedical applications**, *J. Magn. Magn. Mater.*, 2007, **311**, 59–62.

235 F. Chen, G.-Q. Xu and T. S. A. Hor, **Preparation and assembly of colloidal gold nanoparticles in CTAB-stabilized reverse microemulsion**, *Mater. Lett.*, 2003, **57**, 3282–3286.

236 Z. Zhong, S. Patskovskyy, P. Bouvrette, J. H. T. Luong and A. Gedanken, **The Surface Chemistry of Au Colloids and Their Interactions with Functional Amino Acids**, *J. Phys. Chem. B*, 2004, **108**, 4046–4052.

237 M. Casavola, R. Buonsanti, G. Caputo and P. D. Cozzoli, **Colloidal Strategies for Preparing Oxide-Based Hybrid Nanocrystals**, *Eur. J. Inorg. Chem.*, 2008, **2008**, 837–854.

238 T. T. Hien Pham, C. Cao and S. J. Sim, **Application of citrate-stabilized gold-coated ferric oxide composite nanoparticles for biological separations**, *J. Magn. Magn. Mater.*, 2008, **320**, 2049–2055.

239 J. Lyon, D. A. Feming, M. B. Stone, J. L. Lyon, D. A. Fleming, *et al*., **Synthesis of Fe Oxide Core/Au Shell Nanoparticles by Iterative Hydroxylamine Seeding**, *Nano Lett.*, 2004, **4**, - 719.

240 A. R. Tao, S. Habas and P. Yang, **Shape Control of Colloidal Metal Nanocrystals**, *Small*, 2008, **4**, 310–325.

241 C. K. Lo, D. Xiao and M. M. F. Choi, **Homocysteine-protected gold-coated magnetic nanoparticles: synthesis and characterisation**, *J. Mater. Chem.*, 2007, **17**, 2418–2427.

242 L. Wang, J. Luo, Q. Fan, M. Suzuki, I. S. Suzuki, *et al*., **Monodispersed Core-Shell Fe3O4@Au Nanoparticles**, *J. Phys. Chem. B*, 2005, **109**, 21593–21601.

243 L. Wang, H.-Y. Park, S. I.-I. Lim, M. J. Schadt, D. Mott, *et al*., **Core@shell nanomaterials: gold-coated magnetic oxide nanoparticles**, *J. Mater. Chem.*, 2008, **18**, 2629–2635.

244 S. Choi, J. Seo, R. F. H. Bohaty and C. D. Poulter, **Regio- and Chemoselective Immobilization of Proteins on Gold Surfaces**, *Bioconjug. Chem.*, 2014, **25**, 269–275.

245 G. Bayramoğlu and M. Y. Arıca, **Enzymatic removal of phenol and p-chlorophenol in enzyme reactor: Horseradish peroxidase immobilized on magnetic beads**, *J. Hazard. Mater.*, 2008, **156**, 148–155.

246 A. Johnson, A. Zawadzka, L. Deobald, R. Crawford and A. Paszczynski, **Novel method for immobilization of enzymes to magnetic nanoparticles**, *J. Nanoparticle Res.*, 2008, **10**, 1009–1025.

247 T. Kuroiwa, Y. Noguchi, M. Nakajima, S. Sato, S. Mukataka, *et al.*, **Production of chitosan oligosaccharides using chitosanase immobilized on amylose-coated magnetic nanoparticles**, *Process Biochem.*, 2008, **43**, 62–69.

248 R. Konwarh, N. Karak, S. K. Rai and A. K. Mukherjee, **Polymer-assisted iron oxide magnetic nanoparticle immobilized keratinase**, *Nanotechnology*, 2009, **20**, 225107.

249 N. A. Kalkan, S. Aksoy, E. A. Aksoy and N. Hasirci, **Preparation of chitosan-coated magnetite nanoparticles and application for immobilization of laccase**, *J. Appl. Polym. Sci.*, 2011, **123**, 2, 707-716.

250 S. A. Ansari, Q. Husain, S. Qayyum and A. Azam, **Designing and surface modification of zinc oxide nanoparticles for biomedical applications**, *Food Chem. Toxicol.*, 2011, **49**, 2107–2115.

251 K. E. Sapsford, W. R. Algar, L. Berti, K. B. Gemmill, B. J. Casey, *et al*., **Functionalizing Nanoparticles with Biological Molecules: Developing Chemistries that Facilitate Nanotechnology**, *Chem. Rev.*, 2013, **113**, 1904–2074.

252 J. Conde, J. T. Dias, V. Grazu, M. Moros, P. V Baptista, *et al*., **Revisiting 30 years of biofunctionalization and surface chemistry of inorganic nanoparticles for nanomedicine**, *Front. Chem.*, 2014, **2**, 1–27.

253 L. Cao, **Immobilised enzymes: science or art?**, *Curr. Opin. Chem. Biol.*, 2005, **9**, 217–226.

254 F. Khan, M. He and M. J. Taussig, **Double-Hexahistidine Tag with High-Affinity Binding for Protein Immobilization, Purification, and Detection on Ni-Nitrilotriacetic Acid Surfaces**, *Anal. Chem.*, 2006, **78**, 3072–3079.

255 E. Hochuli, W. Bannwarth, H. Dobeli, R. Gentz and D. Stuber, **Genetic Approach to Facilitate Purification of Recombinant Proteins with a Novel Metal Chelate Adsorbent**, *Nat Biotech*, 1988, **6**, 1321–1325.

256 J. Porath, **Immobilized metal ion affinity chromatography**, *Protein Expr. Purif.*, 1992, **3**, 263–281.

257 K.-B. Lee, S. Park and C. A. Mirkin, **Multicomponent Magnetic Nanorods for Biomolecular Separations**, *Angew. Chemie Int. Ed.*, 2004, **43**, 3048–3050.

258 I. S. Lee, N. Lee, J. Park, B. H. Kim, Y.-W. Yi, et al., **Ni/NiO Core/Shell Nanoparticles for Selective Binding and Magnetic Separation of Histidine-Tagged Proteins**, *J. Am. Chem. Soc.*, 2006, **128**, 10658–10659.

259 A. Muñoz and M. Costa, **Elucidating the mechanisms of nickel compound uptake: A review of particulate and nano-nickel endocytosis and toxicity**, *Toxicol. Appl. Pharmacol.*, 2012, **260**, 1–16.

260 J. M. Kogot, H. J. England, G. F. Strouse and T. M. Logan, **Single Peptide Assembly onto a 1.5 nm Au Surface *via* a Histidine Tag**, *J. Am. Chem. Soc.*, 2008, **130**, 16156–16157.

261 O. Cohavi, D. Reichmann, R. Abramovich, A. B. Tesler, G. Bellapadrona, *et al*., **A Quantitative, Real-Time Assessment of Binding of Peptides and Proteins to Gold Surfaces**, *Chem. ? A Eur. J.*, 2011, **17**, 1327–1336.

262 J. C. Love, L. A. Estroff, J. K. Kriebel, R. G. Nuzzo and G. M. Whitesides, **Self-Assembled Monolayers of Thiolates on Metals as a Form of Nanotechnology**, *Chem. Rev.*, 2005, **105**, 1103–1170.

263 M. D. Liptak, K. M. Van Heuvelen and T. C. Brunold, **Computational studies of bioorganometallic enzymes and cofactors**, *Met. Ions Life Sci.*, 2009, **6**, 417–460.

264 E. Boisselier and D. Astruc, **Gold nanoparticles in nanomedicine: preparations, imaging, diagnostics, therapies and toxicity**, *Chem. Soc. Rev.*, 2009, **38**, 1759–1782.

265 P. Tengvall, I. Lundström and B. Liedberg, **Protein adsorption studies on model organic surfaces: an ellipsometric and infrared spectroscopic approach**, *Biomaterials*, 1998, **19**, 407–422.

266 F. X. Zhang, L. Han, L. B. Israel, J. G. Daras, M. M. Maye, *et al.*, **Colorimetric detection of thiol-containing amino acids using gold nanoparticles**, *Analyst*, 2002, **127**, 462–465.

267 G. Hager and A. G. Brolo, **Adsorption/desorption behaviour of cysteine and cystine in neutral and basic media: electrochemical evidence for differing thiol and disulfide adsorption to a Au(1 1 1) single crystal electrode**, *Thin Org. Film.*, 2003, **550-551**, 291–301.

268 K. Arihara, T. Ariga, N. Takashima, K. Arihara, T. Okajima, et al., **Multiple voltammetric waves for reductive desorption of cysteine and 4-mercaptobenzoic acid monolayers self-assembled on gold substrates**, *Phys. Chem. Chem. Phys.*, 2003, **5**, 3758–3761.

269 Y. Zhao, F. Zhou, H. Zhou and H. Su, **The structural and bonding evolution in cysteine-gold cluster complexes**, *Phys. Chem. Chem. Phys.*, 2013, **15**, 1690–1698.

270 J. M. Lee, H. K. Park, Y. Jung, J. K. Kim, S. O. Jung, et al., **Direct Immobilization of Protein G Variants with Various Numbers of Cysteine Residues on a Gold Surface**, *Anal. Chem.*, 2007, **79**, 2680–2687.

271 Z. Shen, G. A. Stryker, R. L. Mernaugh, L. Yu, H. Yan, et al., **Single-Chain Fragment Variable Antibody Piezoimmunosensors**, *Anal. Chem.*, 2005, **77**, 797–805.

272 K. S. Carmon, R. E. Baltus and L. A. Luck, **A Piezoelectric Quartz Crystal Biosensor: The Use of Two Single Cysteine Mutants of the Periplasmic Escherichia coli Glucose/Galactose Receptor as Target Proteins for the Detection of Glucose**, *Biochemistry*, 2004, **43**, 14249–14256.

273 C. Gwenin, M. Kalaji and V. Roberts, **Drug activation system,** WO 2011026898 A2, 10/03/2011.

274 M. D. Roldán, E. Pérez-Reinado, F. Castillo and C. Moreno-Vivián, **Reduction of polynitroaromatic compounds: the bacterial nitroreductases**, *FEMS Microbiol. Rev.*, 2008, **32**, 474–500.

275 C. Gwenin, M. Kalaji, P. Williams and C. Kay, **A kinetic analysis of three modified novel nitroreductases**, *Biodegradation*, 2011, **22**, 463–474.

276 R. Skloot, **The immortal life of Henrietta Lacks,** Crown Publishing, New York, 2010.

277 R. Rahbari, T. Sheahan, V. Modes, P. Collier, C. Macfarlane, et al., **A novel L1 retrotransposon marker for HeLa cell line identification**, *Biotechniques*, 2009, **46**, 277–284.

278 R. A. MacLeod, W. G. Dirks, Y. Matsuo, M. Kaufmann, H. Milch, *et al.*, **Widespread intraspecies cross-contamination of human tumor cell lines arising at source**, *Int. J. cancer.Journal Int. du cancer*, 1999, **83**, 555–563.

279 J. J. M. Landry, P. T. Pyl, T. Rausch, T. Zichner, M. M. Tekkedil, *et al.*, **The Genomic and Transcriptomic Landscape of a HeLa Cell Line**, *G3*, 2013, **3**, 1213–1224.

280 W. F. Scherer, J. T. Syverton and G. O. Gey, **Studies on the propagation in vitro of poliomyelitis viruses: IV. Viral multiplication in a stable strain of human malignant epithelial cells (strain HeLa) derived from an epidermoid carcinoma of the cervix**, *J. Exp. Med.*, 1953, **97**, 695–710.

281 C. Diep, G. Kaur, D. Keppler and A. Lin, **Retroviral expression of human cystatin genes in HeLa cells,** *Cervical Cancer: Methods Mol. Biol.*, 2015, **1249**, 121–131.

282 B. P. Lucey, W. Nelson-Rees and G. M. Hutchins, **Henrietta Lacks, HeLa Cells, and Cell Culture Contamination**, *Arch. Pathol. Lab. Med.*, 2009, **133**, 1463–1467.

283 M. Arbyn, X. Castellsagué, S. de Sanjosé, L. Bruni, M. Saraiya, *et al*., **Worldwide burden of cervical cancer in 2008**, *Ann. Oncol.*, 2011, **22**, 2675–2686.

284 R. Siegel, J. Ma, Z. Zou and A. Jemal, **Cancer statistics, 2014**, *CA. Cancer J. Clin.*, 2014, **64**, 9–29.

285 H. D. Soule, J. Vazquez, A. Long, S. Albert and M. Brennan, **A Human Cell Line From a Pleural Effusion Derived From a Breast Carcinoma**, *J. Natl. Cancer Inst.*, 1973, **51**, 1409–1416.

286 D. E. Sosnovik, M. Nahrendorf and R. Weissleder, **Magnetic nanoparticles for MR imaging: agents, techniques and cardiovascular applications.**, *Basic Res. Cardiol.*, 2008, **103**, 122–30.

287 J. Wang, P. Song, S. Schrieber, Q. Liu, Q. Xu, et al., **Exposure-response relationship of T-DM1: insight into dose optimization for patients with HER2-positive metastatic breast cancer.**, *Clin. Pharmacol. Ther.*, 2014, **95**, 558–64.

288 A. Sparreboom, **Paclitaxel Pharmacokinetics, Threshold Models, and Dosing Strategies**, *J. Clin. Oncol.*, 2003, **21**, 2803–2804.

289 S. C. Walpole, D. Prieto-Merino, P. Edwards, J. Cleland, G. Stevens, *et al*., **The weight of nations: an estimation of adult human biomass.**, *BMC Public Health*, 2012, **12**, 439.

290 C. Sun, J. Lee and M. Zhang, **Magnetic nanoparticles in MR imaging and drug delivery**, *Adv. Drug Deliv. Rev.*, 2008, **60**, 1252–1265.

291 V. Grazú, A. M. Silber, M. Moros, L. Asín, T. E. Torres, et al., **Application of magnetically induced hyperthermia in the model protozoan Crithidia fasciculata as a potential therapy against parasitic infections.**, *Int. J. Nanomedicine*, 2012, **7**, 5351–60.

292 H. Tegel, S. Tourle, J. Ottosson and A. Persson, **Increased levels of recombinant human proteins with the Escherichia coli strain Rosetta(DE3)**, *Protein Expr. Purif.*, 2010, **69**, 159–167.

293 W. Haiss, D. Lackey, J. K. Sass and K. H. Besocke, **Atomic resolution scanning tunneling microscopy images of Au(111) surfaces in air and polar organic solvents**, *J. Chem. Phys.*, 1991, **95**, 2193–2196.

294 K. R. Brown, D. G. Walter and M. J. Natan, **Seeding of Colloidal Au Nanoparticle Solutions. 2. Improved Control of Particle Size and Shape**, *Chem. Mater.*, 2000, **12**, 306–313.

295 H. D. Hill and C. A. Mirkin, **The bio-barcode assay for the detection of protein and nucleic acid targets using DTT-induced ligand exchange**, *Nat.Protocols*, 2006, **1**, 324–336.

296 A. Vanderkooy, Y. Chen, F. Gonzaga and M. A. Brook, **Silica Shell/Gold Core Nanoparticles: Correlating Shell Thickness with the Plasmonic Red Shift upon Aggregation**, *ACS Appl. Mater. Interfaces*, 2011, **3**, 3942–3947.

297 J. M. Berg, J. L. Tymoczko and L. Stryer, *Biochemistry: International Edition*, W. H. Freeman, 6th Edition, 2006.

298 Trevigen Inc., **Calcien AM cell viability kit protocol**, 2011, E2/25/11v1.

299 T. Mosmann, **Rapid colorimetric assay for cellular growth and survival: application to proliferation and cytotoxicity assays**, *J. Immunol. Methods*, 1983, **65**, 55–63.

300 G. A. Prosser, A. V Patterson and D. F. Ackerley, **UvrB gene deletion enhances SOS chromotest sensitivity for nitroreductases that preferentially generate the 4-hydroxylamine metabolite of the anti-cancer prodrug CB1954**, *J. Biotechnol.*, 2010, **150**, 190–194.

301 G. A. Prosser, J. N. Copp, S. P. Syddall, E. M. Williams, J. B. Smaill, *et al*., **Discovery and evaluation of Escherichia coli nitroreductases that activate the anti-cancer prodrug CB1954**, *Biochem. Pharmacol.*, 2010, **79**, 678–687.

302 S. O. Vass, D. Jarrom, W. R. Wilson, E. I. Hyde and P. F. Searle, **E. coli NfsA: an alternative nitroreductase for prodrug activation gene therapy in combination with CB1954** , *Br. J. Cancer*, 2009, **100**, 1903–1911.

303 E. J. Dell, **Detection of NADH and NADPH with the Omega's high speed, full UV/Vis absorabance spectrometer,** *BMG Labtech Appl. Note 170*, 2008, 1–2.

304 A. C. Celotto, V. K. Capellini, C. F. Baldo, M. B. Dalio, A. J. Rodrigues, *et al*., **Effects of acid-base imbalance on vascular reactivity.**, *Braz. J. Med. Biol. Res.*, 2008, **41**, 439–45.

305 M. H. Y. Tang, N. A. Helsby, W. R. Wilson and M. D. Tingle, **Aerobic 2- and 4-nitroreduction of CB 1954 by human liver.**, *Toxicology*, 2005, **216**, 129–39.

306 C. D. Emptage, R. J. Knox, M. J. Danson and D. W. Hough, **Nitroreductase from Bacillus licheniformis: A stable enzyme for prodrug activation**, *Biochem. Pharmacol.*, 2009, **77**, 21–29.

307 P. R. Race, A. L. Lovering, S. A. White, J. I. Grove, P. F. Searle, *et al*., **Kinetic and Structural Characterisation of Escherichia coli Nitroreductase Mutants Showing Improved Efficacy for the Prodrug Substrate CB1954**, *J. Mol. Biol.*, 2007, **368**, 481–492.

308 D. Jarrom, M. Jaberipour, C. P. Guise, S. Daff, S. A. White, *et al*., **Steady-State and Stopped-Flow Kinetic Studies of Three Escherichia coli NfsB Mutants with Enhanced Activity for the Prodrug CB1954**, *Biochem.*, 2009, **48**, 7665-7672.

309 A. Corrias, G. Mountjoy, D. Loche, V. Puntes, A. Falqui, et al., **Identifying Spinel Phases in Nearly Monodisperse Iron Oxide Colloidal Nanocrystal**, *J. Phys. Chem. C*, 2009, **113**, 18667–18675.

310 A. L. Patterson, **The Scherrer Formula for X-Ray Particle Size Determination**, *Phys. Rev.*, 1939, **56**, 978–982.

311 A. Monshi, M. Foroughi and M. Monshi, **Modified Scherrer Equation Estimate More Accurately Nano-Crystallite Size Using XRD**, *World J. Nano Sci. Eng.*, 2012, **2**, 154–160.

312 C. Pereira, A. M. Pereira, C. Fernandes, M. Rocha, R. Mendes, *et al*., **Superparamagnetic MFe2O4 (M = Fe, Co, Mn) Nanoparticles: Tuning the Particle Size and Magnetic Properties through a Novel One-Step Coprecipitation Route**, *Chem. Mater.*, 2012, **24**, 1496–1504.

313 B. Kumar, K. Smita, L. Cumbal and A. Debut, **Biogenic synthesis of iron oxide nanoparticles for 2-arylbenzimidazole fabrication**, *SI Nanomater. Energy Environ. Appl.*, 2014, **18**, 364–369.

314 I. Y. Goon, L. M. H. Lai, M. Lim, P. Munroe, J. J. Gooding, *et al*., **Fabrication and Dispersion of Gold-Shell-Protected Magnetite Nanoparticles: Systematic Control Using Polyethyleneimine**, *Chem. Mater.*, 2009, **21**, 673–681.

315 Y. S. Kang, S. Risbud, J. F. Rabolt and P. Stroeve, **Synthesis and Characterization of Nanometer-Size Fe3O4 and γ-Fe2O3 Particles**, *Chem. Mater.*, 1996, **8**, 2209–2211.

316 J. Jeong, T. H. Ha and B. H. Chung, **Enhanced reusability of hexa-arginine-tagged esterase immobilized on gold-coated magnetic nanoparticles**, *Anal. Chim. Acta*, 2006, **569**, 203–209.

317 A. Ulman, **Formation and Structure of Self-Assembled Monolayers**, *Chem. Rev.*, 1996, **96**, 1533–1554.

318 E. Pensa, C. Vericat, D. Grumelli, R. C. Salvarezza, S. H. Park, *et al.*, **New insight into the electrochemical desorption of alkanethiol SAMs on gold**, *Phys. Chem. Chem. Phys.*, 2012, **14**, 12355–12367.

319 A. Christofferson and J. Wilkie, **Mechanism of CB1954 reduction byEscherichia coli nitroreductase**, *Biochem. Soc. Trans.*, 2009, **37**, 413–418.

320 J. van Meerloo, G. L. Kaspers and J. Cloos, **Cell sensitivity assays: The MTT assay,** in *Cancer Cell Culture Meth. Mol. Biol.* 2011, **731**, 237–245.

321 C. C. Wang, S. Y. Lin, Y. H. Lai, Y. J. Liu, Y. L. Hsu, *et al.*, **Dimethyl Sulfoxide Promotes the Multiple Functions of the Tumor Suppressor HLJ1 through Activator Protein-1 Activation in NSCLC Cells**, *PLoS One*, 2012, **7**, e33772.

322 A. Gole, C. Dash, V. Ramakrishnan, S. R. Sainkar, A. B. Mandale, *et al.*, **Pepsin-Gold Colloid Conjugates: Preparation, Characterization, and Enzymatic Activity**, *Langmuir*, 2001, **17**, 1674–1679.

323 M. Lv, E. Zhu, Y. Su, Q. Li, W. Li, et al., **Trypsin-Gold Nanoparticle Conjugates: Binding, Enzymatic Activity, and Stability**, *Prep. Biochem. Biotechnol.*, 2009, **39**, 429–438.

324 H. Hinterwirth, W. Lindner and M. Lammerhofer, **Bioconjugation of trypsin onto gold nanoparticles: Effect of surface chemistry on bioactivity**, *Anal. Chim. Acta*, 2012, **733**, 90–97.

325 D. H. Palmer, V. Mautner, D. Mirza, S. Oliff, W. Gerritsen, *et al.*, **Virus-Directed Enzyme Prodrug Therapy: Intratumoral Administration of a Replication-Deficient Adenovirus Encoding Nitroreductase to Patients With Resectable Liver Cancer**, *J. Clin. Oncol.*, 2004, **22**, 1546–1552.

326 S. J. DeNardo, G. L. DeNardo, L. A. Miers, A. Natarajan, A. R. Foreman, *et al.*, **Development of tumour targeting bioprobes (^{111}In-chimeric L6 monoclonal antibody nanoparticles) for alternating magnetic field cancer therapy,** *Clin. Cancer Res.;* 2005, **11**, 7087-7092.